

*The Role of Sediments Physical Properties in  
Preconditioning Submarine Landslides Initiation:*  
A Sedimentological and a Numerical Investigation

vorgelegt von / submitted by

**Hadar Elyashiv**

CUMULATIVE DISSERTATION

eingereicht in Erfüllung der Voraussetzungen für die Promotion im Rahmen der Cotutelle-Vereinbarung zwischen dem Fachbereich Geowissenschaften an der Universität Bremen (Germany) und der Fakultät für Naturwissenschaften der Universität Haifa (Israel).

submitted in fulfilment of the requirements for the doctoral degree under the cotutelle agreement between the Faculty of Geosciences of the University of Bremen (Germany) and at the Faculty of Natural Sciences of the University of Haifa (Israel)

Bremen, August 2021



**GUTACHTER / REVIEWERS**

1. Prof. Dr. Katrin Huhn – University of Bremen/MARUM (Germany)
2. Dr. Oded Katz – Israel Geological Survey (Israel)

**DATUM DES PROMOTIONSKOLLOQUIUMS /**

**DATE OF THE DOCTORAL COLLOQUIUM**

04, November 2021



## VERSICHERUNG AN EIDES STATT / *AFFIRMATION IN LIEU OF AN OATH*

gem. § 5 Abs. 5 der Promotionsordnung vom 18.06.2018 /

*according to § 5 (5) of the Doctoral Degree Rules and Regulations of 18 June, 2018*

Ich / I,           Hadar Elyashiv

versichere an Eides Statt durch meine Unterschrift, dass ich die vorliegende Dissertation selbständig und ohne fremde Hilfe angefertigt und alle Stellen, die ich wörtlich dem Sinne nach aus Veröffentlichungen entnommen habe, als solche kenntlich gemacht habe, mich auch keiner anderen als der angegebenen Literatur oder sonstiger Hilfsmittel bedient habe und die zu Prüfungszwecken beigelegte elektronische Version (PDF) der Dissertation mit der abgegebenen gedruckten Version identisch ist. / *With my signature I affirm in lieu of an oath that I prepared the submitted dissertation independently and without illicit assistance from third parties, that I appropriately referenced any text or content from other sources, that I used only literature and resources listed in the dissertation, and that the electronic (PDF) and printed versions of the dissertation are identical.*

Ich versichere an Eides Statt, dass ich die vorgenannten Angaben nach bestem Wissen und Gewissen gemacht habe und dass die Angaben der Wahrheit entsprechen und ich nichts verschwiegen habe. / *I affirm in lieu of an oath that the information provided herein to the best of my knowledge is true and complete.*

Die Strafbarkeit einer falschen eidesstattlichen Versicherung ist mir bekannt, namentlich die Strafan drohung gemäß § 156 StGB bis zu drei Jahren Freiheitsstrafe oder Geldstrafe bei vorsätzlicher Begehung der Tat bzw. gemäß § 161 Abs. 1 StGB bis zu einem Jahr Freiheitsstrafe oder Geldstrafe bei fahrlässiger Begehung. / *I am aware that a false affidavit is a criminal offence which is punishable by law in accordance with § 156 of the German Criminal Code (StGB) with up to three years imprisonment or a fine in case of intention, or in accordance with § 161 (1) of the German Criminal Code with up to one year imprisonment or a fine in case of negligence.*

Israel, 30/08/21

---

Ort / Place, Datum / Date

---

Unterschrift / Signature



This thesis is dedicated  
to the memory of  
*Leah Goldberger*



# Abstract

---

Submarine mass movements, in particular submarine landslides, are the result of slope sediment destabilization and downslope transport of the failed sediments. This downslope movement can damage offshore infrastructure and generate damaging tsunamis, thus submarine landslides pose a risk to populated coastal environments. In the past decades, mapping the size and distribution of submarine landslides revealed differences between submarine landslides on seismically active and passive continental margins. In addition, significant variations in sediments' shear strength were also found between these environments. Although laboratory measurements and numerical modelling have tested the link between sediment shear strength and failure plane formation, key questions still remain regarding the relationship between the conditions in the slope sediments prior to failure and submarine landslides' size and distribution.

The present PhD thesis aims to improve the understanding regarding the influence of sediments' physical properties and shear strength, on the initiation and development of submarine landslides, particularly large-scale, voluminous slides.

To address this aim, in the first part of the thesis, post-slide sediments from a large-scale submarine landslide, the Currituck landslide complex, were analysed by means of geotechnical and sedimentological analyses. This characterization suggested that with similar lithological composition, the consolidation process plays an important role in the sediments' shear strength development. Variations in shear strength control the development of strength interfaces and appear to have a major influence on the factor of safety.

In the second part of the thesis, four sediment endmembers were tested by means of 3D numerical modelling in order to investigate how the size and volume of slope failure changed according to variations in sediment type and shear strength. The analysis suggested that shear

strength plays a major role in controlling the development of the slope area that is susceptible to failure, and that the sediment type is important for the lateral development of shear localization. The results indicated that the following conditions facilitate large-scale slope failure: dense, sandy slope sediments and under- to normally-consolidated clayey slope sediments.

The results of this thesis provide both dependent and independent evidence of the influence of the sediments' physical properties on slope failure, by linking shear strength variations to the size and distribution of slope failure. Thus, bridging between many natural slope-scale observations and laboratory-scale measurements. This thesis emphasises how the Currituck landslide complex can be used as a key site to understand slope failure preconditioning factors in non-glaciated margins. In addition, this work lays the foundation for future numerical simulations exploring the influence of sediment composition and strength on slope stability.

# Zusammenfassung

---

Submarine Massenbewegungen, insbesondere submarine Hangrutschungen, sind das Resultat der Destabilisierung von Hangsedimenten und deren Transport hangabwärts. Diese hangabwärts gerichtete Bewegung kann schädliche Tsunamis auslösen und submarine Hangrutschungen stellen daher eine Gefahr für besiedelte Küstengebiete und die Offshore-Infrastruktur dar. In den vergangenen Jahrzehnten wurden bei der Kartierung der Größe und Verteilung von submarinen Hangrutschungen erhebliche Unterschiede zwischen submarinen Hangrutschungen an seismisch aktiven und passiven Kontinentalrändern festgestellt. Außerdem wurden erhebliche Unterschiede in der Scherfestigkeit der Sedimente aus diesen Gebieten festgestellt. Obwohl Labormessungen und numerische Modelle den Zusammenhang zwischen der Scherfestigkeit der Sedimente und der Entstehung von Versagensebenen untersucht haben, bleiben wichtige Fragen über den Zusammenhang zwischen den Bedingungen in den Hangsedimenten vor dem Versagen und folglich der Größe und Verteilung von submarinen Hangrutschungen offen.

Die vorliegende Doktorarbeit strebt danach, den Einfluss der physikalischen Eigenschaften und Scherfestigkeit der Sedimente auf die Entstehung und Entwicklung submariner Hangrutschungen, insbesondere großräumiger, voluminöser Rutschungen, besser zu verstehen. Zu diesem Zweck wurden im ersten Teil der Arbeit, die post-failure (post-Versagens) Sedimente einer großen submarinen Hangrutschung, die Currituck Rutschung, mit Hilfe geotechnischer und sedimentologischer Analysen untersucht. Bei diesen Untersuchungen wurde festgestellt, dass bei ähnlicher lithologischer Zusammensetzung, die Konsolidierung eine wichtige Rolle für die Entwicklung der Scherfestigkeit der Sedimente spielt. Unterschiede in der Scherfestigkeit kontrollieren die Entwicklung von Festigkeitsgrenzen und scheinen einen großen Einfluss auf den Sicherheitsfaktor zu.

Im zweiten Teil der Arbeit wurden vier Sediment-Endglieder mit Hilfe von numerischer 3D Modellierung simuliert, um Änderungen in Größe und Verteilung von Hangrutschungen in Abhängigkeit von der Sedimentart und der Scherfestigkeit zu untersuchen. Die Analyse ergab, dass die Scherfestigkeit einen großen Einfluss auf die Verteilung des versagensanfälligen Hangbereichs hat und dass die Sedimentart für die laterale Entwicklung der Scherlokalisierung von Bedeutung ist. Die Ergebnisse deuten darauf hin, dass die folgenden Bedingungen eine großflächige Hangrutschung begünstigen: dichte, sandige Hangsedimente und unter- bis normal-konsolidierte tonige Hangsedimente.

Die Ergebnisse dieser Arbeit liefern sowohl ein abhängiges als auch ein unabhängiges Verständnis, indem sie eine Verbindung zwischen Scherfestigkeitsvariationen und Größe und Verteilung von Hangrutschungen herstellen. Damit wird eine Verbindung zwischen vielen natürlichen Beobachtungen an Hängen und Labormessungen geschaffen. Diese Arbeit betont, wie die CurrituckRutschung als Beispiel für die Untersuchung von Faktoren, die zum Versagen von Hängen in nicht vergletscherten Randgebieten führen, genutzt werden kann. Darüber hinaus schafft diese Arbeit die Grundlage für künftige numerische Simulationen, die den Einfluss der Sedimentzusammensetzung und -festigkeit auf die Hangstabilität untersuchen.

# תקציר

תנועות מסה תת-ימיות, בייחוד גלישות תת ימיות, הם תוצר של אי-יציבות סדימנטים במדרון ותנועת הסדימנטים שכשלו במורד המדרון. תנועה זו במורד המדרון יכולה ליצור גלי צונאמי הרסניים ולכן גלישות תת ימיות מהווים סכנה לאזורי החוף המאוכלסים וכן לתשתיות ביים.

בעשורים האחרונים מיפוי גודל ותפוצת גלישות תת ימיות הראה כי קיימים הבדלים בין גלישות הנמצאות על גבי שולי יבשת פעילים סיימת לבין שולי יבשת פאסיביים. בנוסף שינויים משמעותיים בחוזק הגזירה גם כן נמדדו בין אזורים אלו. אף על פי שמדידות מעבדה ומודלים נומריים חקרו את הקשר שבין חוזק הגזירה של הסדימנטים ומישור הכשל שנוצר, עדיין קיימות שאלות מרכזיות הנוגעות ליחסים שבין התנאים הקיימים בסדימנטים שבמדרון לפני היווצרות כשל לבין הגודל והתפוצה של הגלישות הנוצרות כתוצאה מהכשל.

מטרת עבודת התזה הנוכחית היא לשפר את ההבנה הנוגעת להשפעת התכונות הפיזיקליות של הסדימנטים ומאפייני חוזק הגזירה לבין היווצרות והתפתחות גלישות תת ימיות, בעיקר גלישות ענק בעלות נפח סדימנטים גדול.

על מנת לענות על מטרה זו, בחלק הראשון של התזה גלעיני סדימנט שנדגמו מגלישת ענק – מאזור קומפלקס גלישת קריטק (Currituck) שבצפון-מערב האוקיאנוס האטלנטי, נותחו על ידי אנליזות סדימנטולוגיות וגאוטכניות. אפיון זה הראה כי תחת הרכב ליתולוגי דומה, לתהליך הקונסולידציה קיים תפקיד חשוב בהתפתחות חוזק הגזירה עם העומק. שינויים בחוזק הגזירה מווסתים את התפתחות של ממשקי גזירה ונראה כי יש להם השפעה עיקרית על מקדם הבטיחות.

בחלק השני של התזה, ארבעה חומרי קצה המדמים סדימנטים נחקרו על ידי מידול נומרי תלת מימדי, על מנת לבחון כיצד גודל ותפוצת הכשל במדרון משתנים כתוצאה מסוג הסדימנט וחוזק הגזירה. ניתוח התוצאות הראה כי לחוזק הגזירה תפקיד עיקרי בהתפתחות אזור המדרון הרגיש לכשל ובנוסף נראה כי סוג הסדימנט חשוב להתפתחות הלטרלית של אזורי הגזירה. התוצאות מראות ששילוב תנאים מסוימים בסדימנט מאפשרים התפתחות של כשל נרחב

ובעל נפה גדול במדרון: סדימנטים חוליים ודחוסים וסדימנטים חרסיתיים בעלי תת-קונסולידציה או קונסולידציה נורמלית.

התוצאות של התזה מספקות עדויות תלויות וגם עצמאיות להשפעת התכונות הפיזיקליות של הסדימנטים על כשל במדרון על ידי יצירת קשר בין שינויים בחוזק הגזירה לגודל ותפוצת ההתפתחות של אי יציבות במדרון. לכן, עבודה הזו מגשרת בין תצפיות בגודל הנצפה במדרון לבין התצפיות בגודל הנצפה במעבדה.

תזה זו מראה כי קומפלקס הגלישה של קריטק יכול להוות אתר מפתח כדי להבין כיצד תנאים מקדימים לכשל במדרון מתפתחים על גבי מדרון שלא הושפע מתהליכים קרחוניים באופן ישיר. בנוסף עבודה זו מניחה את היסודות עבור מידול נומרי עתידי אשר יחקור את ההשפעה של הרכב הסדימנטים וחוזקם על יציבות המדרון.



# Acknowledgements

---

I would like thanks to all those who helped and supported me throughout the process of completing my Ph.D.

Primarily I would like to thank to my three supervisors, each in their own unique way of support and encouragement.

To Dr. Revital Bookman who walks with me the long path from my masters to the end of this PhD. Beyond the scientific discussions, your words of support and understanding are what every student needs.

To Prof. Uri ten Brink, for every bit of support under every situation and more. I have learned a lot about a scientific approach to problems and how to look into your results.

To Prof. Dr. Katrin Hunh, first and foremost for the opportunity to come to MARUM and see a different scientific culture, the financial support, supporting female scientist and intensive scientific discussions. Mostly for the availability throughout a period of world pandemic.

To Dr Jason Chaytor for the advice and useful conversations about the processes of the North Atlantic and the warm welcome in WHOI.

To Dr Oded Katz and Dr Regina Katzman, for the useful conversation and insights which have greatly improved my scientific understanding and manuscript.

To my friends from MARUM and Bremen. Your support, in every way from scientific to psychological advice and chocolate in case of distress: Sandy, Dharma, Pradeep Marine Morgane, Gita, Andrea, Ricarda, Mona, Yanming, Cenling, Haozhuang, Leonardo, Sussane, Amir, Ardalan, Alexadra, Dina and Damon for the right words always coming at the right time  
To the members of Once Upon A Time for keeping me sane and keeping my passion to science.

To my friends and colleagues in Israel for their support, understanding and warm words: Naama, Gilad, Akos, Or, Ravid, Gala and Yael.

To my group members Gerhard, Lina, Lars, Franzi, Janis, Robert, Killian, Lennart and Anja for all of your help

ולמשפחה שלי. להורי שתמיד תמכו ועודדו להתקדם, לאחי-עמירן ויהונתן על כל הרגעים והחיוכים, לגיסות המדהימות חן וליאור ולכל האחיינים הקטנים על החיבוק.

Thank you, Vielen Dank, תודה





# Table of Contents

---

---

Abstract.....	I
Zusammenfassung.....	III
תקציר (Hebrew abstract).....	V
Acknowledgements.....	VIII
List of Figures.....	XV
List of Tables.....	XVII
<hr/>	
<b>Chapter 1: Introduction.....</b>	<b>1</b>
1.1. Motivation.....	1
1.2. Submarine mass movements.....	3
1.2.1. Types of submarine mass movements.....	3
1.2.2. Distribution of submarine landslides.....	5
1.2.3. Preconditioning factors of submarine landslides.....	5
1.2.4. Sediments shear strength.....	6
1.2.5. Slope stability analysis.....	8
1.3 Regional settings of the Currituck slide area.....	9
1.5.1. Geological settings.....	10
1.5.2. Oceanographic settings.....	13
1.4. Numerical modelling.....	15
1.5. Research objectives and hypothesis.....	17
1.6. Thesis outline.....	19
<hr/>	
<b>Chapter 2: Methods.....</b>	<b>24</b>
2.1. Field data & Analysis.....	24
2.1.1. Materials.....	24
2.1.2. Core physical properties.....	25
2.1.3. Particle size distribution.....	26
2.1.4. X-Ray Fluorescence (XRF) bulk element analysis.....	28
2.1.5. Vane shear tests.....	29
2.1.6. Moisture content.....	30
2.1.7. Slope stability analysis.....	30
2.2. Numerical methods & Analysis.....	31
2.2.1. The discrete element method.....	31

2.2.2. Numerical parametric study.....	33
2.2.3. Numerical slope model setup.....	35
2.2.4. Results analysis and visualization.....	35
<hr/>	
<b>Chapter 3: Currituck slide complex- sediment controls and implications to slope instability</b>	<b>40</b>
Abstract.....	41
3.1. Introduction.....	42
3.2. Regional settings.....	44
3.3. Dataset and methods.....	46
3.3.1. Data.....	46
3.3.2. Sedimentological analysis.....	46
3.3.3. Geochemical analysis.....	47
3.3.4. Geotechnical analysis.....	47
3.3.5. Slope stability analysis (1D).....	48
3.4. Results.....	49
3.4.1. Physical and geotechnical properties of the sediments.....	49
3.4.2. Slope stability analysis.....	54
3.5. Discussion.....	59
3.5.1. Post slide sediment transport into and around the slide complex.....	59
3.5.2. Possible indication for slope failure preconditioning factors.....	60
3.5.3. Slope stability analysis implications.....	64
3.6. Conclusions and outlook.....	65
Appendices:	
<i>Appendix 3A: Multiproxy analysis supplementary material.....</i>	<i>67</i>
<hr/>	
<b>Chapter 4: Numerical Characterization of Cohesive and Non-Cohesive ‘Sediments’ Under Different Consolidation States Using 3D DEM Triaxial Experiments.....</b>	<b>71</b>
Abstract.....	72
4.1. Introduction.....	73
4.2. The Discrete Element Method—Granular and Bonded Approach.....	75
4.2.1. Granular Approach: The Hertz–Mindlin Contact Model (Cohesionless, Elastoplastic).....	75
4.2.2. Granular Cohesive Approach: The Linear Parallel-Bond Contact Model (Cohesive, Elastoplastic).....	76
4.3. Experimental setup.....	79
4.3.1. Model Geometry.....	80
4.3.2. Particle and Bond Micro-Properties.....	81

4.3.3. Model Run Stages of the Numerical Triaxial Tests.....	83
4.3.4. Model Interpretation and Calculations.....	85
4.4. Results.....	86
4.4.1. Stress–Strain Behaviour.....	86
4.4.2. Volumetric Strain, Porosity and Coordination Number.....	89
4.4.3. Strain Localization.....	91
4.5. Discussion.....	93
4.5.1. Parametrization of Numerical ‘Sediments’.....	93
4.5.2. Classification of the Granular Assemblage.....	94
4.5.3. Application.....	98
4.6. Conclusions.....	100
Appendices:	
<i>Appendix 4A: DEM Force–Displacement Calculation.....</i>	102
<i>Appendix 4B: Supplementary material.....</i>	103
<hr/>	
<b>Chapter 5: Submarine mass-movements preconditioned by sediments shear strength: Insights from 3D numerical modelling.....</b>	<b>107</b>
<hr/>	
Abstract.....	108
5.1. Introduction.....	109
5.1.1. Submarine mass movements.....	109
5.2. Methods.....	110
5.2.1. The discrete element method.....	110
5.2.2. Characterization of sediment physical properties in DEM.....	111
5.2.3. Model setup.....	111
5.2.4. Model analysis and interpretation.....	114
5.3. Results.....	116
5.3.1. Slope analysis.....	116
5.3.2. Development of mass movements (displacements) .....	119
5.4. Discussion.....	125
5.4.1. Susceptibility-to-failure development.....	125
5.4.2. Mass movement’s development.....	127
5.4.3. Conceptual models for potential large-scale mass movements.....	129
5.5. Conclusions.....	130
Appendices:	
<i>Appendix 5A.....</i>	133
<hr/>	
<b>Chapter 6: Conclusions &amp; Outlook.....</b>	<b>142</b>
<hr/>	
6.1. Main conclusions.....	142

6.1.1. Possible preconditioning factors to the Currituck submarine landslides complex.....	142
6.1.2. Size and distribution of the area susceptible to failure and the initial volume of failure.....	144
6.2. Recommendations for future work.....	145
Bibliography.....	152

# List of Figures

<b>Figure 1.1:</b> A schematic illustration of submarine mass movements (modified after McHugh et al., 2002)	3
<b>Figure 1.2:</b> A schematic illustration of morphometric parameters and how they are taken.....	4
<b>Figure 1.3:</b> The research area.....	12
<b>Figure 1.4:</b> The oceanographic settings in the research area.....	14
<b>Figure 1.5:</b> A diagram illustrating the gap covered in the thesis.....	19
<b>Figure 2.1:</b> Location of the research area and the cores selected for research. (a) location of the Currituck landslide complex offshore eastern USA (b) physiographic areas of the Currituck slide complex as identified Hill et al., (2017) (c) Core location within the research area. Colourful dots represent cores selected for detailed analysis. White dots represent cores used for across and along slope correlation according to MSCL analysis.....	25
<b>Figure 2.2:</b> Particle size distribution measurements and analysis (a) A schematic illustration of Laser Diffraction Particle Size Analyzer measurement cells and detectors array (b) Light scatter pattern for a coarse particle (c) Light scatter pattern of a fine particle (a-c are modified after Rasmussen, 2020) (d) Sandy sample PSD example from 5PC (10 cm) (e) Muddy (Clayey-silt) sample PSD example from 16PC (642 cm).....	27
<b>Figure 2.3:</b> An abstract illustration representing the mechanical loop of the DEM calculation cycle. A simulation starts by detecting the contacts between particles. If particles are in contact and overlap the force-displacement relationship is calculates. The resulting forces are applied to each particle generating motion. A particles particle acceleration, velocity and displacement is then updated according to Newton’s second law of motion. This loop continues until a predefined number of iterations is reached.....	31
<b>Figure 2.4:</b> A scheme of the numerical sediments parametric and benchmark tests. First benchmark tests were performed to define the major parameter controlling the strength of the sediment and second the material parametric tests as detailed in Chapter 4.....	34
<b>Figure 2.5:</b> An Illustration of the extracted surface particles from the 3D slope model. (a) 3D and (b) a semi-cross section. Blue dots-the entire 3D model particles, purple dots-surface particles.....	36
<b>Figure 2.6:</b> An illustration of the surface particles extracted to calculate the mean slope profile and its derivatives. Blue dots-the entire 3D model particles, purple dots-surface particles, and green dots-particles taken for the mean slope profile.....	37
<b>Figure 3.1.:</b> Location of study area and oceanographic regime, cores location and physiographic units..	44
<b>Figure 3.2:</b> Core photo, lithology, grain size fraction, water content, magnetic susceptibility, undrained shear strength, Ca/Ti ratio of sediment cores along the slope (see Figure 1 for location). From right to left: (a) core 5PC (b) core 7PC and (c) Core 13PC.....	50
<b>Figure 3.3:</b> Cores photo, lithology, grain size fractions, water content, magnetic susceptibility, undrained shear strength, Ca/Ti ratio and Fe/Zr ratio for cores around the slide complex (a) 14PC, Channel and (b) 16PC, intact block. See Figure 3.2 for lithology and grain size distribution frequency legends.....	52
<b>Figure 3.4:</b> Sediments textural analysis presenting variations of the mean and sorting (standard deviation) values for each layer of the sampled cores. (a) all cores (b) core 13PC (c) core 14PC and (d)	54

core 16PC. The sorting of sediments from cores 13PC cover the entire distribution of sampled sediments from all of the cores except the very fine sediments from core 16PC.....	
<b>Figure 3.5:</b> FOS evaluation for each sample and shear strength linear regressions for selected cores. (a) 16PC (intact block), (b) 5PC (Shelf edge), (c) 7PC (upper evacuation zone) and (d) 13PC (lower evacuation zone).....	56
<b>Figure 3.6:</b> Slope stability analysis (a) static and (b) pseudo static. Dashed lines indicate the conditions of the recent Currituck slide.....	57
<b>Figure 3.7:</b> Slope stability analysis for the two units identified in the drape (a) static and (b) pseudo static (for $z=150$ m).....	58
<b>Figure 3.8:</b> A schematic composition of potential strength interfaces that can form during a glacial-interglacial depositional cycle in the environment Currituck. H-high, M-medium, L-low.....	63
<b>Figure 4.1:</b> (a) An illustration of particles interaction according to the Hertz–Mindlin contact model. (b) An illustration of particles interaction according to the linear parallel-bond contact model.....	77
<b>Figure 4.2:</b> The 3D Discrete Element Method (DEM) cubic isotropic sample	80
<b>Figure 4.3:</b> Triaxial tests results for ‘sand’ samples.....	88
<b>Figure 4.4:</b> Triaxial tests results for ‘clay’ samples.....	89
<b>Figure 4.5:</b> Strain localization visualized for deformation stages.....	92
<b>Figure 4.6:</b> Modified Mohr–Coulomb failure envelopes.....	95
<b>Figure 4.7:</b> A comparison between the mechanical behavior (stress–strain) of the numerical results and laboratory experiments of sediments.....	96
<b>Figure 5.1:</b> Initial and final 3D configuration of the particles in the DEM model and subsequent analysis.	112
<b>Figure 5.2:</b> Model 1a-Low shear strength ‘sand’ .....	118
<b>Figure 5.3:</b> Same as Figure 2 but for Model 1b-High shear strength ‘sand’ .....	120
<b>Figure 5.4:</b> Same as Figure 2 but for Model 2a-Low shear strength ‘clay’ .....	123
<b>Figure 5.5:</b> Same as Figure 2 but for Model 2b- High shear strength ‘clay’ .....	124
<b>Figure 5.6:</b> Temporal (slope stages) development of mass movements’ volume and frequency.....	126
<b>Figure 5.7:</b> A conceptual diagram based on the four models, connecting the pre-failure state of sediments (regarding shear strength and sediment type, see circular inset) to the potential initial volume involved in failure.....	130

# List of Tables

---

Table 2.1: A list of cores from the Currituck slide complex and analysed in this study.....	24
Table 2.2: Values for the benchmark tests of sediment type major parameter.....	34
Table 3.1: List of cores from the Currituck slide complex analysed in this study.....	46
Table 3.2: Input parameters for slope stability calculations, A-entire core. UU-upper unit, LU-lower unit..	55
Table 3.3: Significance t-test results for upper and lower units FOS values ( $\alpha=0.05$ ).....	55
Table 4.1. Fixed and tested micro-parameters applied in each of the triaxial tests according to the contact model applied during the test.....	79
Table 4.2. Calculated macro-properties of different material samples: LS: loose ‘sand’, DS: dense ‘sand’, LC-loose ‘clay’, DC-dense ‘clay’. Numbers in brackets are cohesion values, as measured from the linear regression of the failure envelope.....	83
Table 5.1: Numerical sediment properties and parameters in each for the model setup.	113
Table 5.2: Slope stages parameters: critical slope angle under slope conditions of FS=1, the overall-slope angle ( $\theta_{OS}$ ) and the local critical slope zone (%LC).....	121

# 1. Introduction

---

## 1.1. Motivation

In the past decades, technological developments have provided increased capabilities to survey submarine slope failure and other mass movements worldwide (e.g. Harders et al., 2011; Katz et al., 2015a; Migeon et al., 2011; Twichell et al., 2009). These were observed along the majority of sediment bearing continental margins and in many volcanic island flanks, on glaciated and non-glaciated, active or passive margins (Baeten et al., 2013; Gales et al., 2014; Krastel et al., 2018; Piper et al., 2013; Urgeles and Camerlenghi, 2013). In particular, submarine landslides are considered the largest geological process by which sediments are being transported from the shelf edge or slope to the deep ocean basins (Lee et al., 2007; McAdoo et al., 2000; Parsons et al., 2007). Therefore, the movement of large volumes of sediment shapes the seafloor morphology and additionally play coevally an important role in the carbon burial cycle, as it transports sediment from shallow waters to the deep sea (Craig et al., 2020). As such it can potentially participate in the formation of reservoir or sealing features in the hydrocarbon systems (Meckel, 2011; Moernaut et al., 2020; Pope et al., 2017).

Submarine landslides can have substantial socio-economic consequences. As the sediments destabilize and move downslope, a dangerous tsunami wave may form, imposing a hazard to the densely populated coastal environments (Harbitz et al., 2014; ten Brink et al., 2009). The most recent remarkable example of such a landslide tsunami formed offshore Sulawesi Island in 2018. A tsunami wave of approx. seven meters in height formed and killed more than 4000 people, causing massive destruction on its way (Carvajal et al., 2019). Other catastrophic events of submarine landslide tsunamis have been documented offshore eastern Canada (Grand Banks in 1929; Løvholt et al., 2019; Schulten et al., 2018) and offshore southern France (Nice Airport in 1979; Dan et al., 2007). Considering the predicted increase in the coastal population (IPCC, 2007), more people will likely be exposed to such hazards in the future. In addition, submarine landslides can cause damage to important seafloor infrastructure such as communication cables or offshore oil and gas platform infrastructure (Lintern et al., 2019 and references therein). The increased dependency on and development of such seafloor technologies increases the risk of their destruction by future submarine landslides.

Although the continuous efforts to understand submarine landslides, many questions still remain unanswered. In order to cause slope failure an external factor is needed. Previously, earthquakes were assumed the most common trigger, suggesting that seismic loading initiates slope instability by increasing the shear stress on the slope sediments. However, recent studies have shown that this is not always the case. A range of long term processes (e.g. tectonic movements Brothers et al., 2018; e.g. contour currents Gatter et al., 2020) and preconditioning factors (e.g. rapid sedimentation, Brackenridge et al., 2020) were recognized that can contribute to the reduction of sediments shear strength prior to failure. Most studies focus on morphological characterisation from geophysical mapping (e.g. Brothers et al., 2019a; Hill et al., 2020), however, we are unable to observe submarine landslides directly. Some studies have managed to observe turbidity currents (Clare et al., 2017; Hage et al., 2019; Heerema et al., 2020), yet not landslides. Therefore, we are currently strongly dependent on back analysis of submarine sliding events that already happened, which makes the study of submarine landslides much more difficult and subject to bias (Talling et al., 2014).

Mapping the size and distribution of submarine landslides revealed that generally, small and frequent submarine landslides occur along seismically active margins whereas large-scale submarine landslides occur along passive margins though not as often (ten Brink et al., 2016; Urgeles and Camerlenghi, 2013). Geotechnical investigation of submarine sediments have shown that slope sediments along seismically active margins have a higher shear strength compared with slope sediments from passive margins (Sawyer and DeVore, 2015). Thus, indicating a link between sediments shear strength and landslide spatial occurrence and their specific volume.

The development of shear localization and subsequent failure plane evolution, as a result of shear strength variation, has been tested in the laboratory centimetre-to-millimetre scale in various sediment composition (e.g. Wiemer et al., 2015). These tests have demonstrated for example, particle shape and roughness in ash layers can potentially form a weak layer or that variations in fossil content or altered minerals can lead to strain weakening and thus shear localization (Miramontes et al., 2018; Wiemer et al., 2017). In addition, the microscopic scale variations to sediments structure were investigated in numerical modelling (e.g. Huhn et al., 2016). However, linking whether and how these variations of localization further influence landslides in the slope-scale is still missing.

This thesis aims to understand how sediment physical properties, particularly the shear strength and the consolidation, can precondition the size and distribution of a submarine slope failure.

## 1.2. Submarine mass movements

### 1.2.1. Types of submarine mass movements

Submarine mass movements are by far the largest important geological processes encompassing all gravitational processes, which transport and deposit large volumes of sediments in the deep sea environments (Masson et al., 2006). The classification of mass movements identifies endmembers based on their mechanical behaviour of transport. On the one hand, transport mechanisms include slides (brittle deformation) or slumps (plastic deformation). These are characterized by less internal deformation with occasionally also undeformed blocks are transported (Figure 1.1). The resulting deposits from this mechanism of transport mainly reflect the original sediment sequence and composition. On the other hand, failed sediments transported as debris flows exhibit a higher internal deformation. The solid phase controls transport behaviour resulting in typical debris flow deposits. Finally, turbidity currents are transported while incorporating fluids and behave more like a Newtonian fluid. As a result, typical turbidites Bouma sequences are deposited (Hampton et al., 1996; Lee et al., 2007).

By incorporating water, slide and slumps can disintegrate and transform into debris flow and/or turbidites. However, the process which can potentially transport the volumetrically largest amounts of sediments, is a submarine landslide (Shanmugam, 2018).

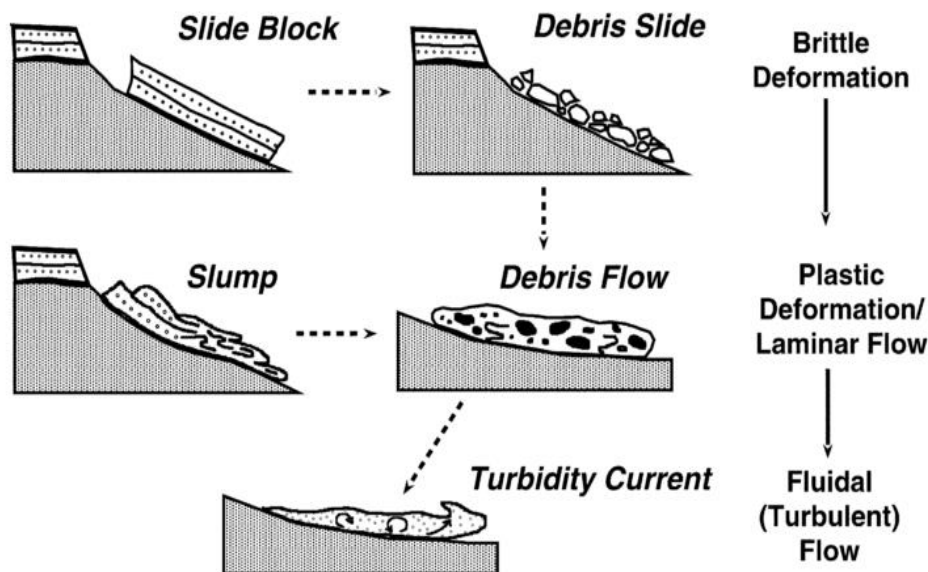


**Figure 1.1:** A schematic illustration of submarine mass movements (modified after McHugh et al., 2002)

Characterizing submarine landslides is based on a morphometric analysis (Mountjoy and Micallef, 2018). This approach measures parameters such as the scar width, height and deposits runout length and other parameters. Importantly, submarine morphometric analysis differentiates between the evacuation zone parameters, which help to assess the pre-slide slope properties, and the parameters of deposition zones, which are important for tsunami and seafloor destruction assessments (Figure 1.2; Clare et al., 2018).

The evaluation of a slide morphological characteristics from the seafloor bathymetry and geophysical data, is a critical step to improve local hazard assessment. For example, the runout distance of the slide, the magnitude and frequency of slide occurrence as well as the emplacement process are factors that directly determine the tsunami potential of a sliding event. Also, the analysis of a slide's volume is important for tsunami modelling (Moscardelli and Wood, 2016). Numerous studies in the past decades have focused on such compilations (Gatter et al., 2021; Hühnerbach and Masson, 2004; Mountjoy et al., 2020). Consistent measurements and a compilation into database are critical steps towards a fundamental understanding of submarine landslides, seafloor morphological evolution and to assess the environmental control on landslides occurrence. However, with every new high resolution mapping campaign, these catalogues have to be updated as new, previously unknown slide events might be observed.

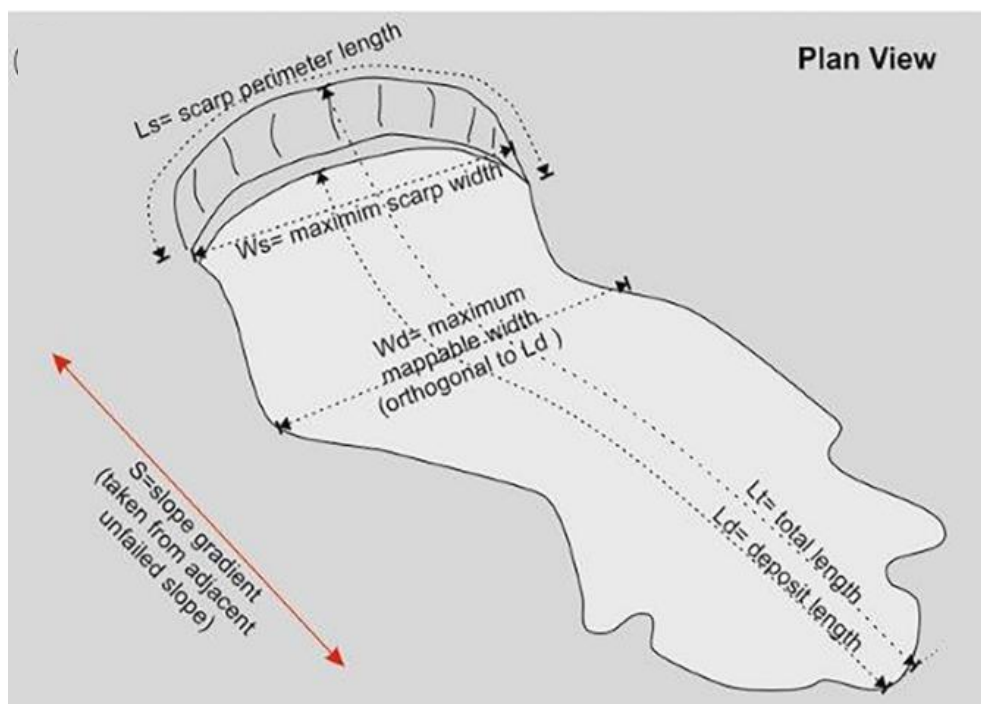


*Figure 1.2: A schematic illustration of the morphometric parameters to be measured from bathymetric and/or seismic data (after Clare et al., 2018).*

### *1.2.2. Distribution of submarine landslides*

Submarine landslides were found in every geological setting, along passive or active margins, in water depths ranging from the coast to the lower slope, on glaciated and non-glaciated margins and volcanic island flanks (Lintern et al., 2019 and references therein).

Despite advancements in surveying seafloor technologies, such surveys are still costly and therefore, our knowledge and understanding of submarine landslide occurrence is limited to the discovered evidence (i.e., scars or deposits) on the seafloor and the resolution of the seismic surveys. This limits our current knowledge for the majority of slopes worldwide as only small portions were mapped, especially of remote environments such as Antarctica.

Integrating the available data, studies were able to evaluate the magnitude distribution of submarine landslides (Chaytor et al., 2009; Owen et al., 2007; Urgeles and Camerlenghi, 2013). An important understanding of such analysis indicated, that the slope gradient has a limited influence on landslide distribution (Hühnerbach and Masson, 2004), thus suggesting that other factors may influence the slope stability.

Analysing the available morphometric data from landslides in the Mediterranean, Urgeles and Camerlenghi (2013), observed many small failures on active margins distinct from large, but few landslides on passive margins. An assessment of submarine mass movements mapped along various margins around the world showed that this relationship exists worldwide, however does not occur on slopes with high rates of sedimentation (ten Brink et al., 2016).

These analyses highlighted the fact that large submarine landslides mostly occur along passive margins and on slopes that are otherwise considered stable ( $<2^\circ$ ). The occurrence of large-scale submarine landslides was further explained by long term preconditioning factors (Urlaub et al., 2015).

### *1.2.3. Preconditioning factors*

Preconditioning factors may act either to reduce or increase the shear strength of the slope sediments. They do not, however, trigger the failure. While these factors are generally known due to the extensive research in the past years (e.g. Hampton et al., 1996; Vanneste et al., 2014), there are still large uncertainties regarding their time-span, influence and interplay (e.g. Brackenridge et al., 2020; Masson et al., 2010; Piper et al., 2013; Urlaub et al., 2015). Understanding preconditioning factors is an important component in the risk

assessment of continental slopes and therefore a site-specific understanding is still needed.

Long-term processes generate the slope stratigraphy. As such, the development of precondition factors to slope failure have been related to the development over time of variations within a layer or between two layers. In particular the weak-layer concept suggests that shear strength differences between prominent layers embedded within the slope stratigraphy serve as preferential a failure plane (i.e., shear strength interface, Gatter et al., 2021, 2019). Other suggested preconditioning factors include the occurrence of gas in the sediments, oversteepening of the slope due to tectonic process (e.g. uplift, Brothers et al., 2018), a process that increasingly reduces the shear strength of the sediments (e.g., Miramontes et al., 2018) or excess pore pressure due to rapid sedimentation (Masson et al., 2010). While these factors and others have been suggested to precondition slope failure, due to the difficulty to predict and observe submarine landslides it is challenging to constrain how they influence slope stability or act in the long term to reduce the sediments' shear strength.

#### *1.2.4. Sediments shear strength*

The Shear strength of sediments is only one parameter among other preconditioning factors of slope stability. However, the shear strength is fundamentally dependent on the sediment's composition, particles shape and size, consolidation and the resulting mechanical behaviour of the particle's interaction. Therefore, global variations in oceanographic, climatic and geological process involved in the transport and depositional processes govern sediment properties and their variations, which in turn significantly affect the geotechnical behaviour of the sediment (Hampton et al 1996; Lee et al 2007). Sediments mechanical behaviour under static or dynamic stresses is a key aspect in understanding sediment failure processes, such as submarine mass movements (Masson et al., 2006; Sultan et al., 2004). The components of the shear strength ( $\tau$ ), the internal angle of friction ( $\theta$ ) and cohesion ( $C$ ) can be expressed by the Mohr-Coulomb failure criterion as:

$$\text{Eq. 1.1} \quad \tau = \sigma'_n(\tan\theta) + C,$$

As  $\sigma'_n$  is the effective normal stress resulting from the difference between the normal stress and pore water pressure changes. The internal angle of friction can also be expressed as the friction coefficient ( $\mu$ ):

$$\text{Eq. 1.2} \quad \mu = \tan\theta.$$

While frictional strength is the result of resistance to sliding between particles, the particles rearrangement or particle crushing, the cohesion is occurring due to the adherence between particles. The possible sources suggested for cohesion are cementation (chemical bonding between particles), electrostatic attraction and adhesion (Mitch and Soga, 2005).

Sediments develop shear strength primarily from the particles' composition (e.g., mineralogy, shape, size distribution, roughness). Variations in clay or sand content act to reduce or increase the shear strength in the sediments. Additionally, the initial depositional micro-fabric also contributes to the sediments shear strength (Mitchell and Soga, 2005).

Post-depositional processes affect the sediments' shear strength due to both spatial and temporal changes in the sediments' micro-fabric, mostly through consolidation (Bennett et al., 1981). Continuous or episodic depositional processes, such as changes in sedimentation rate, the loading and unloading of ice sheets due to glaciation cycles, and mass movements contribute to the increase in shear strength with time and depth. As the vertical stress increases due to increased load, sediments undergo consolidation and, consequently, the shear strength of normally consolidated sediments increases with depth almost linearly (Ikari and Kopf, 2015; Perret et al., 1995). However, in places where a mass movement occurs, overconsolidated sediments may occur in shallow depths due to unroofing (Ikari and Kopf, 2015). In a recent experiment, Yenes et al (2020), indicated that the sedimentation rate can influence the secondary consolidation and aging processes and thus promote the development of apparent overconsolidation in the sediments. Under variations of the sedimentation rate, this may form or promote the formation of a weak layer (see description above) in surficial sediments.

Shear strength has also been used to explain variations with depth of the shear plane. The hypothesis of seismic strengthening has been proposed to explain variations in the shear strength in areas influenced by seismic activity. The hypothesis suggests that in seismic

environments over time, the occurrence of earthquake shaking is increasing the sediments assemblage density by reducing the void ratio after dewatering after non-failure earthquake (Lee et al., 2004). This has been demonstrated from an extensive analysis comparing shear strength variations with depth from IODP, DSDP and ODP cores collected along active and passive margins (DeVore and Sawyer, 2016; Sawyer and DeVore, 2015).

Other properties of the sediments such as the porosity, density and water content are key parameters for the sediments shear strength (Mitchell and Soga, 2005) and to the occurrence of submarine landslides. Using these parameters measured from sediments, variations on the shear strength can be further estimated in a slope stability analysis.

#### 1.2.5. *Slope stability analysis*

Slope stability analysis primarily estimates the future slope failures. Additionally, it can be used to reconstruct the stability conditions prior to the occurrence of a landslide, based on measured parameters outside of a landslide. Not only this analysis estimates the slope susceptibility to failure, but based on the parameters considered in the equations, the impact of various triggers can be evaluated as well. Thus, we can establish the degree of influence of the geologic processes in the area slope stability is assessed.

A slope failure resulting in a landslide occurs when the driving downslope forces acting on the slope sediments overcome the slope resisting forces (Hampton et al., 1996). A simple expression of the forces that control slope stability can be addressed as balance between the resisting and shearing forces, as the ratio between the two forces is the Factor of Safety (FOS):

$$\text{Eq. 1.3} \quad FOS = \frac{\text{resisting forces}}{\text{shearing forces}},$$

where  $FOS \leq 1$  indicates failure or slope that is susceptible to failure, and  $FOS > 1$  indicates a stable slope. A 1D infinite slope analysis is based on a comparison between the downslope forces acting on the slope to cause instability and the slope's resisting forces. Two scenarios were considered here to evaluate the slope stability under undrained conditions.

The first scenario accounts for static slope conditions in which the slope stability is affected by quick changes of the slope geometry or due to fluctuations in the pore pressure. The factor of safety for these conditions is calculated as (Morgenstern, 1967):

Eq. 1.4 
$$FOS = \frac{S_u}{\gamma' * z * \sin \theta \cos \theta},$$

where  $S_u$  is the undrained shear strength,  $\gamma'$  is the buoyant unit weight of the sediments,  $z$  is the depth of failure (overburden depth) and  $\theta$  is the slope angle.

The second scenario accounts for pseudo-static slope conditions in which an earthquake triggers the failure. To account for an earthquake as a triggering scenario, the pseudo static undrained factor of safety is defined as:

Eq. 1.5 
$$FOS = \frac{S_u}{\gamma' * z * [\sin \theta \cos \theta + \kappa (\gamma / \gamma') \cos^2 \theta]},$$

where  $\gamma$  is the bulk unit weight of the sediments and  $\kappa$  is the pseudo static seismic coefficient. When ground motions are induced by an earthquake exceeds a threshold acceleration (along a specific plane), failure occurs along the plane. This threshold of acceleration is the pseudo static seismic coefficient that results in a factor of safety of 1.

Several assumptions are considered before using this approach. (1) The lateral extent of the slide is infinite in comparison to its thickness. (2) The sediment peak strength will be mobilized across the entire failure surface at the time of failure, and also (3) it assumes that the failure surface is a plane, parallel to the slope surface. In light of the current research objectives (see section 1.6), which is to conduct a preliminary assessment of slope stability in the research area with the data available, the assumptions and limitations of the method will be considered during the analysis of the results.

### **1.3. Regional settings of the Currituck slide area**

The Currituck submarine landslide complex is located offshore Albemarle Sound, along the North-Western Atlantic Ocean. These non-glaciated passive margin has experienced increased sedimentary supply during the Quaternary (Poag and Sevon, 1989). Oceanographically, the area is mainly influenced by the North Atlantic Deep Water (NADW) current and its derivatives (sections 1.3.2.). These settings are significant to understand conditions which control the sediments transport and deposition, ultimately shaping the stratigraphy and morphology in this environment and potentially influencing the formation of a failure plane. In the following sections, a general overview of the regional geological and oceanographic settings is provided.

### *1.3.1. Geological settings*

The research area, the Currituck submarine landslide complex, lies within the southern end of the Mid-Atlantic Bight (MAB), along the north-western Atlantic margins. The geology and current morphology of the north-western Atlantic continental margins (off the U.S.A east coast) have been influenced by the tectonic development starting about 200 Ma ago. The Atlantic continental margins had opened in three phases throughout the Mesozoic. The North Atlantic continental margins formed by rifting stage during the Triassic that was followed by hyperextension in the Jurassic and seafloor spreading in the Cretaceous. The process of thermal subsidence development of the western Atlantic margins has contributed to its formation as passive margins. The accumulation of sediments within the basin throughout the Mesozoic to the Cenozoic caused a transition and filling up of the basin from basement of continental, transitional oceanic crust to a basin covered by clastic and carbonates that originated from large reefs (Sheridan, 1987). Up to the Neogene the sedimentation was characterized by a mix of siliciclastic and carbonate deposits that covered a ramp margin morphology (Poag and Sevon, 1989).

During the Quaternary, large volumes of sediments were eroded and deposited unevenly along these margins. Along the reaching in the outer shelf and upper slope the thickness varied reaching between 400 to 800 m (Poag and Sevon, 1989). In the northern extent of the Atlantic margins (i.e., Georges Bank and Southern New-England), this is reflected by glacially derived sediments, transported to the shelf edge by large river systems. On the other hand, in the area extending southward, the mid-Atlantic margins sediment transport and deposition was affected by large river systems. According to reconstructions, their estuaries extended across the shelf creating shelf-edge deltas or deep-sea fans. Additional processes shaping this area involved erosional processes such as sediment flows, spilling over the shelf edge or retrograde erosion and sediment fallout (Obelcz et al., 2014; Vachtman et al., 2013).

The MAB area extends roughly from the eastern tip of Long Island in the north to offshore North Carolina in the south (Fig. 1.3). The continental shelf is widest in the northern MAB (~100 km), narrowing offshore of Cape Hatteras (~40 km). Sediment texture varies, generally consisting of medium and coarse to fine sand closer to the coast and fining to a mixture of silt and clay at the shelf break (McMullen et al., 2011). Surface waves are often the primary force mobilizing sediment across the shelf, from the coast to the mid shelf (Dalyander and Butman, 2015). Currently, the MAB shelf exports little sediments

to the slope, this is dependent on water depth, wave action and bottom currents. Dynamic, near bottom high frequency currents over the outer shelf of the MAB, can approach a velocity of 20 cm/s. These currents primarily form due to internal waves that propagate towards the shore and were proposed to be a major mechanism to mobilize sediments at the shelf edge (Churchill et al., 1994). However, sediments resuspension is induced by major storm events that can generate transport of sediment over the shelf edge (Churchill et al., 1994). The current sediments on the shelf are relicts, representing sediments that were reworked and redeposited during the Pleistocene glacial–interglacial sea level changes (Hathaway, 1972). An analysis of the SEEP-II experiments conducted along the mid-Atlantic shelf and upper slope, indicated that currently a depocenter for sediments occurs on the slope, centred at about 1000 m. This depocenter reflects the maximum of near-bottom vertical flux which coincides with a minimum in current speed (Biscaye et al., 1994).

Geotechnical analysis of sediments from the MAB are not common and not many measurements were conducted to the slope sediments deeper than the upper 2-3 m. Geotechnical measurements taken between Georges Banks to Southeast Georgia Embayment in the south in up to 300 m water depth, indicated that Pleistocene sediments have lower compressibility and are stable (i.e., normally consolidated) whereas about 10% of the clayey samples presented overconsolidation. Only four cores were tested for stability under cyclic loading conditions, however according to Hathaway et al. (1979), these results were premature. With the current understanding of slope morphology and the distribution of shelf-edge to upper slope landslides, possibly every region should be considered separately.

Geotechnical measurements taken in the canyon-incised slope between Georges Bank and the Hudson canyon, also suggested that the current surficial sediments (up to 5 m retrieved sediments) are stable. The study found evidence for mass movement scars (Booth et al., 1981). Additional measurements of surficial sediments (<5 m) along the heavily dissected margins between the Alvin and Powell submarine canyons showed that most surficial sediments are overconsolidated. Calculations of the factor of safety in these environments indicated that the surficial sediments are stable under static conditions. However, it was noted that if deeper sediment are normally-consolidated than the factor of safety would be reduced (Booth et al., 1984).

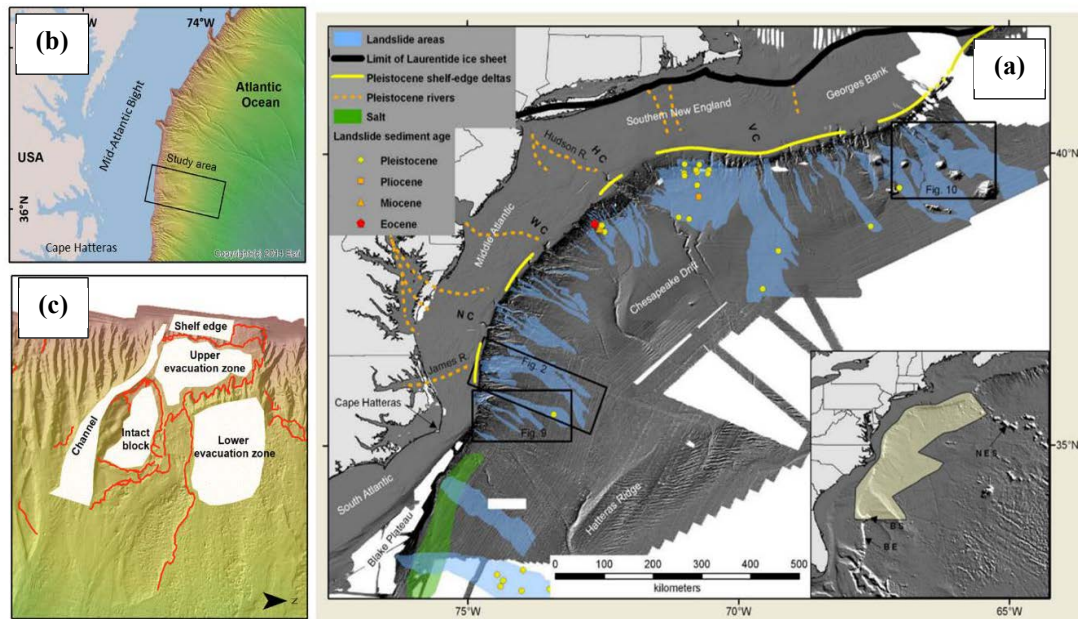


**Figure 1.3:** The research area; (a) the north west Atlantic margins prominent submarine landslide distribution along the north west Atlantic margins (modified after Twichell et al., 2009); (b) location of the Currituck landslide complex along the mid-Atlantic margins; (c) physiographic features of Currituck landslide complex defined by Hill et al. (2017).

### 1.3.1.1. Currituck submarine landslide complex

The prominent submarine morphological features along the MAB are submarine canyons and gullies, and submarine landslide scars and their deposits. The latter are quite abundant covering between 33 to 16% of the slope and rise area (Twichell et al., 2009).

The Currituck submarine landslide is one of the largest open-slope slides occurring on the mid-Atlantic slope (Fig. 1.3). Previous studies identified two main failure headwalls parallel to the slope. However, morphological interpretation (Locat et al., 2009) suggested that sliding occurred along three failure surfaces located vertically above each other. In addition, the analysis suggested that the Currituck submarine landslide occurred as one event (Locat et al., 2009). Further observations in this area indicated that the presence of pock marks, active fluid venting, sandy and foraminifera enriched layers as potential weak layers can serve as potential failure and glide planes (Hill et al., 2004; Locat et al., 2009; Prior et al., 1986).

The deformed area in the Currituck landslide complex surrounds more than 6500 km<sup>2</sup> between the continental slope and the rise. The morphological analysis of Hill et al., (2017) indicated several physiographic features in the landslide complex area (Fig. 1.3).

The slide evacuation zone is defined by the shelf-edge headwall, the upper headwall and the lower headwall. South of the slide, an undetected block of sediments was defined where an ancient, buried mass movement was observed. The upper headwall scarps relief vary from 150 to 250 m, the lower headwall has a stepped scarp of ~400 m altogether, the shelf-edge scarp relief is ~100 m and the sidewall scarps in the lower slope vary between 100 to 200 m. The lower evacuation zone is covered by scattered debris blocks on a low gradient (<2°) seafloor.

Previous attempts to estimate or date the timing of the slide and whether one or two sliding events occurred, suggested a range of 22.5 to 50 ka for the timing (Lee, 2009; Prior et al., 1986). However, new age constraints (Chaytor et al., in preparation) taken from the drape layer in several locations, indicates a unified age to the upper and lower evacuation zones of approximately 16 ka and thus indicate that the sliding occurred in a single event.

### *1.3.2. Oceanographic settings*

The oceanographic regime in the MAB is mainly influenced by the North Atlantic deep water, transporting southward cold water from sources in the Labrador and Norwegian seas (Mosher et al., 2017). The NADW has two components that flow southwards in the research region. The Deep Western Boundary Current that flows between depth of 3000 to 5000 m and the upper Labrador Current that in general flows between 500 to ~2500 m. Originating in the south, off Florida, warm water flows northward forming the Gulf Stream (Labrador C in Fig. 1.4a). North of Cape Hatteras the eastward deflection by the Coriolis force results in the Gulf Stream separating from the U.S. coast (Saba et al., 2016). The Labrador Slope water is characterized with temperatures typically of 4–8° C and salinities of 34.3–35 psu (Fratantoni and Pickart, 2007), whereas the Gulf Stream average surface (0–10 m) water temperatures fluctuate between 24– 29 °C with average salinity ranges between 36 and 36.2 psu (Locarnini et al., 2013). The MAB shelf water was characterized within water depths of 0–100 m as having a characteristic of temperature of 4–15 °C and salinity of 32.5–33.5 psu (Manning, 1991). Near Cape Hatteras these waters converge with the south Atlantic Bight shelf water and form what is known as the Hatteras Front (Savidge, 2002).

Over a region extending roughly 40–200 km north of Cape Hatteras to the Chesapeake Bay mouth, the shelf water exports water to the ocean (Fig. 1.4c) due to the combined effect of the northward flow of the Gulf stream and the southward flow of the Labrador currents shelf and upper slope water components (Churchill and Gawarkiewicz, 2012).

Under the current high stand conditions, it was suggested that when the Gulf Stream is closer to the shelf edge there is an enhanced export of shelf water to the slope. A model-based study suggests that during last glacial period a relatively stronger glacial Labrador Current extended south to Cape Hatteras, which led to cooler water conditions displacing the Gulf Stream position farther south (Hewitt et al., 2003).

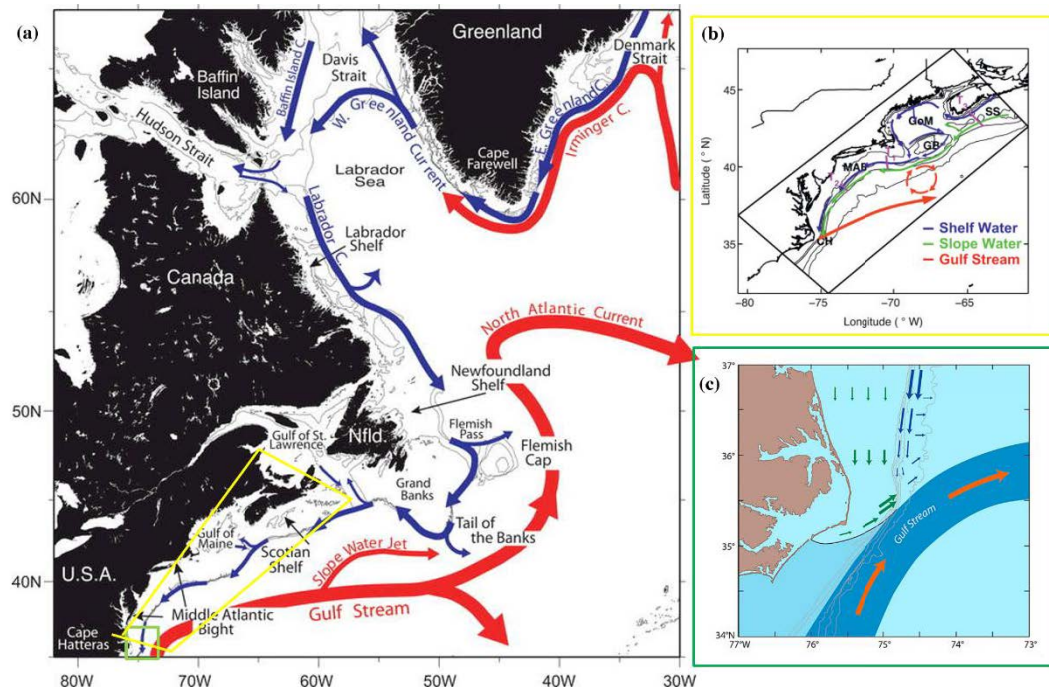


**Figure 1.4:** The oceanographic conditions in the research area: (a) north west Atlantic margins Labrador Current and the Gulf Stream major components (modified after Fratantoni and Pickart, 2007); (b) the division between shelf and slope currents (modified after Zhang et al., 2016); (c) the pattern of shelf water flow, export from the Hatteras shelf and slope region (modified after Churchill and Gawarkiewicz, 2012).

Marshall et al. (2014) has shown that the Labrador Current flow was lower during full glacial conditions and has reduced again in the late Pleistocene (~15 ka) and again in the mid-Holocene. Although evidence were derived from the Flemish Pass, off Canada, knowing that today the current experiences a substantial decrease in volume transport from north to south (Loder et al. 1998) and is mainly weak in Cape Hatteras, any decrease in the past most likely influenced the current ability to transport or influence sediment fluxes arriving from Albemarle Sound.

## 1.4. Numerical modelling

Numerical modelling is an approach widely used to simulate processes that can otherwise not be observed in nature due to the depth position, temporal scale or time span the process occurs. Additionally, numerical modelling allows a control on the boundary conditions, which cannot be achieved in laboratory tests. In doing so, individual aspects of complex geological processes can be investigated separately without facing any temporal or spatial scaling problems as in lab experiments.

Among the various numerical approaches to characterize and simulate natural materials particularly their deformation behaviour, the Discrete Elements Method (DEM, Cundall and Strack, 1979) is an approach used to simulate the discontinuous nature of granular materials such as soils and rocks observed in laboratory experiments (e.g. Thornton, 2000) and in nature.

During the last decades, numerous studies focussed on the interplay between micro-mechanical properties of DEM particles on macro-properties of the material package. All in common is to gain a deeper understanding of that and how the sedimentological and physical properties of sediments promote shear localization in the slope sediments. A number of studies using the DEM approach focused e.g. on the influence of sediment physical properties on the development shear localization on a microscopic (grain-) scale level in 2D (Huhn et al., 2016; Kock and Huhn, 2007a, 2007b). These studies were based on the fundamental 2D DEM research by Morgan (1999) and Morgan and Boettcher (1999) that tested in numerical shear box experiments the influence of particle's (grain's) friction coefficient on the grain rolling behaviour and hence, the strain weakening or hardening of the material package. Other studies established the role of particle shape or particle roughness on the macro-property (e.g. Guo & Morgan, 2004; Kock and Huhn, 2007a; Rothenburg and Bathurst, 1993, 1992; Schöpfer et al., 2009; Thornton, 2000). Furthermore, also particle breakage and fault gouge evolution were also already investigated utilizing the DEM (e.g. De Bono and McDowell, 2014; Mair and Abe, 2008).

Other fundamental studies have used the DEM approach to characterized cohesive clay particles microscopic interaction. Between two clay particles, in addition to the mechanical interactions, a variety of physicochemical interactions are responsible to the cohesive forces (Mitchell and Soga, 2005). The micromechanical behaviour of clay particle resulting from the complexity of microscopic interactions and interparticle forces, is not straight forward to model. For this reason, although an approach to model the fabric of clay particles was developed for DEM (Anandarajah, 2003; Anandarajah and Lavoie, 2002; Yao and Anandarajah, 2003),

incorporating both mechanical and physiochemical interaction in clays, is still limited to consolidation studies (Jaradat and Abdelaziz, 2019; Pagano et al., 2020).

In addition to these small-scale experiments, the DEM is also increasingly used to simulate large-scale geological processes. Extremely large-scale slope models simulated accretionary wedges mass movements formation quantifying the effects of the layer viscosity (Wenk and Huhn, 2013). Other large-scale slope models have simulated kink-band fault-propagation fold forms (Hardy and Finch, 2007) and delta formation in an active tectonic setting (Hardy, 2019).

In addition, for the purpose of simulating macroscopic scaled slope failure events, numerical DEM modelling is also a powerful tool, allowing access to the slide stages, quantities which are difficult, or almost impossible, to obtain directly from laboratory experiments. The DEM allows tracking individual particle trajectories, offsets and calculating which are essential to understand the underlying mechanism and dynamics of the slope failure. However, only a few studies have used this approach to bridge the gap between natural observation and geotechnical measurements of sediments to simulate large-scale landslides.

Modelling landslide along volcanic flanks with DEM, Morgan and McGovern (2005a) were able to show various deformation structures and geometries and compare the results to many volcanic settings as well provide mechanical understanding of the modes control volcanic deformation (Morgan and McGovern, 2005b). Huhn et al. (2016) demonstrated the importance of landslides distribution due to different peak shear strength of the sediments along subsiding basin flanks.

Most of the above-mentioned studies have simulated micro-scale and slope-scale shear processes under two-dimensional (2D) conditions. In micro-scale studies this was observed by Morgan (Morgan, 1999) showing relatively low frictional strength of the simulated granular samples compared with natural samples. Following this, Hazzard and Mair (2003), showed that for simulations modelling micro-scale granular processes, using 2D has an effect on the frictional strength. Their results suggested that for perfectly spherical particles, slightly higher frictional strength was obtained for 3D simulations compared to 2D models.

The effect of the third dimension in large-scale simulations has only been studied in specific case studies (e.g. Verrucci et al., 2019) taking into consideration specific morphological parameters of the slope and calibrating the numerical material accordingly. However, using the 3D approach allows to gain information that currently either cannot be achieved in the field or are very costly.

As mentioned above (section 1.2.1.), one of the characteristics arising from mapping the distribution of submarine landslides is their distribution as discrete features or in a neighbouring manner along continental margins (Urgeles and Camerlenghi, 2013). Although there are possibly other preconditioning factors that contribute to this occurrence (e.g., geological history of the margins), the influence of sediment shear strength is still unclear and a simulation using three dimension is therefore essential to further investigate slope failure as a function of varying sediment physical behaviour.

## **1.5. Research objectives and hypothesis**

This thesis primarily aims to contribute towards an improved understanding of the influence of sediment physical properties as preconditioning factors for slope failure, in particular the shear strength, to the (initial) size and the distribution of submarine landslides. Shear strength variations as a result of sediment type have been recognized to precondition slope failure (e.g. Gatter et al., 2020; Miramontes et al., 2018). However, despite evidence from sampled sediments, these were subjected to environmental and climatic variations and an independent understanding is needed.

Improving our understanding of the influence of sediments physical properties will help to bridge the gap between laboratory-scale measurements and slope-scale observations. On the one hand, laboratory analogue experiments and numerical modelling that tested the microscopic scale properties of sediments have shown that shear localization is dependent on the sediment physical properties, i.e., composition and initial strength (Fig. 1.5A, B). On the other hand, slope-scale observations of submarine landslides distribution and geotechnical measurements (Fig. 1.5C, D) have proposed a link between submarine landslide sizes and distribution to the shear strength of the slope sediments. However, a connection between these two different scales of failure measurements and is still missing.

To reach this aim, in the first part of the thesis (Chapter 3), I tested whether and how the physical properties of the sediments in a slide complex are related to the occurrence of the landslide. The Currituck slide complex is an exemplary site for a large submarine landslide occurring on non-glaciated margins. For this case study, the following questions were considered:

- What are the physical, chemical and sedimentological characteristics of the post-slide sediments?
- Which processes contributed to the different physical properties and consequently the shear strength of the sediments in the Currituck area?
- Are there physical or sedimentological indications for stratigraphic weak layers (also strength interface)? What are their characteristics in the Currituck area?
- Understanding the strength properties and how they (potentially) vary with depth, what is the potential slope stability at depths similar to the observed failure?

The second part of the thesis (Chapters 4 and 5) expands on the hypothesis suggesting that shear strength primarily controls the initial size and distribution of submarine failure. In this part, I tested conceptually how the shear strength of different sediment types and consolidation state influence the size and distribution of landslides in a numerical domain, thus independent of environmental influence. The main questions that were investigated by the model were:

- How does shear strength effect frequency and distributions of the area susceptible to failure?
- How does the sediments shear strength effect the initial size and distribution of mass movements?
- How do the shear strength and consolidation state of the sediments precondition large-scale mass movements?

The results obtained from the models will be placed in context with the currently worldwide known distribution and failure volume (Fig. 1.5E).

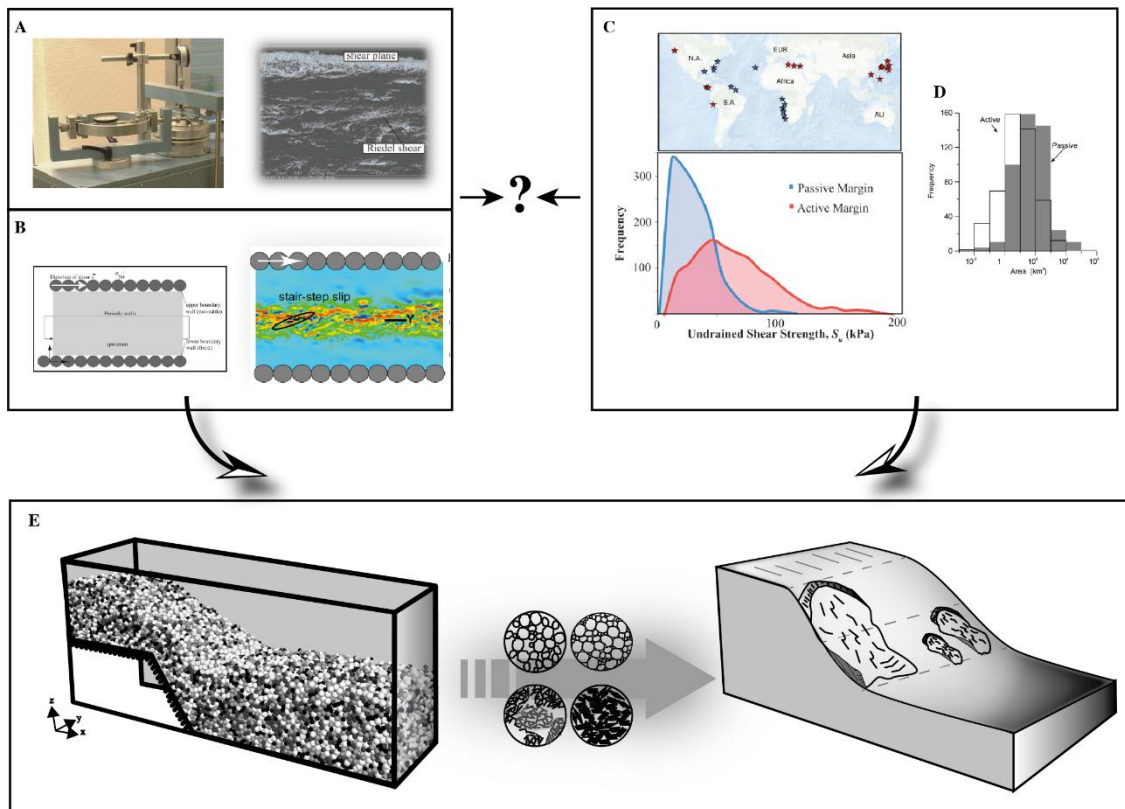


*Figure 1.5: A diagram illustrating the gap covered in the thesis between (A) analogue laboratory experiments and (B) numerical simulations (after Kock and Huhn, 2007b) measuring shear localization in sediments with different physical properties to measurements of shear strength from unfailed slopes (after DeVore and Sawyer, 2016) (C) and (D) observations of landslides distribution and sizes (after Urgeles and Camerlenghi, 2013). In the second part of the thesis (E) a numerical model considered (left) four case studies simulating sediments type and shear strength (circular insets: from left to right clockwise- low shear strength sand, high shear strength sand, high shear strength clay and low shear strength clay). The results are incorporated into slope conceptual models (right).*

## 1.6. Thesis outline

The presented research is a cumulative dissertation i.e., a collection of articles that were published, submitted or are in preparation for publication. In the following, I shortly outline each thesis chapter. Two chapters aim to understand the role of consolidation and shear strength as pre-conditioning factors for large-scale submarine landslides. One chapter used sedimentological, geochemical and geotechnical analyses of sediments from a submarine landslide complex (Chapter 3) and another chapter simulated variations of shear strength and consolidation in slope sediments using the discrete elements numerical method (Chapter 5). In Chapter 4, I test and calibrate numerical material behaviour that can simulate sediments under

various consolidation states (Chapter 4). Thereby, in a broader perspective, each chapter contributes to improve our knowledge on how sediments physical properties precondition large-scale submarine landslides in the deep sea.

**Chapter 1** reviewed the theoretical background and current knowledge of submarine landslides and sediments physical properties. It describes key concepts required to study the influence of sediments physical properties on slope failure. In addition, section 1.3 provides a background for the regional settings of the Currituck landslide complex as a case study in the West Atlantic margins. Section 1.4 provides background and review of the numerical studies that used the DEM to understand shear localization and landslides development.

**Chapter 2** presents an overview of the methods that were used in the research in order to answer the proposed research questions in Chapter 1.6. The methods are divided to (a) laboratory analyses of field data (section 2.1) that was used in the first part of the thesis and to (b) a description of the numerical approach and workflow (section 2.2) that was used in the second part of the thesis.

**Chapter 3** presents a manuscript in preparation for *Marine Geology*, entitled “*Currituck slide complex: sediment controls and implications to slope instability*”. The manuscript is based on sediment cores taken from within and around the Currituck submarine landslide complex, located in the west Atlantic margins, offshore Albemarle Sound, USA. It is comprised of two parts (a) an investigation of the drape and the debris sediments, exploring transport and sedimentation in and around the slide complex in order to understand the possible role of the sediments to precondition the slide. (b) Based on the analysis, a 1-D slope stability analysis was conducted accounting for strength interface as a result of different consolidation states. The results of the sedimentological and geotechnical analysis show that the drape layer represents two units of last interglacial period: the transgressive and the high stand stages. Although the two units are similar lithologically, they were deposited under different fluxes and developed different consolidation states. The latter indicating that within the slide complex, strength interfaces could have formed as a result of the climatic and sea level changes. The averaged slope stability analysis suggests that the slope is stable under static conditions and failure may occur under undrained earthquake conditions. However, evaluating slope stability for each of the identified units suggests under both static and pseudo static conditions the lower unit deposited under high flux conditions is unstable, whereas the unit above is far more stable.

These findings possibly capture how the sediment flux variations within the Currituck area preconditioned the development of a failure plane. In addition, these findings have implications for other studies trying to understand the potential stability of slopes and the influence of the consolidation state. In order to gain deeper understanding we suggest future studies to test different consolidation states and their influence on the initiation of submarine landslides.

---

Author's contribution:

---

The study was designed by Uri ten Brink, Jason Chaytor and me. MSCL data was acquired by Jason Chaytor. I have performed MSCL data analysis. Following, I performed and analysed geotechnical, sedimentological and geochemical measurements. Subsequently I designed and calculated slope stability analysis using these data. Therefore, Katrin Huhn provided the code for the slope stability calculations. Based on these results, I developed and visualized a conceptual model explaining the evolution of the Currituck slope. The manuscript was designed and written by me, with contributions from Uri ten Brink, Jason Chaytor, Revital Bookman and Katrin Huhn.

**Chapter 4** was published in a special issue of *Processes, DEM Simulations and Modelling of Granular Materials*, and is entitled “***Numerical Characterization of Cohesive and Non-Cohesive ‘Sediments’ Under Different Consolidation States, Using 3D DEM Triaxial Experiments***”. The manuscript presents a 3D numerical characterization of sediment using the PFC software. The study addresses the problem of DEM micro-particle properties parameterization to generate a set of different sediment types of the siliciclastic sedimentary system. It compares the application of two contact models, which allows generating both cohesive and cohesionless granular mechanical behaviour. In addition to sediment type, the study also characterized the sediments under different burial depths and consolidation states to see the resulting deformation. The results show how three different levels of parametrization can be applied to generate a range of numerical sediments. The study implications suggest that the processes of parametrization can be used to simulate various sediments and applied to test geological processes models

---

Author's contribution:

---

The study was designed and conceptualized by Hadar Elyashiv and Katrin Huhn. The numerical simulation technique – the DEM code, was utilized by me to test and develop different parameterizations of numerical sediments. Katrin Huhn provided the DEM code as well as the computer infrastructure whereas Lennart Siemann assisted with post-processing routines. The numerical experiment setup, and model runs as well as data analysis and visualization of the results were done by me. The manuscript was designed and written by me, with contributions specifically in the discussion chapter from Uri ten Brink, Lennart Siemann, Revital Bookman and Katrin Huhn.

**Chapter 5** presents the manuscript submitted to *Marine Geology*, entitled “***Submarine mass-movements preconditioned by sediments shear strength: Insights from 3D numerical modelling***”. Using 3D numerical analysis, the study presents unique insights for the development of submarine landslides in time and space; a much-needed contribution to a field, which still cannot directly observe large failure processes. The study addresses the hypothesis in which different consolidation state of sediments affects the occurrence and scale of mass movements. We addressed the spatial and temporal mass movements’ development by simulating four types of slope sediments. The main outcome validated many field observations and statistical studies, demonstrating how slope susceptibility to large-scale failure develops in specific sediments settings. These results could ultimately help to better plan mapping surveys and understand the occurrence and frequency of submarine landslides.

---

Author's contribution:

---

The study was designed and conceptualized by Hadar Elyashiv and Katrin Huhn. The DEM code was provided by Katrin Huhn. The DEM experiments were designed by me and Katrin Huhn whereas the codes were written by me. The experimental runs and data analysis were conducted by me with the overarching aim to simulate in a 3D numerical sandbox model the evolution of submarine slopes to investigate the key role of sediment physical properties on slope failure evolution. In addition, the visualization of the results was done by me. As the major result, the conceptual model for different sedimentary slope systems was designed by me, Katrin Huhn and Uri ten Brink. The manuscript was designed and written by me, with contribution by Uri ten Brink, Revital Bookman and Katrin Huhn.

**Chapter 6** provides a synthesis of the results and conclusions of the previous chapters within the context of the research aims outlined in Chapter 1. In addition, an outlook of future work and approach is suggested.

## 2. Methods

---

Understanding submarine landslide pre-conditioning factors, in particular the role of shear strength, requires a multi-disciplinary approach. In order to gain an understanding of the preconditioning factors to the Currituck complex landslide and to assess the (paleo) stability of the sediments, analysis of the sedimentological composition and geotechnical properties were performed.

The Currituck slide complex is a good example to study the role of sediment physical properties in preconditioning a large submarine landslide; particularly in a sedimentary system that was mainly fluvially-controlled. Nevertheless, to highlight the key role that sediments physical properties play in preconditioning large landslides, a numerical approach was used to test additionally other slope sediments properties. The numerical method chosen for the simulations is the DEM. First, a calibration study was performed to characterize sediment endmembers of different mechanical behaviour. Second, four selected calibrated materials were used in a model to assess the influence of shear strength in terms of volume, frequency and location of submarine landslides.

### 2.1. Field data and analysis

#### 2.1.1. Materials

The dataset for this study is based on cores collected by the R/V Hugh R. Sharp during cruise HRS120929 in 2012. Cores were collected on-board using a piston corer (Chaytor and Shipboard scientific party, 2012). In the current study, five cores were selected for detailed analysis (Table 2.1) representing five physiographic areas of the Currituck slide complex as identified by Hill et al., (2017) (see Fig. 2.1 for the locations). Age of the sediment in the thesis follows Chaytor et al. (in preparation).

*Table 2.1: A list of cores from the Currituck slide complex and analysed in this study.*

<b>Core name</b>	<b>Water depth</b> [mbsl]	<b>Geographic position</b>		<b>Core length</b> [cm]
		Latitude	Longitude	
5PC	339	36.355	74.757	835
7PC	1350	36.347	74.639	633
13PC	1825	36.362	74.589	707.5
14PC	1729	36.146	74.586	474
16PC	1287	36.230	74.587	655

### 2.1.2. Core physical properties

Multi-Sensor Core Logger (MSCL) is an instrument devised to measure sediment cores physical properties continuously and without destruction. The measured physical properties include P-wave velocity, gamma-density, magnetic susceptibility and electrical resistivity. Each of these measurements or their combinations are further used to evaluate the results in terms of lithological and sedimentological characteristics. In addition, the results are used to create a correlation between the cores where radiocarbon dates are not available.

The MSCL data used in this thesis was measured at the University of Rhode Island following their collection. In the current research, the data for the chosen cores was processed to remove outliers and create a stratigraphic correlation where possible.

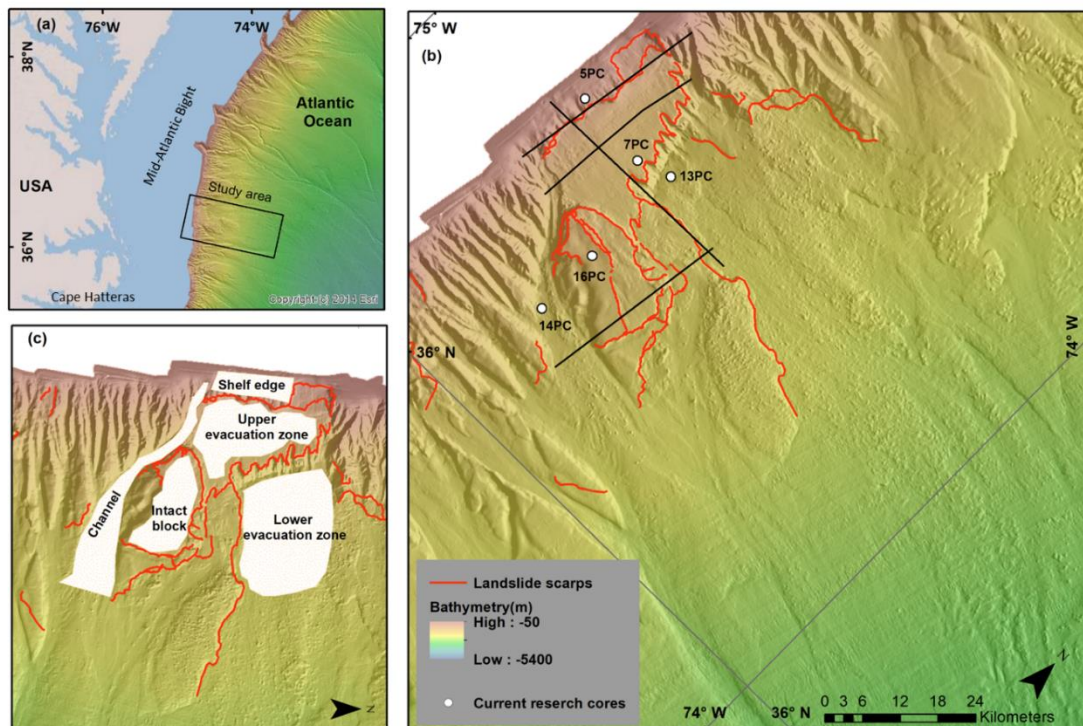


*Figure 2.1: Location of the research area and the cores selected for research. (a) location of the Currituck landslide complex offshore eastern USA (b) physiographic areas of the Currituck slide complex as identified Hill et al., (2017) (c) Core location within the research area. Colourful dots represent cores selected for detailed analysis. White dots represent cores used for across and along slope correlation according to MSCL analysis.*

### 2.1.3. Particle size distribution

Particle Size Distribution (PSD) analysis provides important information on the transport processes and depositional conditions, which highlight environmental and climatic changes (McCave 2007).

In the current study, PSD analysis was performed on five cores from the Currituck slide complex (see Table 2.1 cores 5PC, 7PC, 13PC, 14PC and 16PC). The measurements were obtained at a variable spacing ranging from 30 cm (along homogenous muddy sediments) to 5 cm (along sandy thin layers or sand-clay transition).

Each sample was measured twice, once to observe the bulk sample PSD and second time to observe the terrigenous components of the PSD. In order to isolate the terrigenous fraction from organic material and biogenic carbonate, the following pre-treatment protocol were performed: (1) To a glass with 35 ml deionised water, approx. 1 ml of wet sample was added. (2) A diluted (35%) 10 ml Hydrogen peroxide ( $H_2O_2$ ) was added to the glass. All glasses were put to boil on a heating plate in order to induce a faster reaction and dissolve the organic matter. (3) Deionized water (100 ml) and Hydrochloride acid (10%, 10 ml) were then added to the sample in order to remove the calcium carbonate fraction (biogenic carbonate, e.g., foraminifera and shells). (4) When the reaction ended, a washing procedure was done to remove solution and dissolved material. One litter of deionized water was added and the sample was left settle for 8 hours. (5) After 8 hours, the sample was decanted leaving only 100 ml in the glass. Following, the washing procedure was repeated twice more before measurement.

Prior to the measurement, a dispersing agent, tetra-sodium diphosphate decahydrate ( $Na_4P_2O_7 \cdot 10H_2O$ , 300 mg) was added to all samples to ensure that particles remain disaggregated through the measurements (e.g. Murray, 2002).

The measurements were performed in *The Environmental Sedimentology Laboratory* at the University of Haifa and in the *Particle-Size Laboratory* at MARUM, University of Bremen. Both laboratories hold a Beckman Coulter Laser Diffraction Particle Size Analyzer LS 13320. Following pre-treatment and preparations, a sample was added to the machine pumping unit where it was kept in suspension during measurement. The Beckman has two measurement cells to analyse the coarse fraction (2000-0.4  $\mu m$ ) and the fine fraction (0.4-0.04  $\mu m$ ) of a sample. As sediments are pumped through the measurement cell, the laser beam is projected to the cell and diffracted by the particles. The laser diffraction is then detected by an array of detectors consisting of 92 channels.

The channels are arranged in order to capture the different diffraction angles produced by the particle sizes. Due to the small and large angle scatter produced by coarse and fine particles, respectively (Fig. 2.2), PSD measurements are divided to two cells. The coarse fraction is analysed in a measurement cell with a laser beam with a wavelength of 780 nm. The fine fraction is analysed in a second measurement cell where a polarised light Polarization Intensity Differential Scattering (PIDS) technology is applied to detect the scattered light by the particles.

To ensure similarity between the two machines, a similar pre-treatment protocol was maintained in both institutions. In addition, two samples representative of homogeneous mud and homogeneous sand were measured in both institutes to confirm similarities in the measurements.

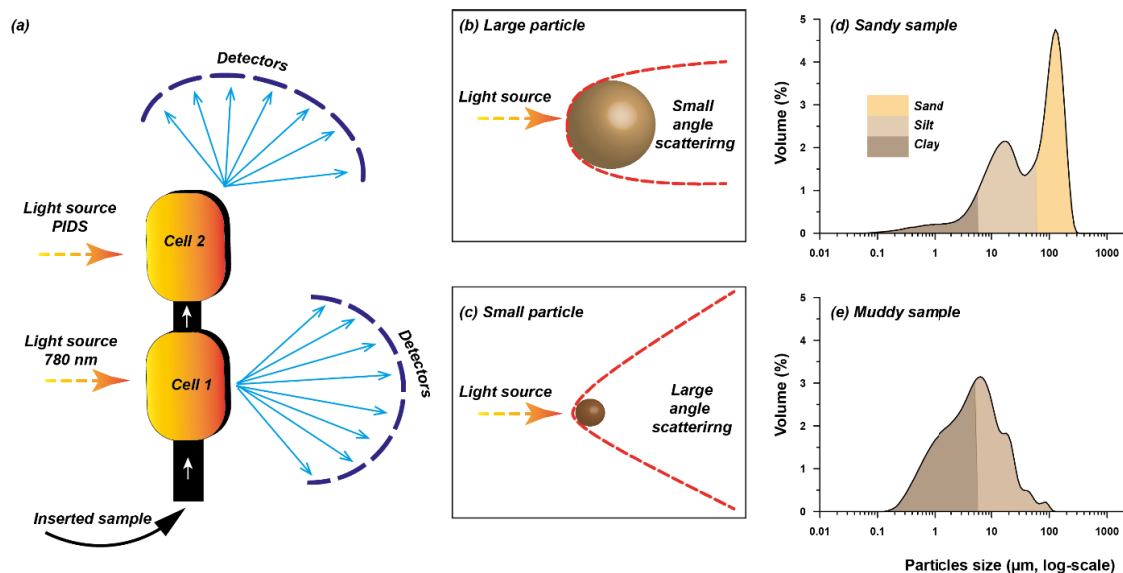


**Figure 2.2:** Particle size distribution measurements and analysis (a) A schematic illustration of Laser Diffraction Particle Size Analyzer measurement cells and detectors array (b) Light scatter pattern for a coarse particle (c) Light scatter pattern of a fine particle (a-c are modified after Rasmussen, 2020) (d) Sandy sample PSD example from 5PC (10 cm) (e) Muddy (clayey-silty) sample PSD example from 16PC (642 cm).

Grain size classification (division to sand, silt and clay fractions) follows Wentworth (1922), however the silt-clay boundary was shifted to 0.06 μm following Rasmussen (2020, and references therein). According to Rasmussen (2020), in the laser diffraction method, clay particles are almost always measured as coarser due to measurements of the longer axis of a clay particle (as opposed to measurements taken by settling method) and

therefore a correction to the silt-clay boundary and therefore the relative volume of the clay fraction needs to be considered.

The statistical analysis of the grain size parameters were obtained from bulk sediment and analysed by the Gradistat application (Blott and Pye, 2001), adopting its grain size scale (Blott and Pye, 2001). Mean grain size, sorting, skewness, and kurtosis were calculated using the method of Folk and Ward (1957).

#### *2.1.4. X-Ray Fluorescence (XRF) bulk element analysis*

X-Ray Fluorescence (XRF) spectrometry is a relatively non-destructive chemical analysis of sediments providing their bulk chemical composition. It is a widely used method to analyse major and trace elements in sediments and rocks due to its relative ease of use, the low cost of sample preparation and the stability of the XRF readings. In the field of marine geology, the analysis of high resolution quasi-continuous (1 mm) sediments record has proved to provide significant information regarding paleoclimate changes, currents changes and early diagenesis processes (Croudace and Rothwell, 2015 and references therein). Here, XRF analysis was performed on discrete samples, following the sampling resolution for PSD. Despite the low resolution (~10 to 30 cm) compared to continuous measurements, the results in the current study proved sufficient, providing the necessary signal to view changes in sedimentary processes along the cores.

In order to prepare the sediment samples for XRF measurements, the samples were first frozen and then freeze-dried to remove liquids. From the dried samples, 1.2-1.5 grams were taken as a representative homogenous aliquot and placed in an agate mortar in order to crush particles into fine dust. The aliquot was then transferred and pressed into Teflon containers atop an X-ray transparent prolene thin film.

Bulk elemental analysis was conducted using a Xenometrix S- Mobile benchtop EDS- X- Ray Fluorescence (XRF). Geochemical analysis of light elements (Al to Fe) was run under low energy range (10 keV) with excitation potential of 25 kV, an x-ray current of 15  $\mu$ A and a count time of 60 seconds. In addition, analysis of heavier elements (Fe to Zr) was run under high-energy range (40 keV) with excitation potential of 50 kV, an x-ray current of 10  $\mu$ A and a count time of 120 seconds. No filter was used in both light and heavy elements analysis. Processing of the spectra was done using CrossRoads Scientific's Fundamental Parameters software suite. All measurements were carried out at the Basin Analysis and Petrophysical laboratory (PetroLab) of the University of Haifa.

From the whole set of measured elements, the records of iron (Fe), titanium (Ti), calcium (Ca), and zirconium (Zr) were used in the results analysis. As the measurements yield relative elements concentrations, the XRF results and their interpretation are further presented as elements ratios. In the current study, the records of [Ca/Ti], [Fe/Zr] were used. As shown in Croudace and Rothwell (2015 and references therein), the ratio Ca/Ti has been widely used to present the change in ratio between biogenic contribution (represented by Ca, derived from calcareous remains, mostly planktic organisms) and the terrigenous supply (represented by Ti that is exclusively of detrital origin) and therefore reflects sediment flux trends (Bahr et al., 2014). The ratio Fe/Zr was used by Hanebuth and Lantzsich (2008) that suggested the ratio to infer transport and sorting mechanism, separating heavy Zr-containing minerals from other siliciclastic grains. Here, this ratio was tested in core 14PC in which possibly turbidity / collapse events deposits were observed following the core splitting and additionally due to the core's location in a submarine channel.

#### *2.1.5. Vane shear tests*

Vane shear tests provide a first order estimation of the sediments undrained shear strength ( $S_u$ ), identifying the trend of characteristic strength along a core's depth. The tests evaluate the shear strength of fine-grained soils (i.e. sediments), however they do not provide a reliable measure of sandy soils (Craig, 2004). For marine sediments,  $S_u$  measurements are taken in-situ, directly from the undisturbed, split open cores; otherwise (i.e., in case of sampled sediments), the shear strength is considered remoulded.

Shear strength measurements were taken from the selected cores (see Table 2.1). The undrained shear strength was measured at spacing of every 10 cm. Smaller (5 cm) or larger (30 cm) spacing measurements were taken due to the occurrence of a sand layer or bioturbated section detected in the x-ray images. For undrained shear strength measurements, no preliminary treatments or preparations are needed.

The measurements were taken as a manual device was pushed vertically to the sediment in the split open core. A rotation of the top of the device was performed while keeping a uniform velocity rotation. Measurements were performed in the USGS Woods Hole Coastal and Marine Science Centre, where cores were held.

Following the measurements, to identify whether the sediments are under-, normally- or over-consolidated, the effective overburden stress is calculated. Using MSCL sediment density values and by assuming hydrostatic pore water pressure by:

Eq. 2.1 
$$\sigma'_{v0} = \gamma' * Z,$$

where  $\gamma'$  the submerged unit weight, and  $Z$  the depth below sea floor. For each core, the vertical effective stress was calculated using averaged grain density from the MSCL data and assuming seawater density of  $1.024 \text{ g/cm}^3$  (Weber et al., 1997). Normally consolidated sediments with an inherent overconsolidation ratio of one, presents a liner increase in shear strength which is in the range of  $0.2 - 0.4 * \sigma'_{v0}$  of the effective overburden stress (Locat and Lee, 2002; Wiemer et al., 2015).

#### 2.1.6. Moisture content

The moisture content or water content ( $w$ ) is a preliminary evaluation of the content of fluids in the sediments. It is taken as the ratio of water weight to the weight of the solids in a given sediment sample (Craig, 2004).

The spacing follows the spacing chosen for the vane test measurements. A sample aliquot of approximately 5 gr was placed in a clean and dry pre-weighed crucible. The samples were then placed to dry in an oven pre-heated to  $105 \text{ C}^\circ$  for a duration of 24 hr. following the sample was weighed again to measure the solids weight. The water content is then calculated as

Eq. 2.2 
$$w = \frac{W_w - W_d}{W_d} * 100,$$

where  $w$  is the water content of the sediment sample (in percentage),  $W_w$  is the wet sample weight and  $W_d$  is the dry sample weight.

#### 2.1.7. Slope stability analysis [1D]

Using equations 1.4 and 1.5 in section 1.2.4., the slope stability analysis was designed to test the stability in the Currituck area. Constant input values such as the bulk and buoyant unit weight are based on the MSCL density measurements. The measured values of the undrained shear strength were used as an input based on an evaluation of their change with depth. A linear regression analysis for each core and separately to each identified unit (Table 2 and supplementary material) was used to evaluate the shear strength variations with depth. The stability analysis in chapter 3 (section 3.3.5.) tested the changes in the research area for variations (Table 2) in the slope angle (changes in the slope

geometry), depth (occurrence of the failure plane), and the horizontal ground accelerations (earthquake magnitude).

## 2.2. Numerical modelling

### 2.2.1. The Discrete Element Method

DEM is a numerical approach introduced by Cundall and Strack (1979) to simulate the interaction between granular particles via discrete contact points. Since its initial development the method has been widely and increasingly used to simulate mechanical behaviour in rocks and/or granular media, e.g. soils and sediments, at microscopic as well as macroscopic levels (e.g. Katz et al., 2014; Kock and Huhn, 2007a; LongJohn et al., 2018; Morgan and Boettcher, 1999; Thornton, 2000).

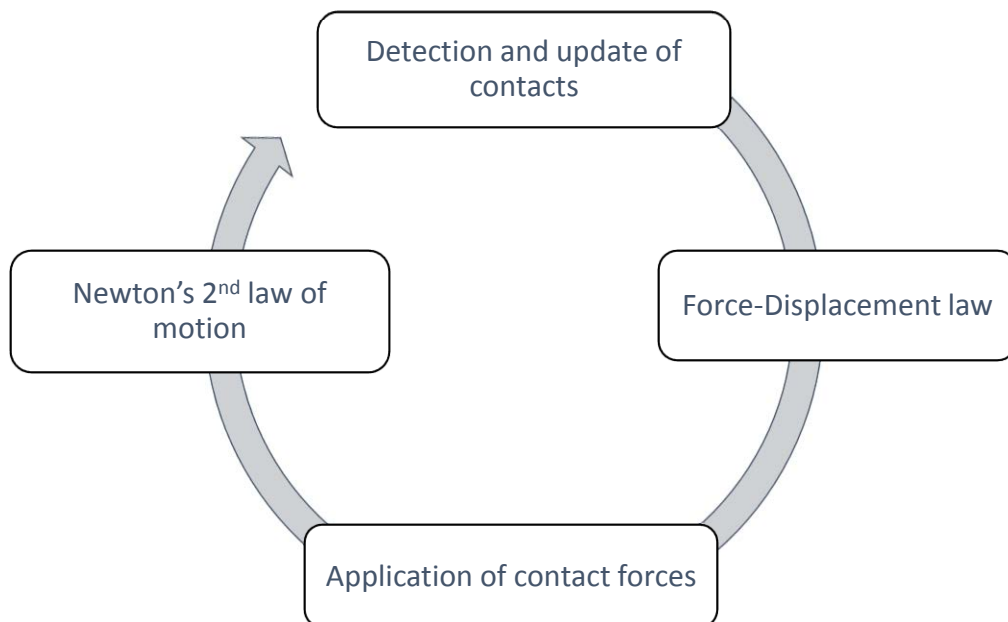


*Figure 2.3: An abstract illustration representing the DEM calculation cycle. A simulation starts by detecting the contacts between particles. If particles are in contact the force-displacement relationship is calculated. The resulting forces are applied to each particle generating motion. A particle acceleration, velocity and displacement are then updated according to Newton's second law of motion. This loop continues until a predefined number of iterations is reached.*

The approach is based on a time-stepping algorithm that continuously updates the particles properties such as position and contacts for every simulation iteration (Fig. 2.3). The displacement of each particle involved in the particle-to-particle interaction is solved by equations based on Newton's second law of motion. The forces exerted by particles

are calculated at the contacts following predefined force-displacement contact laws (also termed contact models, see section 4.2). In such approach, the interaction of particles is monitored via the contacts as the particle's position is continuously traced (Itasca, 2014). A complete overview of the DEM force-displacement calculations is detailed in appendix A of chapter 4.

There are several advantages to the DEM. As a particle based technique the method allows to simulate the deformational behaviour of rocks and sediments (Huhn et al., 2006; LongJohn et al., 2018; Morgan and McGovern, 2005a). During the simulations a detailed information regarding the particle location, orientation, velocity and other data are continuously monitored and can be recorded. As a result, the internal structure of the particle assemblage can be used to monitor the development of deformation. In particular, data availability in time and space allows observing in a high resolution the development of the deformation process, e.g., the localization of faults and failure planes.

Granular materials consisting of discrete particles only interact at contacts. The DEM has been used over a range of applications to model the behaviour of different materials as it uses the microscopic properties of the independent particles allowing to simulate the macroscopic behaviour of the particle assemblage. Practically this means that the micro-properties of the model are adjusted based on the to be simulated macro behaviour of the natural material. Since the normal and shear stresses can be monitored at each time step for the entire model run, macro-properties of the entire particle assemblage (i.e., bulk material) such as bulk friction coefficient or cohesion can be calculated and compared to natural sediment physical properties. This concept of the simulated material macro-properties vs parameterized micro-properties is further outlined in section 4.2 in chapter 4.

Finally, the setup of model micro-properties, boundary and initial conditions allow to control and to reproduce individual model runs. This also allows testing one parameter at a time and viewing the resulting influence on the material mechanical behaviour.

Currently, there are various available DEM codes, both commercially and open source (e.g., YADE). In this thesis, in Chapters 4 and 5, the commercial software Particle Flow Code in three dimensions (PFC3D, v5.0) developed by Itasca was used. Several built-in features facilitate the reproducibility and speed of simulations such as the servo-controlled walls, random seed particles distribution and monitoring unbalanced forces (Itasca, 2014).

### 2.2.2. Numerical parametric study

Due to the manifold behaviour of different materials in nature, various constitutive models have been developed to describe various granular particles interaction behaviour. The application of these contact models in DEM through particles contact interaction allows to model different materials numerically, e.g plastic vs elasto-plastic or viscous etc. In this thesis, two contact models (implemented by Itasca in PFC3D) were chosen. These contact models were selected to account for two distinct behaviours of sediments in nature. The *Hertz-Mindlin* contact model was selected to represent cohesionless, frictional-dependent sediments such as sand and the *Linear-parallel bond* contact model was selected to represent a cohesive sediment such as clay. For each contact model there is a range of micro-properties that are applied to each particle individually, in order to generate an overall bulk (macro-scale) mechanical behaviour of the numerical material. Micro-properties such as friction, density, and the bond's shear and normal forces are assigned at the particle scale. A detailed description of each contact model, the controlling equations and the required micro-properties is found in chapter 4 sections 4.2.1. (*Hertz-Mindlin*) and 4.2.3. (*Linear parallel bond*).

Numerical geotechnical, parametric experiments were carried in order to test the numerical sediment's mechanical behaviour according to different sediment types shear strength, burial depth and consolidation state (material test scheme in Fig. 2.4). In laboratory experiments, there are different types of geotechnical experiments to achieve these parameters such as simple shear or triaxial shear tests. Here, a 3D cubic triaxial shear test was designed (Fig. 4.1) with impermeable walls as boundary walls. The top and bottom servo-controlled walls were imposing normal stress during the test run. A detailed description of the shear cell parameters (size, friction etc.) is found in section 4.2. The particles distribution in the test included 4 particle sizes in order to avoid an artificial granular compaction (Saltzer and Pollard, 1992). During the testing of the material, the position, contact, coordination number, normal and shear stress and strain were continuously monitored via the measure logic provided in PFC3D (see Fig. 4.1).

Prior to the parametric tests, benchmark triaxial tests were performed to characterize for each sediment type the major micro-parameter, which influence on the shear strength (see scheme in Fig. 2.4). For the *Hertz-Mindlin* contact model, the range of values and relationship between Poisson's ratio ( $\nu$ ) and the shear modulus ( $G$ ) was tested (Table 2.2). For the *Linear-parallel bond* contact model, the range of values and relationship

between the bond normal and shear stiffness ( $PB_{kn}$ ,  $PB_{ks}$ ) and the bond cohesive ( $PB_c$ ) and tensile ( $PB_\tau$ ) strengths was tested (Table 2.2). Each couple of parameters was additionally tested under three magnitudes of confined stress of  $\sigma_2 = \sigma_3 = 100, 250$  and  $500$  kPa. In total, 36 preliminary tests were performed.

**Table 2.2:** Values for the benchmark tests of sediment type major parameter

Parameter	Tested values
<i>Hertz-Mindlin</i> contact model	
Poisson's ratio [-]	0.1, 0.25, 0.3
shear modulus [Pa]	$1e^8, 1e^{10}, 1e^{11}$
<i>Linear-parallel bond</i> contact model	
Bond stiffness $PB_{kn}, PB_{ks}$ [Pa]	$1e^3, 1e^5, 1e^7$
Bond cohesive strength $PB_c$ [Pa]	$55e^3, 110e^3, 210e^3$
Bond tensile strength $PB_\tau$ [Pa]	$25e^3, 55e^3, 110e^3$

The tests results have shown that for the Hertz-Mindlin contact model the important parameter is the shear modulus. The Poisson's ratio parameter was set constant on a value of  $\nu = 0.25$  for all the tests applying the Hertz-Mindlin contact model. For the *Linear-parallel bond* contact model, the tests have shown that the important parameters are the bond cohesive and tensile strength. The bond's normal and shear stiffnesses were set to a constant value of  $PB_{kn} = PB_{ks} = 1e^5$  [Pa].

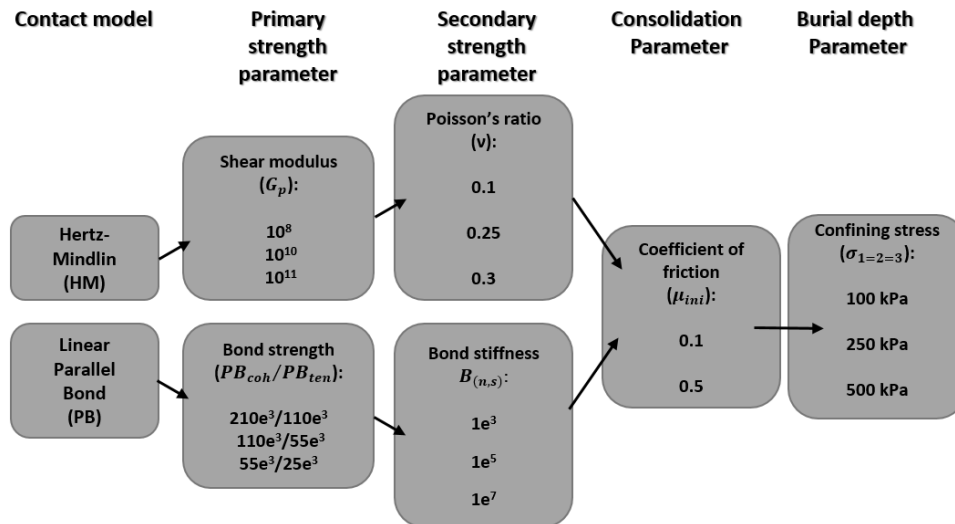


**Figure 2.4:** A scheme of the numerical sediments parametric and benchmark tests. First benchmark tests were performed to define the major parameter controlling the strength of the sediment and second the material parametric tests as detailed in Chapter 4.

### 2.2.3. *Numerical slope model set up*

Based on laboratory analogue sand box experiments, a 3D slope model was designed to simulate the development of increasingly steepened sediment bearing slope. Following the parametric study, four numerical sediments were selected to represent endmembers of the siliciclastic system (Chapter 5, table 5.1). Sand and clay numerical sediments represent two endmembers of the natural sediment composition and low and high shear strength represent endmembers of different consolidation states (under- to normally-consolidated vs. over-consolidated, accordingly).

### 2.2.4. *Results analysis and visualization*

Since the material properties and mechanical behaviour can be recorded throughout the simulations, it is possible to monitor and view various deformation structures (e.g. shear zone Morgan and Boettcher, 1999). Mainly, the particle's location monitored and subsequently the total and relative displacement of particles were calculated here to view deformation in different scales. The approach was adapted from analogue sandbox experiments similar to Kock and Huhn (2007b). The currently used Matlab code was developed by Schmiedel (2017).

The analysis of results in Chapter 4 are based on (a) data monitored within the measurement sphere (See Fig. 4.2) that can be directly plotted and visualized such as the stress-strain curve or the volumetric strain-strain curves (e.g., Fig. 4.3). (b) Strain localization analysis in Chapter 4 is based on analysis and visualization of the relative displacement of particles. To visualize this, based on the stress-strain curve deformation stages were defined (e.g. yield, peak shear stages). The change in the location of particles was then used to calculate the relative displacement. The results were transformed from discrete locations to a continuous mesh and interpolated using the nearest neighbour interpolation approach in MATLAB. These results were further visualized using the ParaView software.

Peak shear strength was then used to calculate and characterize the macro-properties of each material (Fig. 4.1 and Table 4.2). These macro-properties further determined which of the materials can be used in the slope model and also used in calculations of the FOS of each model slope.

The model results in Chapter 5 involved several routines to measure and analyse the development of the slope angle and of the occurrence of landslides.

Particles' location in each simulation stage (also termed slope stage in chapter 5) was used to create a grid representing a bathymetric surface from which mass movement's initiation was observed. A MATLAB subroutine was developed to extract only the surface particles (their location and radius) from the 3D box model (Fig. 2.5). After projecting the particles' location, a grid was created and then interpolated in Surfer® (Golden Software, LLC). A series of slope angles were calculated and used in the analysis of landslides formation. The *overall-slope angle* ( $\theta_{OS}$ ), the *local slope angle* ( $\theta_{LS}$ ) and the *critical slope angle* ( $\theta_C$ ). A detailed description for their calculation or measurements is found in Chapter 5, section 5.4.

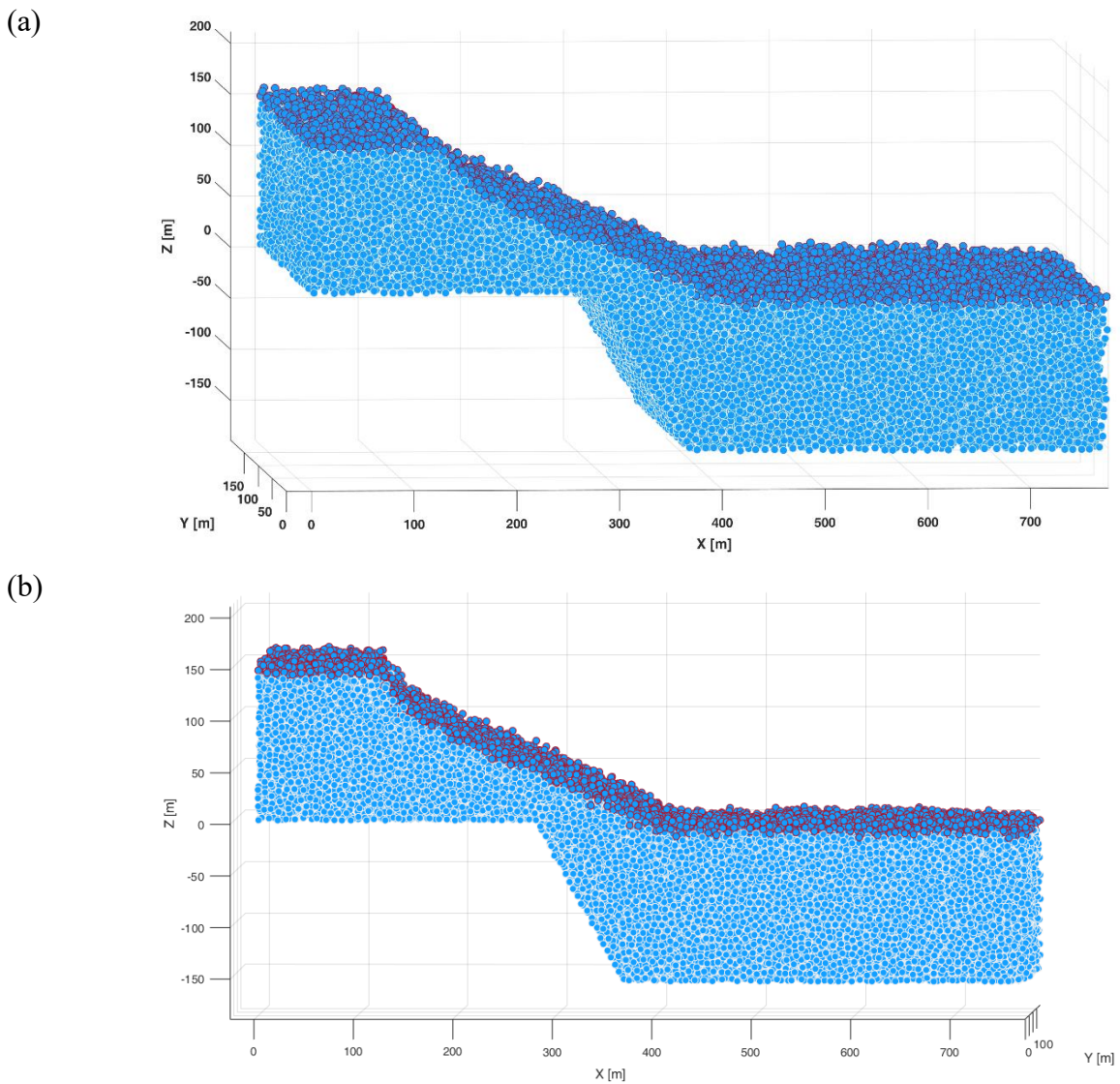


*Figure 2.5: An Illustration of the extracted surface particles from the 3D slope model. (a) 3D and (b) a semi-cross section. Blue dots-the entire 3D model particles, purple dots-surface particles.*

The slope profile and the slope rate of development are two measures based on a mean evaluation of the slope area around  $y = 100 \mp 50$  [m]. The slope was evaluated by an extraction of the surface particles in the chosen range (Fig. 2.6). Using the particle's location, a polynomial fit was created in a MATLAB subroutine for each slope stage (see section 5.2.4.1. for a detailed explanation).

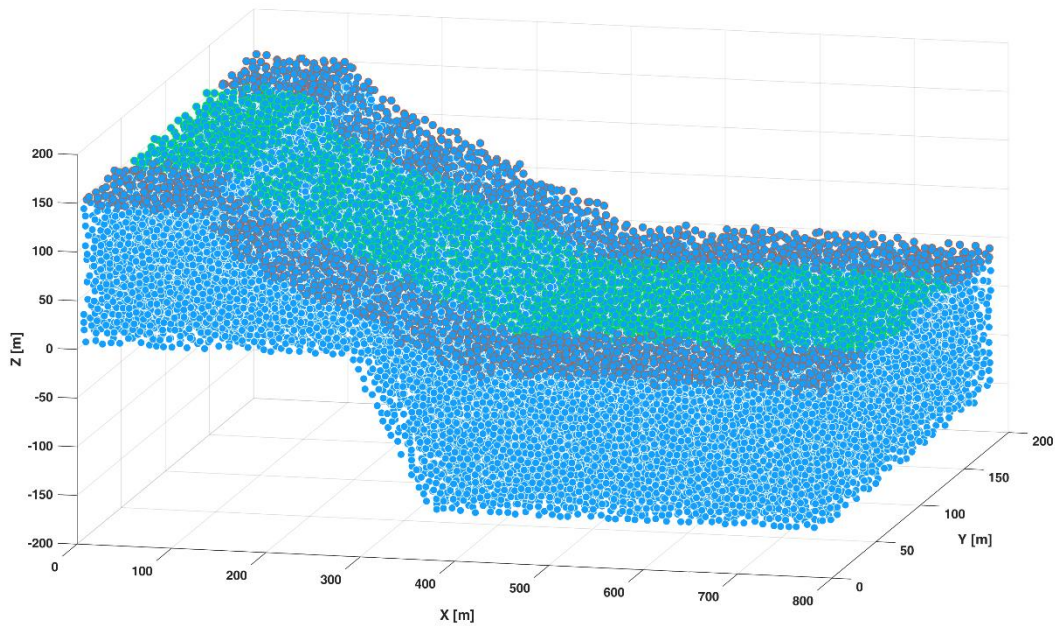


*Figure 2.6: An illustration of the surface particles extracted to calculate the mean slope profile and its derivatives. Blue dots-the entire 3D model particles, purple dots-surface particles, and green dots-particles taken for the mean slope profile.*

Using the entire box model, the total and relative displacement of particles were used to observe landslide surface distribution and their subsurface extent, respectively. A detailed description for the calculation and visualization is found in chapter 5, section 5.2.4.

The final calculation of a single landslide volume observed in a simulation stage is based on a MATLAB algorithm. The algorithm first calculates the particles total displacement and extracts particles that have moved more than a predefined threshold value. This value defines a movement of particles as a landslide. Next, it evaluates individually for each particle, based on its radius whether it is in contact with other particles that were displaced. A group of particles that were displaced more than the threshold value and are in contact are defined as one landslide. The volume of this group of particles is then

calculate according to equation 5.2. A visualization of such particles groups appears in the supplementary material of chapter 5 (see Fig. S5.2).



# Chapter 3

## Understanding the sedimentological controls in Currituck slide complex and implications to slope instability

**Authors:** Hadar Elyashiv (MARUM, University of Bremen, Germany & the Dr. Moses Strauss Department of Marine Geosciences, University of Haifa, Israel)  
Jason Chaytor (U.S. Geological Survey, Woods Hole Coastal and Marine Science Centre, USA)  
Revital Bookman (Dr. Moses Strauss Department of Marine Geosciences, University of Haifa, Israel)  
Katrin Huhn (MARUM, University of Bremen, Germany)  
Uri ten Brink (U.S. Geological Survey, Woods Hole Coastal and Marine Science Centre, USA)

**Status:** In preparation, *Marine Geology*  
to be submitted  
to:

# 3. Understanding the sedimentological controls in Currituck slide complex and implications to slope instability

---

## Abstract

The Currituck submarine landslide complex is one of the major recognized large-scale landslides in the north-west Atlantic margins. The slide complex has been used as a typical slide to model submarine landslide tsunami assessment in the mid-Atlantic margins. However, a fundamental characterization of the sediments, their geotechnical properties and understanding how they possibly preconditioned failure in the Currituck area is still missing. A multiproxy approach combining sedimentological, geochemical and geotechnical tests was used to analyse sediment cores collected from within and around the slide complex. The geochemical and geotechnical results distinguished two units in the drape layer, within the slide complex. Supported by age constraints from a recent study, the lower unit was deposited during the late Pleistocene sea-level transgression, under increased sediments flux conditions. The upper unit was deposited during the Holocene sea-level highstand under relatively decreased sediment flux conditions. The factor of safety (FOS) analysis showed a statistically significant difference between the two units. The results imply that while oceanographic settings and sea level cycles control the sediments sorting, the shear strength and the consolidation are influenced by the sedimentation rate.

Based on the results, a slope stability analysis was calculated. The analysis evaluated the slope stability for each core and individually for each of the two units. The analysis indicates that currently the slope is stable under static undrained conditions, however vulnerable ( $2 < FOS < 1$ ) considering similar depth and slope gradients as documented for the slide. Under undrained earthquake loading conditions, the peak ground accelerations required to initiate slope failure at  $\sim 4^\circ$  slope gradients vary in the range of 0.07-0.15 ( $m/s^2$ ). Slope stability was different however, once each unit's stability was evaluated. Both static and pseudo static analysis show that the lower unit deposited under high flux conditions is unstable, whereas the unit above is far more stable. These results indicate that despite similar lithology, variations in consolidation (normally consolidated vs. slightly overconsolidated) can be significant and most likely control the formation of strength interfaces, promoting shear localization. A glacial-interglacial

sedimentary cycle reconstruction suggests that conceptually only during sea level rise accompanied by high sedimentation rates a significant strength interface could have formed in the Currituck deposits. In general, our approach to evaluate slope stability individually to different stratigraphic units, can potentially estimate and identify important strength interfaces in the sedimentary record.

## **Keywords**

Currituck slide complex; shear strength; consolidation; sea level changes; sediment flux

### **3.1. Introduction**

Along the north-western Atlantic passive margins (NWAM), small and large submarine landslides are a prominent morphological feature, in particular between Georges Bank in the north and Cape Hatteras in the south (Booth et al., 1993; Twichell et al., 2009). In this area the margins morphology is also characterized by submarine canyons and gullies (Brothers et al., 2013; Chaytor et al., 2009; Obelcz et al., 2014; Twichell et al., 2009), where the submarine landslide scars and their deposits cover between 33 to 16% of the slope and rise area (Twichell et al., 2009).

The morphological analysis of the seafloor (Brothers et al., 2013) exposed the extremely large extent of some of the landslides along the NWAM (Chaytor et al., 2009). To characterize the distribution of the landslides Twichell et al., (2009) distinguished between the area from Georges Bank to south New England as glacially influenced margins and between the Hudson canyon and Cape Hatters in the south as fluvially influenced margins; additionally open slope-sourced slides from canyon-sourced slides were distinguished. Further morphological analysis however, suggested that variations in the sedimentary transport mechanism could explain variations in the size and distribution of the landslides (e.g. Brothers et al., 2013; Mosher et al., 2017; Obelcz et al., 2014).

Understanding that such a large scale landslide can generate powerful tsunamis as in the cases of the Grand Banks (Løvholt et al., 2019) or the Nice airport (Dan et al., 2007), raised the need to evaluate the potential hazard along the NWAM. In a preliminary evaluation of the debris flow, the runout distance and the slide volume, Chaytor et al., (2007) suggested that the tsunamigenic landslides along the NWAM are the open-slope sourced failure.

Most of the tsunami models that were developed however, focused only on the Currituck submarine landslide (Geist et al., 2009) and further used it as a regional model for tsunami

hazard assessment (Grilli et al., 2015; Schambach et al., 2019). These tsunami models mainly constrained their parameters using the bathymetry and morphological analysis and the assumption from previous studies that the slide occurred in two phases (Booth et al., 1993; Bunn and McGregor, 1980; Hill et al., 2017; Popenoe et al., 1982; Prior et al., 1986). In Locat et al., (2009) the stability and mobility analysis of Currituck were based on a morphological analysis of the debris layer however, they additionally used an estimation of the strength and water content of a dry and friable clay layer previously observed by Bunn and McGregor (1980) as the possible gliding plane.

However, similar large-scale landslides do not always produce a large tsunami. To properly estimate the tsunamigenic potential of a landslide more parameters should be considered other than the volume assessment. Mainly differences in the failure mechanism and the landslide ability to transform into a fast or slow moving debris flow (Løvholt et al., 2017). The latter considerably depending on the physical properties of the sediments comprising the unfailed slope (Elverhoi et al., 2010; Sawyer et al., 2012).

While recently Chaytor et al., (in preparation) determined that both the upper and lower scars represent a single landslide event, there is no sedimentological or geotechnical data to understand the pre-slide conditions in the sediments and whether they preconditioned the slide formation.

Following recent studies of the Currituck landslide complex (Hill et al., 2017; Locat et al., 2009), several questions remained unclear, in particular what role do the sediments and sea-level changes have in preconditioning the slope instability. We used sediments from the Currituck slide complex and surrounding, aiming to identify evidence of the potential slope failure pre-conditioning factors. We present results from geotechnical and a high-resolution sedimentological analysis. Based on these data we present a new evaluation for the current slope instability and suggest the possible trigger and slope stability conditions in the past.

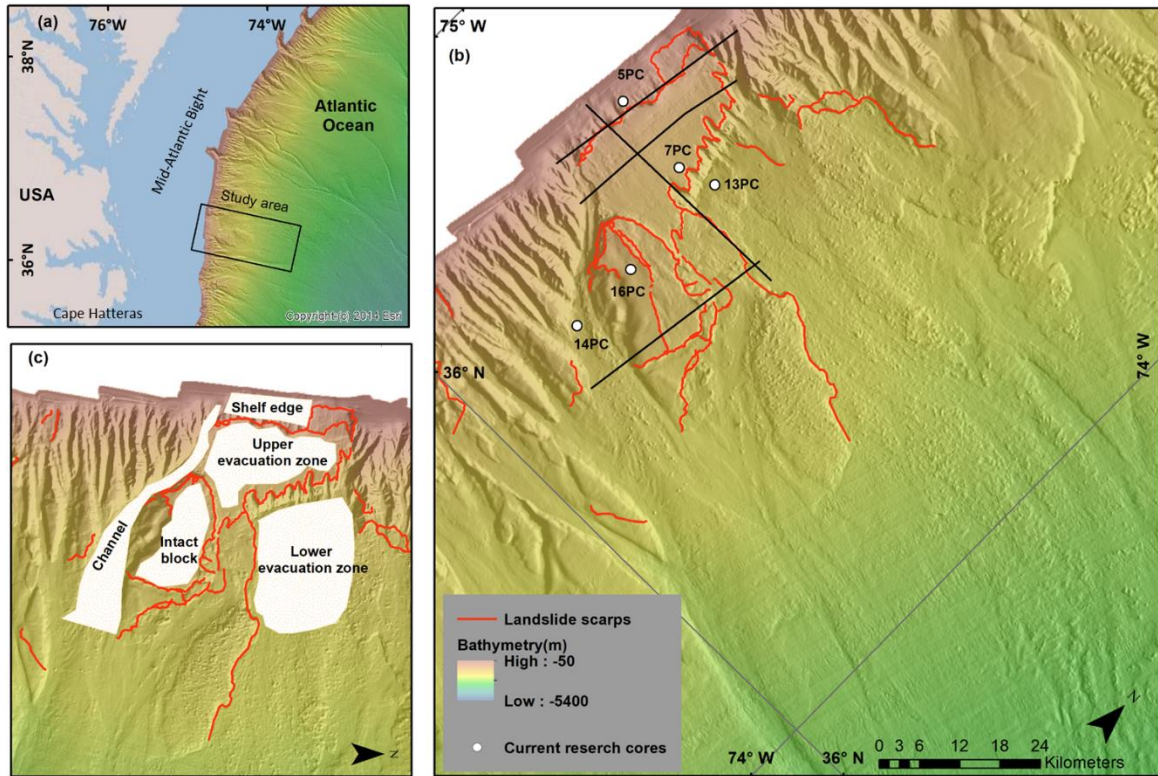


Figure 3.1.: Location of study area and oceanographic regime, core's location and physiographic units.

### 3.2. Regional settings

The Currituck landslide complex is located off Albemarle Sound (Fig. 3.1). Following the development of a rift basin during the Triassic-Jurassic age, a carbonate platform developed until the Middle Cretaceous. The thermal subsidence of the western Atlantic margins has contributed to its formation as passive margins. During most of the Cenozoic, the margins were dominated by siliciclastic sediments deposition, excluding chalk deposition during the Eocene (Poag and Sevon, 1989; Sheridan, 1987). During the Quaternary, large volumes of sediments were eroded and deposited unevenly along these margins, reaching in the outer shelf and upper slope to thickness varying between 400 to 800 m (Poag and Sevon, 1989).

The slide complex is found along a stepped type margins (Mosher et al., 2017) and bounded to the south and north between canyons and gullies incised slope. These areas are characterized by an oblique margin morphology, concave slope profile and a relatively steep ( $>8^\circ$ ) slope. They also show evidence for gravitational processes forming small-scaled mass movements and upper slope sediments bypass (Brothers et al., 2013; Hill et al., 2017; Poag and Sevon, 1989). The Currituck margin however, is characterized by a sigmoidal margin morphology and gentle slope gradients ( $<6^\circ$ ). Additionally there are evidence for large volumes of sediments

delivered to the shelf-edge and upper slope by fluvial systems since the Cretaceous (Poag and Sevon, 1989). The detailed analysis of the shelf edge and upper slope morphology of the Quaternary sedimentation pattern suggests that the Currituck slope area developed under different conditions.

The deformed area in the Currituck landslide complex surrounds more than 6500 km<sup>2</sup> between the continental slope and the rise. The morphological analysis of Hill et al., (2017) indicated several physiographic features in the landslide complex area (Fig. 3.1). The slide evacuation zone is defined by the shelf-edge headwall, the upper headwall and the lower headwall. Southern to the slide an undetached block of sediments was defined where an ancient, buried mass movement was observed. The upper headwall scarps relief vary from 150 to 250 m, the lower headwall has a stepped scarp of ~400 m altogether, the shelf-edge scarp relief is ~100 m and the sidewall scarps in the lower slope vary between 100 to 200 m. The lower evacuation zone is covered by scattered debris blocks on a low gradient (<2°) seafloor.

Currently, there is little export of sediments from the river estuaries to the shelf and further to the upper slope (Churchill et al., 1994; Milliman et al., 1972). Sediments resuspension is mainly induced by major storm events (Churchill et al., 1994). The current sediments on the shelf are relicts, representing sediments that were reworked and redeposited during the Pleistocene glacial–interglacial sea level changes (Hathaway, 1972). The SEEP-II experiments conducted along the mid-Atlantic shelf and upper slope, indicated a depocenter accumulating sediments on the slope, at about 1000 m. This depocenter reflects the maximum of near-bottom vertical flux that coincides with a minimum in current speed (Biscaye et al., 1994).

The oceanographic regime in the MAB is mainly influenced by the North Atlantic Deep Water (NADW, Fig. 3.1a.), transporting southward cold water from sources in the Labrador and Norwegian seas (Mosher et al., 2017). The NADW has two components that flow southwards in the research region. The Deep Western Boundary Current (DWBC, Fig. 3.1a) that flows between depth of 3000 to 5000 m and the upper Labrador Current that in general flows between 500 to 2500 m (Fig. 3.1a). Originating in the south, off Florida, warm water flow northward forming the Gulf Stream. North of Cape Hatteras the eastward deflection by the Coriolis force results in the Gulf Stream separating from the U.S. coast (Saba et al., 2016). Over a region extending roughly 40–200 km north of Cape Hatteras to the Chesapeake Bay mouth the shelf water exports water to the ocean (Fig. 3.1a) due to the combined effect of the northward flow of the Gulf stream and the southward flow of the Labrador currents shelf (Churchill and Gawarkiewicz, 2012). Under the current high stand conditions, it was suggested that when the

Gulf Stream is closer to the shelf edge there is an enhanced export of shelf water to the slope. A model based study suggests the during the last glacial period a relatively stronger glacial Labrador Current extended south to Cape Hatteras, led to cooler water displacing the Gulf Stream position farther south (Hewitt et al., 2003).

### 3.3. Dataset and methods

#### 3.3.1. Data

Cores were collected on board of RV Hugh R. Sharp cruise HRS120929 in 2012 in water depths varying between 250 to 3000 m. The cores selected for further analysis targeted five physiographic areas defined by Hill et al (2017): the shelf edge, upper evacuation zone, lower evacuation zone, intact block section and a side channel (Fig. 1). For each location, one core was chosen for detailed analysis (Table 1). Physical properties analysis (MSCL) was performed at the University of Rhode Island. The radiocarbon dating and their calibration are used here following Chaytor et al (in preparation).

*Table 3.1: List of cores from the Currituck slide complex analysed in this study*

<b>Core</b>	<b>Physiographic location</b>	<b>Water depth [mbsl]</b>	<b>Geographic position</b>		<b>Core length [cm]</b>
			Latitude	Longitude	
5PC	Shelf edge	339	36.355	74.757	835
7PC	Upper evacuation zone	1350	36.347	74.639	633
13PC	Lower evacuation zone	1825	36.362	74.589	707.5
14PC	Channel	1729	36.146	74.586	474
16PC	Intact block	1287	36.230	74.587	655

#### 3.3.2. Sedimentological analysis

A core visual description was performed to identify the main visual lithological variations along the cores. The selected cores were subsampled for grain size measurements every 5 to 30 cm, following on the visual description and the MSCL data. Measurements were performed in The Environmental Sedimentology Laboratory at the University of Haifa and in the Particle-Size Laboratory at MARUM, the University of Bremen. Both laboratories hold a Beckman Coulter Laser Diffraction Particle Size Analyzer LS 13320 measuring the particle size distribution of 0.02 to 2000  $\mu\text{m}$  (clay to sand). A comparison between selected samples was carried to ensure similarity between the machines. Prior to measurements, the samples were treated with hydrogen peroxide ( $\text{H}_2\text{O}_2$ ) to remove organic material (Murray, 2002). The remains were measured as the inorganic-bulk

fraction (terrigenous and biogenic components). A known issue of the laser diffraction method is an underestimation of the clay fraction. To overcome this, the silt-clay boundary is defined here at 0.06  $\mu\text{m}$  following Rasmussen (2020, and references therein). The full particles size distribution is presented in Fig. 3.2 and 3.3. Based on these results, the Folk and Ward method (Blott and Pye, 2001) was used to calculate grain size parameters (i.e. the mean particle size, skewness, sorting and kurtosis in Fig. 3.4 and S3.3).

### 3.3.3. Geochemical analysis

A discrete XRF analysis was performed on core-sampled sediments. Data was collected in intervals following sampling for the grain-size measurements from cores 5PC, 13PC, 14PC and 16PC. Using a Xenometrix S-Mobile benchtop EDS-X-Ray Fluorescence (XRF), measurements were conducted at high-energy range (40 keV) with excitation potential of 50 kV, an x-ray current of 10  $\mu\text{A}$  and a count time of 120 seconds. No filter was used in both light and heavy elements analysis. Processing of the spectra was done using CrossRoads Scientific's Fundamental Parameters software suite. XRF measurements were performed at the Basin Analysis and Petrophysical laboratory (PetroLab) of the University of Haifa.

From the whole set of measured elements, the records of  $[\text{Ca}/\text{Ti}]$ ,  $[\text{Fe}/\text{Zr}]$  were used. The ratio  $\text{Ca}/\text{Ti}$  is used to present the change in ratio between biogenic contribution (represented by Ca, derived from calcareous remains, mostly planktic organisms) and the terrigenous supply (represented by Ti that is exclusively of detrital origin) and therefore reflects sediment flux trends (Bahr et al., 2014; Croudace and Rothwell, 2015). The ratio  $\text{Fe}/\text{Zr}$  was used by Hanebuth and Lantzsich (2008) that suggested the ratio to infer transport and sorting mechanism, separating heavy Zr-containing minerals from other siliciclastic grains. Here, this ratio was tested in core 14PC in which possibly turbidity / collapse events deposits were observed (in the core visual description) and additionally due to the core's location in a submarine channel.

### 3.3.4. Geotechnical analysis

To estimate the geotechnical properties of the sediments along the core, undrained shear tests and water content were measured every 30 cm. Shear tests were performed using a manual shear vane device. Samples were subsequently weighed and oven dried to evaluate water content.

The relationship between the undrained shear strength to vertical effective stress were used as a preliminary estimation for the sediment's consolidation. Sediments undrained shear strength values are considered normally consolidate falling within the range of  $0.2 - 0.4 * \sigma'_v$  (Wiemer et al., 2015). Values below or above this range are under- or over-consolidate, respectively (Locat and Lee, 2002). For each core, the vertical effective stress was calculated using averaged grain density from the MSCL data and assuming seawater density of  $1.024 \text{ g/cm}^3$  (Weber et al., 1997).

### 3.3.5. Slope stability analysis (1D)

A 1D infinite slope analysis evaluates the relationship between the downslope forces acting on the slope and the slope resisting forces. The ratio between the forces was defined as the factor of safety (FOS), where  $FOS \leq 1$  indicates failure or slope that is susceptible to failure and  $FOS > 1$  indicates a stable slope. Here we considered two scenarios to evaluate the slope stability under undrained conditions. For the static scenario, the FOS was calculated as (Morgenstern, 1967):

$$\text{Eq. 3.1} \quad FOS = \frac{S_u}{\gamma' * z * \sin \theta \cos \theta},$$

where  $S_u$  is the undrained shear strength,  $\gamma'$  is the bouyant unit weight of the sediments,  $z$  is the depth of failure (overburden depth) and  $\theta$  is the slope angle.

For the second scenario, pseudo static conditions (earthquake loading) are assumed. FOS was evaluated as:

$$\text{Eq. 3.2} \quad FOS = \frac{S_u}{\gamma' * z * [\sin \theta \cos \theta + \kappa(\gamma/\gamma') \cos^2 \theta]},$$

where  $\gamma$  is the bulk unit weight of the sediments and  $k$  is the pseudostatic seismic coefficient.

This analysis aims to find whether static conditions were unstable and slope instability is attributed completely to the sediments or additionally an earthquake triggered the slope failure.

The values used in the calculations are presented in Table 3.2 and are based on measurements from the current study averaged (e.g., density) or extrapolated (e.g., shear strength). The range of slope angle tested, follows measurements by Hill et al., (2017) for Quaternary strata within the slide complex area. For an earthquake scenario, we estimated a range of peak ground accelerations that may trigger slope failure of a strata at a depth of 150 m along the slope or at a depth of 100 m along the shelf edge.

## 3.4. Results

### 3.4.1. *Physical and geotechnical properties of the sediments*

#### 3.4.1.1. Cores above and within the slide complex

The analysis results of cores 5PC, 7PC and 13PC suggest that the sediments from these cores can be divided into 3 units. At the bottom of cores 7PC and 13PC there is a debris unit, and in all three cores two units that overlay the debris unit and comprise the drape layer (Fig. 3.2). The cores did not penetrate the entire debris unit to the gliding plane. The debris unit can be separated from the overlying drape by a sharp peak in the magnetic susceptibility (Fig. 3.2b, c), or by the density values and other physical properties (Fig. S3.1). The debris unit is characterized by low (<30%) water content and very high (>50 kPa) undrained shear strength. The sediments in the debris unit are trimodal, very poorly sorted and contain very fine mud to very fine sand.

Lithologically, the drape layer both in the upper and lower evacuation zones (Cores 7PC and 13PC, accordingly) is characterized by poorly sorted to very poorly sorted clayey-silt sediments. In the shelf edge (Core 5PC), the upper 2.5 m of the core are characterized by silty-sand or muddy-sand sediments and between 2.5 to the bottom of the core, the sediments are sandy-silt and show a decrease in sorting.

The two units that comprise the drape layer are distinguished based on the magnetic susceptibility, water content, shear strength and the Ca/Ti ratio (Fig. 3.2). The lower unit is characterised by high magnetic susceptibility (>10), a low water content which (~40%), low undrained shear strength values that are found in the range of normal consolidation ( $0.2 < Su/\sigma_{v'} < 0.4$ ) or slightly above and a low Ca/Ti ratio ( $\leq 5$ ). Conversely, the upper unit is characterized by low magnetic susceptibility (<10), a high-water content which (~60-50%), low undrained shear strength values that are found above the range of normal consolidation ( $0.2 < Su/\sigma_{v'} < 0.4$ ) and a high Ca/Ti ratio (> 5).



#### 3.4.1.2. Channel sediments

The sediments in the core from the channel area also indicate two units (Figure 3.3a). The lower unit (2-4.5 m) is very poorly sorted clayey-silt and visually chaotic with large (>2 cm) lithoclasts. The unit is characterized by low water content (<30%), fluctuating magnetic susceptibility values and very high undrained shear strength values (>70 kPa), well above the range of normal consolidation. The Ca/Ti ratio is fluctuating between low and high values. Within the unit, three areas that sampled the lithoclasts show distinct low peaks in the Fe/Zr ratio.

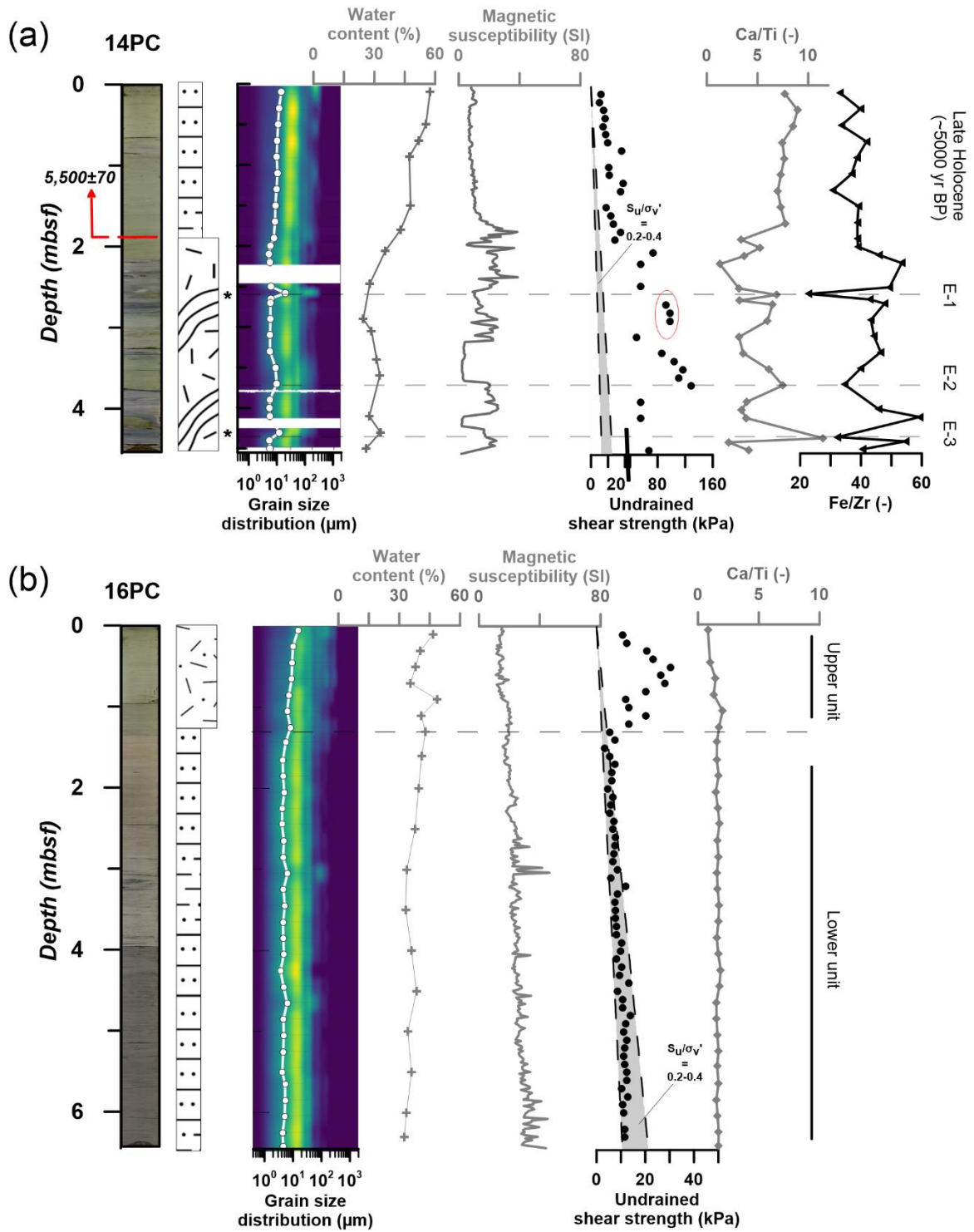


Figure 3.3: Cores photo, lithology, grain size fractions, water content, magnetic susceptibility, undrained shear strength, Ca/Ti ratio and Fe/Zr ratio for cores around the slide complex (a) 14PC, Channel and (b) 16PC, intact block. See Fig. 3.2 for lithology and grain size distribution frequency legends.

The upper unit (0-2 m) is poorly sorted clayey-silt. The unit is characterized by water content that is decreasing from 60% at the top to 30% at the bottom of the unit, low (<40 kPa) undrained shear strength values that are found slightly above the normal consolidation range, a high Ca/Ti ratio (>5) and Fe/Zr ratio that slightly fluctuate.

#### 3.4.1.3. Intact block sediments

The sediments sampled in the core from the intact block show a lithological change from sandy-silt to clayey-silt around 1.5 m depth. This change is not significant in the grain size distribution or the D50 results (Fig. 3.3b). The sediments are characterized by a decrease with depth of the water content and an increase of the undrained shear strength (within the range of normal consolidation) and the magnetic susceptibility. The Ca/Ti ratio shows very low values that do not change with increasing depth. The upper 1.5 m in the core also shows high undrained shear strength values ( $20 < S_u < 40$  kPa) that are well above the range of normal consolidation, correlative to the described lithological composition.

#### 3.4.1.4. Sediment texture

The distinction seen between the two drape units from the magnetic susceptibility, shear strength and Ca/Ti is not strongly apparent in the lithology. However, the mean grain-size and sorting (standard deviation) parameters for each core show that such distinction exists.

The mean grain size in the shelf edge (core 5PC, Fig. 3.4a) is similar to both upper and lower units however the upper unit is better sorted. In the lower evacuation zone (core 13PC, Fig. 3.4b), the upper unit in the drape layer is distinct from the lower unit presenting finer mean grain size and better sorting. The lower unit shows a mean grain size and sorting range similar to the debris unit. The debris unit mean grain size varies over a range that is parallel to the range of the sediment mean grain size in all cores except the fine-grained sediments in core 16PC (Fig. 3.4a). The sorting and mean of the sediments in the channel (14PC, Fig. 3.4c) is similar between the upper and lower units and has a similar mean grain size and sorting range to the drape layer (Fig. 3.4a). The sediments of the intact block (core 16PC, Fig. 3.4d) upper unit presents a similar range of mean particles size and sorting to the drape layer in the lower evacuation zone. However, the lower unit sediments present better sorting and much finer mean grain size, distinctly different from other slope areas (Fig. 4a and 4d).

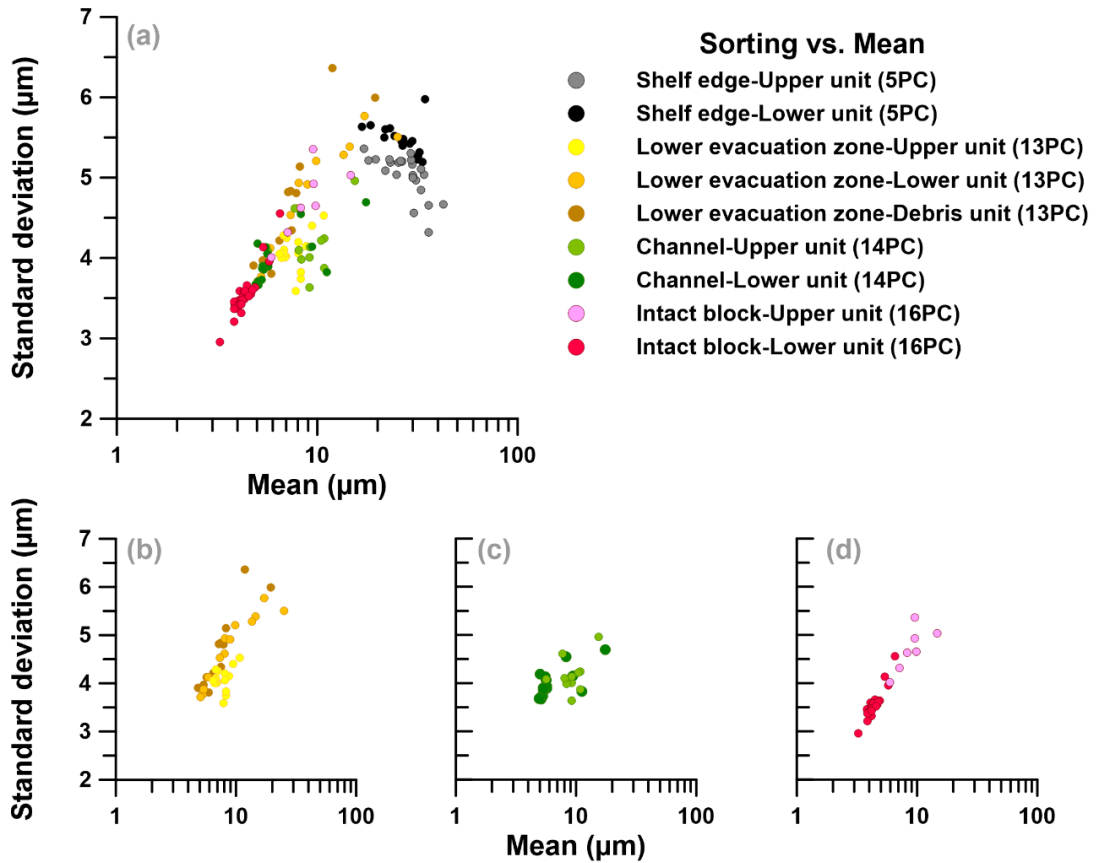


*Figure 3.4: Sediments textural analysis presenting variations of the mean and sorting (standard deviation) values for each layer of the sampled cores. (a) all cores (b) core 13PC (c) core 14PC and (d) core 16PC. The sorting of sediments from cores 13PC cover the entire distribution of sampled sediments from all of the cores except the very fine sediments from core 16PC.*

### 3.4.2. Slope stability analysis

Two scenarios were considered to evaluate slope stability under undrained conditions: static and pseudo static. This was evaluated for four selected cores and additionally for the two units identified by the drupe layer (Table 3.2).

A preliminary calculation used the measured values in the cores (Fig. 3.5 and Table 3.2) to evaluate the present-day stability conditions in the slope. The back analysis tested three parameters to estimate the preconditioning or triggers factors (slope angle, shear strength, failure depth and peak ground accelerations) that could generate the observed failure (Figs. 3.6 and 3.7). The factor of safety was calculated for the static conditions with Eq. 3.1 and for pseudo static conditions with Eq. 3.2.

The preliminary static slope stability analysis showed that assuming maximum slope angle ( $\theta = 5^\circ$ ), the present-day surficial sediments ( $0 < z < \sim 8 \text{ m}$ ) are stable, with

$FOS > 1$  (Fig. 3.5). The minimal FOS value occurs within the lower unit in cores 5PC, 7PC and 13PC (ranging from the shelf edge to the lower evacuation zone in Fig. 3.1), however the location varies between the bottom, the middle and the top of the unit (Fig. 3.5). In core 16PC, lowest FOS values were calculated at the bottom of the core (4.3-5.0 m) and the FOS is almost linearly decreasing with depth (Fig. 3.5). Following the physical properties and geochemical division to an upper unit and a lower unit, we divided the results similarly and tested the significance of the mean FOS between the upper and lower units of each core. The results in Table 3.3 suggest that the FOS is significantly ( $\alpha < 0.05$ ) different between the units.

*Table 3.2: Input parameters for slope stability calculations, A-entire core. UU-upper unit, LU-lower unit*

Core	5PC			7PC			13PC			16PC
	A	UU	LU	A	UU	LU	A	UU	LU	A
<i>Measured / extrapolated parameters</i>										
Undrained shear strength, $S_u$ [kPa]	0.74z +17.1 2	1.73z +14.9 1	0.22z +20.0 6	1.23z +10.0 6	2.55z +9.54	0.34z +8.45	0.51z +10.3 9	4.06z +6.16	0.18z +10.9 0	1.52z +3.21
Undrained shear strength, $S_u$ [kPa] (Pseudo-static)	91.1 [z =100]	187.9 [z =100]	42.0 [z =100]	194.5 [z =100]	392.0 [z =150]	59.4 [z =150]	86.6 [z =150]	615.1 [z =150]	37.0 [z =150]	231.2 [z =150]
Buoyant unit weight, $\gamma'$ [g/cm <sup>3</sup> ]	9.3	8.3	10.5	5.5	5	5.9	5.5	5.1	6	6.3
Bulk unit weight, $\gamma'$ [g/cm <sup>3</sup> ]	18.3	19.4	18.4	20.57	16.69	15.13	16.02	16.57	15.21	16.07
<i>Tested parameters</i>										
Depth (static), $z$ [m]	0-200									
Horizontal acceleration, $\kappa$ [m/s <sup>2</sup> ]	0-0.2									
Slope angle, $\theta$ [°]	0-10									

Based on these results a linear regression was calculated separately for each unit to estimate the shear strength variations with depth (Fig. 3.5, upper and lower units).

*Table 3.3: Significance t-test results for the upper and the lower units FOS values ( $\alpha = 0.05$ )*

Core	Upper unit FOS Mean	Upper unit Standard deviation	Lower unit FOS Mean	Lower unit Standard deviation	T-test	F-test
5PC	17.540	14.316	4.400	1.560	0.00228	1.21E-12
7PC	40.916	43.641	6.043	2.047	0.0015	4.75E-22
13PC	27.775	27.448	5.306	1.621	0.00018	2.18E-20

For the slope stability analysis, the calculation considered parameters that define the current conditions in different parts of the slope (e.g., core 5PC represents the shelf edge in Fig. 3.6). Additionally, based on the significantly different FOS for the upper and lower units, the factor of safety was further evaluated separately to represent the variation with depth for each unit (Fig. 3.7).

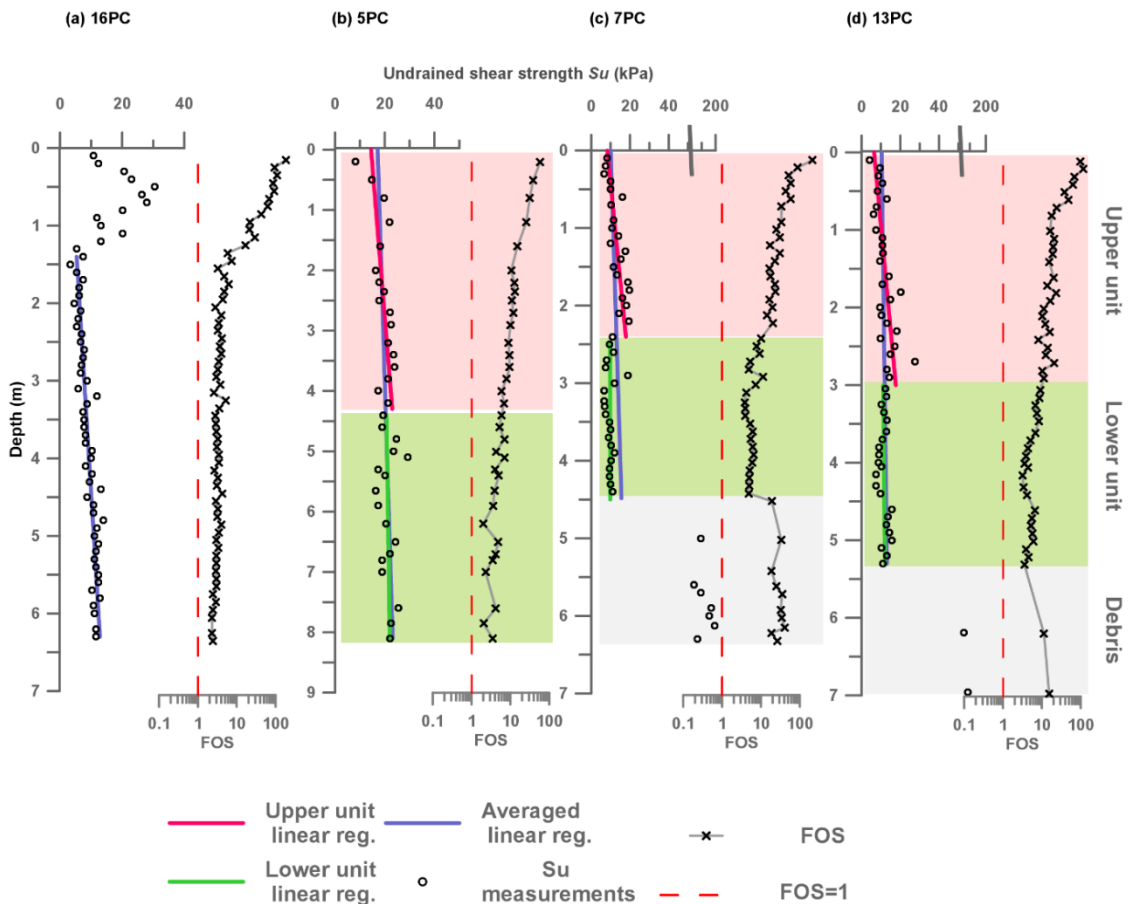


*Figure 3.5: FOS evaluation for each sample and shear strength linear regressions for selected cores. (a) 16PC (intact block), (b) 5PC (Shelf edge), (c) 7PC (upper evacuation zone) and (d) 13PC (lower evacuation zone).*

The static analysis tested variations in the FOS as both depth and slope angle increase. The results (Fig. 3.6a) indicate that the slope in the unfailed area (core 16PC) is stable in the range of the tested variables ( $1 < \theta < 10^\circ$ ;  $10 < z < 200 \text{ m}$ ). The FOS analysis for the area within or above the current headwall, suggests that for slope angles higher than  $5.1^\circ$ , the slope may become susceptible to failure ( $\text{FOS} < 1$ ) with depth. In the range of the currently observed basal shear surface angle ( $\sim 4\text{-}5^\circ$ ) and the depth of the headwall

(approx. 150 m within the evacuation zone and 100 m in the shelf edge), the FOS suggest stability under static conditions, however vulnerable ( $1 < \text{FOS} < 2$ ). Therefore, pore water overpressure does not appear to be the trigger for slope failure under static conditions, yet it possibly contributed to the preconditioning factors that reduced the slope strength.

For the pseudo static analysis, we considered  $\text{FOS}=0.5$  as an indicator for instability in the region following ten Brink et al., (2009), this is discussed with the result in the discussion (section 3.5.3). The pseudo static analysis tested variations in the FOS as both peak ground accelerations and slope angle increase. The results (Fig. 3.6b) indicate that values in the range of 0.025 to 0.15 of the gravitational acceleration,  $g$ , are needed to trigger slope failure similar to the observed failure.

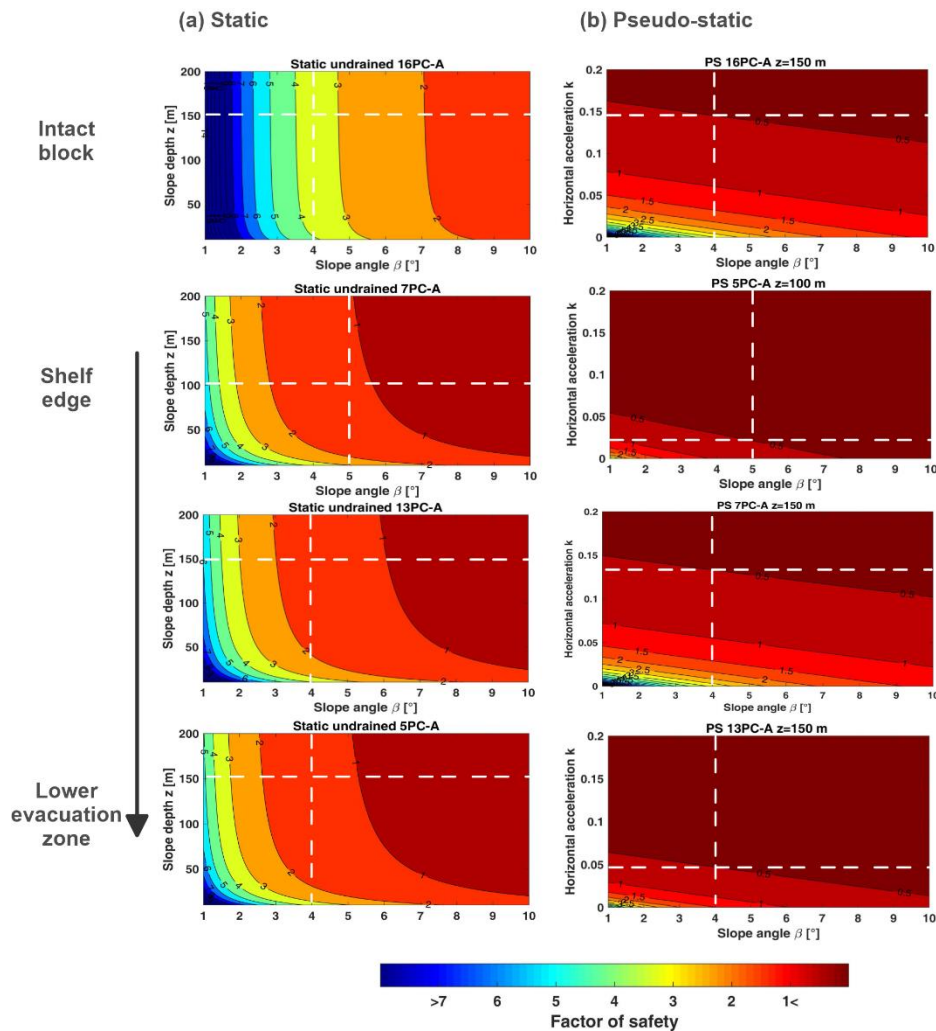


Figure 3.6: Slope stability analysis (a) static and (b) pseudo static. Dashed lines indicate the conditions of the recent Currituck slide

Slope stability tested for each unit individually, presents a different result than for the entire core. In Fig. 3.7a, the upper unit FOS values indicate that the sediments in such unit are stable in the range of the tested variables ( $1 < \theta < 10^\circ$ ;  $10 < z < 200$  m).

However, FOS values in the lower unit indicate that the sediments in such unit are susceptible to failure in depth (200 m) with low slope angles (2-3.8°). In the range of the currently observed basal shear surface angle (~4-5°) and the depth of the headwall (approx. 150 m within the evacuation zone and 100 m in the shelf edge), the  $FOS < 1$ , suggesting that the sediments in such unit are susceptible to failure under static conditions.

Testing the development of FOS for each unit individually for undrained pseudo static conditions, presents a different result than for the entire core under static conditions. In Fig. 3.7b, the upper unit FOS values indicate that the minimal peak ground acceleration needed to trigger slope failure are high ( $\kappa > 0.15$ ) whereas for the lower ( $\kappa < 0.05$ ) unit low peak ground accelerations are needed to trigger slope failure.

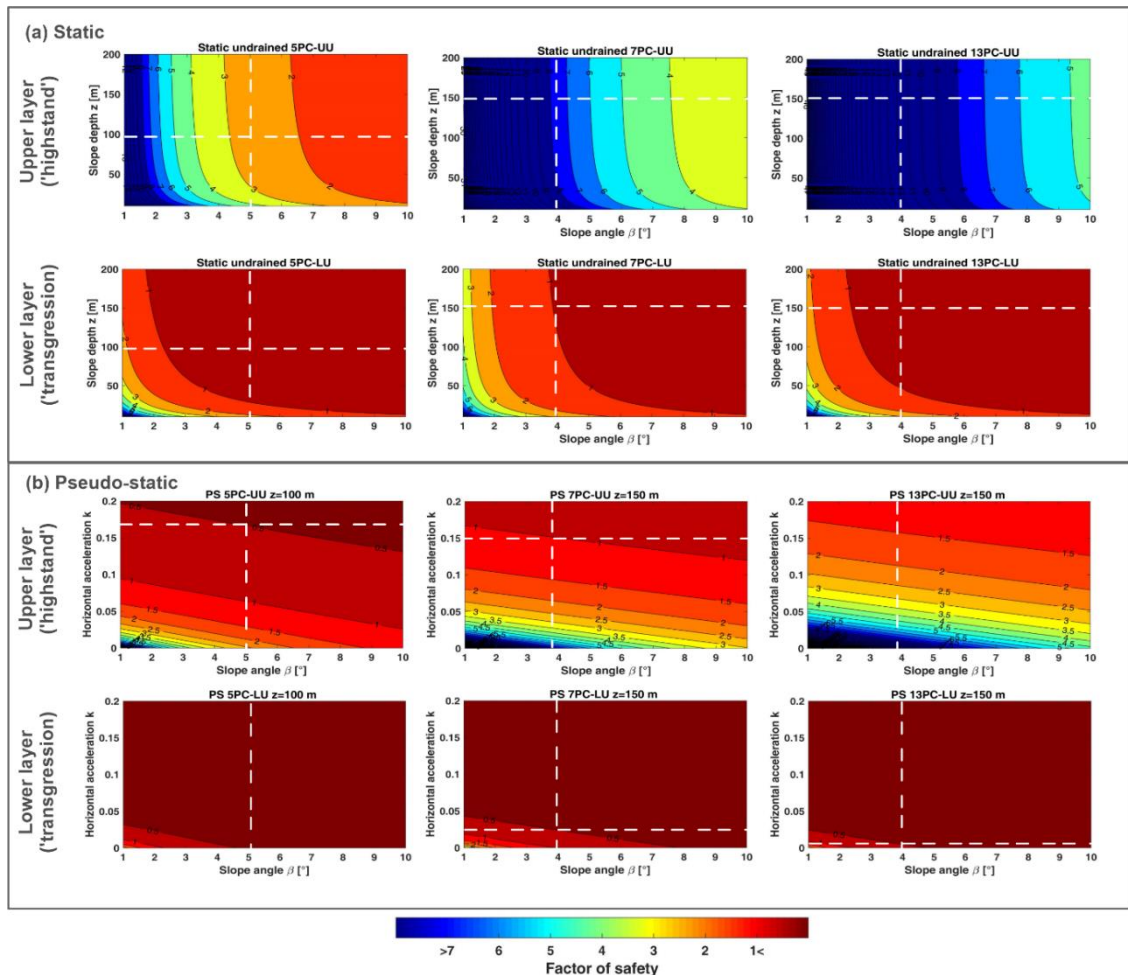


Figure 3.7.: Slope stability analysis for the two units identified in the drape (a) static and (b) pseudo static (for  $z=150$  m).

### 3.5. Discussion

#### 3.5.1. *Post slide sediment transport into and around the slide complex*

Two units were recognized in the drape layer based on the physical properties, geotechnical and geochemical measurements. Variations of these parameters are key to understand the conditions for sediment transport and deposition in the Currituck area. The sediments in the lower unit are characterized by high and fluctuating magnetic susceptibility and low Ca/Ti ratio. These variations are indicative of increased sediment fluxes, specifically increased terrigenous supply (Rothwell and Rack, 2006). The shear strength variations in this unit are within or slightly above the normal consolidation range, which can be related to the constant water content in this unit. The upper unit on the other hand, is characterized by low magnetic susceptibility and high Ca/Ti ratio, the latter indicative of low sediment fluxes and increased biogenic input. The shear strength values in the upper unit however, are apparently overconsolidated and the water of the unit present a linear decrease possibly indicating secondary consolidation (Yenes et al., 2020). Since there are little lithological variations between the two units, it appears that the main cause differentiating the units is the sediment flux from the continent. During the lower unit deposition, high fluxes are inferred from the Ca/Ti ratio, as opposed to inferred decreased sediments fluxes during the upper unit deposition. These variations in the sediment flux influence the secondary consolidation process as lower fluxes (and hence sedimentation rate) allow better structure of sediments to form, thus causing an apparent overconsolidation in the sediments (Yenes et al., 2020). This also supports Chaytor et al. (in preparation) observations, suggesting that the landslide event occurred during a period of high sediment fluxes to the shelf edge. The high sediment fluxes continued after the slide event occurred, covering the slide scar as seen by the Ca/Ti ratio in the lower unit. The age constraints obtained by Chaytor et al. (in preparation), sets the lower unit deposition during the Late Pleistocene ca. 15 ka years ago, and the upper unit deposition during the Holocene period, ca. 8 ka onwards (Fig. 3.1). According to the regional (Engelhart et al., 2011) and global (Peltier and Fairbanks, 2006) sea level reconstructions, the lower unit was deposited during sea level transgression whereas the upper unit deposited under sea level highstand conditions.

As mentioned above, surprisingly the two units do not appear lithologically different from one another (Fig. 3.1). Hathaway (1972) proposed that sea-level changes throughout the Quaternary constantly mixed the shelf sediments with sediments from river estuaries;

consequently, lithological variations as seen here are minor between the documented sea level intervals. The main sedimentological indication differentiating the two units is seen by the textural analysis (Fig. 3.4), showing on average finer sediments and a better sorting of the upper unit sediments (core 13PC, Fig.3.4). During the sea level rise in the early Holocene, the coastline migrated further to the west and as a result reduced the sediments load export to the shelf edge and the upper slope (Engelhart et al., 2011 and references therein; Thieler et al., 2014) and sorting increased with the larger transport distances. Infilling processes of the shelf during the Early Holocene have contributed to the formation of barrier islands in the Albemarle Sound and in Chesapeake and Delaware bays (Brothers et al., 2020; Mallinson et al., 2010; Thieler et al., 2014), thus contributing to reduced sediment fluxes to the shelf edge.

The spatial distribution of both units is confined to the slide evacuation zone (Figs. 3.1 and S3.1). In addition, the geochemical analysis of sediments from the channel (core 14PC) suggests that the upper unit is also present in the channel, indicating similar a mechanism of sediment supply to the slide complex area. However evidence from the heavily canyonized areas northern (Obelcz et al., 2014; Vachtman et al., 2013) and southern (Naughton et al., 2015) to the slide complex suggest that these are influenced by different sediment flux intensities and sediment transport mechanisms. A high-resolution pollen record collected off Cape Hatteras (water depth ~ 1000 m) presented four periods each spanning ~1500 years of increased storm events throughout the Holocene sea level rise exporting pollen mainly from Pee Dee River, Chesapeake and Delaware hydrographic basins (Naughton et al., 2015). Additionally, morphological variations in the Quaternary underlying stratal architecture in canyonized areas, indicate that sediment transport and fluxes have contributed to the morphological differences of the slopes (Hill et al., 2017).

Characteristics of the sediments from the intact slope indicate a different sediment transport mechanism. The sediments are better sorted and finer than measured in the other cores. This possibly represent the hemipelagic sedimentation process in the area as the current velocity decreases (Churchill et al., 1994). Their origin however, is unclear. Due to the complex oceanographic conditions of the area (Figure 3.1a; Churchill and Gawarkiewicz, 2012), further analysis is needed to understand whether these fine grained sediments were transported by a Gulf Stream eddy or suspended material from the transport trajectory that flows into slide complex and channel areas. The evidence

suggests continuous sedimentation, derived from terrigenous supply and a linear increase of shear strength.

### 3.5.2. *Possible indication for slope failure preconditioning factors*

Seismic analysis of Currituck slide complex (Hill et al., 2017), has suggested that rapid sedimentation promoted pore water overpressure in the sediments and that lateral migration of pore fluids along the subparallel bedded strata structure could have preconditioned the slope failure. Although our cores were not able to penetrate the debris layer, the collected evidence in the current study already implies possible strength variations due sedimentation rate and further influence on the consolidation of the sediments.

Previous studies suggested that during sea-level lowstands fluvial erosion was enhanced, and rivers and stream-drainage networks were incised into the shelf and possibly upper slope (Colman et al., 1990; e.g. Colman and Mixon, 1988; Hobbs, 2004). The debris layer in our record most likely represents a mixture of sediments deposited during various glacial-interglacial stages. The observed range of particle size mode of between the debris and the sediments from the shelf edge and the slope shows a similar range (Fig. 3.4). This observation thus constrains the assumption that the sediments transported and deposited along the shelf edge and slope of Currituck were similar. However, the variations observed result from differences in sorting and distance to the coastline. Within the MAB, the IODP record off Hudson Bay showed that during lowstands, silty-sandy sediments were deposited by turbidity currents (McHugh and Olson, 2002). Although fluxes to the Hudson canyon area were probably much higher than the river fluxes that transported sediments to Currituck in the Pleistocene, this is the best continuous record since the penultimate interglacial (i.e., MIS 5e) found in the fluvially influenced MAB. Combining our record with the Hudson record, we have constructed a conceptual glacial-interglacial slope sediments record to estimate sea level and climatic variation in the slope sediments. We evaluate whether the flux, sediments sorting and consolidation are high, medium or low (Fig. 3.8). Observing the variations between sea-level system tracts can reveal possible strength interfaces in Currituck stratigraphic record (Fig. 3.8). This schematic record indicates that the most likely a “weak layer” is forming in the Currituck area during sea level transgression. Since the deposits are a mixture of fine and coarse sediments, and the unit is not able to expel water properly under a high sedimentation rate, lower consolidation conditions therefore develops. The important strength interface is possibly

forming between this unit and the underlying lowstand dense turbidity sands and silts (Fig. 3.8b). This conceptual analysis however does not consider climatic variability that might change the record (e.g. Ducassou et al., 2009) and turbidites were considered only during sea level lowstand.

Although turbidity systems were traditionally considered active only during sea level lowstands (e.g. Mulder and Syvitski, 1996), the immense evidence gathered together with direct monitoring and measurements, suggests that turbidity currents can be active in a variety of margins (e.g. starved margins, Normandeau et al., 2020) and under a variety of conditions (Hizzett et al., 2018).

The Nile delta is a prominent example of a fluvially-fed margin and a shelf edge delta, where small to extremely large-scale mass movements were documented, occurring on very low slope gradients (Garziglia et al., 2008). Additionally, extensive evidence for Quaternary turbidity currents activity were documented on its slope (Ducassou et al., 2009). Correlating the Nile deep-sea turbidity system to climate and sea level variations yielded a dual response to both sea level and climate variations between wet and arid conditions. However, while the evidence for climatic variations in the Nile delta are well constrained, there are still large uncertainties and knowledge gaps to establish such understanding along the NWAM and in the Currituck area specifically.

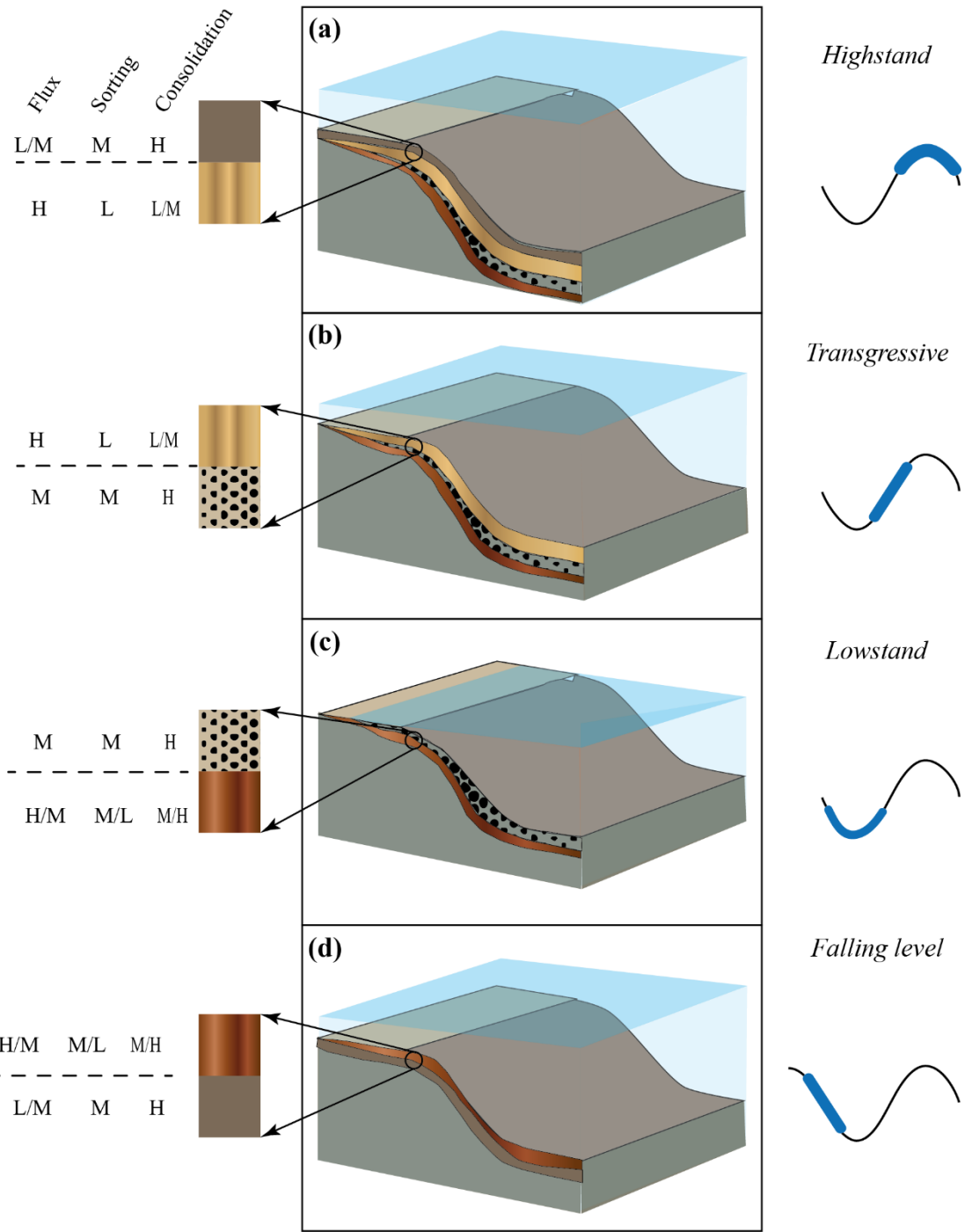


**Figure 3.8:** A schematic composition of potential strength interfaces that can form during a glacial-interglacial depositional cycle in the environment Currituck. H-high, M-medium, L-low.

### 3.5.3. Slope stability analysis and implications

Slope stability undrained static analysis suggests that for the averaged parameters estimation the slope is stable at similar slope depths where the failure was observed, however, vulnerable ( $FOS < 2$ ). The pseudo static undrained analysis suggests that slope failure maybe triggered in the event of seismic accelerations of at least  $PGA > 0.02$ . The estimated seismicity to the Currituck area is very low (U.S. ten Brink et al., 2009), however Locat et al., (2009) suggested that faults activity southern to Currituck slide could generate seismic acceleration to trigger a landslide.

The stability undrained static analysis that the lower unit is currently unstable at similar depths that Currituck slide is observed however, sliding did not occur in Currituck for the past approx. 15 ka. Based on previous empirical studies of Lee et al., (2000) and Hynes-Griffin and Franklin (1984), ten Brink et al., (2009) estimated a lower FOS value for slope stability analysis. The value proposed is  $FOS = 0.15$ , which according to the empirical studies suggest that although shear localization may already initiate, there is enough friction not to allow the sediments to move downslope rapidly. This re-evaluated FOS, explains the current static stability in Currituck. However, further research is needed on this topic.

Although this concludes that the slope is currently stable and most likely similar units in depth are stable as well, the stability analysis supports our strength differences assessment. According to the consolidation, the stability analysis and the schematic record (Fig. 3.8), the lower unit is predominantly weaker. The pseudo static analysis illustrates how unstable this unit can be given a seismic trigger (Fig. 3.7b) with  $FOS = 0.5$  as a conservative assessment. Other possible strength interfaces in the sedimentary record of the Currituck environment are possible, however as mentioned in the previous section, we are currently lacking such comprehensive data.

This current understanding of the sedimentary units, the sediments physical and geotechnical properties indicates a different slope stability than previously calculated by Locat et al., (2009) in which a very strong earthquake or very high pore pressure were suggested to initiate the Currituck landslide. Our results mainly stress the importance of using geotechnical measurements when possible. Importantly, our observations, though incomplete, suggest that the Currituck submarine landslide complex should not be used as a regional model for tsunami generation, due to the different sediment transport mechanism compared to the north canyon incised margins of the NWAM (Obelcz et al., 2014), yet further research is needed.

### 3.6. Conclusions

In the current study, cores taken inside the slide complex captured the most recent post-slide drape layer and part of the debris sediments. Additional cores collected around the slide complex provided information regarding sediment transport processes during the equivalent time (to the drape layer). The recently obtained age constraints highlighted the importance of site-specific study to understand slide dynamic, indicating the current scars in the Currituck slide complex are part of a single failure event. In the current study, we further stress the importance of the failure deposits origins and the environmental context of their deposition to understand where potential failure can occur and how this can further influence slide mobility. These are also valuable constraints, important for tsunami modelling.

The multi-proxy analyses of the sediments divided the drape layer into two units that represent the late Pleistocene to Holocene transgression and the Holocene highstand stages.

A detailed analysis of the sediments shows a genetic relationship between the debris sediments and the drape sediments indicating a similar sedimentary system transporting the sediments possibly throughout the glacial – interglacial cycle.

A first order evaluation of the drape sediments strength and consolidation suggest that sedimentation rate and consolidation processes precondition the formation of a strength interface (*sensu* Gatter et al., 2021) in the Currituck area. Possibly as a result of different glacial-interglacial sediment transport and climate variability. Despite lithological similarity, the initial conditions of deposition play a critical role in the development of consolidation.

A simplified schematic glacial-interglacial sedimentary record indicated that a significant strength interface most likely occurs between lowstand sediments that are overlain by transgressive sediments.

A slope stability analysis indicated that the slope is currently stable, yet additional trigger mechanisms would be required to initiate failure. Calculating the stability of each unit separately however, indicated that the unit deposited under high sedimentation rate during sea level transgression, can generate a weak interface with the deposits above or below.

The current analysis provided an understating how sea level and climatic variations influenced the sediments transport and consequently the stability of post-slide sediments. These results suggest that the sediments deposited in the Currituck area could potentially precondition mass movements. Unfortunately, the cores could only provide information of part of the last glacial-interglacial cycle. As we observed different water content and possibly consolidation variations, further understanding of the consolidation of deeper strata of a full glacial-interglacial cycle

(i.e., a complete system tract record) and their distribution could contribute to the understanding of the development of failure in this area.

The challenges met in the current study present the difficulties such deep-sea studies face worldwide. In order to develop deeper insights, the specific contribution of the sediment physical properties to the development of submarine landslides other tools such as numerical modelling or laboratory experiments can be used to overcome the issues met in deep-sea studies.

### **Acknowledgments**

HE would like to Yannick Zender for his assistance in the code development.

### **Authors' contribution**

Hadar Elyashiv: Conceptualization, Methodology, Formal analysis, Investigation, Writing - Original Draft, Writing - Review & Editing, Visualization; Jason Chaytor: Data collection, Writing - Review & Editing; Revital Bookman: Writing - Review & Editing, Supervision; Katrin Huhn: Code resources, Writing - Review & Editing, Supervision; Uri ten Brink: Writing - Review & Editing, Supervision.

# Appendix 3A: Multiproxy analysis supplementary material

Figure S3.1: Complete sedimentological and MSCL data for cores (a) 5PC and (b) 7PC and 13PC

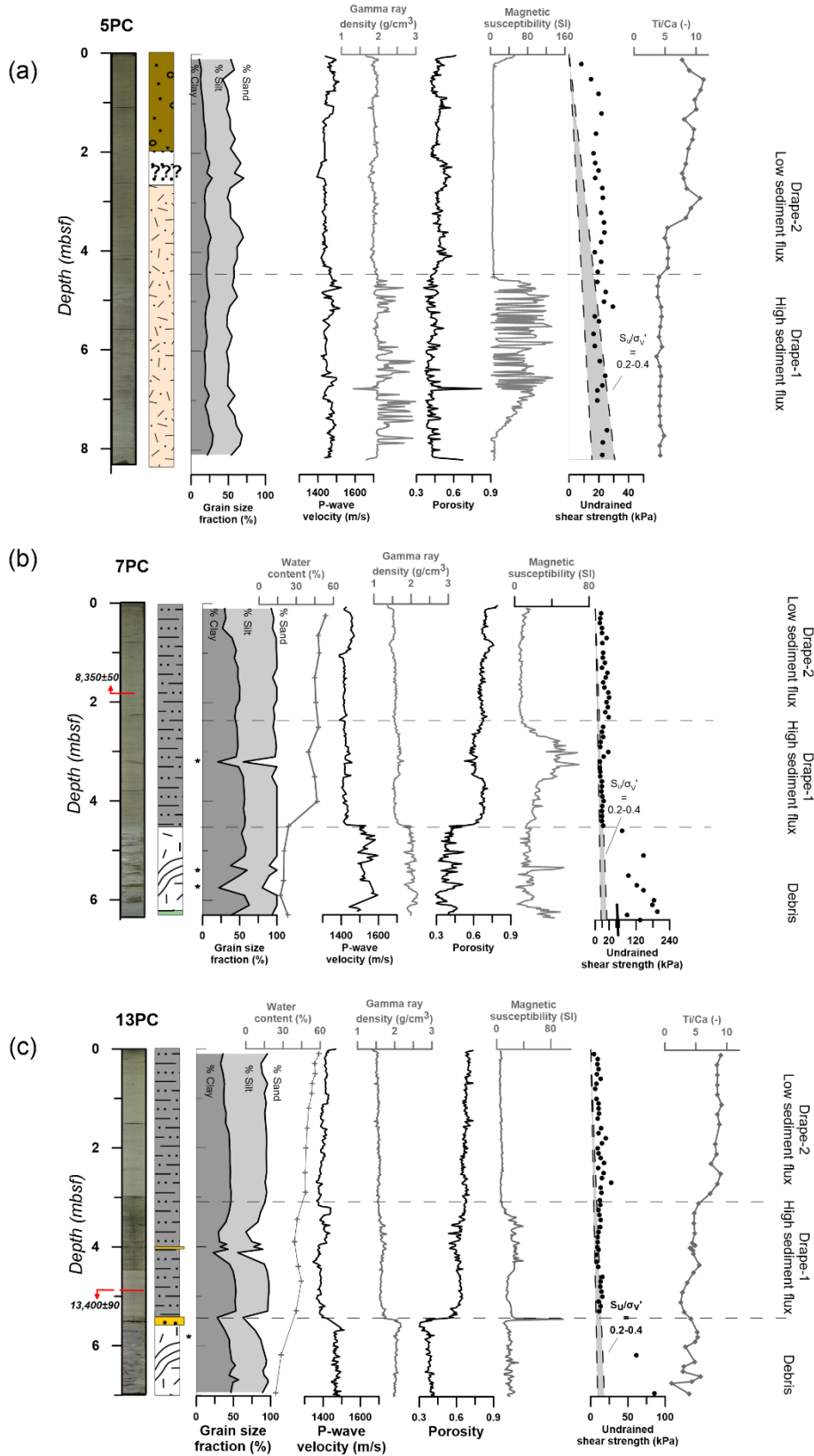
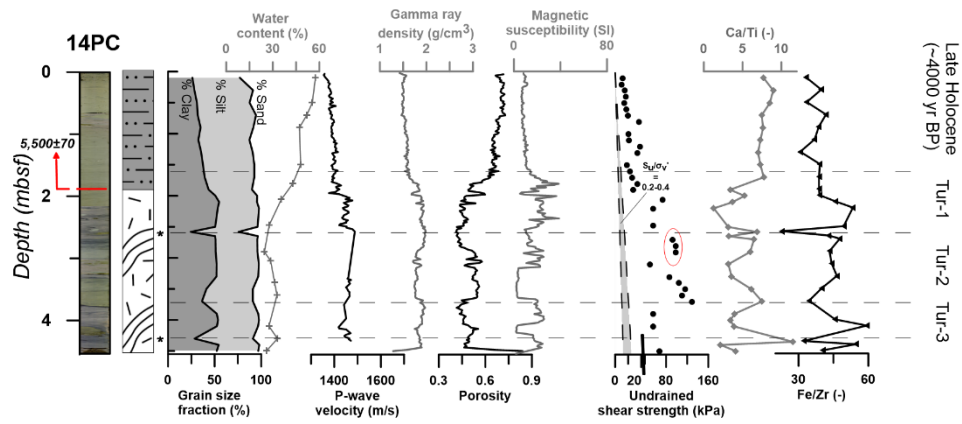


Figure S3.2: Complete sedimentological and MSCL data for cores (a) 14PC and (b) 16PC

(a)



(b)

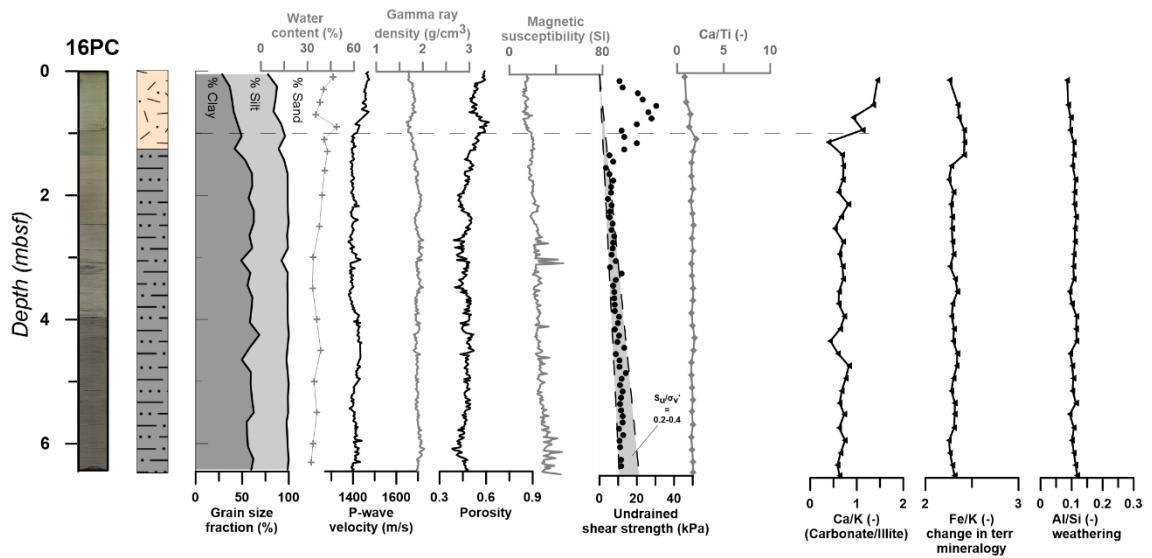
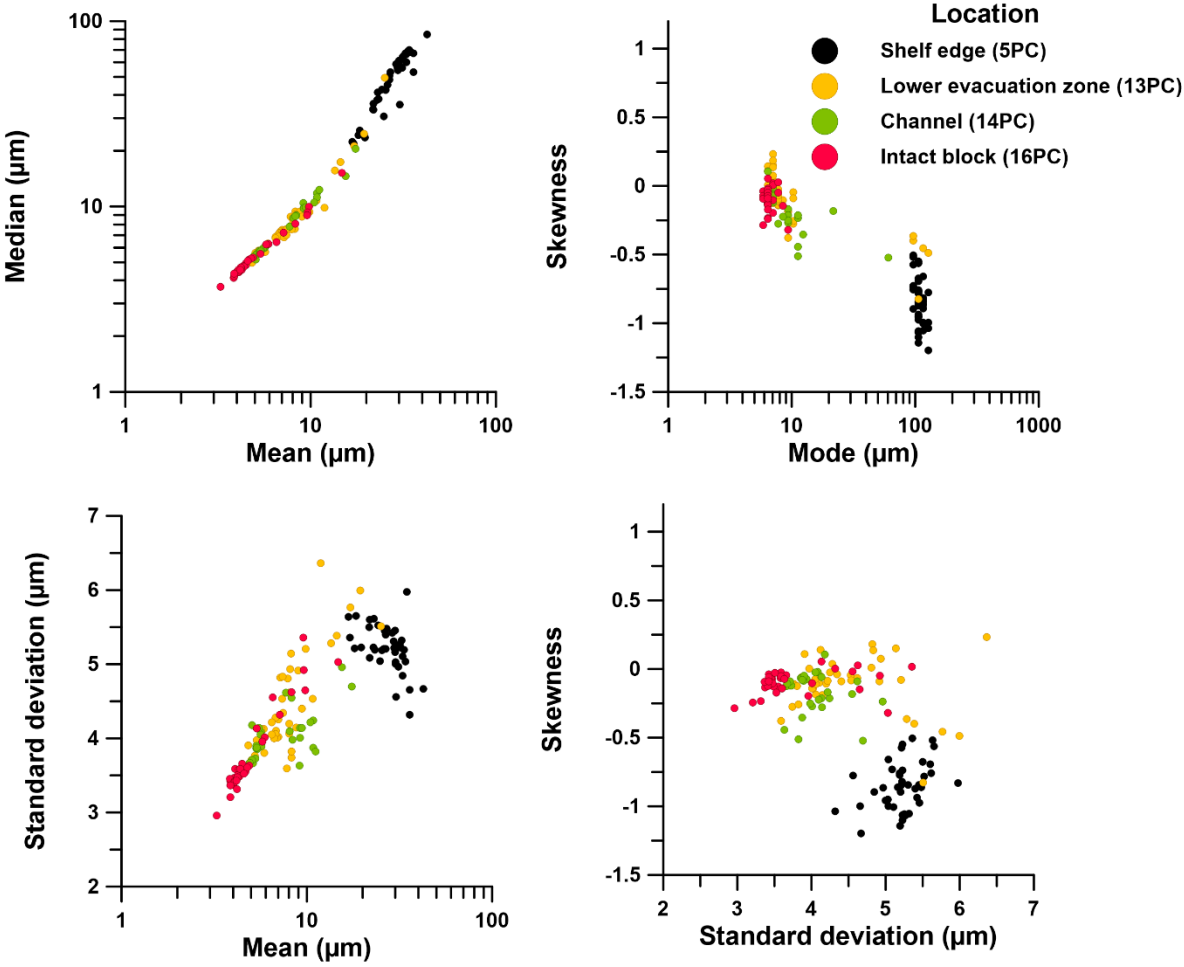


Figure S3.3: Textural analysis of sediments from four physiographic locations.





# Chapter 4

## Numerical Characterization of Cohesive and Non-Cohesive ‘Sediments’ Under Different Consolidation States Using 3D DEM Triaxial Experiments

**Authors:** Hadar Elyashiv (MARUM, University of Bremen, Germany & the Dr. Moses Strauss Department of Marine Geosciences, University of Haifa, Israel)

Revital Bookman (Dr. Moses Strauss Department of Marine Geosciences, University of Haifa, Israel)

Lennart Siemann (MARUM, University of Bremen, Germany & Leibniz University of Hannover, Germany)

Uri ten Brink (U.S. Geological Survey, Woods Hole Coastal and Marine Science Centre, USA)

Katrin Huhn (MARUM, University of Bremen, Germany)

**Status:** **Published, in:** *Processes* 2020, 8(10), 1252;  
doi: 10.3390/pr8101252  
(5 October 2020)

# 4. Numerical Characterization of Cohesive and Non-Cohesive ‘Sediments’ Under Different Consolidation States Using 3D DEM Triaxial Experiments

---

## Abstract

The Discrete Element Method has been widely used to simulate geo-materials due to time and scale limitations met in the field and laboratories. While cohesionless geo-materials were the focus of many previous studies, the deformation of cohesive geo-materials in 3D remained poorly characterized. Here, we aimed to generate a range of numerical ‘sediments’, assess their mechanical response to stress and compare their response with laboratory tests, focusing on differences between the micro- and macro-material properties. We simulated two endmembers—clay (cohesive) and sand (cohesionless). The materials were tested in a 3D triaxial numerical setup, under different simulated burial stresses and consolidation states. Variations in particle contact or individual bond strengths generate first order influence on the stress–strain response, i.e., a different deformation style of the numerical sand or clay. Increased burial depth generates a second order influence, elevating peak shear strength. Loose and dense consolidation states generate a third order influence of the endmember level. The results replicate a range of sediment compositions, empirical behaviours and conditions. We propose a procedure to characterize sediments numerically. The numerical ‘sediments’ can be applied to simulate processes in sediments exhibiting variations in strength due to post-seismic consolidation, bioturbation or variations in sedimentation rates.

## Keywords

DEM; cohesion; sediments; peak shear strength; consolidation state

## 4.1 Introduction

Many new and comprehensive datasets characterize the sediment physical behaviour of subaerial and submarine sediments based on laboratory experiments (Guo and Su, 2007; Hattab et al., 2013; Ikari and Kopf, 2011; van Gent et al., 2010) and in-situ measurements monitoring stress conditions and deformation processes (Dugan and Daigle, 2011). However, despite new technological developments, our knowledge of sediment behaviour cannot always sufficiently explain the deformational processes. This gap in the knowledge arises from the fact that many deformational processes cannot be directly observed, being too fast or too slow to be directly monitored (e.g., gravitational mass movements) or because they occur below the Earth's surface (e.g., failure plane and fault mechanics at different depth levels). Under these circumstances, numerical process simulations have been applied to develop conceptual models for such processes (e.g. Kock and Huhn, 2007a; LongJohn et al., 2018).

In addition to classical continuum models, numerical granular techniques, such as the Discrete Element Method (DEM, Cundall and Strack, 1978), have been used to investigate the full range of deformational processes—for example, simulating the large-scale long-term evolution of fold-and-thrust belts (Miyakawa et al., 2010), short-term mass-movements kinematics (Campbell et al., 1995) or small-scale geo-processes on various time scales (Kock and Huhn, 2007a; Mair and Abe, 2008).

The DEM is based on a granular approach where the model domain contains an assembly of individual, discrete particles. Interactions between these particles are subjected to contact models and individual particle properties (micro-properties; see section 2; Cundall and Strack, 1979). Depending on the applied particle contact model and the particle properties, different material behaviours can be simulated. This includes elastoplastic deformation following the Mohr–Coulomb brittle criteria (LongJohn et al., 2018) to a viscous deformation (Wenk and Huhn, 2013).

A particularity of numerical granular media is that the macro-properties of a particle assembly differ from the defined micro-properties of individual particles (Morgan and Boettcher, 1999). For example, the particle's friction coefficient micro-property influences the particle rolling behaviour and therefore the shear strength of the bulk material (Rothenburg and Bathurst, 1992). Another important property is the influence of particle shape and roughness (e.g. Guo and Morgan, 2004; Kock and Huhn, 2007a; Rothenburg and Bathurst, 1993, 1992; Schöpfer et al., 2009; Thornton, 2000). Using elliptical and ellipsoidal shaped particles, Thornton (2000) proposed that particle shape effects the deformation behaviour of the material, whereas Guo and Morgan (2004) showed that an angular particle shape results in a higher frictional strength.

Focusing on the micro-fabric break down, Kock and Huhn (2007a) demonstrated subsequent shear zone localization. Though elliptically shaped particles capture the deformation behaviour of granular materials such as sands very well, most researchers use disc and spherical particles since the calculation algorithms of elliptical particles significantly increase computation time (Antonellini and Pollard, 1995; Ask and Kopf, 2004; Campbell et al., 1995; Iwashita and Oda, 1999; Mair and Abe, 2008; Mora and Place, 1994; Morgan, 1999; Morgan and Boettcher, 1999; Schöpfer et al., 2009).

The current study aims to test specific DEM micro-particle properties to generate a set of different sediment types and their deformation behaviour in 3D. Our simulations focused on mimicking sand and clay mechanical behaviour with a wide range of cohesion and strength values. Sand and clay were chosen as the two compositions are endmembers of siliciclastic sediments. The shear strength of these endmembers was chosen as the main focus, because it strongly influences the rate and style of deformation (Abe et al., 2011; Ikari and Kopf, 2011; Mair et al., 2002; Wenk and Huhn, 2013; Yamamuro et al., 2011).

We applied the bonded numerical approach to simulate clay cohesive strength between particles (i.e., bonded materials), which is not present in cohesionless material (i.e., granular materials) (Morgan, 1999). Several studies used this approach in 2D but mainly focused on simulating brittle deformation in rocks (e.g. Anantanasakul et al., 2012; LongJohn et al., 2018). To the best of our knowledge, granular (cohesionless) vs. bonded materials (cohesive) have not yet been comprehensively tested in 3D and their applicability for the simulation of sand and clay sediments has not been investigated. Additionally, we tested the role of the consolidation state, which can be indicated by loose and dense particle packing for both granular and bonded materials. These endmember properties simulate a range of ‘sands’ and ‘clays’. Finally, we tested three different stress states to simulate different burial depths of the ‘sediments’ to achieve different responses to loading.

We adopted the approach and procedures used in geotechnical and numerical tests to build numerical 3D triaxial tests (e.g. Guo and Su, 2007; Itasca, 2014). Analyses of these numerical triaxial tests enabled the collection of detailed information regarding different particle packing states: (i) their stress–strain curve or deformation behaviours, and (ii) the resulting macro-properties, e.g., cohesion.

## 4.2. The Discrete Element Method—Granular and Bonded Approach

The Discrete Element Method is a numerical technique to simulate the interactions between solid granular particles via discrete contact points. Within a model domain, each particle is defined by a set of micro-properties such as density ( $\rho_p$ ; in the following index, ‘p’ indicates micro-properties defined for individual particles) and coefficient of friction ( $\mu_p$ ). These micro-properties are included in the force calculation at each contact point using pre-defined contact models (Cundall and Strack, 1978). Contact models (also termed contact laws) control the overall physical behaviour of particle assemblages and define the interaction between particles. The force–displacement calculations are described in detail in Appendix 4A.

We used the commercial software Particle Flow Code 3D (PFC3D) by ITASCA™ to investigate the mechanical behaviour of numerical ‘sediments’. The software implements the DEM technique following principles defined by Cundall and Strack (1979) and offers several contact models to generate different mechanical behaviours (Sadek et al., 2011). We selected the Hertz–Mindlin contact model to generate a cohesionless granular material (sand-like; see Section 2.1.) and the linear parallel-bond contact model to generate a cohesive, elastoplastic behaviour (clay-like, see Section 2.2.). Both contact models were previously applied using PFC and other discrete element software to generate a range of geo-materials such as soils and rocks (Anantanasakul et al., 2012; Potyondy, 2015; Sadek et al., 2011; Thornton, 2000).

It is important to note that, although in each model parameters are assigned per particle as micro-properties, we do not assume that a single particle represents a single sediment grain. The overall assembly of particles represents an averaged macro-mechanical behaviour of a bulk sediment sample. To make DEM applicable and achieve insights into the mechanical deformation behaviour of a natural material, some micro-properties need to be adjusted so that the particle assemblage behaves macroscopically as an elastoplastic material. Therefore, it does not reproduce the whole range of sediment behaviour (e.g., neglecting clay electro-chemical forces) but rather a first-order approximation of stress–strain behaviour (e.g. Huhn et al., 2006; Pichel et al., 2019).

### *4.2.1. Granular Approach: The Hertz–Mindlin Contact Model (Cohesionless, Elastoplastic)*

The contact between two spherical elements is a spherical 3D contact that becomes a circular area once load is applied (Wang and Zhu, 2013). The Hertz theory accounts for such a non-linear interaction contact behaviour between smooth and elastic spheres. To

account for the frictional behaviour, the Mindlin model describes the tangential forces that develop at the contact between two spherical elements (Mindlin and Deresiewicz, 1953). The combined Hertz–Mindlin contact model applies the Hertz approach as an elastic response in the normal direction, and the Mindlin approach in the tangential direction along with Coulomb’s friction model (Mindlin and Deresiewicz, 1953). The Hertz–Mindlin contact model has been previously used to simulate sands, soils and fault gouge material (Manchanda et al., 2012; Morgan, 1999; Yimsiri and Soga, 2011) and is applied here as well to simulate sand mechanical behaviour.

In PFC3D, the input parameters for the Hertz–Mindlin contact model are the elastic constants of the particles, namely the micro-shear modulus ( $G_p$ ) and the micro-Poisson’s ratio ( $\nu_p$ ). These two are the required elastic constants to calculate the forces in the normal and tangential directions ( $F_n$  and  $F_s$ , accordingly). The shear modulus is the elastic stiffness of a material and defines the material resistance to shearing deformation. Under small strains, the shear modulus of a bulk material depends on the confining pressure stress and the packing condition (i.e., porosity) of the particles and therefore it is an indicator of the material’s structure and strength (Yamamoto et al., 1994). A fixed micro-coefficient of friction ( $\mu_p$ ) and density ( $\rho_p$ ) values are also assigned to each particle. The micro-shear modulus and micro-Poisson’s ratio are implemented in the normal and tangential stiffness ( $k_n$  and  $k_s$ , accordingly) calculations (Fig. 4.1a) according to the following Equations:

$$\text{Eq. 4.1} \quad k_n = \left( \frac{2G_p \cdot \sqrt{2\bar{R}}}{3(1-\nu_p)} \right),$$

$$\text{Eq. 4.2} \quad k_s = \left( \frac{2 \left( 3G_p^2 (1 - \nu_p \bar{R}) \right)^{1/3}}{2 - \nu_p} \right) \cdot F_n^{1/3},$$

where  $\bar{R}$  is the average radius of the two particles that are in contact (Itasca, 2014).

#### 4.2.2. Granular Cohesive Approach: The Linear Parallel-Bond Contact Model (Cohesive, Elastoplastic)

Cohesive strength in clay-like sediments originates from the electrostatic attraction between clay particles and is a stress-independent component of the shear strength (Mitchell, 2005). In DEM, however, the bonds implemented between the particles are used to simulate the interaction, the resulting forces and the strength that the bond can sustain. The linear parallel-bond contact model was created to simulate a cemented

granular material (Potyondy and Cundall, 2004). The model introduces a rigid inter-particle bonding, thus generating cementation or cohesive strength (Potyondy, 2015; Potyondy and Cundall, 2004). Such an approach provides the mechanical behaviour of a glue-like piece, which connects two particles in contact and adjusts the sliding interaction between them. In PFC3D, the linear parallel-bond is applied as a flat cylinder (Figure 4.1b). The bonds are able to transmit both forces and moments between the particles. The bond is modelled by a set of two springs with constant normal and shear stiffnesses (red rectangle, Figure 4.1b). The bond breaks once the shear or axial stress applied at the contact area exceeds the bond's strength (Itasca, 2014). Once a bond is broken, it does not regenerate. We therefore refer to the cohesive strength as an initial cohesive strength.

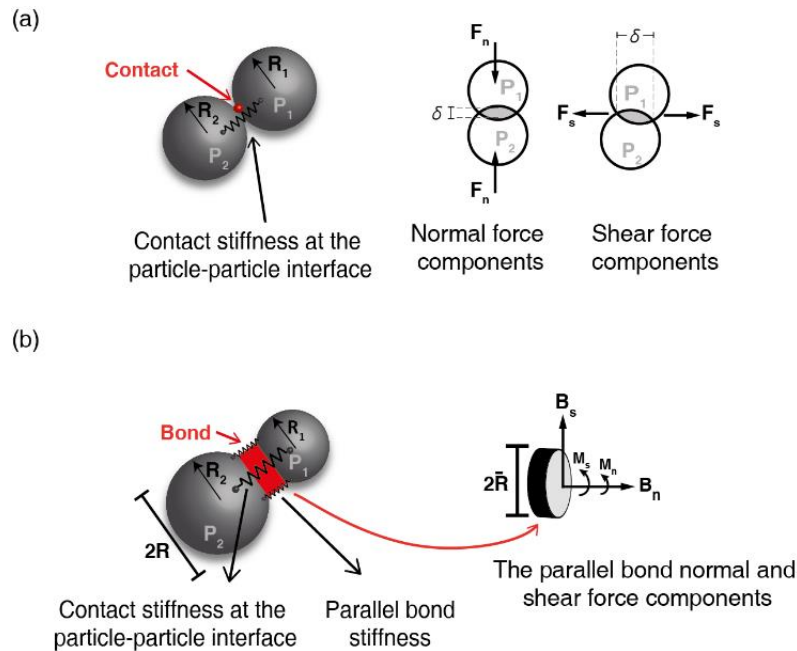


**Figure 4.1.** (a) An illustration of particles interaction according to the Hertz–Mindlin contact model. (Left) The contact point is illustrated as a red sphere and the contact stiffness as a spring.  $R_1$  and  $R_2$  represent the radii of particles  $P_1$  and  $P_2$ , accordingly. (Right) A 2D cross section of the acting normal ( $F_n$ ) and shear ( $F_s$ ) forces and the particle's overlapping  $\delta$ . (b) An illustration of particles interaction according to the linear parallel-bond contact model. (Left) In addition to a contact at the interacting point of two particles (contact stiffness presented as a spring), a bond is implemented as a cylindrical disk (in red), and its interaction is illustrated by two parallel springs.  $R_1$  and  $R_2$  represent the radius of particles  $P_1$  and  $P_2$ , accordingly. (Right) A 3D illustration of the bond's normal ( $B_n$ ) and shear ( $B_s$ ) forces and the moments ( $M_n$  and  $M_s$ ) that result from the applied force. The size of the applied bond is according to the average radius of the two interacting particles and represented as an average  $2R$ .

After a bond is removed, the interaction between particles is influenced only by the particle's stiffness (normal and shear) and friction (elastic–frictional) according to the linear contact model (Itasca, 2014).

In PFC3D, the linear parallel-bond model requires at least ten micro-parameters to define both the contact and the bond behaviour (Itasca, 2014)(Table 4.1). In addition to the density and friction coefficient assigned to each particle, the contact behaviour requires two micro-parameters (similar to the linear contact model), the normal and tangential stiffness of the contact, as follows:

$$\text{Eq. 4.3} \quad F_n = k_n \cdot \delta,$$

$$\text{Eq. 4.4} \quad \Delta F_s = -k_s \cdot \delta,$$

where  $\Delta F_s$  is the incremental tangential force and is similar to the Hertz–Mindlin model,  $\delta$  is the overlap between particles.

The bond requires six micro-parameters: the normal and shear stiffnesses of the bond ( $B_n, B_s$ ), the tensile strength of the bond ( $PB_{ten}$ ), the cohesive strength of the bond ( $PB_{coh}$ ), the bond friction coefficient ( $\mu_{bond}$ ) and a bond radius multiplier ( $\lambda$ ). The bond radius multiplier is a parameter that determines the size of the bond by considering the radii of the particles in contact:

$$\text{Eq. 4.5} \quad \bar{R} = \lambda_{min}(R^a, R^b),$$

where  $R^a, R^b$  are the radii of two particles in contact (Figure 4.1b). For the bond behaviour, the forces ( $F_n^{PB}, F_s^{PB}$ ) and the moments ( $M_n, M_s$ ) are calculated as follows:

$$\text{Eq. 4.6} \quad F_n^{PB} = B_n \cdot \delta \cdot A,$$

$$\text{Eq. 4.7} \quad F_s^{PB} = -B_s \cdot \delta \cdot A,$$

$$\text{Eq. 4.8} \quad M_n = -B_n \cdot \Delta\theta_n \cdot J,$$

$$\text{Eq. 4.9} \quad M_s = -B_s \cdot \Delta\theta_s \cdot I,$$

where A, J and I are the area, moment of inertia and polar moment of inertia of the bond cross section, respectively.  $\Delta\theta_n$  and  $\Delta\theta_s$  are the normal and shear increments of the rotation between two bonded particles, respectively. On the periphery of the bond, tensile ( $\bar{\sigma}_{max}$ ) and shear ( $\bar{\tau}_{max}$ ) stresses are calculated according to:

$$\text{Eq. 4.10} \quad \bar{\sigma}_{max} = \frac{-F_n^{PB}}{A} + \frac{|M_s|}{I} \bar{R},$$

$$\text{Eq. 4.11} \quad \bar{\tau}_{max} = \frac{|F_n^{PB}|}{A} + \frac{|M_n|}{J} \bar{R}.$$

Once the stress in the shear or tensile directions exceeds the assigned tensile and cohesive strengths ( $\bar{\sigma}_{max} \geq PB_{ten}$ ;  $\bar{\tau}_{max} \geq PB_{coh}$ ), the bond breaks and the inter-particle interaction follows the linear contact model (Itasca, 2014; Potyondy and Cundall, 2004).

*Table 4.1. Fixed and tested micro-parameters applied in each of the triaxial tests according to the contact model applied during the test.*

Parameters	Unit of Measure	Symbol	Value
<b>Fixed Properties</b>			
Sample dimensions: width; height; length	(m)		220; 220; 220
Total number of particles in a sample			21,172
Radius (particles)	(m)	$R_p$	3.7; 3.9; 4.6; 5.5
Particle density	(kg/m <sup>3</sup> )	$\rho_p$	2650
Damping coefficient		$damp$	0.7
Particle friction coefficient (during triaxial test)		$\mu_{test}$	0.5
Particle friction coefficient (initial)		$\mu_{setup}$	0.1 (dense) 0.5 (loose)
<b>Wall properties</b>			
Wall friction coefficient		$\mu_{(wall)}$	0.0
Wall normal stiffness	(Pa)	$k_{n(wall)}$	1e <sup>12</sup>
<b>Hertz–Mindlin micro-properties ('sand')</b>			
Poisson's ratio	dimensionless	$\nu$	0.25
Shear modulus (small; medium; large)	(Pa)	$G_p$	1e <sup>11</sup> ; 1e <sup>10</sup> ; 1e <sup>8</sup>
<b>Parallel-bond micro-properties ('clay')</b>			
Parallel-bond contact normal and shear stiffness	(Pa)	$k_{n,s}$	1e <sup>10</sup>
Bond radius multiplier		$\lambda$	1
Bond friction coefficient		$\mu_{bond}$	0.54
Bond stiffness	(Pa)	$B_{n,s}$	1e <sup>5</sup>
Bond cohesive strength (small; medium; large)	(Pa)	$PB_{coh}$	210e <sup>3</sup> ; 110e <sup>3</sup> ; 55e <sup>3</sup>
Bond tensile strength (small; medium; large)	(Pa)	$PB_{ten}$	110e <sup>3</sup> ; 55e <sup>3</sup> ; 25e <sup>3</sup>

### 4.3. Experimental Setup

To generate a spectrum of different numerical materials mimicking a 'sand'-like and 'clay'-like sediment physical behaviour, we created a 3D numerical triaxial test (Figure 4.2). Confined triaxial testing is a method used in soil mechanics to empirically characterize the mechanical behaviour of sediments (Gylland et al., 2014; Sadek et al., 2011; Yamamuro et al., 2011). In

addition to the mechanical and deformation behaviour of the numerical 'sediments', we quantified the numerical material's physical bulk properties.

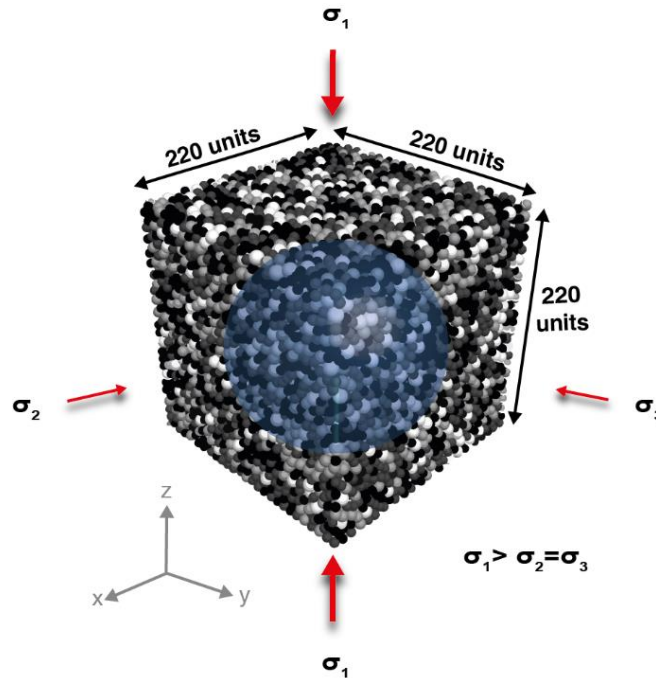


*Figure 4.2. The 3D Discrete Element Method (DEM) cubic isotropic sample. The initial particle setup for the triaxial test is under strain ( $\epsilon_z$ ) = 0%. The blue sphere in the centre of the pre-tested cubic sample presents the location of the measurement sphere. The main stress ( $\sigma_1$ ) is acting parallel to the z-axis;  $\sigma_2$  and  $\sigma_3$  are equal and act parallel to axes x and y, respectively.*

#### 4.3.1. Model Geometry

The model setup uses the software's internal model meter scale units (i.e., m). To ensure that the model results are reproducible on other scales, a self-similarity test was conducted (see supplementary explanation in Appendix 4A and Figure 4.S1).

We designed the numerical triaxial cubic shear box with uniform dimensions of 220 m (Figure 4.2), following a simplified laboratory approach. Inside this volume, an isotropic cubic sample with equal dimensions of 220 m was generated in order to avoid sample size effects and to achieve a ratio that is at least 20× the particle size. This makes sure that the measured material macro-properties such as peak shear strength and coefficient of friction are not sensitive to particle size (Potyondy and Cundall, 2004). Each sample contained 21,172 ideal spherical particles with four different radii (R) ranging from 3.7 to 5.5 m (Table 4.1; Figure 4.2). The particles were randomly distributed within the cubic

volume to produce arbitrary isotropic packing (Potyondy and Cundall, 2004). The chosen random distribution and the radius uniform spectrum prevent unrealistic deformation, such as that caused by a symmetrical particle packing (Saltzer and Pollard, 1992), thus minimizing the influence of particle size and distribution on the results.

During the entire model run, solid and frictionless boundary walls confine the particles. Similar to Mair and Abe (2011) and Potyondy and Cundall (2004), this is done to reduce frictional boundary effects due to the interactions of particles with the walls. The walls were assigned a normal stiffness to prevent particles escaping (see  $k_{n(wall)}$  and other wall properties in Table 4.1). Confinement effects by rigid or flexible walls were studied in 2D and 3D by Cheung and O’Sullivan (2008), showing that wall rigidity is important to the post-peak behaviour and particle-scale response rather than on the macro-scale. Based on these results, the current work focuses on the pre-peak and peak shear strength behaviour of the material, and the effect of wall rigidity is neglected.

#### *4.3.2. Particle and Bond Micro-Properties*

A specific contact model was defined first to simulate either a sand-like mechanical behaviour via the Hertz–Mindlin contact model or a clay-like behaviour via the linear parallel-bond contact model. Independent of the specific contact model, density and coefficient of friction were defined for each particle during all triaxial tests. All particles were assigned a similar density of 2650 (kg/m<sup>3</sup>) and a constant micro-coefficient of friction of  $\mu_p = 0.5$ ; the latter lies in the range observed for values of siliciclastic sediments (Mitchell and Soga, 2005). Both parameters were kept constant throughout the model set-up and the entire simulation run (Table 4.1). The contribution of the coefficient of friction to the sediment shear strength has been extensively studied, both in laboratory tests (Morrow et al., 2017; Rathbun and Marone, 2010) and DEM experiments (Kock and Huhn, 2007b, 2007a; Morgan and Boettcher, 1999). Here, we focus on the influence of other micro-parameters—the micro shear modulus and the micro cohesive bond strength—on the cohesive and overall shear strength. In both contact models, the sliding of particles is governed by Coulomb’s friction law and is always controlled by the assigned identical constant micro coefficient of friction ( $\mu_p$ ). For the Hertz–Mindlin contact model, the Poisson’s ratio was also kept constant, as it does not show a significant effect on the sediments’ mechanical behaviour in the laboratory (Nandanwar and Chen, 2017) or DEM tests (Manchanda et al., 2012). In the linear parallel-bond contact model,

we assigned the contact parameters ( $k_{n,s}$ ), the bond stiffness ( $B_{n,s}$ ), the bond friction coefficient ( $\mu_{bond}$ ) and radius multiplier ( $\lambda$ ) as constant values (Table 4.1) to minimize the amount of free micro-parameters in the model. In addition, the values of the normal and shear stiffnesses for both the contact ( $k_{n,s}$ ) and bond ( $B_{n,s}$ ) were fixed with a ratio of 1 (Table 4.1).

#### 4.3.2.1. Hertz–Mindlin Contact Model—Granular ‘Sand-Like’ Materials

In the Hertz–Mindlin contact model, the micro-shear modulus ( $G_p$ ) was tested to investigate its influence on the numerical material’s shear strength. The values for the shear modulus (low, medium and high, Table 4.1) were modified from previous numerical tests to apply them to 3D simulations (Kock and Huhn, 2007b, 2007a) and were chosen to support an elastic–plastic deformation behaviour, reproducing the behaviour of natural sand (Turcotte and Schubert, 2014).

#### 4.3.2.2. Linear Contact Bond Model—Cohesive ‘Clay-Like’ Materials

In the linear parallel-bond contact model, the two bond strengths micro-parameters, the bond cohesive strength ( $PB_{coh}$ ) and the bond tensile strength ( $PB_{ten}$ ) were tested to investigate their influence on the numerical material’s cohesive and shear strength. Here, the three values tested for the bond’s strength were assigned as the ratio between the micro-cohesive bond strength ( $PB_{coh}$ ) and the bond micro-tensile strength ( $PB_{ten}$ ) was maintained around 0.5 ( $=PB_{ten}/PB_{coh}$ ). Cheung et al., (2013) studied the effect of micro-parameters on the macro-behaviour of this contact model when simulating cemented sands. Their results indicated that the overall material stiffness and peak strength are influenced by the bond-to-contact stiffnesses ratio and the size of the assigned tensile and cohesive strengths, respectively. Simulating a numerical cohesive material, Abe et al. (2011) showed shallow deformational processes using a close value of tensile to cohesive strength ratio (c. 0.4). The assigned fixed values to the contact and the bond, and the tested values of the bond strength, were adjusted from previous numerical studies using the linear and parallel-bond contact models to simulate natural sedimentary rocks (Abe et al., 2011; Huhn et al., 2016; Kock and Huhn, 2007a) (see Table 4.1).

### 4.3.3. Model Run Stages of the Numerical Triaxial Tests

The numerical confined triaxial tests were carried out in three stages: (a) sample generation, (b) isotropic compression, and (c) triaxial shear. In stage (a), particles were randomly distributed within the cubic box (an initial particle arrangement identical in all tests; Figure 4.2) and assigned an initial consolidation state. To simulate loose or dense initial particle consolidation states, we applied a micro- coefficient of friction ( $\mu_{ini,p}$ ) to generate either a loose ( $\mu_{ini,p}=0.5$ ) or a dense ( $\mu_{ini,p}=0.1$ ) sample configuration. Previous studies used this approach to control the sample's initial density (Feng et al., 2017; Morgan, 1999; Potyondy and Cundall, 2004; Thornton, 2000). Subsequently, the final material consolidation states were designated as L or D for loose and dense packed samples, respectively, and the material itself S or C for 'sand' or 'clay', respectively (e.g., in Table 4.2, densely packed 'sand' is DS).

**Table 4.2.** Calculated macro-properties of different material samples: LS: loose 'sand', DS: dense 'sand', LC-loose 'clay', DC-dense 'clay'. Numbers in brackets are cohesion values, as measured from the linear regression of the failure envelope.

Experiment	Mean Normal Stress (kPa)	Peak Shear Strength ( $\tau_{max}$ ) (kPa)	Macro-Friction Coefficient ( $\mu_M$ )	Bulk Cohesion C (kPa)	Experiment	Mean Normal Stress $\sigma_3$ (kPa)	Peak Shear Strength ( $\tau_{max}$ ) (kPa)	Macro-Friction Coefficient ( $\mu_M$ )	Bulk Cohesion (kPa)				
<b>'Sand'</b>													
LS-3 ( $G_p = 1e^8$ Pa)	153 382 754	53.3 132.4 254.5	0.35	(3.1)	DS-3 ( $G_p = 1e^8$ Pa)	241 624 1280	141.9 374.0 780.0	0.64	(33.3)				
LS-2 ( $G_p = 1e^{10}$ Pa)	191 425 808	91.2 175.2 308.7			0.37	(26.1)	DS-2 ( $G_p = 1e^{10}$ Pa)			224 504 976	124.1 254.1 475.9	0.52	(21.2)
LS-1 ( $G_p = 1e^{11}$ Pa)	190 513 903	90.6 263.4 403.7					0.47			(23.3)	DS-1 ( $G_p = 1e^{11}$ Pa)		
<b>'Clay'</b>													
LC-3 ( $PB_{co} = 55e^3$ Pa)	287 528 911	187.6 278.4 411.4	0.38	92.6	DC-3 ( $PB_{co} = 55e^3$ Pa)	531 801 1291		431.7 551.8 791.5	0.53		199		
LC-2 ( $PB_{co} = 110e^3$ Pa)	226 537 906	126.2 287.2 406.4			0.44	52.8	DC-2 ( $PB_{co} = 110e^3$ Pa)	390 679 1174		290.4 429.9 674.4		0.55	112
LC-1 ( $PB_{co} = 210e^3$ Pa)	223 452 884	123.0 202.8 384.8					0.43	32		DC-1 ( $PB_{co} = 210e^3$ Pa)			

In stage (b), the sample was brought to equilibrium conditions under a controlled confining stress and a controlled axial load applied by the rigid box walls. As the sample reached the assigned confining stress, the tested micro-parameters were assigned to contacts and bonds. At this point, the constant micro-friction coefficient ( $\mu_p=0.5$ ) was assigned to all particles (Table 4.1). Each sample was tested under three magnitudes of confined stress of  $\sigma_2 = \sigma_3 = 100, 250$  and  $500$  kPa. These stresses are in agreement with a wide range of laboratory tests on sandy and clayey sediments (Hattab et al., 2013; Marri et al., 2012; Wanatowski and Chu, 2008; Yamamuro et al., 2011). Triaxial tests using confining stresses higher than  $1000$  kPa were reported to initiate grain fracturing (e.g. De Bono and McDowell, 2014), which we do not attempt to simulate here.

Following the isotropic compression, the triaxial loading stage (c) was initiated. During the test, a sample was axially loaded with an increasing stress, which was symmetrically applied via the top and bottom walls ( $\sigma_1$ ; parallel to the z-axis; Figure 4.2). A constant velocity of  $0.4$  m/s was applied on the upper and lower walls and an axial strain rate of  $0.00002$  m/s, maintaining the quasi-static loading of the walls. This velocity is in the range of the loading velocities used in various DEM studies (Ding et al., 2014) and the relatively low axial strain rate does not influence the resulting bulk sample macro-properties (e.g. Ding et al., 2014; LongJohn et al., 2018; Potyondy and Cundall, 2004). The velocity of the confining walls was kept constant during the test to maintain a constant confining stress (Itasca, 2014). The tests were carried out until the prescribed axial strain was achieved ( $\epsilon_z = 20\%$ ), similar to laboratory triaxial tests, e.g., (Wanatowski and Chu, 2008).

#### 4.3.4. Model Interpretation and Calculations

During the triaxial tests, stresses and strains were monitored continuously in the x, y, and z directions. The stress measurements were used to calculate the differential stress (i.e., the stress deviator ( $q$ )), which represents the stress under which the bulk material failed:

$$\text{Eq. 4.12} \quad q = \sigma_1 - \sigma_3,$$

where  $\sigma_1$  and  $\sigma_3$  are the maximum vertical stress and the confining stress measured and applied for each test, respectively. Combined with the associated axial strain  $\varepsilon_z$ , these stress–strain curves give an insight into the deformation behaviour, including determination of the peak strength, strain hardening and softening effects, etc. (Figures 4.3a and 4.4a).

The volumetric strain, the coordination number and the porosity (Figures 4.3b–d and 4.4b–d) were monitored using a measurement sphere placed in the middle of the sample to avoid boundary effects on the measured parameters (Figure 4.2). The measurement sphere allowed us to measure and calculate quantities within the defined volume using the particles' contacts and volumes (Itasca, 2014; Potyondy and Cundall, 2004). We defined the radius of the measurement sphere as  $R = 90 \text{ m}$ , which enabled us to record more than one quarter of the model volume. Such a quantity is considered representative of the entire model (Schöpfer et al., 2013). The quantities were then taken as averages over the volume.

To observe significant intervals of deformation, the normalized gradient of displacement was calculated and plotted for a predefined deformation interval along a vertical cutting surface (Figure 4.5). This plot enables us to identify zones of high relative displacement between individual particles during a certain time interval. These zones could be interpreted as failure planes (Figure 4.5a–e).

The modified failure envelope was illustrated using  $\sigma_1$  and  $\sigma_3$ . According to Craig (2004), any state of stress can be presented by a point of stress by plotting the mean  $\frac{1}{2}(\sigma_1 + \sigma_3)$  against the maximum  $\frac{1}{2}(\sigma_1 - \sigma_3)$  stress. The maximum shear stress and the mean normal stress were plotted in the modified failure envelope  $\tau_{max} - \sigma_{mean}$  space (Figure 4.6 and Table 4.2) as:

$$\text{Eq. 4.13} \quad \tau_{max} = \frac{1}{2}(\sigma_1 - \sigma_3),$$

Eq. 4.14

$$\sigma_{mean} = \frac{1}{2}(\sigma_1 + \sigma_3),$$

Note that since we performed consolidated drained tests, pore pressure was not considered and therefore the effective stress can be considered as the total stress. The peak shear strength ( $\tau_{max}$ ), macro-friction coefficient ( $\mu_M$ ) and bulk cohesion ( $C$ ) for all tests are presented in Table 4.2 and were determined from the linear extrapolation of the modified failure envelopes. Bulk cohesion is used here in the same context as cohesion measured in laboratory experiments (over bulk material) and in Equation A4 in Appendix 4A.

#### 4.4. Results

The 3D triaxial test results present the effect of granular contact and granular bonding ability to simulate cohesionless, sand-like and cohesive, clay-like mechanical behaviour. The sensitivity of the two material endmembers was carried under different consolidation states (loose vs. dense packing) for which three different material strengths were then tested ('sand':  $G_p = 1e^{11}, 1e^{10}, 1e^8$  Pa; 'clay':  $PB_{coh} = 55e^3, 110e^3, 210e^3$  Pa). These 12 materials were deformed under different loading conditions of 100, 250 and 500 (kPa), simulating different burial depths. In total, 36 experimental material settings were tested, 18 for each material type (Table 4.1).

From here onwards, the results of the Hertz–Mindlin contact model and the linear parallel-bond contact model will be referred as 'sand' and 'clay', respectively.

##### 4.4.1. Stress–Strain Behaviour

Under triaxial loading, loose 'sand' samples showed a gradual increase in deviator stress up to 10% of axial strain (Figure 4.3a). The peak deviator stress, defined as the highest differential stress  $q$  (see Equation 4.12), is reached between 15 to 20% of axial strain. Stress values fluctuated around this peak value. Increasing the value of the micro-shear modulus ( $G_p$ ) in the samples resulted in reaching the peak shear strength under a lower strain (in Figure 4.3a,  $G_p = 1e^{11}$  Pa samples reached a peak at around 15% strain, whereas samples with  $G_p = 1e^8$  Pa reached a peak only at around 17–18% strain).

The stress–strain curves of densely packed 'sand' samples showed a rapid increase and reached the peak deviator stress at axial strains of 0.5 to 5% (Figure 4.3a). Following the peak, there is a rapid decrease in stress until 20% strain. These results showed that an

increased micro-shear modulus ( $G_p$ ), resulted in lower peak deviator stress under lower axial strain (Figure 4.3a and Table 4.2). The opposite trend was observed in loose 'sand' samples (an increased micro-shear modulus  $G_p$  leads to an increased peak deviator stress, Table 4.2). A slightly different stress–strain curve of densely packed 'sand' was observed for samples with a low micro-shear modulus ( $G_p=1e^8$  Pa). Samples with a high micro-shear modulus show a high rate of increasing stress (Figure 4.S2 in the Supplementary Materials), whereas samples of  $G_p=1e^8$  Pa micro-shear modulus presented a moderate rate of change in stress and reached peak deviator stress at around 2–7.5% strain.

The stress–strain curves of 'clay' samples primarily differed from 'sand' due to the additional bond (Figure 4.4a). The results of the loose 'clay' samples showed a general rapid increase in the deviator stress until a peak deviator stress was reached between 0.1 and 2% of strain (Figure 4.4a). As the peak stress was reached, all samples presented a local variability in the rate at which the stress was changing (Figure 4.S2 in the Supplementary Materials). Samples with low micro-cohesive bond strength ( $PB_{coh} = 55e^3$  Pa) showed a decrease in the residual strength (for confining stresses of 100 and 250 kPa) or a decrease followed by a slight increase up to the previous peak value (confining stress of 500 kPa). In loose 'clay' samples, by increasing the micro-cohesive bond strength ( $PB_{coh}$ ), a lower peak strength was achieved under lower axial strain (rapid failure under lower stresses).

The stress–strain curves of densely packed 'clay' samples (Figure 4.4a) showed a rapid increase up to peak deviator stress. The stress rate changed in a similar manner to loose 'clay' samples. The peak stress was reached at 0.5–2% strain, followed by a rapid decrease in stress until 20% strain was reached. Similar to loose 'clay' samples, a prominent peak deviator stress was observed. The stress at 20% strain is equal or slightly higher compared to the value observed for loose 'clay' samples at 20% strain.

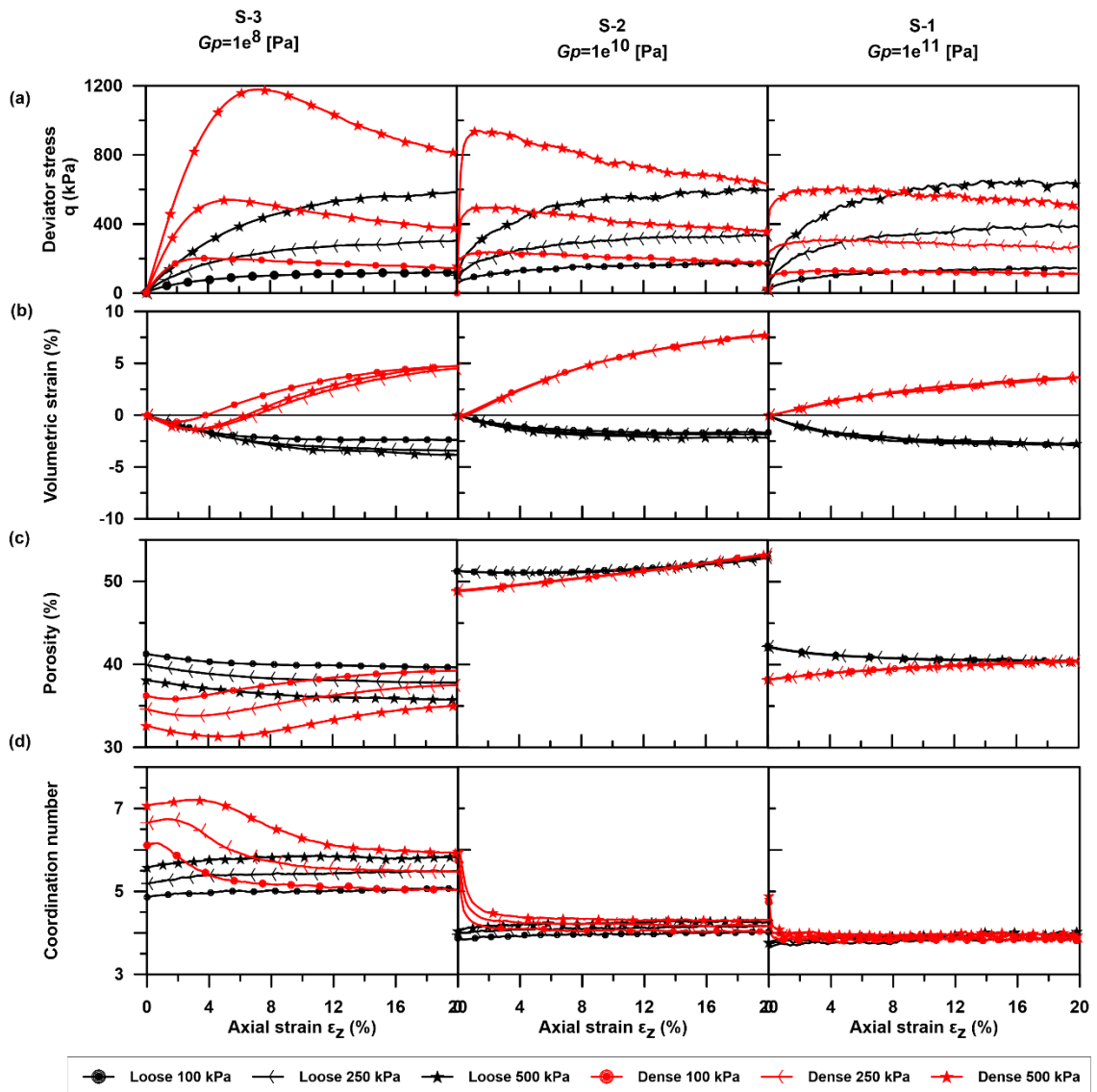
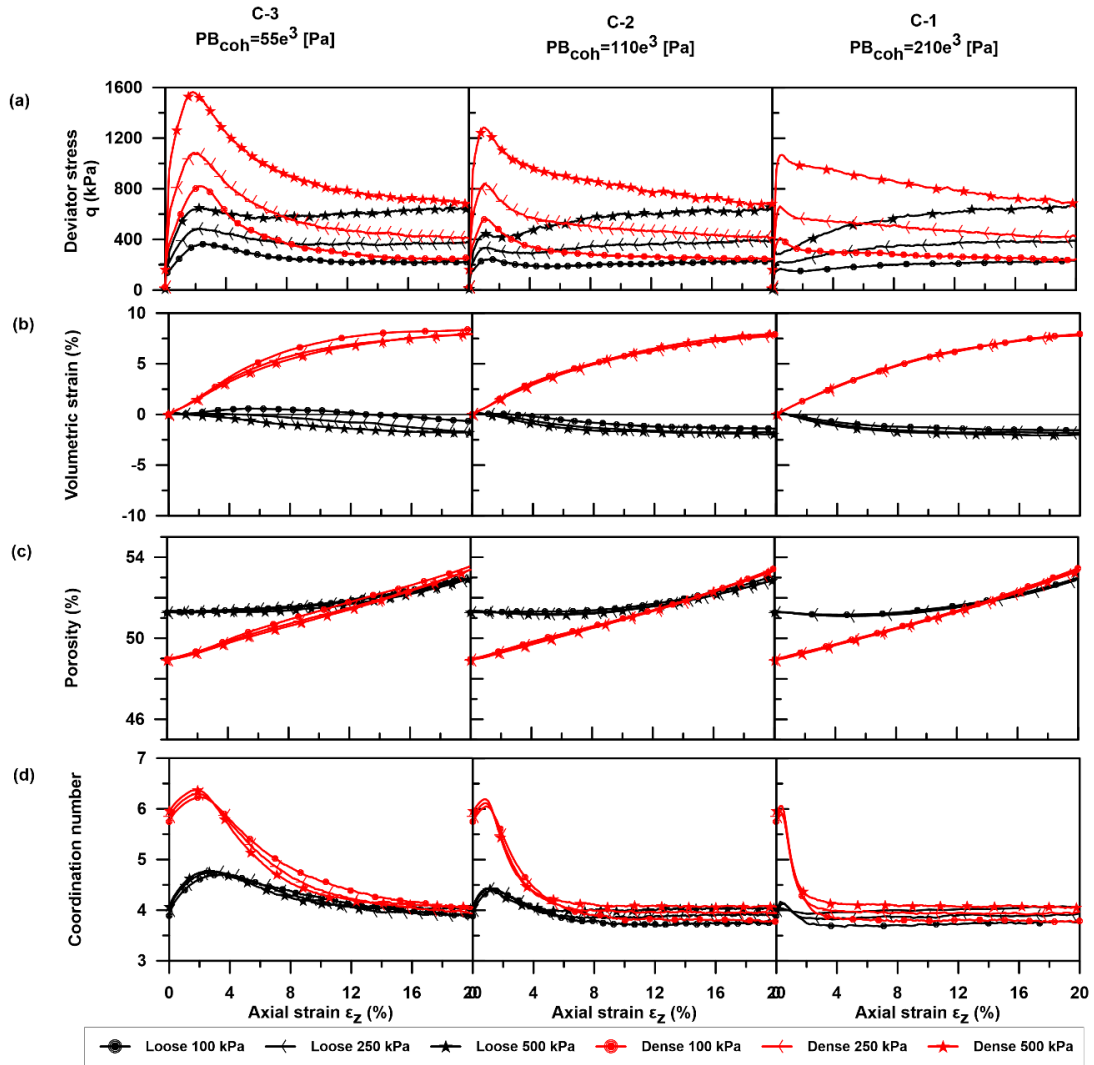


Figure 4.3. Triaxial tests results for 'sand' samples presented as (a) the deviator stress, (b) the volumetric strain, (c) the porosity and (d) the coordination number over the axial strain; the micro-shear modulus ( $G_p$ ) is increasing from left to right. Black lines represent loose packed samples and red lines represent dense packed samples. Each confining stress is represented by a different symbol for 100, 250 and 500 kPa.



*Figure 4.4. Triaxial tests results for ‘clay’ samples presented as (a) the deviator stress, (b) the volumetric strain, (c) the porosity and (d) the coordination number over the axial strain; the micro-cohesive bond strength ( $PB_{coh}$ ) is increasing from left to right. Black lines represent loose packed samples and red lines represent dense packed samples. Each confining stress is represented by a different symbol for 100, 250 and 500 kPa.*

#### 4.4.2. Volumetric Strain, Porosity and Coordination Number

Volumetric strain results for all tests are presented in Figures 4.3b and 4.4b. The general trend observed for both ‘sand’ and ‘clay’ loose samples showed a nonlinear negative volumetric change—a volumetric contraction. Regardless of the value of the assigned micro-parameters in all samples, the values decreased to 2.5% of volumetric strain. An exception were the loose ‘clay’ samples with low micro-cohesive bond strength ( $PB_{coh} = 55e^3$  Pa). The loose ‘clay’ showed a slight initial increase in volumetric strain, yet after

10% of strain the trend changed and showed a decrease in volumetric strain to 1–2% (Figure 4.4b).

The trend of volumetric strain observed for densely packed samples was generally similar for both ‘sand’ and ‘clay’ and showed a nonlinear positive volumetric change—a volumetric dilatation. For ‘sand’ samples, the values increased up to 5% or 8% of volumetric strain (Figure 4.3b). For ‘clay’ samples, regardless of the value of the assigned micro-cohesive bond strength ( $PB_{coh}$ ), all samples showed a similar trend of volumetric increases up to 8% of volumetric strain (Figure 4.4b). In general, under different confining stresses, the trend observed is similar for most samples. A slightly different trend was observed for ‘sand’ samples with a low micro-shear modulus ( $G_p = 1e^8$  Pa), where a volumetric decrease was seen up to 2% of strain, followed by a volumetric strain increase.

The results observed for average porosity changes for loose ‘sand’ samples showed a decrease in porosity of about 1–3% (Figure 4.3c) for low and high  $G_p$  values, whereas, for medium  $G_p$  values, little change in porosity was observed. Densely packed ‘sand’ samples showed porosity changes in most samples, demonstrating an increase of 2–4%. Porosity results for samples with a low micro-shear modulus ( $G_p = 1e^8$  Pa), showed a different trend where a porosity decrease of 2% of strain was followed by a porosity increase of up to 4%. ‘Clay’ samples showed a general trend of increasing porosity. Loose ‘clay’ samples showed a slight change in porosity, increasing by about 1% from the initial value. Densely packed ‘clay’ samples showed a larger increase in porosity of 4% from the initial value.

Coordination numbers are presented for ‘sand’ and ‘clay’ in Figures 4.3d and 4.4d, respectively, and represent the average number of contacts per particle. In general, as high strain is reached in the triaxial test ( $\epsilon_z = 20\%$ ), most samples, regardless of their initial average coordination number, reached an average value of four contacts per particle. Loose ‘sand’ samples showed a slight averaged increase in the mean coordination number of 0.2 contacts per particle. Densely packed ‘sand’ samples showed a decrease in the mean coordination number of one to two contacts per particle. Exceptional behaviour was observed for both loose and densely packed ‘sand’ samples with a low micro-shear modulus ( $G_p = 1e^8$  Pa), where the initial and the final mean coordination number were higher than in other samples. ‘Clay’ samples showed a similar trend for both loose and densely packed samples, which varied only in their rate of change at similar strain values. An increase in the mean

coordination number (from 0.2 to 0.8 average contacts per particle) was observed under low strain (<5%). The average increase in the number of contacts per particle is inverse to the samples' micro-cohesive bond strength ( $PB_{coh}$ ). The stronger the micro-cohesive bond strength ( $PB_{coh}$ ), the smaller the change in the mean number of contacts per particle. As strain increases (>5%), the mean coordination number decreases down to an average of four contacts per particle. The range of the decrease in the mean number of contacts per particle is of two contacts per particle for dense samples and 0.2 to 0.8 contacts per particle for loose samples. The decrease in the coordination number of both loose and densely packed 'clays' to a similar averaged coordination number value, is a result of bond breakage, leading to local dilation even in the loose samples, along a with similar coefficient of friction.

#### 4.4.3. Strain Localization

Strain localization is observed in all samples, as indicated by the maximum positive or negative gradient of relative displacement values (Figure 4.5). Between the yield (1) to peak (2) stages, a low magnitude of deformation appears along the sample (Figure 4.5a). Elongated narrow zones of high relative displacements indicate the position of localized slip zones (Figure 4.5b–e; black lines).

The gradient of relative displacement in loose 'sand' samples appears as a low magnitude of deformation of very discrete and short localized slip planes (Figure 4.5b). Localized deformation seems to occur at the perimeters of the sample.

In densely packed 'sand' (Figure 4.5c), a higher magnitude of deformations occurs along several elongated zones. These appear as developed slip planes, with higher gradient values, which occur at the centre of the sample as well.

In loose 'clay' samples, well-defined zones of strain localization occur under smaller strain values ( $\epsilon_z = 12\%$ ) and are limited to the perimeter of the sample (Figure 4.5d). As bonds break, the mode of failure alternates between slip along shear planes and focused areas of compression (Supplementary Video 4.S3). In densely packed 'clay' samples, strain was widely distributed within the sample with both maximum positive and negative gradient values (Figure 4.5e). The number of shear planes is highest in this material.

The post-peak behaviour presented in all samples shows two emerging patterns that follow the pre-conditioned dense/loose packing. For loose samples, strain is localized to

distinct areas in Figure 4.5b,d, whereas a wider area of strain localization is observed in the densely packed samples in Figure 4.5c,e.

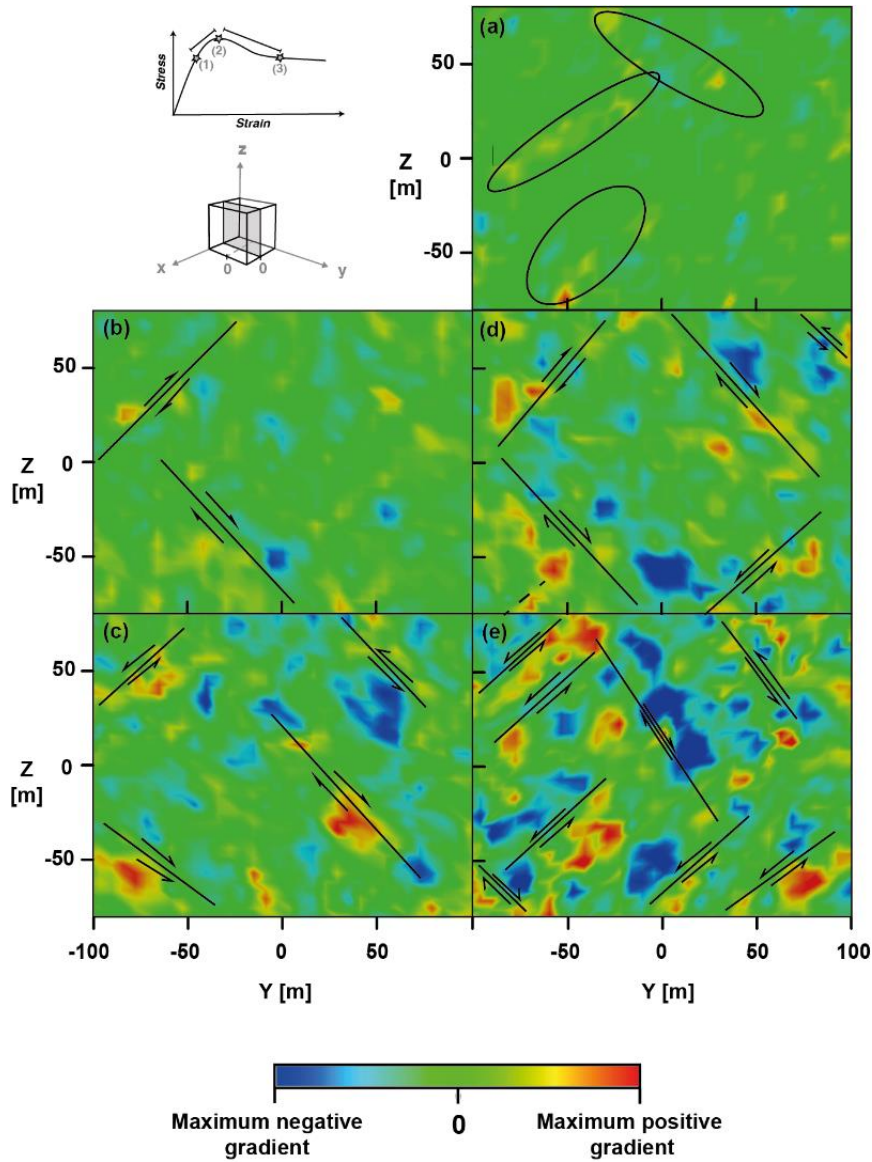


**Figure 4.5.** Strain localization visualized for deformation stages. Deformation stages are defined between points (1) and (3) along a typical stress–strain curve, where (1) is the yield stress, (2) the peak stress and (3) the post-peak situation. Deformation is imaged along a vertical cross section of the 3D test (location indicated by the grey cross section). (a) Initiation of strain localization highlighted by oval circles (between stages 1 and 2, Experiment DC-2). Localization is presented for four samples tested under confining stress  $\sigma_{2,3} = 250$  kPa. (b) Experiment LS-2, loose 'sand' ( $G_p = 1e^{10}$  Pa) taken after 17% of strain. (c) Experiment DS-2, dense 'sand' ( $G_p = 1e^{10}$  Pa) taken after 17% of strain. (d) Experiment LC-2, loose 'clay' ( $PB_{coh} = 110e^3$  Pa) taken after 12% of strain. (e) Experiment DC-2, dense 'clay' ( $PB_{coh} = 110e^3$  Pa) taken after 12% of strain. Black lines indicate selected areas of strain localization further explained in the text.

## 4.5. Discussion

### 4.5.1. Parametrization of Numerical ‘Sediments’

Each tested parametrization level influenced the numerical ‘sediments’ to a different extent. The three parametrization levels — (I) endmember material strength (namely, micro-parameter  $G_p, PB_{coh}$ ), (II) burial depth and (III) initial consolidation state (loose vs. densely packed)—have first, second and third orders of influence on the material’s mechanical behaviour, accordingly.

Changing an intrinsic micro-parameter affects the ability of each material to carry stress under increasing strain conditions. For loose ‘sand’ samples, higher  $G_p$  contributed to an increased macroscopic coefficient of friction and a higher peak shear strength due to strain hardening (Figure 4.3a, Table 4.2). An opposite trend was observed for densely packed ‘sand’ samples. A lower peak shear strength was observed with a decrease in the macroscopic coefficient of friction due to a higher  $G_p$  value. This inverse relationship could be due to a change in the micro-fabric (structure of the particles) during the confining pressure stage. Higher  $G_p$  values created stiffer particles, which reduced the average contacts between particles; thus, a lower average coordination number generated fewer contact forces. This relationship between the micro-shear modulus (stiffness) and the contact forces was indicated by Lommen (2014). However, here, we additionally observed the effect of the sample packing density, which showed that, due to the initial dense consolidation state and the increase in the stiffness, the stiffer material fails under smaller strains.

Both loose and dense ‘clay’ samples presented an inverse trend to the expected impact: under higher applied micro-cohesive bond strength ( $PB_{coh}$ ), the resulting material failed under smaller strain levels (Figure 4.4a) and the shear strength and bulk cohesion decreased (Table 4.2). Cheung et al. (2013) showed that a high bond multiplier ( $\lambda = 1$ , Section 4.3.2.) resulted in an increased material stiffness and peak strength. In our experiments, we assigned a very low bond-to-contact stiffness ratio to maintain low stiffness (see Section 4.3.2.); however, the results presented the opposite. We suggest that the imposed bond multiplier is the micro-parameter most likely affecting the samples’ stiffness. Overall, the ‘clay’ behaviour results present an inverse relationship between the bond micro-strength and the final material strength, which results from the bond multiplier ( $\lambda$ ). The higher assigned micro-cohesive bond strength generates a weaker

material—as the bond micro-strength increases, the bulk material shows a decrease in the cohesion and peak shear stress.

The three tested confining stresses (proportional to shallow burial depth of sediments) produced, within each material setup (e.g., DS-1), an increased peak shear strength, accordingly (Table 4.2). Moreover, in agreement with the inverse relationship seen above for densely packed ‘sands’ and ‘clays’, higher peak shear strength values were observed in samples with lower applied micro-properties ( $G_p$  or  $PB_{coh}$ ).

Differences between loose and dense packing are apparent from the porosity, volumetric strain and coordination number results (Figures 4.3b–d and 4.4b–d). These results exhibit differences between loose and dense packing; however, no influence was observed due to changes in the confining pressure. In particular, the initial mean coordination number displays a clear difference between loose and dense ‘sediments’. In densely packed sediments, more particles are in contact than in loosely packed samples. The similar final mean coordination number (approx. 4), observed in most tests (including both dense and loose ‘sediments’), is related to (A) the uniform particle size distribution and (B) the micro coefficient of friction. The coordination number is a function of the range of particle sizes, and the ratio between the mean particle size and the smallest and biggest particle sizes. Here, this ratio was set to 30% following Saltzer and Pollard (1992), i.e., the particle size distribution was uniform throughout the tests. The applied coefficient of friction was also similar in all tests, resulting in similar final mean coordination numbers and post-peak mechanical behaviour (i.e., residual strength). The endmembers’ response to loose and dense packing is visible in the post-peak strain localization gradient (Figure 4.5) and the peak shear strength (Table 4.2). Loose ‘sand’ samples show deformation modes of strain hardening that are controlled mainly by compaction. The deformation appears in restricted areas of the sample, closer to the boundaries. The high stiffness and consolidation of densely packed ‘sand’, on the other hand, shows deformation controlled by dilatation. In ‘clay’ samples, both loosely and densely packed samples exhibit dilation due to bond breakage and particle movement, which are initiated under increasing stress. As stress increases, strain localization is increasingly concentrated where bonds break, and the resulting shear and deformation occurs along specific diagonal lines.

#### *4.5.2. Classification of the Granular Assemblage*

The ability to simulate the two endmembers’ mechanical behaviour—cohesionless and cohesive—is important due to their different deformation behaviours in laboratory

experiments (Eisenstadt and Sims, 2005). For samples with a Hertz–Mindlin contact model, a ‘sand’-like frictional-dependent deformational behaviour is observed, as the diverging failure envelopes indicate weakening due to a reduction in the friction coefficient (Table 4.2). For samples with a linear parallel-bond contact model, a ‘clay’-like cohesive deformational behaviour is seen, as the sub-parallel failure envelopes indicate a weakening due to a reduction in cohesion (Table 4.2).

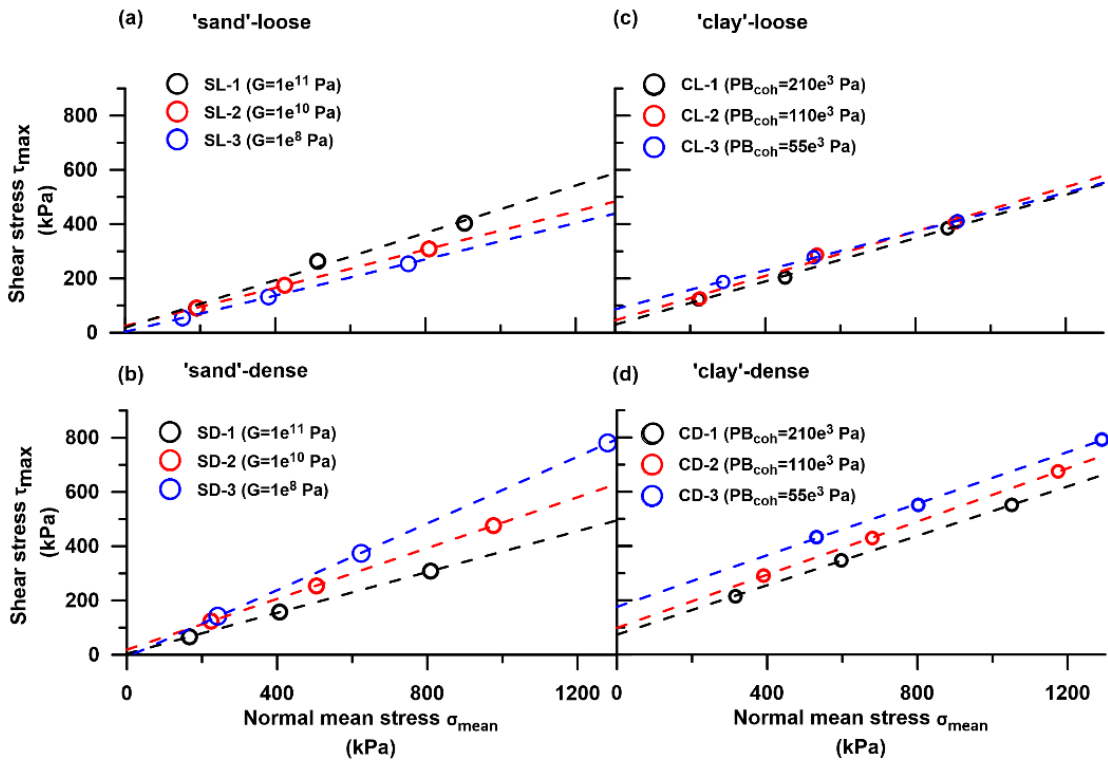
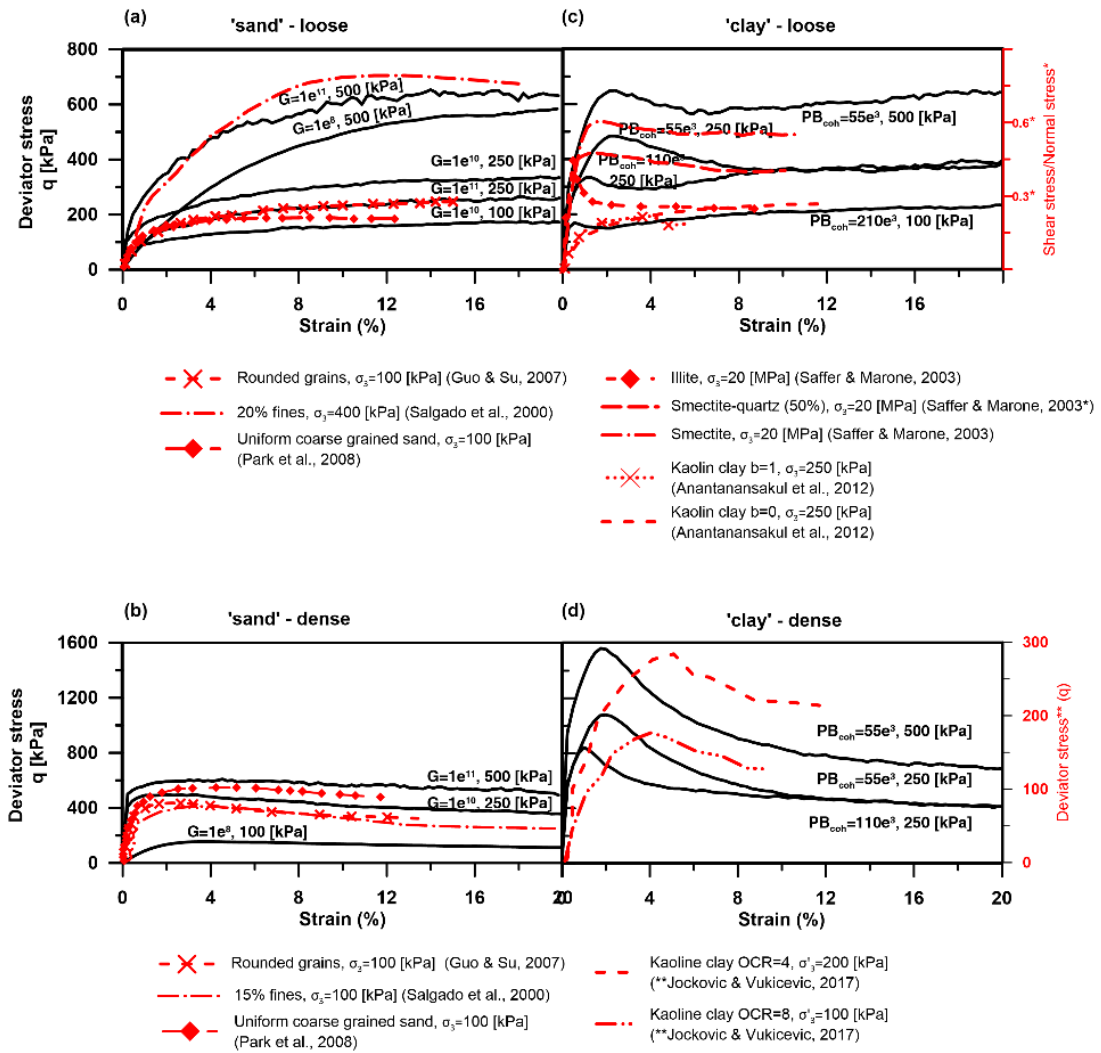


Figure 4.6. Modified Mohr–Coulomb failure envelopes for (a) loose ‘sand’ (b) dense ‘sand’ (c) loose ‘clay’ and (d) dense ‘clay’ samples. Circles denote the differential peak shear strength measured in each test under the appropriate normal stress.

It should be noted that, for loose and densely packed ‘sand’ samples, bulk cohesion values were linearly extrapolated from the failure envelopes presenting low (3 kPa) to medium (33 kPa) cohesion values (see Table 4.2), though cohesive forces or bonds are not assigned in the Hertz–Mindlin contact model. Schellart (2000) suggested that these are the result of a linear extrapolation of the Mohr–Coulomb failure envelope and that the envelope has a concave upwards shape rather than a straight line. Therefore, the extrapolated cohesion value should be neglected from the ‘sand’ samples’ macro-properties.

In some experiments, the applied micro-property is inversely proportional to the resulting macro-properties (see Table 4.2) and the resulting shear strength is proportional to the applied confining stress and consolidation state. Therefore, once the relationship between micro- and macro-properties is established, it is possible to use the new numerical material.

The modelled mechanical behaviour is compatible with a range of results from analogue experiments, as seen in Figure 4.7. ‘Sand’ experiments are compared with laboratory tests (Figure 4.7a,b) of uniformly distributed sand (loose and densely packed) (Park et al., 2008), rounded sand (van Gent et al., 2010) and varying amounts of fines within sand (Salgado et al., 2000). This suggests that a high micro-shear modulus ( $G_p$ ) can simulate a loose, rounded and uniformly distributed sand sample under low stresses, or loose sand with up to 20% fines content under high stresses. In a densely packed state (overconsolidation), medium values of the micro-shear modulus can also be used.



**Figure 4.7.** A comparison between the mechanical behaviour (stress–strain) of the numerical results and laboratory experiments of sediments. Laboratory experiments of loose and dense sands and normally consolidated and overconsolidated clays are respectively compared to the numerical results. (a) loose ‘sand’ (b) dense ‘sand’ (c) loose ‘clay’ (d) dense ‘clay’. Solid black lines are results from the DEM simulations, found to resemble empirical lab results. Above each line, the micro-parameter size and confining stress are detailed. Dashed and dotted red lines are results of empirical triaxial tests on natural sediments. Data from Guo and Su [3] were recalculated to fit the deviatoric stress axis. For other data ([65,66]), the original y-axis is present on the right-hand side (red labels).

The modelled loose ‘clay’ is compared with analogue tests of different normally consolidated clays (Saffer and Marone, 2003) or normally consolidated clay particle anisotropy (Anantanasakul et al., 2012) (Figure 4.7c). The densely packed ‘clay’ results are compared with over-consolidated kaolinite tests exhibiting different overconsolidation ratios (Jocković and Vukićević, 2017) (Over Consolidation Ratio-OCR in Figure 4.7d). In the ‘clay’, the applied micro-cohesive bond strength ( $PB_{coh}$ ) influences the timing (amount

of strain) at which peak shear stress is reached. Strengthening, which appears in some of the normally consolidated ‘clay’ experiments, is analogous to the breakage of aggregates (peak) and then the reorientation of platy particles. Anantanasakul et al. (2012) demonstrated that peak stress could form due to the anisotropy of kaolinite particles during deposition. As the platy clay particles are parallel or semi-parallel to the main stress ( $\sigma_1$ ), strain hardening occurs as the platy particles reorient, thus increasing shear resistance until peak shear strength is reached. The anisotropy of clayey sediments was also noted by Hicher et al. (2000) as a source of increased stiffness and strength in clays.

The applied medium and low micro-cohesive bond strengths ( $PB_{coh}$ ) of densely packed ‘clay’ are best comparable to analogue experiments of overconsolidated clay. Empirical tests of overconsolidated (i.e., dense) clay indicate that a higher overconsolidation ratio of clay requires a lower loading stress to reach peak shear strength (Jocković and Vukićević, 2017). This is most likely due to the reorientation of the platy particles that already occurred under previous sediment loading (Hattab and Fleureau, 2010), leading to a rapid and smooth transition from contractive to dilative behaviour. The modelled densely packed ‘clay’ presents a comparable mechanical behaviour; however, peak shear strength occurs under lower strains.

The abovementioned laboratory experiments have demonstrated the varied response of clay minerals as well as the response of intact and remoulded clay to load. The primary mechanism suggested to generate failure in clay sediments is particle reorientation, forming a shear zone as the load increases (Djéran-Maigre et al., 1998). However, Hattab et al. (Hattab et al., 2015) proposed that the mechanism of particle reorientation also depends on the content of specific clay minerals, showing that a shear plane is more likely to develop in montmorillonite as opposed to kaolinite. The stiffer and more brittle behaviour of clay also results from remoulding and mottling processes (Mitchell and Soga, 2005). Although clay particle reorientation was not simulated in our experiments, the shear strength of the modelled overconsolidated clay (i.e., dense clay) can be related to this process. Such mechanical behaviour can also be used for various process simulations.

#### *4.5.3. Application*

The range of current simulated materials provide an opportunity to examine sediments with varying shear strengths and particle arrangements. Most commonly, in nature, post depositional processes lead to a change in shear strength. Sediments develop shear strength primarily from the particles’ composition (e.g., mineralogy, shape, size distribution,

roughness) and the initial depositional micro-fabric (Mitchell and Soga, 2005). Post-depositional processes affect the sediments' shear strength due to both spatial and temporal changes in the sediments' micro-fabric, mostly through consolidation (Bennett et al., 1981). These effects, generated in nature (due to variations in porosity, grain size distribution and friction coefficient), can be used to simulate the resulting sediments of post depositional processes and the deformation, such as discrete or distributed shear zones, as seen in Figure 4.5. These are applied in the form of an increased shear strength, different mechanical behaviour and consolidation states.

Simulating changes in shear strength in sediments (without changes in depth or consolidation state) can be done by changing the micro-parameter  $G_p$  in sand or  $PB_{coh}$  in clay. The resulting new material can be used to simulate and compare the mechanical behaviours of sediments that experienced a change in their initial shear strength (e.g., following different levels of bioturbation in shallow sediments). A process such as bioturbation, which remoulds the sediment, can modify the sediments' shear strength (Locat et al., 2002). During bioturbation, water is removed, and the sediment shear strength is increased (Locat et al., 2002). Alternatively, bioturbation can break the cohesive bonds in clay sediments and lead to the decreased shear strength of the sediment (Davis, 1993). Utilizing the  $PB_{coh}$  micro-parameter also allows for the simulation of the influence of shear strength due to microbial organic (Perret et al., 1995) or calcite cement (Feng et al., 2017) following early diagenetic processes.

The numerical sediments can simulate sediments in which both shear strength and consolidation states changed post deposition (without a change in depth) by utilizing the micro-property ( $G_p$  or  $PB_{coh}$ ) and an initial consolidation state via the initial micro-coefficient of friction ( $\mu_p$ ). The new material can simulate the numerical behavior of sediments that have undergone strengthening through various actions such as waves or seismic activity, and their consolidation changes as a result of the process.

Finally, the numerical materials can simulate sediments in which shear strength is being temporally or spatially changed by utilizing all three parameters tested here, namely introducing a micro-property value ( $G_p$  or  $PB_{coh}$ ) for a specific mechanical behavior, applying an initial consolidation state via the initial micro-coefficient of friction ( $\mu_p$ ), and applying a burial depth through the initial confining pressure. Continuous or episodic depositional processes, such as changes in sedimentation rate, the loading and unloading of ice sheets due to glaciation cycles, and mass movements contribute to the increase in

shear strength with time and depth. As the vertical stress grows due to increased load, sediments undergo consolidation and, consequently, the shear strength of normally consolidated sediments increases with depth almost linearly (Ikari and Kopf, 2015; Perret et al., 1995). However, in places where a mass movement occurs, overconsolidated sediments may occur in shallow depths due to unroofing (Ikari and Kopf, 2015). The above-presented numerical range will enable a quick setup of specific sediment behaviours for the simulation of various deformational processes in 3D.

#### 4.6. Conclusions

A series of 3D triaxial numerical experiments simulated the mechanical behaviour of two sediment endmembers—cohesionless and cohesive. Each endmember also presented an increased shear strength under increasing burial stress and a dense consolidation state. These results showed good agreement with laboratory tests of natural sediments under varying consolidation states and a range of compositions. It is thus suggested that the resulting shear strength in natural sediments, due to depositional and post depositional processes, can be simulated by varying the size of a micro-property (i.e., the micro-shear modulus for cohesionless sediments and micro-cohesive bond strength for cohesive sediments) without a complex particle shape or complex contact law for cohesive strength. This approach can reduce the extent of material calibration and enable studies to generate numerical sediments according to a desired process and geological history (i.e., to generate sediments that have undergone increasing or decreasing shear strength processes).

In order to apply our results in future simulations of sediments, one to three levels of parametrization should be used. The level of parametrization sets the order of influence of the sediments' mechanical behaviour under an applied stress. Prior to the parametrization, the appropriate contact model should be considered and set to produce cohesionless or cohesive numerical sediments.

In order to simulate sediments with the first order of influence (i.e., material shear strength), it is recommended to apply a high or a low micro-parameter ( $G_p$  for sands and  $PB_{coh}$  for clays). This will enable the simulation of shallow sediments, for which only shear strength has changed—such as inherited shear strength due to original deposited sediment micro-fabric, or shear strength altered by bioturbation or early diagenesis cementation.

In order to simulate sediments with a second order of influence (i.e., consolidation), it is recommended to use both the initial micro coefficient of friction to generate loose or dense

sediment packing and, additionally, to apply a high or low micro-parameter. This parametrization simulates sediments for which a change in consolidation state has also occurred—volumetric change as well as a change in shear strength, such as after a strengthening event.

In order to simulate sediments with a third order of influence—burial depth—it is recommended to use all three parameters, i.e., the abovementioned parameters and a confining stress appropriate to the burial depth. This parametrization simulates sediments for which a change in the burial depth or a cycle of burial and exposure has occurred, such as after deglaciation or a mass movement event.

**Supplementary Materials:** The following are available online at [www.mdpi.com/2227-9717/8/10/1252/s1](http://www.mdpi.com/2227-9717/8/10/1252/s1), Figure 4.S1: Self-similarity test, Figure 4.S2: Stress rate, Video S1: Sample LS-2 3D deformation, Video S2: Sample DS-2 3D deformation, Video S3: Sample LC-2 3D deformation, Video S4: Sample DC-2 3D deformation.

**Author Contributions:** Conceptualization, H.E. and K.H.; methodology, H.E. and L.S.; validation, H.E. and L.S.; formal analysis, H.E.; writing—original draft preparation, H.E.; writing—review and editing, H.E.; K.H.; R.B.; L.S.; and U.t.B.; visualization, H.E.; supervision, K.H; R.B. and U.t.B. All authors have read and agreed to the published version of the manuscript.

**Funding:** This research received no external funding.

**Acknowledgments:** HE would like to thank Jannis Kuhlmann and Ricarda Gatter for their review and valuable comments. In addition, we thank Adrian Garcia and three anonymous reviewers for their useful comments. Use of trade, product, or firm names is for descriptive purposes only and does not imply endorsement by the U.S. government.

**Conflicts of Interest:** The authors declare no conflicts of interest.

## Appendix 4A: DEM Force–Displacement Calculation

Particles that interact are allowed to overlap according to the soft particle approach, in which, geometrically, particles remain rigid and only small deformations occur at contact points [7,30]. The particle properties as well as the applied boundary conditions, e.g., gravity, determine the magnitude of the particles' overlap ( $\delta$ , Figure 4.1), which, in turn, is used to calculate the forces that act on individual particle contacts. Each contact relates to both the normal  $F_n$  and tangential  $F_s$  forces.

The forces are calculated for 3D spheres in the case of an elastoplastic contact model or material behaviour, respectively [8,30], via:

$$F_n = k_{p(n)} \cdot \delta_n^{3/2}, \quad (A1)$$

$$F_s = k_{p(s)} \cdot \delta_s^{3/2}, \quad (A2)$$

where  $F_n$  and  $F_s$  are the normal and tangential forces acting at each particle contact point;  $k_{n,p}$  and  $k_{s,p}$  are the normal and tangential stiffnesses, respectively, and  $\delta_n^{3/2}$  and  $\delta_s^{3/2}$  are the particle overlap in the normal and tangential directions as well (Figure 4.1).

To evaluate the subsequent motion of a particle, Newton's second law is used. Therefore, all normal  $F_n$  and shear  $F_s$  forces are summed up for each individual particle to calculate a so-called net force  $F_n$  which then reveals the acceleration and potential subsequent displacement of each individual particle. As the calculation is repeated, in order to dissipate the energy in the system, at each time step, a local damping component (Table 4.1, damp) is applied.

To allow particle contacts to break and subsequently let particles slip one past the other, a slip condition is introduced. The slip condition is defined as a critical shear force value  $F_{s(max)}$ , which, once exceeded, means that slip will occur:

$$F_{s(max)} = \mu_p \cdot F_n, \quad (4.A3)$$

where  $F_n$  is the normal force at a contact point and  $\mu_p$  is the minimum friction coefficient of the two particles in contact. It should be noted that the shear forces at each contact point add up at each calculation step. When the added shear force is  $F_{s,p} > F_{s(max)}$ , sliding occurs between two particles and the contact breaks. Following this, it is possible to evaluate the maximum shear stress of the bulk numerical material (the overall particles assemblage) via the Mohr–Coulomb criterion:

$$\tau_{(max)} = C + (\mu \cdot \sigma_n), \quad (4.A4)$$

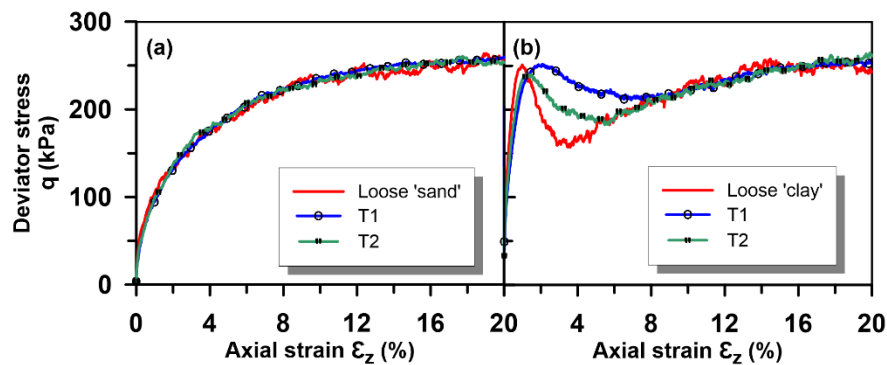
where  $\tau_{(max)}$  is the maximum shear strength the bulk material can sustain,  $C$  is the cohesion,  $\mu$  is the bulk material friction coefficient and  $\sigma_n$  is the normal stress.

To summarize, in each calculation step, the simulation starts by detecting particles that are in contact. The forces exerted by particles are then calculated according to selected contact models based on the particles' overlap and micro-properties via Equations (A1) and (A2). The newly calculated contact forces are combined for each particle and used to calculate subsequent particle movements based on Newton's second law of motion:

$$F_N = \rho_p \left(\frac{4}{3}\right) \pi R_p^3 a, \quad (4.A5)$$

where  $\rho_p$  is a particle's density,  $R_p$  is a particle's radius and  $a$  is the acceleration. Particles' velocity and displacement, as well as the resultant new particle contacts, are updated at the end of each iteration [30].

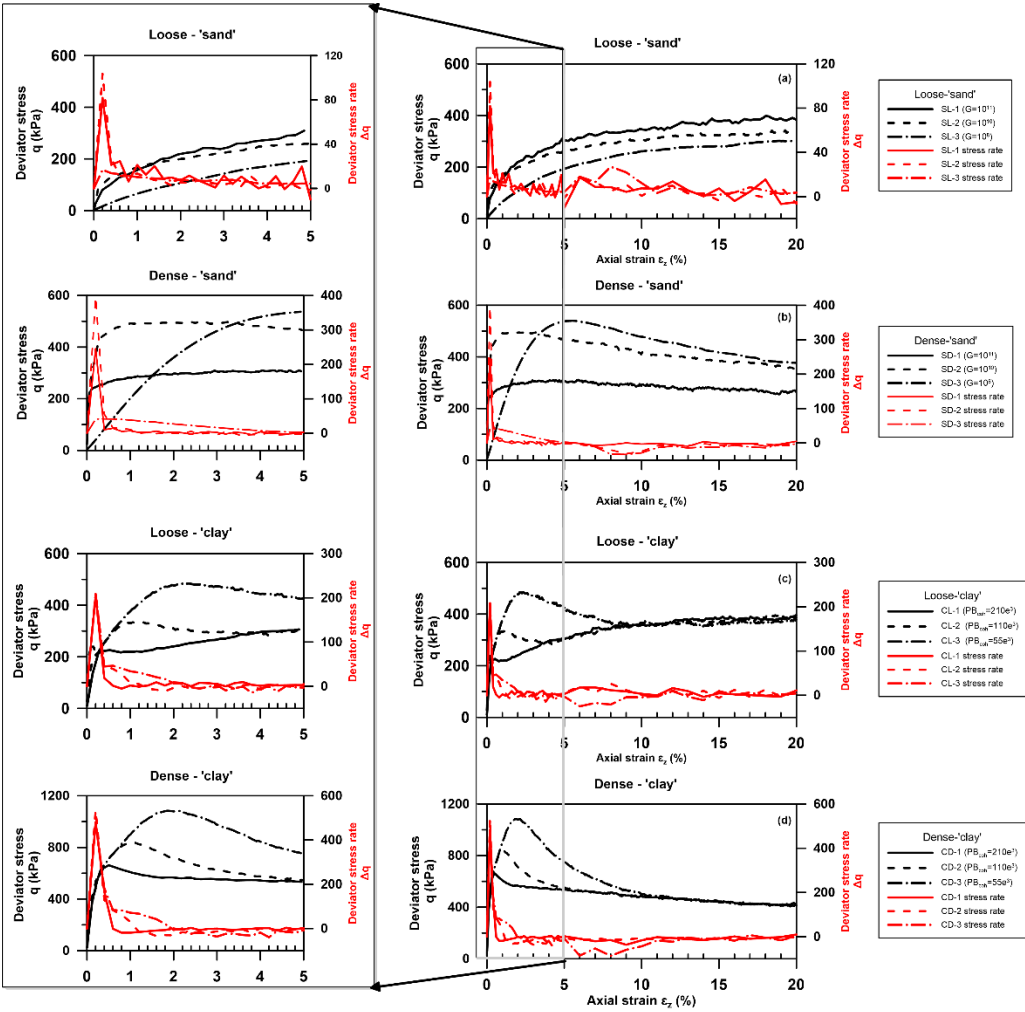
#### Appendix 4B – Supplementary material



**Supplementary figure 4.S1.** A self-similarity test was performed to assess results with the software internal model meter scale units and to show that the numerical results are not size dependent and can be further compared with laboratory tests. We carried self-similarity tests for each endmember type, by using the same triaxial setup - fixing the volume constant ( $220 \times 220 \times 220$  [m]) while reducing the particle radius by a predefined factor.  $R_{\text{original}}$  is the range of radii presented in table 4.1. In test 1 (T1), the particle's radius was reduced by a factor of two (i.e.,  $R_{\text{original}}/2$ ) resulting in a range of  $1.85 < R < 2.75$ . In test (T2), the particle's radius was reduced by a factor of 1.33 (i.e.,  $R_{\text{original}}/1.33$ ) resulting in a range of  $2.77 < R < 4.12$ . (Note: any smaller factor would have produced more than 2 million particles within the volume, which is beyond the limit of computer calculation power).

The results in figure 4.S1 are presented for the tests performed under a confining stress of 250 kPa. (a) 'Sand' endmember. The red line indicates the samples tested with  $R_{\text{original}}$ , blue line for test T1 and green line for test T2. (b) 'Clay' endmember. The red line indicates the samples

tested with Roriginal, blue line for test T1 and green line for test T2. Loose-‘sand’ tests show a very similar stress-strain behaviour whereas loose-‘clay’ tests similarity is only apparent in the peak value and residual stress. It appears that in ‘clay’ samples the cohesive strength is influenced by the rate at which the bonds breaks, once the peak shear strength is reached. As we mainly focused on the peak behaviour and further deformation was evaluated over strain intervals, we find this similarity satisfactory for the purpose of the current study.



**Supplementary figure 4.S2.** The stress rate was calculated for intervals of 1% of strain. Results are presented for samples tested under confining stress ( $\sigma_3=$ ) 250 [kPa]. Stress-strain curves are in black lines and stress rate in red lines. (a) Loose-‘sand’ (b) Dense-‘sand’ (c) Loose-‘clay’ and (d) Dense-‘clay’ samples. The rectangular inset in a-d represents zooming-in for the behaviour between 0-5 % of strain in the figures on the left for each material.

Supplementary videos 4.S1-4. Animation of the formation and progress of deformation within a 3D diagonal cross section for each of the representative experiments in figure 4.5 (LS-2; DS-2; LC-2; DC-2). In each animation on the left: the z-component of the gradient is presented and on the right: the total (vector) gradient is presented. Here, the gradient was calculated at intervals of 1% Strain, whereas in figure 4.5, the gradient was calculated and presented for an interval of major deformation, namely between peak and post peak which represents an interval of 5-7% of strain. Areas of maximum and minimum gradient (red and blue respectively) highlight the zones in which deformation will focus and eventually generate slip planes. Comparing the vector and z-component of the gradient animations, highlights that most of the localization is originating from movement along the z-axes.

Video S1: Sample SL-2 (confining stress of 250 [kPa]). Strain localization is initially observed in the centre of the sample and demonstrates the compression, which occurs at low strain. As the deformation progresses it migrates away from the centre of the samples towards the walls.

Video S2: Sample SD-2 (confining stress of [250 kPa]). Strain localization also occurs initially around the centre of the sample. As deformation progresses, shear zones form presenting an activation and reactivation behaviour, possibly due to the dense state.

Video S3: Sample CL-2 (confining stress of 250 [kPa]). Strain localization is resulting from two modes of failure. One mode of failure resulting from bonds breaking forming slip planes and shear zones. A second mode of failure is localized areas in which compression can occur. These deformation behaviours are activated/reactivated as deformation progresses.

Video S4: Sample CD-2 (confining stress of [250 kPa]). Strain localization also develops here from areas where bonds break however this occurs all over the sample and as deformation progresses larger- elongated areas of deformation occurs all over the sample.



# Chapter 5

## Submarine mass-movements preconditioned by sediments shear strength: Insights from 3D numerical modelling

**Authors:** Hadar Elyashiv (MARUM, University of Bremen, Germany & the Dr. Moses Strauss Department of Marine Geosciences, University of Haifa, Israel)  
Uri ten Brink (U.S. Geological Survey, Woods Hole Coastal and Marine Science Centre, USA)  
Revital Bookman (Dr. Moses Strauss Department of Marine Geosciences, University of Haifa, Israel)  
Katrin Huhn (MARUM, University of Bremen, Germany)

**Status:** Submitted, to: Marine Geology

# 5. Submarine mass-movements preconditioned by sediments shear strength: Insights from 3D numerical modelling

---

## Abstract

Sediments shear strength plays a key role in the initiation of submarine mass movements. Its effects on the sliding mass volume, frequency and location was so far determined from case studies and subsequent statistical analysis. Using the Discrete Elements Method, we designed a 3D numerical slope model to observe the shear strength effects on the development of submarine mass movements. We characterized two sediment types - sand and clay numerically, and assigned each of them low and high shear strength; in total, four models. Model geometry followed analogue sandbox experimental designs, where mass movements are triggered by slope oversteepening. In all models, slope development generated a segmentation to an upper and lower slope. Mass movements formed locally in unstable slope areas. Large-scale mass movements developed in three of the models (high strength sand and high and low strength clay), forming a single or a slide complex, covering the upper or entire slope. Under the modelled conditions and as slope susceptibility-to-failure increased, large-scale slope failure formed in over-consolidated (high shear strength) “sandy” sediments. In normally consolidated (low shear strength) “clayey” sediments, as slope susceptibility-to-failure increased, complex and massive slope failure was observed. The results suggest that both sediments type and shear strength influence the distribution of slope instability. Based on the compatibility of our results with field observations, these four conceptual models provide an independent understanding of the link between sediments shear strength and the potential of continental margins to produce large-scale mass movements.

## Keywords

Submarine mass movements, Slope instability, susceptibility-to-failure, Discrete Element numerical modelling, Shear strength

## 5.1. Introduction

### 5.1.1. *Submarine mass movements*

Submarine mass movements, which result from slope instabilities, can transport significant volumes of up to thousands of cubic kilometres of sediment from the continental slope to the deep ocean (Clare et al., 2018; Lee et al., 2007; Vanneste et al., 2014). They pose a major threat to marine and submarine infrastructure (Pope et al., 2017; Talling, 2014), and can form destructive tsunamis that threaten coastal populations (Brothers et al., 2016; Carvajal et al., 2019; Parsons et al., 2014). Additionally, their voluminous deposits may form important oil and gas reservoirs for the hydrocarbon industry (Moernaut et al., 2020) and can promote gas seepage into the seafloor and water column.

Extensive mapping of submarine mass movements in recent decades, has shown that large-scale mass movements are less frequent and occur along passive margins whereas smaller mass movements occur on active margins (Casas et al., 2016; Moore et al., 2019; Moscardelli and Wood, 2016; Twichell et al., 2009; Urgeles and Camerlenghi, 2013). Statistical analysis additionally demonstrated that small-scale mass movements are underrepresented in all mapped margins either because small earthquakes cannot generate sufficient acceleration needed to trigger slope failure (U. S. ten Brink et al., 2009) or because of low mapping resolution, (Urgeles and Camerlenghi, 2013) or due to burial by recent mass movements (Casas et al., 2016). The maximum landslide size can be estimated from the magnitude of the triggering earthquake, but the observed sizes and volumes are typically much smaller owing to local variability in pre-conditioning factors and the location of the rupture relative to the slope (U. S. ten Brink et al., 2009). Therefore, understanding the physical conditions that cause slope instability is essential to constrain the spatial and temporal distribution of mass movements and will help hazard management strategies (Harbitz et al., 2014).

Despite the lack of direct observations of submarine slope failure processes, previous studies proposed a number of factors influencing the occurrence of mass movements. Of the many suggested preconditioning factors (e.g. sedimentation rate, ten Brink et al., 2016; fluid flow and pore pressure, Vanneste et al., 2014), the sediments shear strength was suggested as the key control on the occurrence and initial scale of mass movements. Both geotechnical and statistical analysis have suggested that seismic acceleration in active margins leads to densification and increased shear strength of the sediments, therefore reducing the occurrence of mass movements (Sawyer and DeVore, 2015; ten

Brink et al., 2016). However, conditions such as rapid oversteepening or rapid sedimentation, counteract shear strengthening and enhance slope instability in active margins (Brothers et al., 2019b, 2019a; Sawyer et al., 2017; ten Brink et al., 2016).

Given the importance of shear strength to mass movement occurrence arising from the aforementioned studies, it is necessary to understand and test the relationship between the pre-failure sediments strength and the scale and location of the subsequent mass movement formation.

Here, we aimed to test how the sediment shear strength controls the spatial, temporal and volumetric distribution of mass movements. We used numerical modelling, namely the Discrete Element Method, to overcome limitations arising from mapping uncertainties and the lack of direct observations. The importance of shear strength in mass movement occurrence was previously addressed (Hutton and Syvitski, 2004; Stoecklin et al., 2020), but was limited to simulation dimensions (i.e. 2D) and sediment type (only clay). We use here a 3D approach to explore mass movement initiation along and across the slope in four numerical models. The results provide a conceptual understanding of shear strength influence on the initial volume available for mass movements.

## 5.2. Methods

### 5.2.1. *Discrete Element Method*

The Discrete Element Method (DEM) is a numerical approach that describes deformation in granular materials (Cundall and Strack, 1979). The modelling technique uses discrete particles that interact according to pre-defined physical laws in order to generate a bulk material behaviour. In contrast to continuous methods (i.e. finite difference and finite element), DEM can simulate large-scale deformations in brittle (Mohr–Coulomb) material and allow monitoring of large offset of particles relative to each other. Therefore, DEM enables the simulation of both short-term processes, such as instant landslides (e.g. Morgan and McGovern, 2005a), as well as long-term margin evolution (Wenk and Huhn, 2013). Wide parameter spectra, and hence, various sedimentological settings, can be simulated and tested (Elyashiv et al., 2020) in contrast to limited material spectra and boundary conditions in analogue sandbox experiments (e.g. Yamada et al., 2010).

Previous DEM simulations of slope deformation mainly used 2D simulations mainly to observe the effect of frictional strength variations (e.g. Huhn et al., 2016; Katz et al., 2014; Morgan and McGovern, 2005a). However, 3D simulations are needed to

understand lateral deformation development (e.g. Verrucci et al., 2019). Here, using 3D simulations we were able to assess large-scale mass movement events forming both across and along the slope and to observe whether contiguous failure occurs in different sediment types. We used the commercial software Particle Flow Code 3D (PFC3D, Itasca, 2014) that utilizes the discrete elements approach.

### 5.2.2. *Characterization of sediment physical properties in DEM*

To simulate slope sediments we defined two distinct sediment types: sandy sediments which are primarily cohesionless, and clayey sediments which are primarily cohesive. Based on the granular approach, micro-properties of individual particles have to be designed in order to control the mechanical behaviour, i.e. the macro-properties of the slope material. For example, the particle coefficient of friction must be adjusted so that the peak shear strength of the numerical slope “sediments” corresponds to that of natural materials (Elyashiv et al., 2020; Kock and Huhn, 2007a; Morgan and Boettcher, 1999; Morgan and McGovern, 2005a). Numerical shear and triaxial tests are used for this purpose. The mechanical behaviour of the selected micro-properties was tested (Elyashiv et al., 2020) to generate two numerical “sediment” types with low and high shear strength. Following the standard protocol (Elyashiv et al., 2020), first the appropriate contact model was chosen (Table 5.1) to generate a cohesive or cohesionless behaviour. Second, the value of the major micro-property (Table 5.1) needed to control the mechanical behaviour of the peak shear strength was determined. Lastly, the value of the initial micro coefficient of friction (Table 5.1) was defined to generate a dense or loose particles arrangement.

All the parameters, including contact models and particle micro-properties, are detailed in Table 1 for each simulated material. From here onwards, all the properties discussed in the text refer to the macro-properties of the simulated “sediments”.

### 5.2.3. *Model setup*

Adopting geometries from analogue (Yamada et al., 2010) and numerical sandbox experiments (Huhn et al., 2016; Wenk and Huhn, 2013), we created a 3D rectangular “sandbox” (Figure 5.1a). The modelled box was defined by five fixed, impermeable boundary walls; four sidewalls and a box bottom (see wall properties in Table 5.1).

The initial box dimensions were of 700 [m] length, 200 [m] width and 160 [m] height. The entire box was filled with an undisturbed “sediment” layer. The layer was generated

by 64,250 spherical particles, distributed by a random seed number available in PFC3D (see Itasca, 2014). We used four particles radii ( 3.7 to 5.5 [m], table 5.1), randomly distributed to prevent an unrealistic deformation (i.e. Saltzer and Pollard, 1992). The randomly distributed particles were settled by gravity until finally creating a 160 [m] thickness of numerical “sediments” (Figure 5.1a). The application of similar initial conditions in all four models, allowed during analysis to compare between the models and assign any variability to the initial packing or the assigned physical properties as tested in Elyashiv et al., (2020).

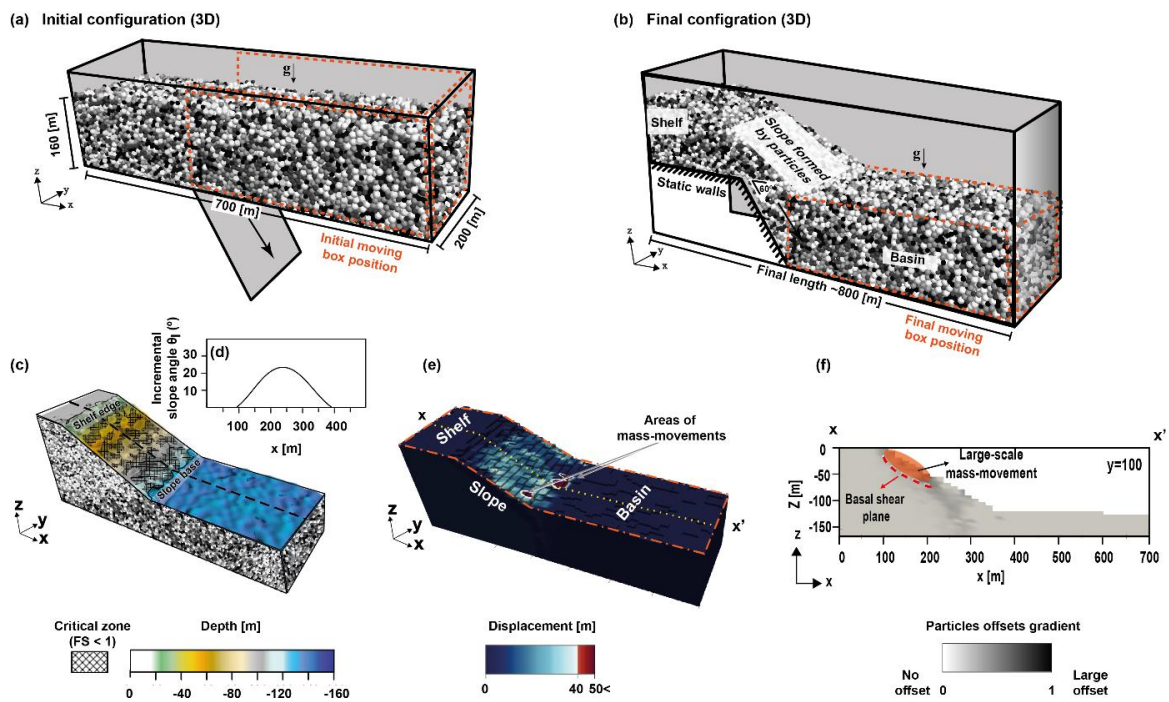


**Figure 5.1:** Initial and final 3D configuration of the particles in the DEM model and subsequent analysis. (a) 3D initial setup. Particles are confined within impermeable walls (front walls are transparent in the figure). Moving walls are marked by dashed orange lines. A fixed diagonal wall is placed at the bottom of the box. (b) 3D final configuration of the model, following 160 [m] of vertical movement. Box length (x axis) was extended to approximately 800 [m] as a result. Particles are shaded according to their diameter. (c) Draped map view of a bathymetric map generated from the surface particles of the model. Shaded areas designate the unstable slope. (d) The incremental slope angle calculated from the surface particles extracted along  $Y=100\pm 50$  [m] (marked in (c) by a dashed black line). (e) A 3D analysis of the total displacement (areas of mass movements in red). (f) A 2D cross section of the normalized displacement gradient at  $y=100$  [m] ( $x-x'$  location is marked in (e) by a dotted yellow line).

A self-forming slope was generated by dividing the model box into two parts. On the left hand-side, a static, non-moving box (a third of the initial size, Figure 5.1a) created a “shelf” (Figure 5.1b). On the right hand-side, a moving box (two thirds of the initial size),

was displaced downwards along a 60° sloping wall forming a self-organized slope evolution and a “basin” (Figure 5.1b).

*Table 5.1: Numerical sediment properties and parameters in each for the model setup.*

Model setup properties		
Number of particles	64,250	
Particle radii (m)	3.7, 3.9, 4.2, 5.5	
Particles friction coefficient $\phi_p$	0.5	
Particle density (kg/m <sup>3</sup> )	2650	
Wall friction coefficient $\mu_{(wall)}$	0.0	
Wall normal stiffness $kn_{(wall)}$ (Pa)	$1e^{12}$	
Type 1: ‘sand’		
	(1a) Low shear strength	(1b) High shear strength
Contact model	Hertz-Mindlin	Hertz-Mindlin
	<u>Micro-properties</u> (input parameters)	
Poisson’s ratio $\nu$	0.25	0.25
shear modulus G (Pa)	$1e^{11}$	$1e^8$
	<u>Macro-properties</u> (output parameters)	
Friction coefficient of the material $\phi_m$	0.4	0.64
Type 2: ‘clay’		
	(2a) Low shear strength	(2b) High shear strength
Contact model	Linear parallel bond	Linear parallel bond
	<u>Micro-properties</u> (input parameters)	
Micro- Bond cohesive strength (Pa)	$210e^3$	$55e^3$
	<u>Macro-properties</u> (output parameters)	
Friction coefficient of the material $\phi_m$	0.5	0.53
Cohesion C (KPa)	81	199

The downward movement continued until a total vertical offset was gained, equal to the original thickness (160 m). Every 10-12 [m] the movement was stopped and the resulting particle displacements (and the slope evolution) were recorded. In doing so, a range of slope angles were generated and analysed with respect to slope geometry and failure occurrence. In total, sixteen slope stages were recorded along the 160 [m] of vertical offset, such that stage t-1 represents a movement of ~10 [m], stage t-2 represents a total movement of ~20 [m] etc.

Simulating different slope angle scenarios via a quasi-static movement of the particles have been successfully used in similar investigations (e.g. Huhn et al., 2016). The simple oversteepening mechanism formed by self-controlled evolution of slope inclination, follows previous field studies of mass movement events associated with oversteepening (Brothers et al., 2019b; Mosher et al., 2004). As the bottom walls were not imparting stresses on the particles, the resulting slope geometry was only dependent on the particles’

physical properties and on the progressive increase in shear stress on the slope by the developing slope angle with model steps.

To observe how the sediment shear strength and cohesion precondition the development of mass movements, we simulated four models: (1a) Low shear strength ‘sandy’ slope, (1b) High shear strength ‘sandy’ slope, (2a) Low shear strength ‘clayey’ slope, and (2b) high shear strength ‘clayey’ slope. Fluids and pore pressure were not incorporated in the current model as quasi-static conditions were maintained throughout the simulations. This approach follows previous DEM (Huhn et al., 2016) and analogue sandbox experiments (Yamada et al., 2010) of mass movements studies.

Despite these simplifications, our simulations captured different stages of mass movement events. The simulations allowed us to map the location of head and sidewalls of mass movement events (section 5.3.2). The resulting information regarding the interplay between physical properties of slope sediments, different geometries (volume and source location) and emplacement processes (timing, kinematics and dynamics) are key to better estimate tsunami hazards.

#### 5.2.4. Model analysis and interpretation

Particles positions were mapped and saved at each slope stage (t-1, t-2 etc.) and at least 10 times (every 1 [m]) in between stages. From these data, we extracted information for each model stage regarding the temporal and spatial development of the slope and mass movements (see Fig.S5.1).

##### 5.2.4.1. Slope analysis

For each slope stage, we generated a bathymetric grid from the surface particles of the model. We used the resulting grid (a 10x10 [m] cell size, Fig. 5.1c) to evaluate the slope stability by calculating the factor of safety for each slope stage. The factor of safety ( $FS$ ) was calculated for each model under static conditions (Morgenstern, 1967) :

$$\text{Eq. 5.1} \quad FS = \frac{C + \gamma z ((\cos \theta_{OS})^2 - \lambda) \tan \varphi_m}{\gamma z \sin \theta_{OS} \cos \theta_{OS}},$$

where  $C$  is the cohesion,  $\gamma$  is a unit weight of a dry bulk material,  $z$  is the depth of the sediments taken at 50 [m] is and  $\varphi_m$  is the internal angle of friction (i.e., macro-properties of the numerical “sediment”). The *overall-slope angle* ( $\theta_{OS}$ ) represents the mean slope inclination, averaged over the whole area between the shelf break and the slope base (See

slope boundaries in Figure 5.1c). We considered the overpressure ratio  $\lambda = 0$ , as fluids were not considered in the model. The cohesion and internal angle of friction were taken from numerical triaxial tests results in Elyashiv et al., (2020) for each material (see Table 5.1).

To define unstable areas along the slope, a second slope angle was defined between two neighbouring cells in the bathymetric grid as the *local slope angle* ( $\theta_{LS}$ ). When  $FS = 1$ , for each model  $\theta_C$  is the critical slope angle at which the slope sediments become unstable (See Table 5.2). According to this definition, unstable part of the slope are areas where the local slope angle is higher than the critical slope angle, namely  $\theta_{LS} > \theta_C$ . In every slope stage, a critical slope zone was draped over the bathymetric maps in Figures 5.2-5.5 (Figure 5.1c, denoted critical zone) and calculated as the percentage of the entire slope area (In Figure 5.6).

Additionally, a 1D slope profile and its derivatives with time (i.e. slope stages) were analysed in detail to study the development of the slope angle and its influence on the development of mass movements. Slope profiles were extracted for each slope stage along an averaged cross section around the centre of the model ( $Y=100$  [m]). To avoid boundary effects, we calculated an average of surface particles at  $Y=100\pm 50$  (Figure 5.1c, d) and further characterized each profile by a polynomial fit. The *incremental slope angle* ( $\theta_I$ ) was calculated at an incremental step of  $x=1$  m along the x-axis. The rate of slope development ( $\delta\theta_I/\delta t$ ) was calculated along discrete horizontal slope profiles for  $x=100, 150, 200, 300, 350$  and  $400$  (see supplementary material S2). The averaged development for each model is presented in Figure 5.6.

#### 5.2.4.2. Mass movement events analysis

Mass movements were observed by calculating the displacement of the particles between two slope stages (Huhn et al., 2016; Wenk and Huhn, 2013). We defined a threshold value of particles displacement  $\geq 40$  [m] to be considered as a mass movement event during one slope stage. This threshold evaluates in total the movement of a particle twice the size of the largest particle, to exclude particles moving into locally forming traps (22 [m]), the downward movement of the moving box at each slope stage (10 [m]) and additional 10 [m] buffer area. To view the starting point of a mass movement, displacements are presented in a map view (surface X-Y, orange dashed line in Figure 5.1e) at the initial slope stage (of the two stages taken for the calculation). The development of

displacements for each model can be found in the supplementary material (Figures S5.4-5.7). The surface expression of mass movements is marked in red, headwalls and sidewalls are defined by a white line in Figure 1e and further results (Figures 5.2c-5.5c). The subsurface extent of mass movements and their basal shear plane (also failure plane) are presented in terms of the particles offsets gradient (Figure 5.1f). This relative field of displacement shows the incremental strain, revealing areas where particles were largely offset relative to their neighbouring particles (Morgan and Boettcher, 1999). The relative displacement field results are normalized and presented in Figure 1f on a scale where no offset is 0 (grey) and the largest offset is 1 (black). Such gradients are presented in figures 5.2-5.5 as cross sectional slices (2D) along X-Z surfaces at either Y=50, 100 and 150 [m]. Areas of maximum offsets are interpreted in the cross-sections as the sliding mass (red lines). The contact between regions of maximum offset and minimal offset is considered here to be the basal shear plane of a mass movement.

#### 5.2.4.3. *Frequency and volume of displacements*

The frequency and volume of mass movements were calculated for each slope stage (Figure 5.6). We defined a single mass movement, as a group of particles that overlapped according to their radius and location and additionally were displaced equally or more than the threshold value of displacement (>40 [m], see supplementary material Fig.S5.2). The number of mass movement events (i.e. frequency) was determined for each stage. The total volume ( $V$ ) of the mass was then calculated as the sum of all moving particles' volume:

$$\text{Eq. 5.2} \quad V = \Sigma \left( \frac{4}{3} \pi * r_s^3 \right),$$

where  $r_s$  is the radius of a particle that was part of the mass movement.

## 5.3. Results

### 5.3.1. *Slope analysis*

In each model, a slope stage corresponds to a newly developed overall slope angle ( $\theta_{OS}$ ). In total, 16 slope stages were generated (t-0 to t-15) for each model. In all simulations, an inclined slope with varying slope segments and slope angles evolved. However, slope

extension and angles of different segments (upper and lower slope) varied noticeably as a function of the slope material properties.

The incremental slope angle ( $\theta_I$ ) evolution exhibits a general trend for each model, starting with a unimodal slope through a transitional stage to a bimodal slope. The model stages, in which these transitions occurred, varied between the models (Figures 5.2-5.5a). In model 1a (Figure 5.2a), simulating low shear strength “sandy” slopes, the unimodal shape ended in t-7, whereas in model 1b (Figure 5.3a), simulating high shear strength “sandy” slopes it ended in t-8. In “clayey” slopes, models 2a (Figure 5.4a) and 2b (Figure 5.5a), low and high shear strength, respectively; the unimodal slopes remained stable until t-9 and t-7, respectively. The transitional phase is slightly different and accommodated one to three slope stages. Both low shear strength “sandy” and “clayey” models began developing a bimodal shape in t-11 whereas both high shear strength “sandy” and “clayey” models already showed in t-10 a bimodal shape (See t-10 in Figures 5.2-5.5a). All models showed a bimodal shaped slope with an upper and a lower segment (see next paragraph) by stage t-15 (See t-14 in Figures 5.2-5.5a).

A detailed analysis of the specific angles associated with the development of segmentation showed that in the early stages an almost symmetrical behaviour with similar slope angles develop along the upper and lower slope (unimodal e.g. t-7, Figures 5.2-5.5a). The transition area between the upper and lower slope segments was at approximately  $x = 250$  [m] in all simulations and was characterised by steepest slope angles. Symmetry in slope angles along the upper and lower slope segments was maintained in models “sandy” 1a and “clayey” 2b (Figures 5.2a, 5.5a) throughout their development. For these models, the upper and lower slope segments of the bimodal shaped slopes, showed similar slope angles. The transition zone between upper and lower slope was marked by a local slope angle minimum which is located around  $200 < x < 260$  [m]. In contrast to these symmetrical slopes, models 1b of high shear strength “sandy” slope and 2a of low shear strength “clayey” slope showed an asymmetry in slope angles between the two segments (Figures 5.3a, 5.4a). Model 1b was moderately asymmetrical with higher slope angles ( $\sim 27$ - $29^\circ$ ) along the lower slope segment at the latest stages of the simulations. Model 2a however, was strongly asymmetrical with higher slope angles along the upper slope (Figure 5.4a). Nevertheless, even in these models, both slope segments were separated by a slope-angle minimum which is located approximately at  $x = 250$  [m].

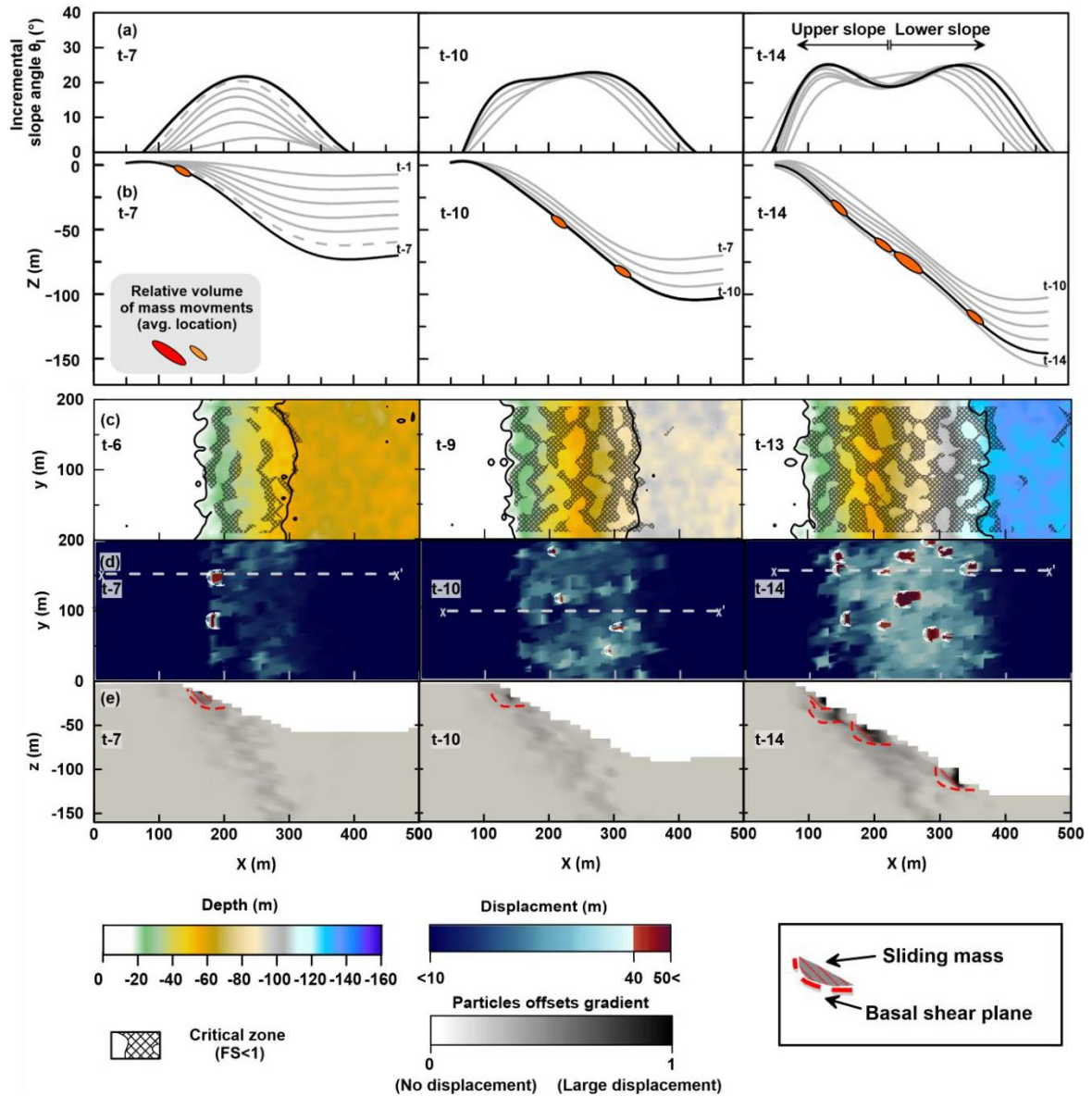


**Figure 5.2:** Model 1a-Low shear strength 'sand'. Model stages (left to right): t-7, t-10 and t-14. (a) Mean slope angle evolution up to the presented stage. (b) Mean slope profile evolution up to the presented stage. The averaged location of mass movements (coloured ovals) is plotted as an averaged location of their initial location. (c) Bathymetric surface of the preceding slope stage (i.e. t-6, t-9 and t-13). Black contours define the shelf break and slope base. Shaded slope areas represent unstable slope ( $FS < 1$ ). (d) Map view of mass movements (in red) covering the slope. A mass movement is defined at each stage as particles displacement  $> 40$  [m] from the previous stage. Dashed grey lines are cross sections presented below. (e) Cross section of the displacement gradient along the dashed line shown in (d). Gradient scale indicates the largest relative displacement.

In addition to the slope angles, the simulations also provided deeper insights into the expansion of the slope in space and time. In general, the lateral expansion of the slope itself

as well as the width of the different segments varied both between the models as well as in each model stage. However, while the width of the entire slope in the first stage (t-1) is  $243\pm 14$  [m] and in the final stage (t-15) was  $424\pm 22$  [m] in all simulated slopes, the rate of slope development varied significantly across different parts of the slope (see Fig.S5.3).

### 5.3.2. *Development of mass movements (displacements)*

Displacements of particles identified as mass movements (i.e. displacement beyond the threshold value), were observed in all simulations at different slope stages. However, their location, dimension and frequency differed significantly according to the “sediment” type and shear strength. Parallel to the transition from a uni- to bimodality, all models show an increasing of the slope instability and events of mass movements.

#### 5.3.2.1. Model 1- ‘sand’

Model 1a simulated low shear strength “sandy” slope sediments (Figure 5.2) with a critical slope angle  $\theta_c = 22.1^\circ$  at  $FS = 1$  (Table 5.2). Between t-0 to t-15 the overall-slope angles ( $\theta_{OS}$ ) changed from  $0^\circ$  to  $22.7^\circ$ . As outlined above, the slope eventually developed a bimodal shape, here with a narrow upper slope and a lower slope whereas with a greater lateral extension (Figure 5.2a, b). Coevally, specific slope zones were unstable from t-6 onwards (see “critical zone” in Figure 5.2c). Note that while the critical slope zone (Figures 5.2c-5.5c) was calculated over the entire width of the slope (2D analysis), the slope profile (Figure 5.2b) and the slope angle (Figure 5.2a) represent an average analysis taken across  $y=100\pm 50$  with  $\Delta X=1$  (1D).

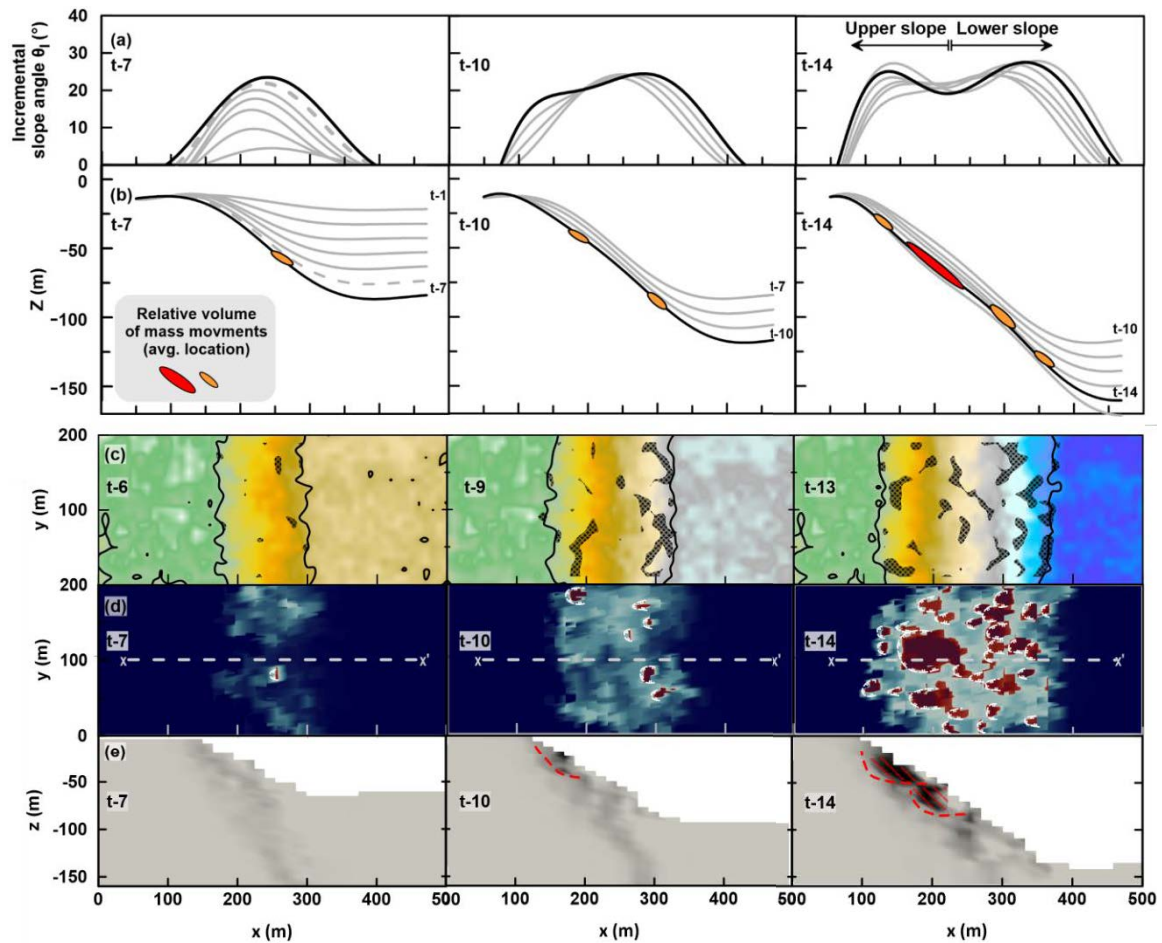


Figure 5.3: Same as Figure 2 but for Model 1b-High shear strength 'sand'

Mass movement events were observed from stage t-6 to onwards (Figure 5.2b, d, e). In the early unimodal slope stages (Figure 5.2c, t-7), mass movements were observed only in the upper slope, whereas during the following stages (t-10 and t-14, Figure 5.2d, e) mass movements were observed in the upper and lower slope. A good correlation exists between the distribution of the critical slope zone in the preceding stage (t-6 in Figure 5.2c) and the location of mass movements of the following slope stage (t-7 in Figure 5.2d).

As the width of both slope segments increased and a bimodal slope developed, larger portions of the slope became critical and therefore the frequency and number of mass movement events increased (Figure 5.2d and S5.4).

**Table 5.2:** Slope stages parameters: critical slope angle under slope conditions of  $FS = 1$ , the overall-slope angle ( $\theta_{OS}$ ) and the local critical slope zone (%LC).

Model	Critical slope angle ( $\theta_c$ )		Unimodal	Transitional	Bimodal
1a (‘sand’, low shear strength)	22.1°	$\theta_{OS}$ %LC	0-19° 0-41%	19-22° 41-60%	22-22.7° 59-62%
1b (‘sand’, high shear strength)	32.7°	$\theta_{OS}$ %LC	0-21.8° 0-7%	21.8-22.2° 7-12%	22.2-24.2° 12-18%
2a (‘clay’, low shear strength)	30.7°	$\theta_{OS}$ %LC	0-23.2° 0-20%	22.8-23.4° 20-26%	23.4-24.2° 26-31%
2b (‘clay’, high shear strength)	37.0°	$\theta_{OS}$ %LC	0-20.2° 0-1%	20.2-21.7° 1-2%	21.7-23.6° 2-5%

The relative displacement gradients highlight the subsurface extension of mass movements and their basal shear plane (Figure 5.2e); thereby enabling us to estimate the volumes of destabilized material. In model 1a, areas that displayed the largest relative displacements in the subsurface (Figure 2e) correspond to surface mass movements observed in the map view (Figure 5.2d). In the low strength “sandy” sediments only shallow, small-scaled and small-volume ( $>1 \text{ km}^3$ ) mass movement events were observed. In addition, basal shear planes were observed without a clear surface expression along the upper slope in stages t-10 and t-14 (Figure 5.2e). They represent a pre-state of mass movements that will fail in the next stage.

Model 1b simulated high shear strength “sandy” slope sediments (Figure 5.3) with a critical slope angle  $\theta_c = 32.7^\circ$  at  $FS = 1$  (Table 5.2). Between t-0 to t-15 the overall-slope angles ( $\theta_{OS}$ ) changed from  $0^\circ$  to  $24.2^\circ$ , accordingly. In the final stages, the bimodal slopes formed a moderate asymmetry and a steeper lower slope extension (Figure 5.3a, b), exhibiting unstable slope zones from t-6 onwards (Figure 5.3c).

Large-scale mass movements were observed in the upper slope in stages t-14 and t-15 (t-14 in Figure 5.3d and t-15 in S5.5), in addition to observation of mass movements from stage t-6 onwards (Figure 5.3b, d, e). Mass movements location along the slope differed between model transitions, from the mid-lower slope (t-7, Figure 5.3d), to the uppermost slope (t-10, Figure 5.3d), and finally covering the upper to lower slope (t-14, Figure 5.3d). Their location correlated well with the critical zone of the preceding slope stage (see

Figure 5.3c vs 5.3d), however for larger-scale mass movements the critical zone correlated only with the edges of the observed mass movement.

In model 1b, the areas that displayed the largest relative displacements in the subsurface (Figure 5.3e) correspond to surface mass movements observed in map view (Figure 5.3d). However, the surface map presented a large, continuous mass movement (t-14, Figure 5.3d) whereas the subsurface presented a widespread shear plane at the bottom (t-14, Figure 5.3e). Additionally, a basal shear plane was observed without a clear surface expression along the upper slope in stage t-10 (Figure 5.3e) and was interpreted as a subsurface pre-state of mass movements.

### 3.2.2 Model 2 – ‘clay’

Model 2a simulated low shear strength “clayey” slope sediments (Figure 5.4) with a critical slope angle  $\theta_c=30.7^\circ$  at  $FS = 1$  (Table 5.2). Between t-0 to t-15 the overall-slope angles ( $\theta_{OS}$ ) changed from  $0^\circ$  to  $24.1^\circ$ , accordingly. In the final stages, the bimodal slope was characterized by a steep upper slope and a wider and relatively flatter lower slope (Figure 5.4a, b), exhibiting unstable slope zones from t-5 onwards (Figure 5.4c).

These low strength “clayey” sediments showed the largest-scale mass movement event. Contiguous large-scale mass movements were observed in the upper slope (t-14 in Figure 5.4d and t-15 in S5.6) in addition to observation of mass movements from stage t-5 onwards (Figure 5.4b, d, e). Mass movements location along the slope differed between model transitions, restricted to the upper slope (t-7, Figure 5.4d), then upper and middle slope (t-10, Figure 5.4d), and finally along the entire slope (t-14, Figure 5.4d).

Their location correlated as well with the critical zone of the preceding slope stage (see Figure 5.4c vs 5.4d), however the local critical zone only bordered the observed larger-scale mass movements. In the last stages, large and contiguous slope zones became critical notably across the upper slope (Figure 5.4c).

For model 2a (low shear strength clay), the areas that displayed the largest relative displacements in the subsurface (Figure 5.4e) corresponded to surface mass movements observed in the maps (Figure 5.4d). Specifically, a complex development of contiguous mass movements and a shallow continuous basal shear plane initiated large-scale mass movements (t-14, Figure 5.4d, e). Also in the clayey model a basal shear plane was observed without a clear surface expression along the upper slope in stage t-10 (Figure 5.4e), characterizing areas which could subsequently fail in the next simulation stage.



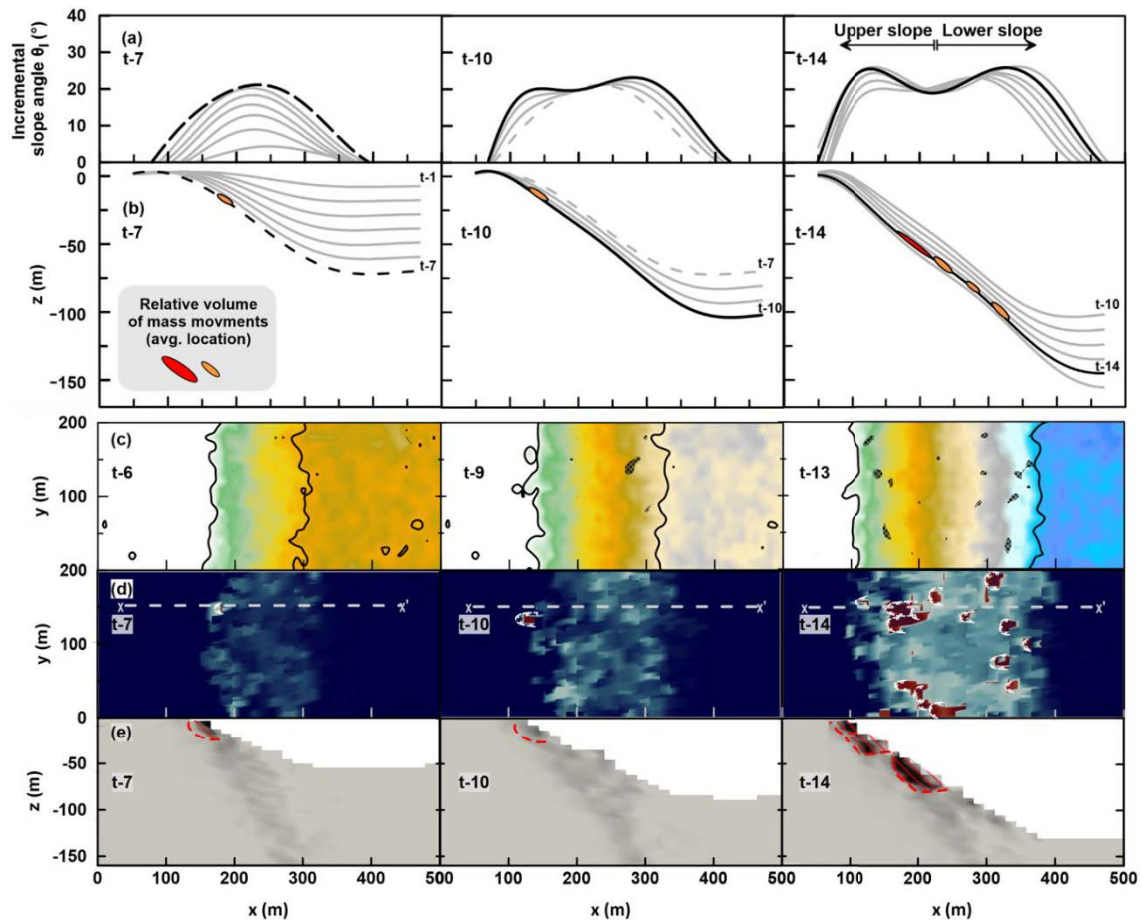


Figure 5.5: Same as Figure 2 but for Model 2b- High shear strength 'clay'.

Mass movements initiation was observed in all slope stages from t-7 onwards (Figure 5b, d, e), except t-8 (Figure S5.7). Similar to the clayey model 2a, mass movements initiated only in the upper slope (t-7 and t-10, Figure 5.5d) and finally along the entire slope (t-14, Figure 5.5d).

In model 2b, a very low percentage of the slope ( $\geq 5\%$  in Table 5.2) was unstable compared to all previous models. Similar to the largest mass movements seen in the previous clayey model, the critical zone (Figure 5.5c) bordered all the observed headwall of initiated mass movements (Figure 5.5d). Although the critical slope zone was patchy and showed very little growth compared to previous models, the number and spatial distribution of mass wasting events increased as the slope developed.

Similar to previous models, areas of largest relative displacements in the subsurface (Figure 5.5e) correspond to the observed mass movements (Figure 5.5d). Contrary to previous models, only in stage t-14 a basal shear plane was observed in cross section 4

(Figure 5.5e), although not entirely correlative in the displacement map view (Figure 5.5d).

## 5.4. Discussion

Testing sediment type and shear strength numerically, we were able to observe the influence of these preconditioning factors on slope failure. We next discuss (1) the evolution of slope susceptibility-to-failure, and (2) mass movements' development, especially large-scale mass movement events in our models and in natural settings. Finally, we discuss how our model results can provide insights to mass movement events and volume observed in the field and their pre-conditioning settings.

### 5.4.1. *Susceptibility-to-failure development*

The development of unstable slope areas ("critical zone", Figures 5.2c-5.5c) in the models characterized the slope susceptibility-to-failure in the following stage(s). The lateral distribution of unstable slope area (Figures 5.2c-5.5c) together with the percentage of the unstable slope (Figure 5.6a-di), predicted widely distributed and spatially contiguous unstable areas in low shear strength slopes, as opposed to the discretely and scarcely distributed unstable areas predicted in high shear strength slopes. These relationship points to the principal role shear strength plays defining the distribution of potential failure across the slope. For example, in areas such as shelf edge deltas, high sedimentation rates lead to underconsolidated deposits i.e., sediments with low shear strength. Such a wide continuous stratigraphic unit covering the upper slope (Steventon et al., 2020), creates a contiguous area that is susceptible-to-failure. This could develop to large-scale mass movements as seen along the west Atlantic margins (Twichell et al., 2009).

The sediment type seemingly plays a secondary role, controlling the extent of the distribution along the slope and additionally influencing the focus of unstable areas to one of the slope segments (i.e., upper or lower slope). Under the modelled conditions, these distributions suggest that in clayey slopes, failure will focus in the upper slope whereas in sandy slopes failure will be discretely distributed along the entire slope. These results resemble previous 2D numerical models predicting failure focusing in upper-to-middle clayey slopes (e.g. Hutton and Syvitski, 2004). Field observations or numerical examples for purely submarine sandy slopes are rare as the distribution of sands in the deep sea is

either a distinct stratigraphic layer or is focused in deep sea fans. Since our models were homogenous, it is currently difficult to constrain our results to such observations. Together however, the sediment type and the shear strength predefine the lateral distribution of submarine mass movements.

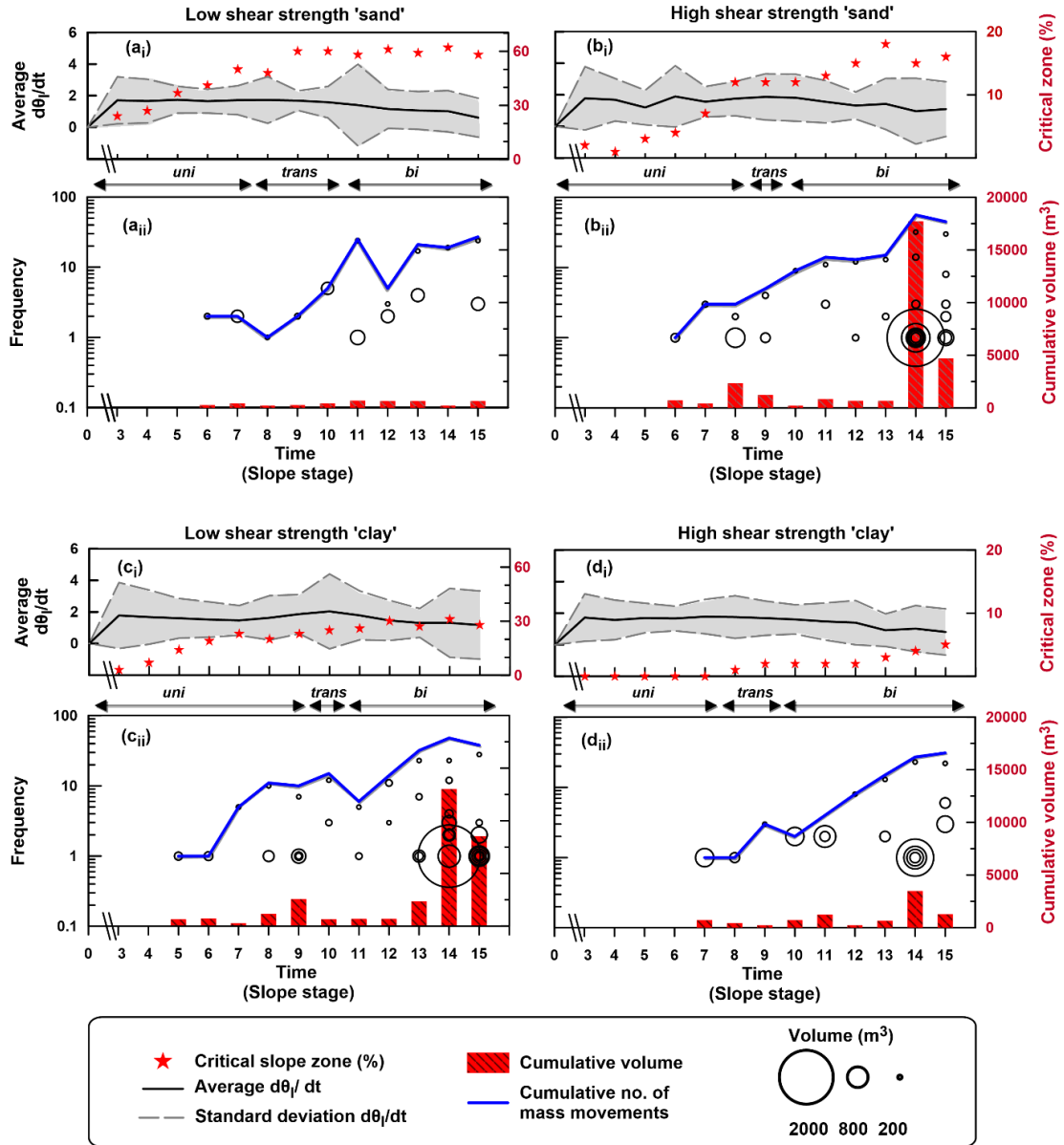


**Figure 5.6:** Temporal (slope stages) development of mass movements' volume and frequency in (a) Model 1a-low strength 'sand' (b) Model 1b-high strength 'sand' (c) Model 2a-low strength 'clay' (d) Model 2b-high strength 'clay'. In each model (i) the rate of the slope temporal development was averaged (black line) and plotted with its standard deviation (shaded grey area). Red stars show the percent of unstable slope at each stage (ii) the temporal development of the mass movements' volume (linear scale) and frequency (semi-log, bubble plot). The bubble's size represents mass movements' volume. The cumulative frequency (blue line) and the cumulative volume (red bars) taken over one slope stage.

## 5.4.2. *Mass movements development*

### 5.4.2.1. Distribution

Mass movements distribution followed the locations predicted by the unstable slope areas. Small-scaled failure was completely correlative with the unstable slope at the preceding stage, whereas medium and large-scaled failure correlated only with the headwall scar. It is important to note though, that mass movements did not form in every localization of a preceding unstable slope. To understand the difference between the predicted susceptible-to-failure areas and the areas eventually forming mass movements, we need to consider the underlying micromechanical processes during deformation. In each stage of the simulations, parts of the slope reached stability due to particles rearrangement acquiring a new stable position (Kock and Huhn, 2007a), thus delaying the occurrence of failure. In the following stage, the newly acquired positions could generate either failure or further maintain stability. A metastable state ( $FS < 1$ ) has been evaluated or measured in many submarine environments in which the increased rates of deposition and changes in the groundwater movements (pore pressure) were inferred as the main causes (e.g. Kopf et al., 2016). Here the comparison between the predicted and occurring failure helps us understand which of the models will eventually produce larger volumes which predominantly resulting from the sediments shear strength (see section 5.4.3.3. and Figure 5.6).

### 5.4.2.2. Frequency of failure events

The overall frequency of failure events also increases with increasing slope susceptibility-to-failure (blue lines, Figure 5.6). Yet there are episodic drops in the overall frequency of mass movement events that occur in the low shear strength slopes but not in the high shear strength slopes. This relationship between the overall frequency and the shear strength is similar to our observations of the stabilizing slope areas in between stages. It is associated with the underlying micromechanics initiating failure in numerical “sediments” (Elyashiv et al., 2020). Whereas low shear strength-loosely packed sediments fail through contraction, leading temporarily to the stabilization of the sediment particles micro-structure, the high shear strength-densely packed sediments fail through dilation, leading to volume expansion (Mitchell and Soga, 2005). Eventually in all models increasing instability of those slope areas.

#### 5.4.2.3. Potential initial volume involved in failure

Voluminous slope failures formed only in high shear strength sand and low shear strength clay models (Figure 5.6a-d<sub>ii</sub>), as the frequency of failure increased. Each of these two models also distinctly produced a single, extremely large-scale mass movement (2-6 km<sup>3</sup>, Figure 5.6b<sub>ii</sub>, c<sub>ii</sub>). Although a high percentage of the slope is observed to be unstable in low shear strength models, the occurrence of large-scale failure events is actually consistent with the trigger, i.e., the oversteepening or the slope rate of development. The link can be observed in Figure 6, where large-scale mass movements coincide with a local increase in the variability of slope rate of change. Averaged along the y-axis (100±50 m), the changes in the slope development rate ( $d\theta/dt$ ) are observed from variations in the standard deviation of the rate (grey zones in Fig. 5.6b<sub>i</sub> and 5.6c<sub>i</sub>). This suggests that when some parts of the slope steepen faster than the lower or upper parts of the slope, the susceptibility to large-scale mass movement events increases.

Small-scale mass movements frequency increased in all of our models, yet such trend seems to be underrepresented in mapping inventories (e.g. Urgeles and Camerlenghi, 2013). Around the Mediterranean, it has been attributed either to insufficient mapping resolution or to limited preservation of head-scares (Casas et al., 2016; Urgeles and Camerlenghi, 2013). However, ten Brink and Geist (2021) suggested that under a regional trigger (e.g. earthquake) a finite number of small-scale mass movements could form along a slope (e.g. the South-eastern Mediterranean, Katz et al., 2015b). As such, it is possible that characteristics of our model (e.g., a limited number of sizes of particles) generates an overestimated number of small-scale mass movements. However, we suggest that the multiple small-scale mass movements represent multiple nucleating sources, which in nature under additional factors (e.g. pore pressure) could merge to generate a larger slide complex (Casas et al., 2016; ten Brink and Geist, 2021). Evidence for this process can be observed from our modelled basal shear planes (sensu Masson et al., 2010 and Gatter et al. in press). Several connecting failure planes formed in “sandy” slopes contrary to a continuous failure plane in “clayey” slopes (Fig. 3d vs. 4d, respectively). This indicates that the sediment type has a control on the development of initial failure plane and subsequently on the dynamics that leads to large-scale, voluminous mass movements. A detailed analysis is needed however, to confirm this. The possibility to view different failure planes developing into extremely large mass movements, presents an opportunity to use the DEM approach in the future to observe how the basal failure plane evolves

(top-bottom or bottom-top, i.e. Masson et al., 2010) in different settings or in response to different triggers.

Our modelling thus suggests that specific shear strength and sediment composition can generate extremely voluminous mass movements regardless of excess pore pressure. It should be noted, that although the current models did not simulate additional processes (e.g. pore pressure, Stoecklin et al., 2017; sedimentation rate, ten Brink et al., 2016), these may contribute to generation of large-scale failure (Urlaub et al., 2015) and could significantly increase the frequency of mass movements events (Dugan and Flemings, 2002).

#### *5.4.3. Conceptual models for potential large-scale mass movements*

Based on our models we offer a conceptual understanding of the influence and interplay between sediment type, shear strength and the initial volume involved in the failure. The sediment type and the sediment micro-structure resulting from the consolidation state, contribute to the sediment shear strength are conceptually linked to the slope susceptibility-to-failure and the resulting mass movements (Figure 5.7a-d). The occurrence of mass movements along the slope increased as the slope steepness increased (Figure 5.7a) as seen in sandy environments such as canyon heads (Mollison et al., 2020) shelf and estuary environments (Carter et al., 2020; Mosher et al., 2004); where both low and high shear strength sands are present. However, extremely large-scale mass movement events are more likely to occur along densely packed sandy slopes (Figure 5.7b) or in under- to normally-consolidated clayey slopes (Figure 5.7c). For example the extensive, large-scale mass movements along the seismically active Algerian margins were related to dense sandy deposits (Dan et al., 2009). Conversely, along the passive west Atlantic margins large-scale complex and contiguous mass movements were related to deltaic settings with high sedimentation rates possibly leading to under- to normally consolidation state of the sediments (Twichell et al., 2009). According to the high shear strength clayey slope model, medium- to large-scale single mass movement events will develop where clayey sediments are highly or slightly over-consolidated (Figure 5.7d). The latter, for example resembles mass movements possibly derived from oversteepening along the seismically-active Japanese margins (Moore et al., 2019) where many small-scale mass movement were observed but a single large one is also present.

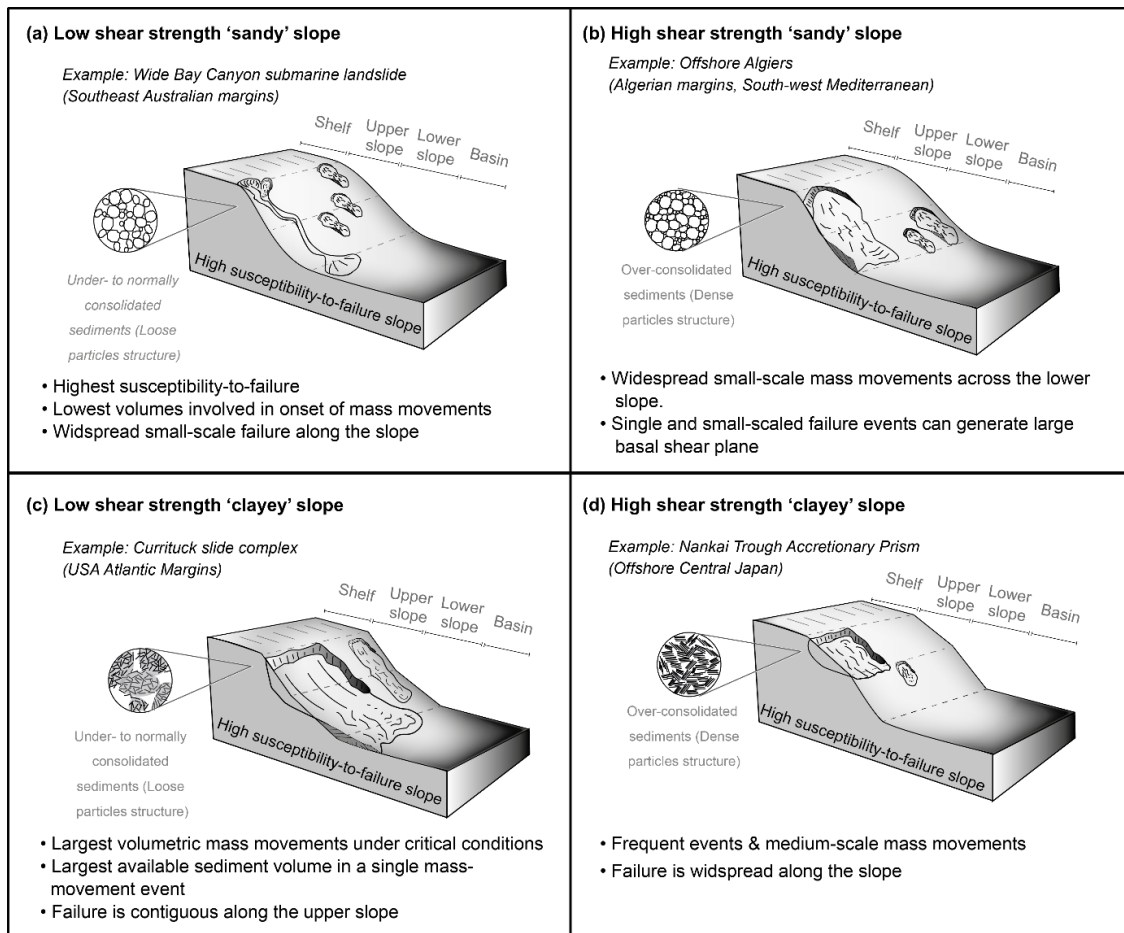


*Figure 5.7: A conceptual diagram based on the four models, connecting the pre-failure state of sediments (regarding shear strength and sediment type, see circular inset) to the potential initial volume involved in failure. Under increased slope susceptibility-to-failure conditions, each model illustrates the location and distribution of mass movements based four exemplary field observations worldwide .(a) Low shear strength 'sandy' slope; example from the Australian margins (after Mollison et al., 2020) (b) High shear strength 'sandy' slope; example from the Algerian margins (after Dan et al., 2009) (c) Low shear strength 'clayey' slope; example from the USA Atlantic margins (after Hill et al., 2017) (d) High shear strength 'clayey' slope; example from the Japanese margins (Moore et al., 2019). Slopes are not to scale.*

## 5.5. Conclusions

Using 3D numerical modelling we produced four models with varying sediment type and shear strength in which failure was induced by the development of a self-organizing slope oversteepening. The varying sediment properties influenced the distribution of unstable slope area, their initial location, the frequency of slope failure, and the initial volume of the modelled mass movements. Specifically, the models identify the properties that are conducive to the development of large-scale failures. A limitation of the current results is that pore pressure, a property that can also increase the initial mass movement volume, was not incorporated.

Nevertheless, the models' results were found compatible with observations and with statistical analysis of submarine mass movements emerging worldwide.

The following conclusions can be drawn from our models:

- (1) The sediment shear strength primarily controls the development of slope susceptibility-to-failure, particularly its lateral extension. Low shear strength slope models (under to normally consolidated sediments) show an extensive and contiguous development of unstable slope areas compared with discrete development of unstable slope areas in high shear strength slope models (over-consolidated sediments).
- (2) Distribution of mass movements follows the unstable slope areas at the preceding model stages however in the models not all the preceding unstable areas fail due to local stabilization processes (particles rearrangement) as slope steepening increases (i.e. increasing stress conditions). Local stabilization in natural slopes may occur as increased consolidation through compaction, chemical and biological processes.
- (3) Variations in shear strength offers an explanation for the frequency of mass movements, highlighting particularly the influence of the underlying micromechanics on both local stabilization and overall potential failure of slope sediments.
- (4) Although the model were set under drained conditions, it suggests that a specific consolidation state together with a specific sediment type are prerequisites for voluminous mass movements. The occurrence of extremely large-scale mass movements evident only in low shear strength clayey and high shear strength sandy slope models coincided with increased localized slope steepening.
- (5) As suggested by previous studies, in response to a regional trigger (oversteepening), failure planes formed simultaneously along the slope, within the range of predicted instability. Failure planes formation presented a first step toward a detailed analysis of a single 3D submarine landslide events kinematics. Future numerical simulations are required to understand how the failure planes evolve in the presence of pore pressure and under varying stratigraphic geometries in which strength contrast occurs.

### **Acknowledgments**

HE would like to thank Gerhard Bartzke and Marine Le Minor for their useful advice in processing the results. HE work was supported by the Minerva Stiftung.

### **Author contributions**

**Hadar Elyashiv:** Conceptualization, Methodology, Software, Formal analysis, Investigation, Writing - Original Draft, Writing - Review & Editing, Visualization. **Uri ten Brink:** Writing - Review & Editing, Supervision. **Revital Bookman:** Writing - Review & Editing, Supervision. **Katrin Huhn:** Conceptualization, Resources, Writing - Review & Editing, Supervision.

## Appendix 5A

### List of symbols

$\theta_S$	Overall slope angle
$\theta_L$	Local slope angle
$C$	Cohesion
$\gamma$	A unit weight of a dry bulk material
$z$	Depth taken at 50 m
$\varphi_m$	The internal angle of friction
$\lambda$	Overpressure ratio
$\theta_C$	<i>Critical slope angle</i>
$\%\theta_C$	Percentage of the critical slope zone

### Figure S5.1: Model analysis and interpretation

Map view of bathymetric map (right) generated from the surface particles of the model (left). Shaded area designates calculated local critical slope zone. (b) Averaged slope profile (blue) and incremental slope angle (black) (right) calculated from the surface particles extracted along the centre of the model (left). Red lines are projected in Figure S3 as averaged rate of slope angle development (c) Map view of the model surface of total displacement (areas of mass movement in red) (right) and a 3D view of the total displacement (left). (b) Cross sections of the normalized displacement gradient along (top to bottom):  $y=50, 100$  and  $150$  [m] (right) and a 3D view of the relative displacement gradient (left). Dashed lines mark the location of the cross sections.

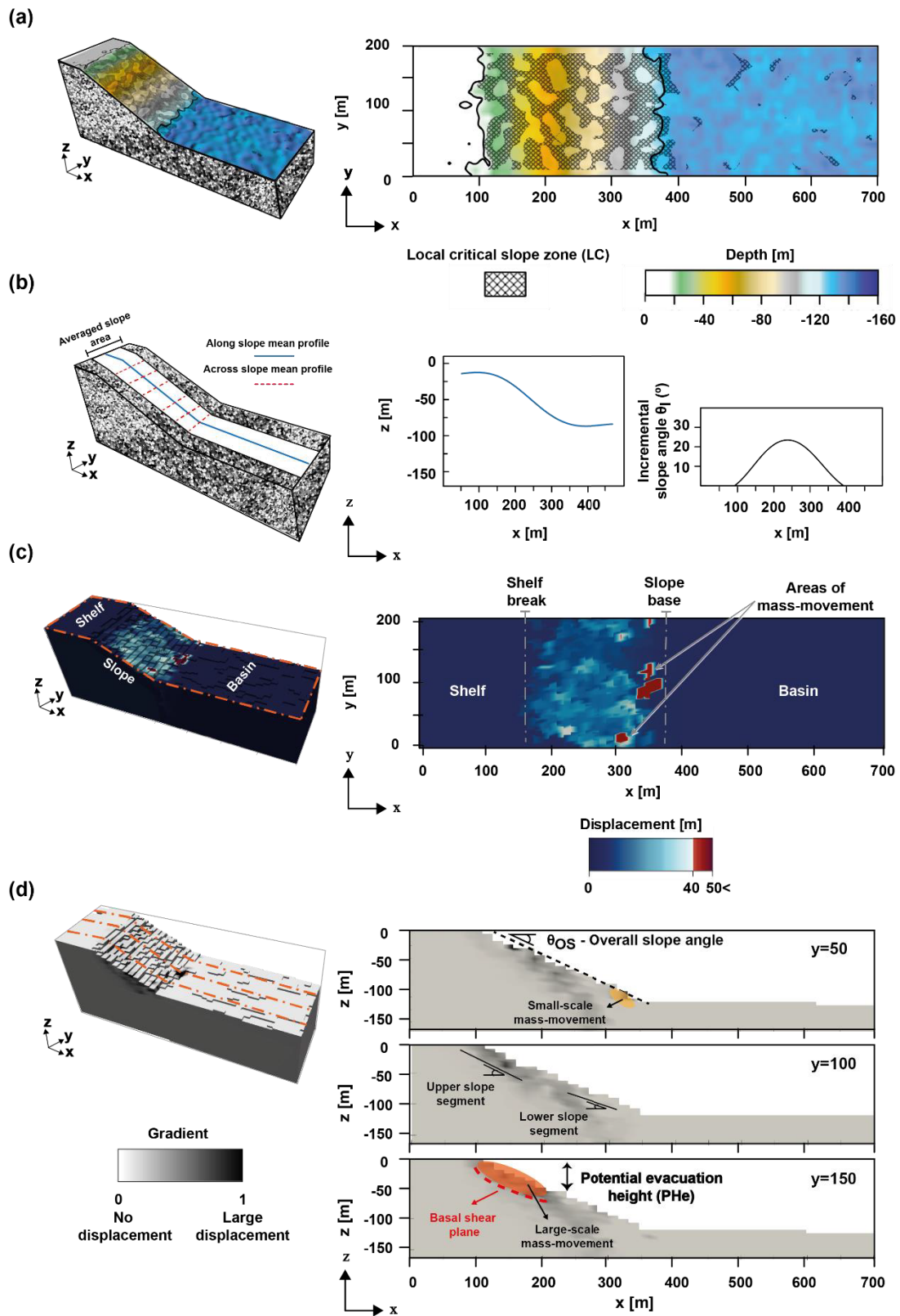


**Figure S5.2:** Defining a mass movements by a group of particles.

A group of particles were defined “connected” according to a connectivity test. The condition for connectivity was given as follows: particles that moved more than 40 m during one slope stage and were in contact - based on their radius during the same slope stage. Figure S2 illustrates the results that were further used to calculate the volumes of mass movements in Figure 6. The X- and Y-axis in the figure are the length and the width of the model, respectively (the x-axis is between 100 and 400 m to presenting only the slope). Each colour represents a new group according to the number of particles (E.g. green- a group of five particles etc.).

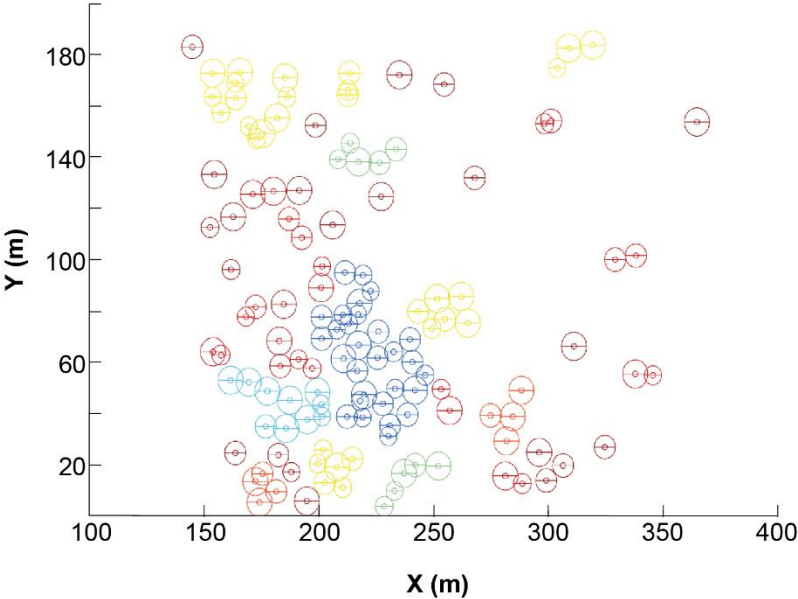


**Figure S5.3:** (a) The incremental slope angle development ( $\theta_I$ ) in models 1a, 1b, 2a and 2b. Black dashed lines present the change in the slope angle pattern of unimodal, transitional and bimodal, corresponding to slope angle at model stages t-7, t-10 and t-14, accordingly. For profile location, see blue line in the model illustration. The rate of slope angle change with model stages ( $\delta\theta_I/\delta t$ ) was averaged across discrete parts of the slope (see location in model illustration, red lines) for the upper (b) and (c) lower segments of the slope.

The rate of slope development presents significant variations across different parts of the slope. The development of the outermost parts of the slope, at  $x = 100$  [m] and  $x = 400$  [m] is delayed in all models whereby the latter always formed last (Figure S3b, c). At  $x=100$  [m], slope development started at approximately t-4 in the symmetrical slopes (models 1a and 2b) and slightly later at t-7 in the asymmetrical slopes (models 1b and 2a). The lowermost part of the slope at  $x = 400$  [m] always formed at last in all models at t-7 or t-8 (Figure S3c). The profile at  $x = 200$  [m] (above the mid-slope terrace) presented a sharp increase of slope angle development rate immediately at the beginning of all simulations at t-1, followed by an almost linear decrease (Figure 3b). The same applies to the profile just below the mid-slope terrace at  $x = 300$  [m] (Figure S3c). In both cases, negative values of the angle development rate also occur at later stages ( $> t-12$ ). Both reflect the change from an initial unimodal with a very centre steep, to a later bimodal slope with a flat mid-slope terrace.

The profile at  $x = 150$  [m] across the upper slope, shows a plateau without significant fluctuations of slope rate after reaching an intermediate rate of development in all models (Figure S3b). However, along the lower slope the profile at  $x = 350$  [m] a fluctuating rate of slope angle changes over long periods in models 1a, 2a and 2b and short terms in model 1b, varying between zero to intermediate rate of change (Figure S3c).

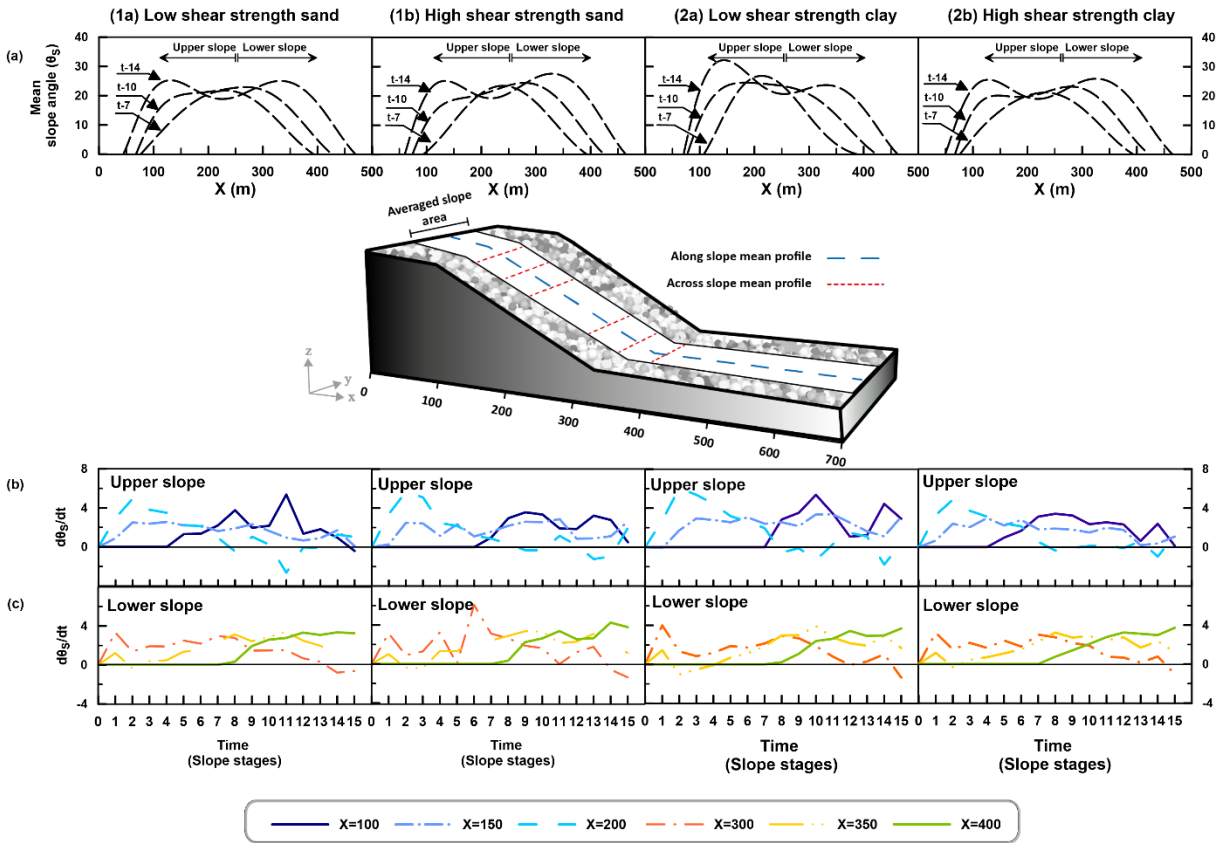


**Figure S5.4: Model 1a (Low shear strength ‘sand’)**

Left to right: bathymetry map view, draped with the “critical slope zone (FS<1)”; displacements map view of the initial location of a mass movement; displacements map view of the final location (total displacement of 40 m and beyond) of a mass movement; Gradient cross section at y=50 m; Gradient cross section at y=100 m; Gradient cross section at y=150 m

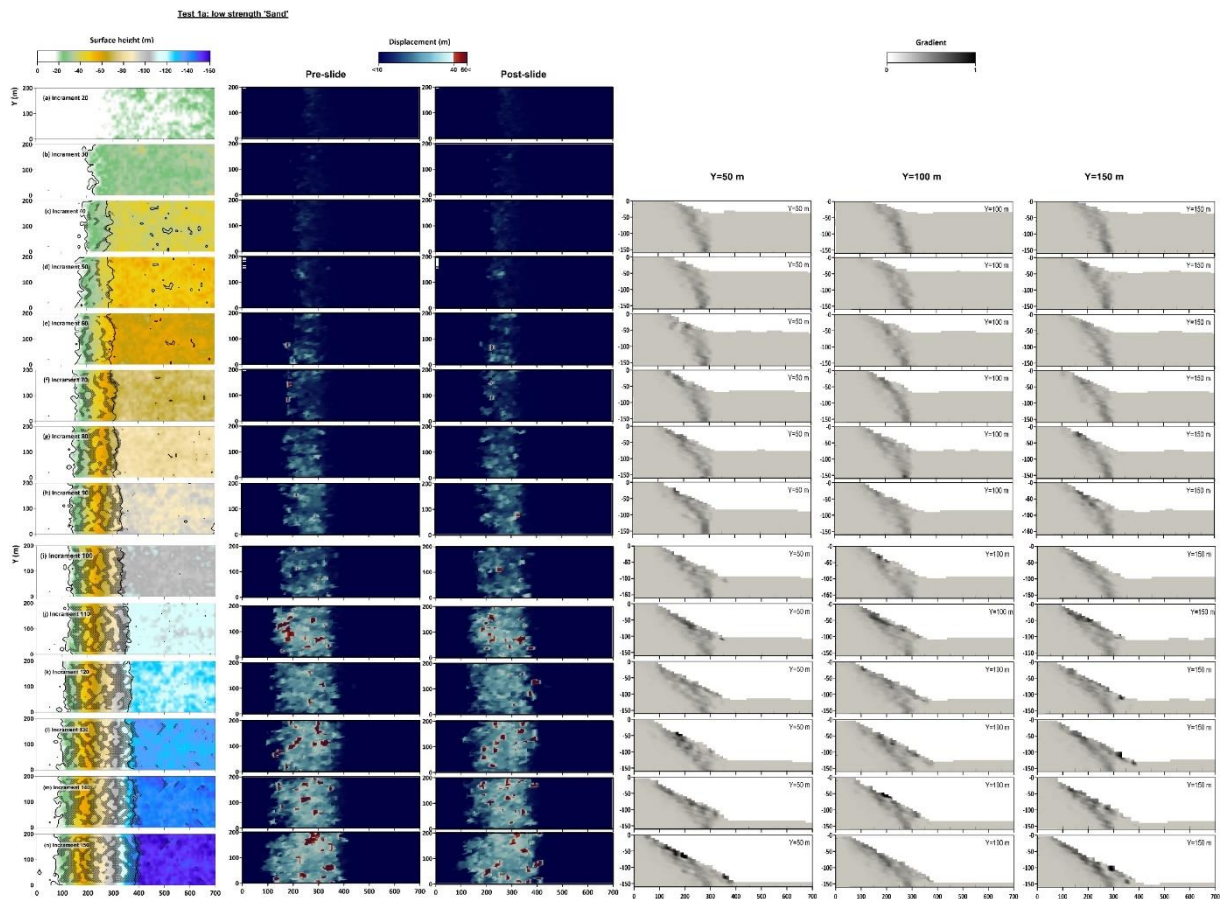


**Figure S5.5: Model 1b (High shear strength ‘sand’)**

Left to right: bathymetry map view, draped with the “critical slope zone (FS<1)”; displacements map view of the initial location of a mass movement; displacements map view of the final location (total displacement of 40 m and beyond) of a mass movement; Gradient cross section at y=50 m; Gradient cross section at y=100 m; Gradient cross section at y=150 m.

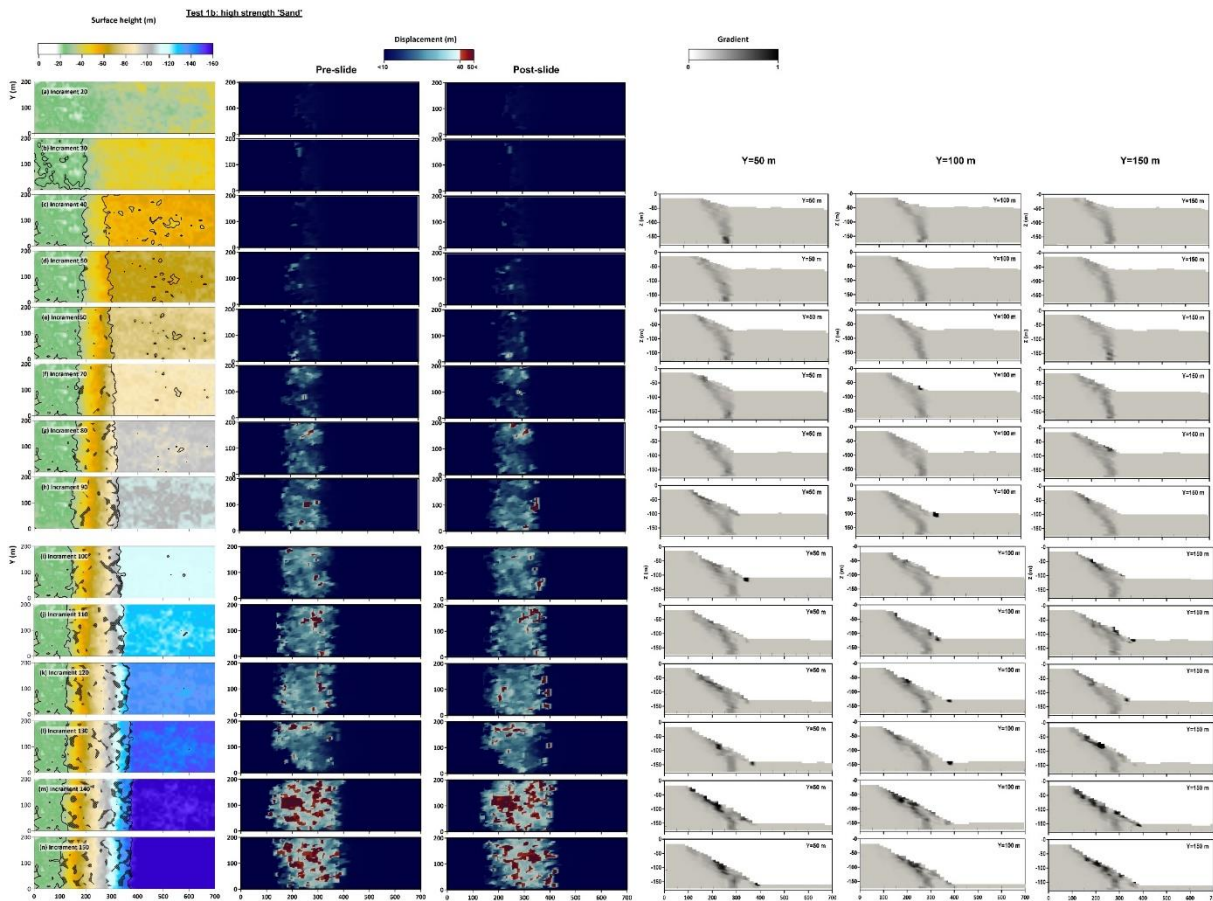
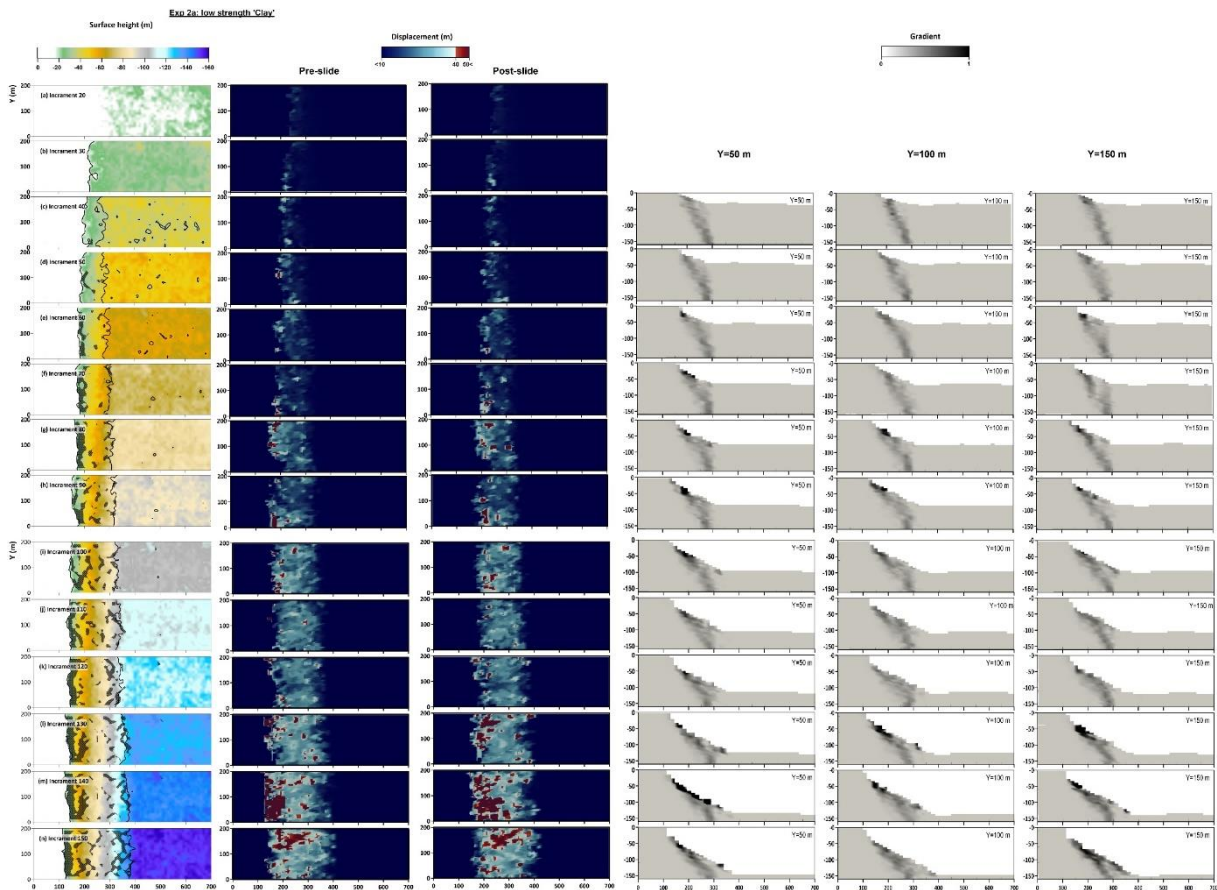


**Figure S5.6: Model 2a (Low shear strength ‘clay’)**

Left to right: bathymetry map view, draped with the “critical slope zone (FS<1)”; displacements map view of the initial location of a mass movement; displacements map view of the final location (total displacement of 40 m and beyond) of a mass movement; Gradient cross section at y=50 m; Gradient cross section at y=100 m; Gradient cross section at y=150 m.





## 6. Conclusions and outlook

---

---

This thesis explored how different sediment physical properties precondition the formation of submarine landslides. Its main aim was to bridge the gap between observations made in numerical and laboratory experiments, and field observations from various submarine landslides locations. The Currituck submarine landslide complex has been used in previous studies as a regional example to estimate tsunami risk along the USA Atlantic coasts. Here, we analysed sediments cores that sampled the slide complex to estimate how variations in sediments physical properties and shear strength could have preconditioned the slide. To qualitatively assess the role of sediments shear strength a numerical slope model was designed to estimate its influence on the size and distribution of submarine landslides along the slope. In this thesis, I defined four types of numerical sediments, with different shear strength, analogues to different occurrences of natural sediments. Implementing the numerical sediments in the slope models further enabled to observe in a macroscopic, slope-scale the size and distribution of landslides. Thus, the mechanical behaviour of the sediments implemented in the slope model, was microscopically controlled by variations of physical properties and macroscopically controlled the development of the slope.

In the following we summaries our results and relate them to the questions/hypothesis outlined in Chapter 1.6.

### 6.1. Main conclusions

#### *6.1.1. Possible preconditioning factors for the Currituck submarine landslide complex*

In recent years, the Currituck landslide complex was used as regional example of a large-scale landslide as potential tsunami source along the US Atlantic margins (Grilli et al., 2015; Schambach et al., 2019). Among the exposed large landslide along the western Atlantic margins, the style of deformation, morphology and well constrained volume have made Currituck slide available for tsunami modelling, despite the lack of physical properties and geotechnical characterization of the slide complex sediments. In the first part of this thesis (Chapter 3), cores that sampled the Currituck slide complex area were

analysed in detail, exploring the post-slide sediment physical properties and shear strength using sedimentological and geotechnical approaches.

The following questions were considered in the research:

- What are the physical, chemical and sedimentological characteristics of the post-slide sediments?
- Which processes contributed to the different physical properties and consequently the shear strength of the sediments in the Currituck area?
- Are there physical or sedimentological indications for stratigraphic weak layers (also strength interface)? What are their characteristics in the Currituck area?
- Understanding the strength properties and how they (potentially) vary with depth, what is the potential slope stability at depths similar to the observed failure?

Within the slide complex area, the cores penetrated the debris and the drape layer covering it. First, the sedimentological analysis of the cores suggests that the failed and unfailed slope sediments are characterized by differences in sediment sorting and particle size mode. Second, despite the lithological similarity throughout the drape layer, two units were distinguished based on the geochemical and geotechnical analysis. A post-slide, lower unit was deposited during the end of the Pleistocene, under sea level transgressive conditions and an increased sediment flux from the continent. The upper unit was deposited during the Holocene under sea level high stand conditions and a decreased sediment flux from the continent.

The variations in sediment flux and sea level appear to control the formation of possibly key stratigraphic successions interfaces, which invoke a change in the sediment's consolidation in response to different sediment accumulation rates (Chapter 3), illustrating normally consolidated sediments in the lower unit and apparently overconsolidated sediments in the upper unit. Although the variations in shear strength between the two units are relatively small, the FOS results demonstrate that they are statistically significant and have considerable influence on the present-day slope stability. The slope stability analysis indicated that the slope is currently stable yet additional trigger mechanisms such as an earthquake would be required to initiate failure. These conclusions however vary when slope stability analysis was applied separately to each

unit, indicating that the sediments deposited under high sedimentation rate and during sea level transgression, can generate a weak interface with the deposits above or below.

I therefore suggested that the formation of a shear plane in the Currituck slide complex can potentially occur at strength interfaces resulting from different consolidation conditions. These strength interfaces potentially also contribute to the partially blocky mobility appearance of the slide debris.

Though the current study observations focus on Currituck, the current oceanographic regime and the known sediment transport mechanism in the area today, I suggest that the Currituck slide complex is an example in which the main preconditioning factors relate to climatically-controlled fluvial variations in sediment flux along the slope.

#### *6.1.2. Size and distribution of the area susceptible to failure and the initial volume of failure*

The numerical approach used in this thesis first numerically characterized sediments based on variations in their physical properties and shear strength (Chapter 4) and second, used these results to model slope failure (Chapter 5). Though variations in sediment type are recognized as a major influence on shear strength variations, this understanding is mainly based on knowledge gathered from different locations. The numerical approach used in the thesis provides an independent understanding of the shear strength major role. Using 3D triaxial numerical experiments, the mechanical behaviour of two sediment endmembers, sand (cohesionless) and clay (cohesive) was simulated. The shear strength of each endmember was tested under different burial depth and consolidation states. This produced three levels of numerical sediments parametrization and showed that the extent of material calibration can be reduced for future characterization of numerical sediments. More importantly, the range of numerical characterization of sediments effectively reproduced results from laboratory examples of natural sediments under different consolidation states and over a range of compositions. From this range of numerical sediments, four were chosen to simulate endmembers of slope sediments.

The main questions that were investigated by the slope model were:

- How does shear strength effect frequency and distributions of the area susceptible to failure?
- How does the sediments shear strength effect the initial size and distribution of mass movements?

- How do the shear strength and consolidation state of the sediments precondition large-scale mass movements?

This study (Chapter 5) provided an independent understanding of slope failure initiation, the initial size and slope distribution considering the sediment type and variations in shear strength and consolidation. The simulation results showed how shear strength effectively preconditions the size and volume of a landslide.

*The sediments shear strength controls the lateral extension of area that is susceptible-to-failure.* The models showed that slopes characterized by under- to normally-consolidated sediments, susceptible-to-failure slope areas were extensive and contiguous areas. That is in contrast to slopes characterized by over-consolidated slope sediments susceptible-to-failure slope areas were discrete.

*The overall frequency of slope failure events in the models, is mainly controlled by consolidation.* This particularly highlights the influence of the underlying micromechanics on local stabilization of slope sediments as the slope overstepping is increasing.

Analysing the model simulations that have produced large-scale volume failure. While some types of sediment are more prone to failure than others, the same type of sediment can have different shear strength and consolidation states, which will further influence the size of failure. The models showed that particular conditions facilitate large-scale slope failure: dense sandy slope sediments and under- to normally-consolidated clayey slope sediments.

The results integrated with the current knowledge from submarine landslide recognized around the world, has produced accordingly four slope types of the potential failure characteristics.

## **6.2. Recommendations for future work**

This thesis has demonstrated the key influence of shear strength and consolidation of slope sediments on the initial location, extent and volume of a submarine landslide. Particularly the numerical modelling provided new knowledge showing the influence of physical properties on the size and distribution of slope failure. However, future direct measurements of slope sediments pre- and post-failure, gaining constraints of variations in consolidation from deeper slope sediments and simulating complex scenarios are essential future steps to gain deeper

understanding of slope failure processes and the influence of other preconditioning factors on slope failure.

*6.2.1. Understanding preconditioning factors in Currituck area due to climatic and depositional processes.*

The current study has pointed to a potential weak layer formation and thereby strength interface in the geological record of the Currituck area, however the information was limited to the last glacial interval (Chapter 3). The influence of the last glacial interval could have only been inferred from a study in the Hudson slope to the north. Current climate change predictions indicate an increase of storm events and their strength as well fire and flood events; altogether, these could potentially increase sediment fluxes from the continent to the slope. Current climate change predictions point towards increased frequency of events such as Atlantic tropical storms and hurricanes or floods which may alter the sediment flux from the continent to the slope (e.g. Little et al., 2015; Voudoukas et al., 2018). It is thus important to recognize whether previous Quaternary failure events in Currituck are also related to increased fluxes and sedimentation rates on the slope. An analysis of the sedimentary succession of a full glacial–interglacial cycle by means of sedimentological and geotechnical methods will offer a better understanding of potential weak layer formation in the sedimentary record. An analysis of older quaternary strata may offer insights into the potential of pore water dissipation in the Currituck area and whether excess pore pressure generation may play a role in preconditioning slope failure. Another approach to understand the preconditioning factors development in the Currituck area could be to use existing geophysical data. New age constraints for the Currituck landslide complex (Chaytor et al., in preparation) enabled a comparison between modelling results that demonstrated climatically-controlled sediment flux increase and slope failure. A first step to recognize previous submarine landslides in the Currituck area can be to analyse headwalls that were recognized by Hill et al., (2017) in the Quaternary seismic record. Observations from the relationship between the headwall scars and the reflectors of the sediments filling them (e.g., onlap, downlap), could generate preliminary constraints to the landslide occurrence relative to sea-level changes in the quaternary. Additional constraints for sea level variations can be obtained from the recently achieved seismic stratigraphic framework of the continental shelf offshore Delmarva. The extensive study (Brothers et al., 2020) has found evidence for extreme erosion on the shelf during Pleistocene glacial and interglacial cycles. Linking these erosional surfaces

to the shelf edge and slope area, could perhaps indicate gliding planes or strength interfaces in the slope.

*6.2.2. The area between Georges Bank and the mid-Atlantic as an archetype for preconditioning factor variations between glaciated and non-glaciated margins*

Understanding preconditioning factors of slope failure along passive margins is particularly important due to the lack of obvious triggers and the evidence of extremely large-scale landslides (ten Brink et al., 2016; Urgeles and Camerlenghi, 2013) and tsunamigenic potential (Løvholt et al., 2015). Along the USA Atlantic continental margins, several large-scale submarine landslides have been recognized, mainly between Georges Bank and the mid-Atlantic margins (Twichell et al., 2009). Despite different morphological characteristics of these slides, the Currituck submarine landslide morphology and estimated volume have been used to model the tsunami hazard along New England and the mid-Atlantic margins (Grilli et al., 2015; Schambach et al., 2019). Analysing the sedimentological and geotechnical characteristics of the drape sediments in Currituck landslide complex, has demonstrated the value of understanding paleo environmental conditions and the sedimentary processes that influence the shear strength and consolidation of the sediments (Chapter 3). The results further suggest that these conditions may have also influenced the style of deformation. Since the sediment core penetrated slope sediments down to a depth of ~8 m, only the last interglacial sediments interval was characterized. This characterization implies that the Currituck landslide complex should not be used as a key site to model the potential tsunami hazard along the USA Atlantic margins. However, it rather demonstrated that the Currituck is a key site to study submarine landslides in fluvially influenced, non-glaciated margins. By further studying submarine landslides from the glacially influenced Georges Bank margins, the two environments can promote the understanding of latitudinal influence on the development of slope failure preconditioning factors. It might also be important to understand the formation of large-scale landslides between glaciated to non-glaciated margins.

As detailed in section 1.3 and in Chapter 3, the geological and oceanographic settings have led to the formation of a continuous system that varies from north to south due to the decrease of a direct glacial influence and input and as well, the weakening of the main oceanographic current as it flows southward. In addition, the main sediment input is the continent from the west.

In this latitudinal continuous, these settings position the Currituck landslide complex as an endmember representing non-glaciated margins with a defined river-fed sedimentary input. The other endmember of the system is the slide complex off Georges Bank slide complex that directly was influenced by glacial sediment transport systems.

These conditions set the area between Georges Bank and the mid-Atlantic margins, as a natural laboratory to understand preconditioning factors that vary between glaciated to non-glaciated margins due to climatic variations and the resulting lithological variability, transport and depositional conditions.

Evaluating parameters such as sedimentary succession cycles, geotechnical parameters, current intensities, storms paths and intensities along the shelf, will help to identify potential variations in preconditioning factors between fluviially (non-glaciated) and glacially influenced slope failures.

Though challenging, this long-term objective will contribute to understanding slide mobility and via geotechnical and sedimentological characterization of the sediments will provide constraints to the failure mechanism and thus help to properly evaluate the tsunami hazard.

### *6.2.3. Future utilization of DEM to understand sediments mechanical behaviour and submarine landslides*

In the past two decades, DEM has proved the ability to simulate a range of geological scenarios and material behaviour. This was done for a particular set of parameters or a case study on the one hand (e.g. Peng et al., 2019) and a range of parameters to create a conceptual understanding of a geological process on the other hand (e.g. Katz et al., 2014; Morgan and McGovern, 2005). The procedure that was developed in Chapter 4 is used to simplify the range of parameters considered for siliciclastic sediments in numerical modelling and the slope models in Chapter 5 brought new insights to the role of shear strength as a preconditioning factor for submarine landslides. Continuing to use the DEM in future research, has a great potential to increase our understanding of these processes in various spatial and temporal scales under relatively low costs.

### *Modelling a single landslide – from initiation to the resting point*

The slope model in Chapter 5 simulated the initiation of slope failure under variations of shear strength and consolidation state. This was achieved by allowing the particles to reach equilibrium after every movement of approximately 1 m of the underlying box. The

analysis of the displacement gradient, highlighting the difference between particles that were displaced to those remained in place, allowed to observe the development of the shear plane. Increasing the calculation steps in future numerical experiments will increase the model resolution and may allow for more details regarding the shear plane to be observed. As demonstrated in the current study, a 3D evaluation of the shear plane development will be of much value to explore how complex landslides evolve. A potential additional complexity can be studied by incorporation pore pressure following the analysis of (Kock and Huhn, 2010).

### Modelling stratigraphic strength interfaces in slope setups

In Chapter 5, the numerical simulations have demonstrated how submarine landslides develop on monotype homogenous slopes; however, it has to be noted that the composition and texture of sediments along continental margins are more complex, in texture and geometry. The most recent understanding of weak layers by Gatter et al., (in review), suggests that failure planes usually form in the vicinity of an interface between distinct lithologies that together comprise a weak layer. In order to understand under which conditions, i.e., failure mechanisms, weak layers form and how they may affect slope stability, advanced geotechnical tests of sediment samples from the undisturbed sediment sequences are needed. Such samples, however, are often not readily available and it is difficult to reproduce and measure natural processes in a laboratory environment. Kock et al. (2007) has demonstrated the potential of using DEM to simulate the development of failure planes on a micro-scale; however, our understanding of failure plane formation for a given slope geometry and under specific geological constraints remains unknown. Using DEM, Liu and Koyi (2013) have demonstrated how both lithological and structural parameters are important to pre-condition subaerial landslides size and runout distance. Utilizing this approach to model lithological and structural difference together with the DEM-CFD approach that incorporates fluid pressure, could provide insights to the characteristics and the development of a shear plane. This may also show how the slide volume remains intact or disintegrate and evolve as a result of different lithological composition and slope geometries.

*Mechanical behaviour characterization of sediments containing microplastics:*

Documentation of deep sea sediments distribution in recent years has shown how human pollution, particularly microplastics and other forms of particulates (e.g. pesticides and pharmaceuticals) are transported to- and distributed in the deep marine environments (Kane et al., 2020; Pohl et al., 2020). Understanding the long- and short-term stability of sediments containing pollutants or particulate microplastics is still not known. Studies aiming to understand mixed sediments and microplastic resistance to transport (Chubarenko et al., 2018; e.g. Khatmullina and Chubarenko, 2019) and further the post-deposition potential increase or decrease of the soil's strength (e.g. O'Kelly et al., 2021) are only now emerging. The recently documented influence of bottom currents on the distribution of seafloor microplastics (Kane et al., 2020; Kane and Clare, 2019), poses the question whether these may have the potential to form weak layers and how they may influence slope stability. The impact of mixed sediments and pollutants release as result of a mass movement is unknown but may pose a considerable threat to the marine food web and further influence the economics of developing countries islands that relay on fishing (Hodgson et al., 2018). Understanding the mechanical behaviour of mixed sediments and particulate pollutants / plastics in terms of pore water dissipation, consolidation and ultimately shear strength is therefore important.

The wide variety in types of microplastics suggests that laboratory experiments would be expensive and time consuming. The approach developed in Chapter 4, calibrating a range of numerical materials using DEM will provide an inexpensive and relatively fast approach to explore sediment-microplastics mixtures and their mechanical behaviour. Such an approach may further allow to deepen our understanding of slope stability along highly polluted fluvial, coastal and deep marine environments.



# Bibliography

---

- Abe, S., van Gent, H., Urai, J.L., 2011. DEM simulation of normal faults in cohesive materials. *Tectonophysics* 512, 12–21. <https://doi.org/10.1016/j.tecto.2011.09.008>
- Anandarajah, A., 2003. Discrete element modeling of leaching-induced apparent overconsolidation in Kaolinite. *Soils Found.* 43, 1–13.
- Anandarajah, A., Lavoie, D., 2002. Numerical simulation of the microstructure and compression behavior of Eckernförde Bay sediments. *Mar. Geol.* 182, 3–27. [https://doi.org/10.1016/S0025-3227\(01\)00226-2](https://doi.org/10.1016/S0025-3227(01)00226-2)
- Anantanasakul, P., Yamamuro, J.A., Lade, P. V., 2012. Three-dimensional drained behavior of normally consolidated anisotropic kaolin clay. *Soils Found.* 52, 146–159. <https://doi.org/10.1016/j.sandf.2012.01.014>
- Antonellini, M.A., Pollard, D.D., 1995. Distinct element modeling of deformation bands in sandstone. *J. Struct. Geol.* 17, 1165–1182. [https://doi.org/10.1016/0191-8141\(95\)00001-T](https://doi.org/10.1016/0191-8141(95)00001-T)
- Ask, M.V.S., Kopf, A., 2004. Constraints on the state of in situ effective stress and the mechanical behavior of ODP Leg 186 claystones in the Japan Trench forearc. *Isl. Arc* 13, 242–257. <https://doi.org/10.1111/j.1440-1738.2003.00423.x>
- Baeten, N.J., Laberg, J.S., Forwick, M., Vorren, T.O., Vanneste, M., Forsberg, C.F., Kvalstad, T.J., Ivanov, M., 2013. Morphology and origin of smaller-scale mass movements on the continental slope off northern Norway. *Geomorphology* 187, 122–134. <https://doi.org/10.1016/j.geomorph.2013.01.008>
- Bahr, A., Jiménez-Espejo, F.J., Kolasinac, N., Grunert, P., Hernández-Molina, F.J., Röhl, U., Voelker, A.H.L., Escutia, C., Stow, D.A. V., Hodell, D., Alvarez-Zarikian, C.A., 2014. Deciphering bottom current velocity and paleoclimate signals from contourite deposits in the Gulf of Cádiz during the last 140 kyr: An inorganic geochemical approach. *Geochemistry, Geophys. Geosystems* 15, 3145–3160. <https://doi.org/10.1002/2014GC005356>
- Bennett, R.H., Bryant, W.R., Keller, G.H., 1981. Clay Fabric of Selected Submarine Sediments: Fundamental Properties and Models. *SEPM J. Sediment. Res.* 51. <https://doi.org/10.1306/212f7c52-2b24-11d7-8648000102c1865d>
- Biscaye, P.E., Flagg, C.N., Falkowski, P.G., 1994. The shelf edge exchange processes experiment, SEEP-II: an introduction to hypotheses, results and conclusions. *Deep. Res. Part II* 41, 231–252. [https://doi.org/10.1016/0967-0645\(94\)90022-1](https://doi.org/10.1016/0967-0645(94)90022-1)

- Blott, S.J., Pye, K., 2001. Gradistat: A grain size distribution and statistics package for the analysis of unconsolidated sediments. *Earth Surf. Process. Landforms* 26, 1237–1248. <https://doi.org/10.1002/esp.261>
- Booth, J., O’Leary, D., Popenoe, P., Danforth, W., 1993. U.S. Atlantic Continental Slope Landslides: Their Distribution, General Attributes, and Implications, in: Lee, H.J., Schwab, W., Twichell, D.C. (Eds.), *Submarine Landslides: Selected Studies in the U.S. Exclusive Economic Zone*. pp. 14–22.
- Booth, J.S., Circe, R.C., Dahl, A.G., 1984. Geotechnical characterization and mass-movement potential of the United States North Atlantic Continental Slope and Rise.
- Booth, J.S., Farrow, R.A., Rice, T.A., 1981. Geotechnical properties and slope stability analysis of surficial sediments on the Georges Bank continental slope.
- Brackenridge, R.E., Nicholson, U., Sapiie, B., Stow, D., Tappin, D.R., 2020. Indonesian throughflow as a preconditioning mechanism for submarine landslides in the makassar strait, in: *Geological Society Special Publication*. Geological Society of London, pp. 195–217. <https://doi.org/10.1144/SP500-2019-171>
- Brothers, D.S., Andrews, B.D., Walton, M.A.L., Greene, H.G., Barrie, J.V., Miller, N.C., ten Brink, U., East, A.E., Haeussler, P.J., Kluesner, J.W., Conrad, J.E., 2019a. Slope failure and mass transport processes along the Queen Charlotte Fault, southeastern Alaska. *Geol. Soc. London, Spec. Publ.* 477, 69–83. <https://doi.org/10.1144/SP477.30>
- Brothers, D.S., Haeussler, P.J., Liberty, L., Finlayson, D., Geist, E., Labay, K., Byerly, M., 2016. A submarine landslide source for the devastating 1964 Chenega tsunami, southern Alaska. *Earth Planet. Sci. Lett.* 438, 112–121. <https://doi.org/10.1016/j.epsl.2016.01.008>
- Brothers, D.S., Maier, K.L., Kluesner, J.W., Conrad, J.E., Chaytor, J.D., 2019b. The santa cruz basin submarine landslide complex, southern california: Repeated failure of uplifted basin sediment. *SEPM Spec. Publ.* 110, 117–134. <https://doi.org/10.2110/sepmsp.110.05>
- Brothers, D.S., Maier, K.L., Kluesner, J.W., Conrad, J.E., Chaytor, J.D., 2018. The Santa Cruz Basin Submarine Landslide Complex, southern California: repeated failure of inverted basin sediment. *From Mt. to Abyss Calif. Borderl. as an Arch. South. Calif. Geol. Evol.* <https://doi.org/10.2110/sepmsp.110.05>
- Brothers, D.S., ten Brink, U.S., Andrews, B.D., Chaytor, J.D., 2013. Geomorphic characterization of the U.S. Atlantic continental margin. *Mar. Geol.* 338, 46–63. <https://doi.org/10.1016/j.margeo.2012.12.008>
- Brothers, L.L., Foster, D.S., Pendleton, E.A., Baldwin, W.E., 2020. Seismic stratigraphic framework of the continental shelf offshore Delmarva, U.S.A.: Implications for Mid-

- Atlantic Bight Evolution since the Pliocene. *Mar. Geol.* 428, 106287.  
<https://doi.org/10.1016/j.margeo.2020.106287>
- Bunn, A.R., McGregor, B.A., 1980. Morphology of the North Carolina continental slope, western North Atlantic, shaped by deltaic sedimentation and slumping. *Mar. Geol.* 37, 253–266. [https://doi.org/10.1016/0025-3227\(80\)90105-X](https://doi.org/10.1016/0025-3227(80)90105-X)
- Campbell, C.S., Cleary, P.W., Hopkins, M., 1995. Large-scale landslide simulations: Global deformation, velocities and basal friction. *J. Geophys. Res.* 100, 8267.  
<https://doi.org/10.1029/94JB00937>
- Carter, G.D.O., Cooper, R., Gafeira, J., Howe, J.A., Long, D., 2020. Morphology of small-scale submarine mass movement events across the northwest United Kingdom. *Geomorphology* 365, 107282. <https://doi.org/10.1016/j.geomorph.2020.107282>
- Carvajal, M., Araya-Cornejo, C., Sepúlveda, I., Melnick, D., Haase, J.S., 2019. Nearly Instantaneous Tsunamis Following the Mw 7.5 2018 Palu Earthquake. *Geophys. Res. Lett.* 46, 5117–5126. <https://doi.org/10.1029/2019GL082578>
- Casas, D., Chiocci, F., Casalbore, D., Ercilla, G., de Urbina, J.O., 2016. Magnitude-frequency distribution of submarine landslides in the Gioia Basin (southern Tyrrhenian Sea). *Geo-Marine Lett.* 36, 405–414. <https://doi.org/10.1007/s00367-016-0458-2>
- Chaytor, J.D., Shipboard scientific party, T., 2012. Cruise Report HRS120928JC: Investigation of Submarine Landslides along the Mid-Atlantic Slope, Currituck and Baltimore Canyon Regions. <https://doi.org/10.7284/901149>
- Chaytor, J.D., ten Brink, U.S., Solow, A.R., Andrews, B.D., 2009. Size distribution of submarine landslides along the U.S. Atlantic margin. *Mar. Geol.* 264, 16–27.  
<https://doi.org/10.1016/j.margeo.2008.08.007>
- Chaytor, J.D., Twichell, D.C., ten Brink, U.S., Buczkowski, B.J., Andrews, B.D., 2007. Revisiting submarine mass movements along the u.s. atlantic continental margin: implications for tsunami hazards, in: *Submarine Mass Movements and Their Consequences*. pp. 395–403.
- Cheung, G., O’Sullivan, C., 2008. Effective simulation of flexible lateral boundaries in two- and three-dimensional DEM simulations. *Particuology* 6, 483–500.  
<https://doi.org/10.1016/j.partic.2008.07.018>
- Cheung, L.Y.G., O’Sullivan, C., Coop, M.R., 2013. Discrete element method simulations of analogue reservoir sandstones. *Int. J. Rock Mech. Min. Sci.* 63, 93–103.  
<https://doi.org/10.1016/j.ijrmms.2013.07.002>
- Chubarenko, I., Esiukova, E., Bagaev, A., Isachenko, I., Demchenko, N., Zobkov, M.,

- Efimova, I., Bagaeva, M., Khatmullina, L., 2018. Behavior of Microplastics in Coastal Zones, in: *Microplastic Contamination in Aquatic Environments*. Elsevier, pp. 175–223. <https://doi.org/10.1016/B978-0-12-813747-5.00006-0>
- Churchill, J.H., Gawarkiewicz, G.G., 2012. Pathways of shelf water export from the Hatteras shelf and slope. *J. Geophys. Res. Ocean.* 117, n/a-n/a. <https://doi.org/10.1029/2012JC007995>
- Churchill, J.H., Wirick, C.D., Flagg, C.N., Pietrafesa, L.J., 1994. Sediment resuspension over the continental shelf east of the Delmarva Peninsula. *Deep Sea Res. Part II Top. Stud. Oceanogr.* 41, 341–363. [https://doi.org/10.1016/0967-0645\(94\)90027-2](https://doi.org/10.1016/0967-0645(94)90027-2)
- Clare, M., Chaytor, J., Dabson, O., Gamboa, D., Georgiopoulou, A., Eady, H., Hunt, J., Jackson, C., Katz, O., Krastel, S., León, R., Micallef, A., Moernaut, J., Moriconi, R., Moscardelli, L., Mueller, C., Normandeau, A., Patacci, M., Steventon, M., Urlaub, M., Völker, D., Wood, L., Jobe, Z., 2018. A consistent global approach for the morphometric characterization of subaqueous landslides, in: *8th International Symposium on Submarine Mass Movements and Their Consequences, ISSMMTC 2018*. pp. 455–477. <https://doi.org/10.1144/SP477.15>
- Clare, M.A., Vardy, M.E., Cartigny, M.J.B., Talling, P.J., Himsforth, M.D., Dix, J.K., Harris, J.M., Whitehouse, R.J.S., Belal, M., 2017. Direct monitoring of active geohazards: Emerging geophysical tools for deep-water assessments. *Near Surf. Geophys.* 15, 427–444. <https://doi.org/10.3997/1873-0604.2017033>
- Colman, S.M., Halka, J.P., Hobbs III, C.H., Mixon, R.B., Foster, D.S., 1990. Ancient channels of the Susquehanna River beneath Chesapeake Bay and the Delmarva Peninsula. *Geol. Soc. Am. Bull.* 102, 1268–1279. [https://doi.org/10.1130/0016-7606\(1990\)102<1268:ACOTSR>2.3.CO;2](https://doi.org/10.1130/0016-7606(1990)102<1268:ACOTSR>2.3.CO;2)
- Colman, S.M., Mixon, R.B., 1988. The record of major quaternary sea-level changes in a large coastal plain estuary, Chesapeake Bay, Eastern United States. *Palaeogeogr. Palaeoclimatol. Palaeoecol.* 68, 99–116. [https://doi.org/10.1016/0031-0182\(88\)90033-8](https://doi.org/10.1016/0031-0182(88)90033-8)
- Craig, M.J., Baas, J.H., Amos, K.J., Strachan, L.J., Manning, A.J., Paterson, D.M., Hope, J.A., Nodder, S.D., Baker, M.L., 2020. Biomediation of submarine sediment gravity flow dynamics. *Geology* 48, 72–76. <https://doi.org/10.1130/G46837.1>
- Craig, R.F., 2004. *Craig's soil mechanics*. CRC Press.
- Croudace, I.W., Rothwell, R.G., 2015. *Micro-XRF Studies of Sediment Cores: Applications of a non-destructive tool for the environmental sciences*, *Developments in Paleoenvironmental Research*. Springer Netherlands, Dordrecht.

- <https://doi.org/10.1007/978-94-017-9849-5>
- Cundall, P.A., Strack, O.D.L., 1979. A discrete numerical model for granular assemblies. *Geotechnique* 29, 47–65. <https://doi.org/10.1680/geot.1979.29.1.47>
- Cundall, P.A., Strack, O.D.L., 1978. BALL — A program to model granular media using the distinct element method, Technical Note. London.
- Dalyander, P.S., Butman, B., 2015. Characteristics of storms driving wave-induced seafloor mobility on the U.S. East Coast continental shelf. *Cont. Shelf Res.* 104, 1–14. <https://doi.org/10.1016/j.csr.2015.05.003>
- Dan, G., Sultan, N., Savoye, B., 2007. The 1979 Nice harbour catastrophe revisited: Trigger mechanism inferred from geotechnical measurements and numerical modelling. *Mar. Geol.* 245, 40–64. <https://doi.org/10.1016/j.margeo.2007.06.011>
- Dan, G., Sultan, N., Savoye, B., Deverchere, J., Yelles, K., 2009. Quantifying the role of sandy-silty sediments in generating slope failures during earthquakes: Example from the Algerian margin. *Int. J. Earth Sci.* 98, 769–789. <https://doi.org/10.1007/s00531-008-0373-5>
- Davis, W.R., 1993. The role of bioturbation in sediment resuspension and its interaction with physical shearing. *J. Exp. Mar. Bio. Ecol.* 171, 187–200. [https://doi.org/10.1016/0022-0981\(93\)90003-7](https://doi.org/10.1016/0022-0981(93)90003-7)
- De Bono, J.P., McDowell, G.R., 2014. DEM of triaxial tests on crushable sand. *Granul. Matter* 16, 551–562. <https://doi.org/10.1007/s10035-014-0500-x>
- DeVore, J.R., Sawyer, D.E., 2016. Shear strength of siliciclastic sediments from passive and active margins (0–100 m below seafloor): insights into seismic strengthening, in: *Submarine Mass Movements and Their Consequences*. Springer, Cham, pp. 173–180.
- Ding, X., Zhang, L., Zhu, H., Zhang, Q., 2014. Effect of Model Scale and Particle Size Distribution on PFC3D Simulation Results. *Rock Mech. Rock Eng.* 47, 2139–2156. <https://doi.org/10.1007/s00603-013-0533-1>
- Djéran-Maigre, I., Tessier, D., Grunberger, D., Velde, B., Vasseur, G., 1998. Evolution of microstructures and of macroscopic properties of some clays during experimental compaction. *Mar. Pet. Geol.* 15, 109–128. [https://doi.org/10.1016/S0264-8172\(97\)00062-7](https://doi.org/10.1016/S0264-8172(97)00062-7)
- Ducassou, E., Migeon, S., Mulder, T., Murat, A., Capotondi, L., Bernasconi, S.M., Mascle, J., 2009. Evolution of the Nile deep-sea turbidite system during the late quaternary: Influence of climate change on fan sedimentation. *Sedimentology* 56, 2061–2090. <https://doi.org/10.1111/j.1365-3091.2009.01070.x>

- Dugan, B., Daigle, H., 2011. Data report: permeability, compressibility, stress state, and grain size of shallow sediments from Sites C0004, C0006, C0007, and C0008 of the Nankai accretionary complex, in: Kinoshita, M., Tobin, H., Ashi, J., Kimura, G., Lallemand, S., Screaton, E.J., Curewitz, D., Masago, H., Moe, K.T., Scientists, the E. 314/315/316 (Eds.), Proc. IODP, 314/315/316. Washington, DC.  
<https://doi.org/10.2204/iodp.proc.314315316.208.2011>
- Dugan, B., Flemings, P.B., 2002. Fluid flow and stability of the US continental slope offshore New Jersey from the Pleistocene to the present. *Geofluids* 2, 137–146.  
<https://doi.org/10.1046/j.1468-8123.2002.00032.x>
- Eisenstadt, G., Sims, D., 2005. Evaluating sand and clay models: Do rheological differences matter? *J. Struct. Geol.* 27, 1399–1412. <https://doi.org/10.1016/j.jsg.2005.04.010>
- Elverhoi, A., Breien, H., De Blasio, F. V., Harbitz, C.B., Pagliardi, M., 2010. Submarine landslides and the importance of the initial sediment composition for run-out length and final deposit. *Ocean Dyn.* 60, 1027–1046. <https://doi.org/10.1007/s10236-010-0317-z>
- Elyashiv, H., Bookman, R., Siemann, L., ten Brink, U., Huhn, K., 2020. Numerical Characterization of Cohesive and Non-Cohesive ‘Sediments’ under Different Consolidation States Using 3D DEM Triaxial Experiments. *Processes* 8, 1252.  
<https://doi.org/10.3390/pr8101252>
- Engelhart, S.E., Peltier, W.R., Horton, B.P., 2011. Holocene relative sea-level changes and glacial isostatic adjustment of the U.S. Atlantic coast. *Geology* 39, 751–754.  
<https://doi.org/10.1130/G31857.1>
- Feng, K., Montoya, B.M., Evans, T.M., 2017. Discrete element method simulations of bio-cemented sands. *Comput. Geotech.* 85, 139–150.  
<https://doi.org/10.1016/j.compgeo.2016.12.028>
- Fratantoni, P.S., Pickart, R.S., 2007. The Western North Atlantic Shelfbreak Current System in Summer. *J. Phys. Oceanogr.* 37, 2509–2533. <https://doi.org/10.1175/JPO3123.1>
- Gales, J.A., Leat, P.T., Larter, R.D., Kuhn, G., Hillenbrand, C.D., Graham, A.G.C., Mitchell, N.C., Tate, A.J., Buys, G.B., Jokat, W., 2014. Large-scale submarine landslides, channel and gully systems on the southern Weddell Sea margin, Antarctica. *Mar. Geol.* 348, 73–87. <https://doi.org/10.1016/j.margeo.2013.12.002>
- Garziglia, S., Migeon, S., Ducassou, E., Loncke, L., Mascle, J., 2008. Mass-transport deposits on the Rosetta province (NW Nile deep-sea turbidite system, Egyptian margin): Characteristics, distribution, and potential causal processes. *Mar. Geol.* 250, 180–198.  
<https://doi.org/10.1016/j.margeo.2008.01.016>

- Gatter, R., Clare, M.A., Huhn, K., 2019. The significance of weak layers for submarine slope failure, in: *Geophysical Research Abstracts*.
- Gatter, R., Clare, M.A., Hunt, J.E., Watts, M., Madhusudhan, B.N., Talling, P.J., Huhn, K., 2020. A multi-disciplinary investigation of the AFEN slide: The relationship between contourites and submarine landslides. *Geol. Soc. Spec. Publ.* 500, 173–193.  
<https://doi.org/10.1144/SP500-2019-184>
- Gatter, R., Clare, M.A., Kuhlmann, J., Huhn, K., 2021. Characterisation of weak layers, physical controls on their global distribution and their role in submarine landslide formation. *Earth-Science Rev.* 223, 103845.  
<https://doi.org/10.1016/j.earscirev.2021.103845>
- Geist, E.L., Lynett, P.J., Chaytor, J.D., 2009. Hydrodynamic modeling of tsunamis from the Currituck landslide. *Mar. Geol.* 264, 41–52.  
<https://doi.org/10.1016/j.margeo.2008.09.005>
- Grilli, S.T., O'Reilly, C., Harris, J.C., Bakhsh, T.T., Tehranirad, B., Banihashemi, S., Kirby, J.T., Baxter, C.D.P., Eggeling, T., Ma, G., Shi, F., 2015. Modeling of SMF tsunami hazard along the upper US East Coast: detailed impact around Ocean City, MD. *Nat. Hazards* 76, 705–746. <https://doi.org/10.1007/s11069-014-1522-8>
- Guo, P., Su, X., 2007. Shear strength, interparticle locking, and dilatancy of granular materials. *Can. Geotech. J.* 44, 579–591. <https://doi.org/10.1139/T07-010>
- Guo, Y., Morgan, J.K., 2004. Influence of normal stress and grain shape on granular friction: Results of discrete element simulations. *J. Geophys. Res. Solid Earth* 109, 1–16.  
<https://doi.org/10.1029/2004JB003044>
- Gylland, A.S., Jostad, H.P., Nordal, S., 2014. Experimental study of strain localization in sensitive clays. *Acta Geotech.* 9, 227–240. <https://doi.org/10.1007/s11440-013-0217-8>
- Hage, S., Cartigny, M.J.B., Sumner, E.J., Clare, M.A., Hughes Clarke, J.E., Talling, P.J., Lintern, D.G., Simmons, S.M., Silva Jacinto, R., Vellinga, A.J., Allin, J.R., Azpiroz-Zabala, M., Gales, J.A., Hizzett, J.L., Hunt, J.E., Mozzato, A., Parsons, D.R., Pope, E.L., Stacey, C.D., Symons, W.O., Vardy, M.E., Watts, C., 2019. Direct Monitoring Reveals Initiation of Turbidity Currents From Extremely Dilute River Plumes. *Geophys. Res. Lett.* 46, 11310–11320. <https://doi.org/10.1029/2019GL084526>
- Hampton, M.A., Lee, H.J., Locat, J., 1996. Submarine landslides. *Rev. Geophys.* 34, 33–59.  
<https://doi.org/10.1029/95rg03287>
- Hanebuth, T.J.J., Lantzsch, H., 2008. A Late Quaternary sedimentary shelf system under hyperarid conditions: Unravelling climatic, oceanographic and sea-level controls (Golfe

- d'Arguin, Mauritania, NW Africa). *Mar. Geol.* 256, 77–89.  
<https://doi.org/10.1016/j.margeo.2008.10.001>
- Harbitz, C.B., Løvholt, F., Bungum, H., 2014. Submarine landslide tsunamis: How extreme and how likely? *Nat. Hazards* 72, 1341–1374. <https://doi.org/10.1007/s11069-013-0681-3>
- Harders, R., Ranero, C.R., Weinrebe, W., Behrmann, J.H., 2011. Submarine slope failures along the convergent continental margin of the Middle America Trench. *Geochemistry, Geophys. Geosystems* 12. <https://doi.org/10.1029/2010GC003401>
- Hardy, S., 2019. Novel discrete element modelling of Gilbert-type delta formation in an active tectonic setting—first results. *Basin Res.* 31, 77–91. <https://doi.org/10.1111/bre.12309>
- Hardy, S., Finch, E., 2007. Mechanical stratigraphy and the transition from trishear to kink-band fault-propagation fold forms above blind basement thrust faults: A discrete-element study. *Mar. Pet. Geol.* 24, 75–90. <https://doi.org/10.1016/j.marpetgeo.2006.09.001>
- Hathaway, J.C., 1972. Regional clay mineral fades in estuaries and continental margin of the United States east coast. *Mem. Geol. Soc. Am.* 133, 293–316.  
<https://doi.org/10.1130/MEM133-p293>
- Hathaway, J.C., Poag, C.W., Valentine, P.C., Miller, R.E., Schultz, D.M., Manheim, F.T., Kohout, F.A., Bothner, M.H., Sangrey, D.A., 1979. U.S. geological survey core drilling on the Atlantic shelf. *Science* (80-. ). 206, 515–527.  
<https://doi.org/10.1126/science.206.4418.515>
- Hattab, M., Fleureau, J.M., 2010. Experimental study of kaolin particle orientation mechanism. *Geotechnique* 60, 323–331. <https://doi.org/10.1680/geot.2010.60.5.323>
- Hattab, M., Hammad, T., Fleureau, J.M., 2015. Internal friction angle variation in a kaolin/montmorillonite clay mix and microstructural identification. *Geotechnique* 65, 1–11. <https://doi.org/10.1680/geot.13.P.081>
- Hattab, M., Hammad, T., Fleureau, J.M., Hicher, P.Y., 2013. Behaviour of a sensitive marine sediment : microstructural investigation. *Géotechnique* 63, 71–84.
- Hazzard, J.F., Mair, K., 2003. The importance of the third dimension in granular shear. *Geophys. Res. Lett.* 30. <https://doi.org/10.1029/2003GL017534>
- Heerema, C.J., Talling, P.J., Cartigny, M.J., Paull, C.K., Bailey, L., Simmons, S.M., Parsons, D.R., Clare, M.A., Gwiazda, R., Lundsten, E., Anderson, K., Maier, K.L., Xu, J.P., Sumner, E.J., Rosenberger, K., Gales, J., Mcgann, M., Carter, L., Pope, E., 2020. What determines the downstream evolution of turbidity currents? *Earth Planet. Sci. Lett.* 532, 116023. <https://doi.org/10.1594/IEDA/324529>

- Hewitt, C., Stouffer, R., Broccoli, A., Mitchell, J., Valdes, P.J., 2003. The effect of ocean dynamics in a coupled GCM simulation of the Last Glacial Maximum. *Clim. Dyn.* 20, 203–218. <https://doi.org/10.1007/s00382-002-0272-6>
- Hicher, P.Y., Wayudi, H., Tessier, D., Hicher, P.Y., Wayudi, H., Tessier, D., 2000. Microstructural analysis of inherent and induced anisotropy in clay. *Mech. Cohesive-Frictional Mater.* 5, 337–341.
- Hill, J.C., Brothers, D.S., Craig, B.K., ten Brink, U.S., Chaytor, J.D., Flores, C.H., 2017. Geologic controls on submarine slope failure along the central U.S. Atlantic margin: Insights from the Currituck Slide Complex. *Mar. Geol.* 385, 114–130. <https://doi.org/10.1016/j.margeo.2016.10.007>
- Hill, J.C., Driscoll, N.W., Weissel, J.K., Goff, J. a., 2004. Large-scale elongated gas blowouts along the U.S. Atlantic margin. *J. Geophys. Res. B Solid Earth* 109, B09101. <https://doi.org/10.1029/2004JB002969>
- Hill, J.C., Watt, J.T., Brothers, D.S., Kluesner, J.W., 2020. Submarine canyons, slope failures and mass transport processes in southern cascadia, in: *Geological Society Special Publication. Geological Society of London*, pp. 453–475. <https://doi.org/10.1144/SP500-2019-169>
- Hizzett, J.L., Hughes Clarke, J.E., Sumner, E.J., Cartigny, M.J.B., Talling, P.J., Clare, M.A., 2018. Which Triggers Produce the Most Erosive, Frequent, and Longest Runout Turbidity Currents on Deltas? *Geophys. Res. Lett.* 45, 855–863. <https://doi.org/10.1002/2017GL075751>
- Hobbs, C.H., 2004. Geological history of Chesapeake Bay, USA. *Quat. Sci. Rev.* 23, 641–661. <https://doi.org/10.1016/j.quascirev.2003.08.003>
- Hodgson, D.M., Bernhardt, A., Clare, M.A., Da Silva, A.-C., Fosdick, J.C., Mauz, B., Midtkandal, I., Owen, A., Romans, B.W., 2018. Grand Challenges (and Great Opportunities) in Sedimentology, Stratigraphy, and Diagenesis Research. *Front. Earth Sci.* 6, 173. <https://doi.org/10.3389/feart.2018.00173>
- Huhn, K., Kock, I., Kopf, A.J., 2006. Comparative numerical and analogue shear box experiments and their implications for the mechanics along the failure plane of landslides. *Nor. Geol. Tidsskr.* 86, 209–220.
- Huhn, K., Strozyk, F., Kock, I., 2016. Quantifying the key role of slope material peak strength – using discrete element simulations, in: *Advances in Natural and Technological Hazards Research. Springer, Cham*, pp. 537–545. [https://doi.org/10.1007/978-3-319-20979-1\\_54](https://doi.org/10.1007/978-3-319-20979-1_54)
- Hühnerbach, V., Masson, D.G., 2004. Landslides in the North Atlantic and its adjacent seas:

- An analysis of their morphology, setting and behaviour. *Mar. Geol.* 213, 343–362.  
<https://doi.org/10.1016/j.margeo.2004.10.013>
- Hutton, E.W.H., Syvitski, J.P.M., 2004. Advances in the numerical modeling of sediment failure during the development of a continental margin. *Mar. Geol.* 203, 367–380.  
[https://doi.org/10.1016/S0025-3227\(03\)00316-5](https://doi.org/10.1016/S0025-3227(03)00316-5)
- Hynes-Griffin, M.E., Franklin, A.G., 1984. Rationalizing the seismic coefficient method. Ian Nicholas McCave, 2007. Deep-Sea Sediment Deposits and Properties Controlled by Currents. *Dev. Mar. Geol.* 1, 11–12.
- Ikari, M.J., Kopf, A.J., 2015. The role of cohesion and overconsolidation in submarine slope failure. *Mar. Geol.* 369, 153–161. <https://doi.org/10.1016/j.margeo.2015.08.012>
- Ikari, M.J., Kopf, A.J., 2011. Cohesive strength of clay-rich sediment. *Geophys. Res. Lett.* 38, 1–5. <https://doi.org/10.1029/2011GL047918>
- IPCC, 2007. Climate change 2007 synthesis report, in: Pachauri, R., Reisinger, A. (Eds.), Contribution of Working Groups I, II and III to the Fourth Assessment Report of the Intergovernmental Panel on Climate Change. IPCC (Intergovernmental Panel on Climate Change), Geneva, p. 104.
- Itasca, 2014. PFC — Particle Flow Code, Ver. 5.0. Minneapolis.
- Iwashita, K., Oda, M., 1999. Mechanics of granular materials: an introduction. CRC press.
- Jaradat, K.A., Abdelaziz, S.L., 2019. On the use of discrete element method for multi-scale assessment of clay behavior. *Comput. Geotech.*  
<https://doi.org/10.1016/j.compgeo.2019.05.001>
- Jocković, S., Vukićević, M., 2017. Bounding surface model for overconsolidated clays with new state parameter formulation of hardening rule. *Comput. Geotech.* 83, 16–29.  
<https://doi.org/10.1016/j.compgeo.2016.10.013>
- Kane, I.A., Clare, M.A., 2019. Dispersion, Accumulation, and the Ultimate Fate of Microplastics in Deep-Marine Environments: A Review and Future Directions. *Front. Earth Sci.* 7. <https://doi.org/10.3389/feart.2019.00080>
- Kane, I.A., Clare, M.A., Miramontes, E., Wogelius, R., Rothwell, J.J., Garreau, P., Pohl, F., 2020. Seafloor microplastic hotspots controlled by deep-sea circulation. *Science* (80-. ). 368, 1140–1145. <https://doi.org/10.1126/science.aba5899>
- Katz, O., Aharonov, E., Morgan, J.K., Dugan, B., 2014. Controls on the size and geometry of landslides: Insights from discrete element numerical simulations. *Geomorphology* 220, 104–113. <https://doi.org/10.1016/j.geomorph.2014.05.021>
- Katz, O., Reuven, E., Aharonov, E., 2015a. Submarine landslides and fault scarps along the

- eastern Mediterranean Israeli continental-slope. *Mar. Geol.* 369, 100–115.  
<https://doi.org/10.1016/j.margeo.2015.08.006>
- Katz, O., Reuven, E., Aharonov, E., 2015b. Submarine landslides and fault scarps along the eastern Mediterranean Israeli continental-slope. *Mar. Geol.* 369, 100–115.  
<https://doi.org/10.1016/j.margeo.2015.08.006>
- Khatmullina, L., Chubarenko, I., 2019. Transport of marine microplastic particles: why is it so difficult to predict? *Anthr. Coasts* 2, 293–305. <https://doi.org/10.1139/anc-2018-0024>
- Kock, I., Huhn, K., 2010. How does fluid inflow geometry control slope destabilization? *Submar. Mass Movements Their Consequences - 4th Int. Symp.* 28, 191–201.  
[https://doi.org/10.1007/978-90-481-3071-9\\_16](https://doi.org/10.1007/978-90-481-3071-9_16)
- Kock, I., Huhn, K., 2007a. Influence of particle shape on the frictional strength of sediments - A numerical case study. *Sediment. Geol.* 196, 217–233.  
<https://doi.org/10.1016/j.sedgeo.2006.07.011>
- Kock, I., Huhn, K., 2007b. Numerical investigation of localization and micromechanics in a stratified soil specimen. *J. Struct. Geol.* 29, 1679–1694.  
<https://doi.org/10.1016/j.jsg.2007.07.013>
- Kopf, A.J., Stegmann, S., Garziglia, S., Henry, P., Dennielou, B., Haas, S., Weber, K.C., 2016. Soft sediment deformation in the shallow submarine slope off Nice (France) as a result of a variably charged Pliocene aquifer and mass wasting processes. *Sediment. Geol.* 344, 290–309. <https://doi.org/10.1016/j.sedgeo.2016.05.014>
- Krastel, S., Li, W., Urlaub, M., Georgiopoulou, A., Wynn, R.B., Schwenk, T., Stevenson, C., Feldens, P., 2018. Mass wasting along the NW African continental margin, in: 8th International Symposium on Submarine Mass Movements and Their Consequences, ISSMMTC 2018. The Geological Society of London, pp. 151–167.  
<https://doi.org/10.1144/SP477.36>
- Lee, H.J., 2009. Timing of occurrence of large submarine landslides on the Atlantic Ocean margin. *Mar. Geol.* 264, 53–64. <https://doi.org/10.1016/j.margeo.2008.09.009>
- Lee, H.J., Locat, J., Dartnell, P., Minasian, D., Wong, F.L., 2000. A GIS-based regional analysis of the potential for shallow-seated submarine slope failure, in: *Proc. 8th Int. Sympos. on Landslides*. Cardiff, pp. 26–30.
- Lee, H.J., Locat, J., Desgagnés, P., Parsons, J.D., McAdoo, B.G., Orange, D.L., Puig, P., Wong, F.L., Dartnell, P., Boulanger, E., 2007. Submarine Mass Movements on Continental Margins, in: *Continental Margin Sedimentation*. Blackwell Publishing Ltd., Oxford, UK, UK, pp. 213–274. <https://doi.org/10.1002/9781444304398.ch5>

- Lee, H.J., Orzech, K., Locat, J., Boulanger, E., Konrad, J.M., 2004. Seismic strengthening, a conditioning factor influencing submarine landslide development, in: 57th Canadian Geotechnical Conference. Can. Geotech. Soc., Quebec.
- Lintern, D.G., Mosher, D.C., Moscardelli, L., Bobrowsky, P.T., Campbell, D.C., Chaytor, J.D., Clague, J., Georgiopoulou, A., Lajeunesse, P., Normandeau, A., Piper, D.J.W., Scherwath, M., Stacey, C., Turner, D., 2019. Subaqueous Mass Movements and their Consequences: Assessing Geohazards, Environmental Implications and Economic Significance of Subaqueous Landslides. Geological Society of London Special Publications, London.
- Little, C.M., Horton, R.M., Kopp, R.E., Oppenheimer, M., Vecchi, G.A., Villarini, G., 2015. Joint projections of US East Coast sea level and storm surge. *Nat. Clim. Chang.* 5, 1114–1120. <https://doi.org/10.1038/nclimate2801>
- Liu, Z., Koyi, H.A., 2013. The impact of a weak horizon on kinematics and internal deformation of a failure mass using discrete element method. *Tectonophysics* 586, 95–111. <https://doi.org/10.1016/j.tecto.2012.11.009>
- Locat, J., Lee, H., Kayen, R., Israel, K., Savoie, M.C., Boulanger, É., 2002. Shear strength development with burial in Eel River margin slope sediments. *Mar. Georesources Geotechnol.* 20, 111–135. <https://doi.org/10.1080/03608860290051831>
- Locat, J., Lee, H., ten Brink, U.S., Twichell, D., Geist, E., Sansoucy, M., 2009. Geomorphology, stability and mobility of the Currituck slide. *Mar. Geol.* 264, 28–40. <https://doi.org/10.1016/j.margeo.2008.12.005>
- Locat, J., Lee, H.J., 2002. Submarine landslides: advances and challenges. *Can. Geotech. J.* 39, 193–212. <https://doi.org/10.1139/t01-089>
- Lommen, S., Schott, D., Lodewijks, G., 2014. DEM speedup: Stiffness effects on behavior of bulk material. *Particuology* 12, 107–112. <https://doi.org/10.1016/j.partic.2013.03.006>
- LongJohn, T., Morgan, J.K., Dugan, B., 2018. Microstructural Evolution of Porosity and Stress During the Formation of Brittle Shear Fractures: A Discrete Element Model Study. *J. Geophys. Res. Solid Earth* 123, 2228–2245. <https://doi.org/10.1002/2017JB014842>
- Løvholt, F., Bondevik, S., Laberg, J.S., Kim, J., Boylan, N., 2017. Some giant submarine landslides do not produce large tsunamis. *Geophys. Res. Lett.* 44, 8463–8472. <https://doi.org/10.1002/2017GL074062>
- Løvholt, F., Pedersen, G., Harbitz, C.B., Glimsdal, S., Kim, J., 2015. On the characteristics of landslide tsunamis. *Philos. Trans. R. Soc. A Math. Phys. Eng. Sci.* 373, 2053.

- <https://doi.org/10.1098/rsta.2014.0376>
- Løvholt, F., Schulten, I., Mosher, D., Harbitz, C., Krastel, S., 2019. Modelling the 1929 grand banks slump and landslide tsunami. *Geol. Soc. Spec. Publ.* 477, 315–331.  
<https://doi.org/10.1144/SP477.28>
- Mair, K., Abe, S., 2011. Breaking Up: Comminution Mechanisms in Sheared Simulated Fault Gouge. *Pure Appl. Geophys.* 168, 2277–2288. <https://doi.org/10.1007/s00024-011-0266-6>
- Mair, K., Abe, S., 2008. 3D numerical simulations of fault gouge evolution during shear: Grain size reduction and strain localization. *Earth Planet. Sci. Lett.* 274, 72–81.  
<https://doi.org/10.1016/j.epsl.2008.07.010>
- Mair, K., Frye, K.M., Marone, C., 2002. Influence of grain characteristics on the friction of granular shear zones. *J. Geophys. Res. Solid Earth* 107, ECV 4-1-ECV 4-9.  
<https://doi.org/10.1029/2001JB000516>
- Mallinson, D.J., Culver, S.J., Riggs, S.R., Thieler, E.R., Foster, D., Wehmiller, J., Farrell, K.M., Pierson, J., 2010. Regional seismic stratigraphy and controls on the Quaternary evolution of the Cape Hatteras region of the Atlantic passive margin, USA. *Mar. Geol.* 268, 16–33. <https://doi.org/10.1016/j.margeo.2009.10.007>
- Manchanda, R., Olson, J.E., Sharma, M.M., 2012. Mechanical, failure and flow properties of sands: Micro-mechanical models. 46th US Rock Mech. / Geomech. Symp. 2012 3, 1555–1569.
- Manning, J., 1991. Middle Atlantic Bight salinity: interannual variability. *Cont. Shelf Res.* 11, 123–137. [https://doi.org/10.1016/0278-4343\(91\)90058-E](https://doi.org/10.1016/0278-4343(91)90058-E)
- Marri, A., Wanatowski, D., Yu, H.S., 2012. Drained behaviour of cemented sand in high pressure triaxial compression tests. *Geomech. Geoenviron.* 7, 159–174.  
<https://doi.org/10.1080/17486025.2012.663938>
- Marshall, N.R., Piper, D.J.W., Saint-Ange, F., Campbell, D.C., 2014. Late Quaternary history of contourite drifts and variations in Labrador Current flow, Flemish Pass, offshore eastern Canada. *Geo-Marine Lett.* 34, 3–4. <https://doi.org/10.1007/s00367-014-0377-z>
- Masson, D., Harbitz, C., Wynn, R., Pedersen, G., Løvholt, F., 2006. Submarine landslides: processes, triggers and hazard prediction. *Philos. Trans. R. Soc. A Math. Phys. Eng. Sci.* 364, 2009–2039. <https://doi.org/10.1098/rsta.2006.1810>
- Masson, D.G., Wynn, R.B., Talling, P.J., 2010. Large Landslides on Passive Continental Margins: Processes, Hypotheses and Outstanding Questions. *Submar. Mass Movements Their Consequences* 28, 153–165. [https://doi.org/10.1007/978-90-481-3071-9\\_13](https://doi.org/10.1007/978-90-481-3071-9_13)

- McAdoo, B.G., Pratson, L.F., Orange, D.L., 2000. Submarine landslide geomorphology, US continental slope. *Mar. Geol.* 169, 103–136. [https://doi.org/10.1016/S0025-3227\(00\)00050-5](https://doi.org/10.1016/S0025-3227(00)00050-5)
- McHugh, C.M., Olson, H.C., 2002. Pleistocene chronology of continental margin sedimentation: New insights into traditional models, New Jersey. *Mar. Geol.* 186, 389–411. [https://doi.org/10.1016/S0025-3227\(02\)00198-6](https://doi.org/10.1016/S0025-3227(02)00198-6)
- McHugh, C.M.G., Damuth, J.E., Mountain, G.S., 2002. Cenozoic mass-transport facies and their correlation with relative sea-level change, New Jersey continental margin. *Mar. Geol.* 184, 295–334. [https://doi.org/10.1016/S0025-3227\(01\)00240-7](https://doi.org/10.1016/S0025-3227(01)00240-7)
- Meckel, L.D., 2011. Reservoir Characteristics and Classification of Sand-Prone Submarine Mass-Transport Deposits, in: *Mass-Transport Deposits in Deepwater Settings*. SEPM (Society for Sedimentary Geology), pp. 423–452. <https://doi.org/10.2110/sepm.096.423>
- Migeon, S., Cattaneo, A., Hassoun, V., Larroque, C., Corradi, N., Fanucci, F., Dano, A., de Lepinay, B.M., Sage, F., Gorini, C., 2011. Morphology, distribution and origin of recent submarine landslides of the Ligurian Margin (North-western Mediterranean): Some insights into geohazard assessment. *Mar. Geophys. Res.* 32, 225–243. <https://doi.org/10.1007/s11001-011-9123-3>
- Milliman, J.D., Pilkey, O.H., Ross, D.A., 1972. Sediments of the continental margin off the eastern United States. *Bull. Geol. Soc. Am.* 83, 1315–1334. [https://doi.org/10.1130/0016-7606\(1972\)83\[1315:SOTCMO\]2.0.CO;2](https://doi.org/10.1130/0016-7606(1972)83[1315:SOTCMO]2.0.CO;2)
- Mindlin, R.D., Deresiewicz, H., 1953. Elastic Spheres in Contact under Varying Oblique Forces. *J. Appl. Mech.* 20, 327–344.
- Miramontes, E., Sultan, N., Garziglia, S., Jouet, G., Pelleter, E., Cattaneo, A., 2018. Altered volcanic deposits as basal failure surfaces of submarine landslides. *Geology* 46, 663–666. <https://doi.org/10.1130/G40268.1>
- Mitchell, J.K., Soga, K., 2005. *Fundamentals of Soil Behavior*, 3rd ed. John Wiley & Sons, Hoboken, NJ.
- Mitchell, N.C., 2005. Interpreting long-profiles of canyons in the USA Atlantic continental slope. *Mar. Geol.* 214, 75–99. <https://doi.org/10.1016/j.margeo.2004.09.005>
- Miyakawa, A., Yamada, Y., Matsuoka, T., 2010. Effect of increased shear stress along a plate boundary fault on the formation of an out-of-sequence thrust and a break in surface slope within an accretionary wedge, based on numerical simulations. *Tectonophysics* 484, 127–138.

- Moernaut, J., Wiemer, G., Kopf, A., Strasser, M., 2020. Evaluating the sealing potential of young and thin mass-transport deposits: Lake villarrica, Chile. *Geol. Soc. Spec. Publ.* 500, 129–146. <https://doi.org/10.1144/SP500-2019-155>
- Mollison, K.C., Power, H.E., Clarke, S.L., Baxter, A.T., Hubble, T.C.T., 2020. Sedimentology, structure, and age of the Wide Bay Canyon submarine landslide on the southeast Australian continental slope. *Mar. Geol.* 419. <https://doi.org/10.1016/j.margeo.2019.106063>
- Moore, G.F., Lackey, J.K., Strasser, M., Yamashita, M., 2019. Submarine Landslides on the Nankai Trough Accretionary Prism (Offshore Central Japan). pp. 247–259. <https://doi.org/10.1002/9781119500513.ch15>
- Mora, P., Place, D., 1994. Simulation of the frictional stick-slip instability. *Pure Appl. Geophys.* 143, 61–87.
- Morgan, J.K., 1999. Numerical simulations of granular shear zones using the distinct element method: 2. Effects of particle size distribution and interparticle friction on mechanical behavior. *J. Geophys. Res. Solid Earth* 104, 2721–2732. <https://doi.org/10.1029/1998JB900056>
- Morgan, J.K., Boettcher, M.S., 1999. Numerical simulations of granular shear zones using DEM 1. Shear zone kinematics and micromechanics. *J. Geophys.*
- Morgan, J.K., McGovern, P.J., 2005a. Discrete element simulations of gravitational volcanic deformation: 1. Deformation structures and geometries. *J. Geophys. Res. Solid Earth* 110, 1–22. <https://doi.org/10.1029/2004JB003252>
- Morgan, J.K., McGovern, P.J., 2005b. Discrete element simulations of gravitational volcanic deformation: 2. Mechanical analysis. *J. Geophys. Res. Solid Earth* 110, 1–13. <https://doi.org/10.1029/2004JB003253>
- Morgenstern, N.R., 1967. Submarine slumping and the initiation of turbidity currents, in: Richards, A. (Ed.), *Marine Geotechnique*. University of Illinois Press, pp. 189–220.
- Morrow, C.A., Moore, D.E., Lockner, D.A., 2017. Frictional strength of wet and dry montmorillonite. *J. Geophys. Res. Solid Earth* 122, 3392–3409. <https://doi.org/10.1002/2016JB013658>
- Moscardelli, L., Wood, L., 2016. Morphometry of mass-transport deposits as a predictive tool. *Bull. Geol. Soc. Am.* 128, 47–80. <https://doi.org/10.1130/B31221.1>
- Mosher, D.C., Campbell, D.C., Gardner, J.V., Piper, D.J.W., Chaytor, J.D., Rebesco, M., 2017. The role of deep-water sedimentary processes in shaping a continental margin: The Northwest Atlantic. *Mar. Geol.* 393, 245–259.

- <https://doi.org/10.1016/j.margeo.2017.08.018>
- Mosher, D.C., Monahan, P.A., Barrie, J. V., Courtney, R.C., 2004. Coastal submarine failures in the Strait of Georgia, British Columbia: Landslides of the 1946 Vancouver Island earthquake. *J. Coast. Res.* 20, 277–291. [https://doi.org/10.2112/1551-5036\(2004\)20\[277:csfits\]2.0.co;2](https://doi.org/10.2112/1551-5036(2004)20[277:csfits]2.0.co;2)
- Mountjoy, J., Micallef, A., 2018. Submarine Landslides. pp. 235–250. [https://doi.org/10.1007/978-3-319-57852-1\\_13](https://doi.org/10.1007/978-3-319-57852-1_13)
- Mountjoy, J.J., Georgiopoulou, A., Chaytor, J., Clare, M.A., Gamboa, D., Moernaut, J., 2020. Subaqueous mass movements in the context of observations of contemporary slope failure. *Geol. Soc. London, Spec. Publ.* 500, SP500-2019–237. <https://doi.org/10.1144/SP500-2019-237>
- Mulder, T., Syvitski, J.P.M., 1996. Climatic and Morphologic Relationships of Rivers: Implications of Sea-Level Fluctuations on River Loads. *J. Geol.* 104, 509–523. <https://doi.org/10.1086/629849>
- Murray, M., 2002. Is laser particle size determination possible for carbonate-rich lake sediments? *J. Paleolimnol.* 27, 173–183.
- Nandanwar, M., Chen, Y., 2017. Modeling and measurements of triaxial tests for a sandy loam soil. *Can. Biosyst. Eng.* 59, 2.1-2.8. <https://doi.org/10.7451/CBE.2017.59.2.1>
- Naughton, F., Keigwin, L., Peteet, D., Costas, S., Desprat, S., Oliveira, D., de Vernal, A., Voelker, A., Abrantes, F., 2015. A 12,000-yr pollen record off Cape Hatteras - Pollen sources and mechanisms of pollen dispersion. *Mar. Geol.* 367, 118–129. <https://doi.org/10.1016/j.margeo.2015.06.003>
- Normandeau, A., Bourgault, D., Neumeier, U., Lajeunesse, P., St-Onge, G., Gostiaux, L., Chavanne, C., 2020. Storm-induced turbidity currents on a sediment-starved shelf: Insight from direct monitoring and repeat seabed mapping of upslope migrating bedforms. *Sedimentology* 67, 1045–1068. <https://doi.org/10.1111/sed.12673>
- O’Kelly, B.C., El-Zein, A., Liu, X., Patel, A., Fei, X., Sharma, S., Mohammad, A., Goli, V.S.N.S., Wang, J.J., Li, D., Shi, Y., Xiao, L., Kuntikana, G., Shashank, B.S., Sarris, T.S., Hanumantha Rao, B., Mohamed, A.M.O., Paleologos, E.K., Nezhad, M.M., Singh, D.N., 2021. Microplastics in soils: an environmental geotechnics perspective. *Environ. Geotech.* 1–33. <https://doi.org/10.1680/jenge.20.00179>
- Obelcz, J., Brothers, D., Chaytor, J., ten Brink, U., Ross, S.W., Brooke, S., 2014. Geomorphic characterization of four shelf-sourced submarine canyons along the U.S. Mid-Atlantic continental margin. *Deep. Res. Part II Top. Stud. Oceanogr.* 104, 106–119.

- <https://doi.org/10.1016/j.dsr2.2013.09.013>
- Owen, M., Day, S., Maslin, M., 2007. Late Pleistocene submarine mass movements: occurrence and causes. *Quat. Sci. Rev.* 26, 958–978.  
<https://doi.org/10.1016/j.quascirev.2006.12.011>
- Pagano, A.G., Magnanimo, V., Weinhart, T., Tarantino, A., 2020. Exploring the micromechanics of non-active clays by way of virtual DEM experiments. *Geotechnique* 70, 303–316. <https://doi.org/10.1680/jgeot.18.P.060>
- Park, L.K., Suneel, M., Chul, I.J., 2008. Shear strength of jumunjin sand according to relative density. *Mar. Georesources Geotechnol.* 26, 101–110.  
<https://doi.org/10.1080/10641190802022445>
- Parsons, J.D., Friedrichs, C.T., Traykovski, P.A., Mohrig, D., Imran, J., Syvitski, J.P.M., Parker, G., Puig, P., Buttles, J.L., Garca, M.H., 2007. The Mechanics of Marine Sediment Gravity Flows, in: Nittrouer, C.J., Austin, M., Field, J., Syvitski, Wiberg P (Eds.), *Continental Margin Sedimentation*. Blackwell Publishing Ltd., Oxford, UK, pp. 275–337. <https://doi.org/10.1002/9781444304398.ch6>
- Parsons, T., Geist, E.L., Ryan, H.F., Lee, H.J., Haeussler, P.J., Lynett, P., Hart, P.E., Sliter, R., Roland, E., 2014. Source and progression of a submarine landslide and tsunami: The 1964 Great Alaska earthquake at Valdez. *J. Geophys. Res. Solid Earth* 119, 8502–8516.  
<https://doi.org/10.1002/2014JB011514>
- Peltier, W.R., Fairbanks, R.G., 2006. Global glacial ice volume and Last Glacial Maximum duration from an extended Barbados sea level record. *Quat. Sci. Rev.* 25, 3322–3337.  
<https://doi.org/10.1016/j.quascirev.2006.04.010>
- Peng, W., Song, S., Yu, C., Bao, Y., Sui, J., Hu, Y., 2019. Forecasting Landslides via Three-Dimensional Discrete Element Modeling: Helong Landslide Case Study. *Appl. Sci.* 9, 5242. <https://doi.org/10.3390/app9235242>
- Perret, D., Locat, J., Leroueil, S., 1995. Strength development with burial in fine-grained sediments from the Saguenay Fjord, Quebec. *Can. Geotech. J.* 32, 247–262.
- Pichel, L.M., Finch, E., Gawthorpe, R.L., 2019. The Impact of Pre-Salt Rift Topography on Salt Tectonics: A Discrete-Element Modeling Approach. *Tectonics* 38, 1466–1488.  
<https://doi.org/10.1029/2018TC005174>
- Piper, D.J.W., Mosher, D.C., Campbell, D.C., 2013. Controls on the distribution of major types of submarine landslides, in: Clague, J.J., Stead, D. (Eds.), *Landslides*. Cambridge University Press, Cambridge, pp. 95–107.  
<https://doi.org/10.1017/CBO9780511740367.010>

- Poag, C.W., Sevon, W.D., 1989. A record of Appalachian denudation in postrift Mesozoic and Cenozoic sedimentary deposits of the U.S. middle Atlantic continental margin. *Geomorphology* 2, 119–157.
- Pohl, F., Eggenhuisen, J.T., Kane, I.A., Clare, M.A., 2020. Transport and Burial of Microplastics in Deep-Marine Sediments by Turbidity Currents. *Environ. Sci. Technol.* 54, 4180–4189. <https://doi.org/10.1021/acs.est.9b07527>
- Pope, E.L., Talling, P.J., Carter, L., 2017. Which earthquakes trigger damaging submarine mass movements: Insights from a global record of submarine cable breaks? *Mar. Geol.* 384, 131–146. <https://doi.org/10.1016/j.margeo.2016.01.009>
- Popenoe, P., Coward, E.L., Cashman, K.V. 1982 . A regional assessment of potential environmental hazards to and limitations on petroleum development of the southeastern United States Atlantic continental shelf, slope, and rise, offshore North Carolina. .
- Potyondy, D.O., 2015. The bonded-particle model as a tool for rock mechanics research and application: current trends and future directions. *Geosystem Eng.* 18, 1–28. <https://doi.org/10.1080/12269328.2014.998346>
- Potyondy, D.O., Cundall, P.A., 2004. A bonded-particle model for rock. *Int. J. rock Mech. Min. Sci.* 41, 1329–1364.
- Prior, D.B., Doyle, E.H., Neurauter, T., 1986. The Currituck Slide, mid-Atlantic continental slope — Revisited. *Mar. Geol.* 73, 25–45. [https://doi.org/10.1016/0025-3227\(86\)90109-X](https://doi.org/10.1016/0025-3227(86)90109-X)
- Rasmussen, C., 2020. Particle Sizing in Geosciences: Explanation of various techniques and pre-treatments, Particle Sizing in Geosciences: Explanation of various techniques and pre-treatments. Aarhus University Library. <https://doi.org/10.7146/aul.374>
- Rathbun, A.P., Marone, C., 2010. Effect of strain localization on frictional behavior of sheared granular materials. *J. Geophys. Res.* 115. <https://doi.org/10.1029/2009jb006466>
- Rothenburg, L., Bathurst, R.J., 1993. Influence of particle eccentricity on micromechanical behavior of granular materials. *Mech. Mater.* 16, 141–152.
- Rothenburg, L., Bathurst, R.J., 1992. Micromechanical features of granular assemblies with planar elliptical particles. *Geotechnique* 42, 79–95.
- Rothwell, R.G., Rack, F.R., 2006. New techniques in sediment core analysis: an introduction. *Geol. Soc. London, Spec. Publ.* 267, 1–29. <https://doi.org/10.1144/GSL.SP.2006.267.01.01>
- Saba, V.S., Griffies, S.M., Anderson, W.G., Winton, M., Alexander, M.A., Delworth, T.L., Hare, J.A., Harrison, M.J., Rosati, A., Vecchi, G.A., Zhang, R., 2016. Enhanced

- warming of the North Atlantic Ocean under climate change. *J. Geophys. Res. Ocean.* 121, 118–132.  
<https://doi.org/10.1002/2015JC011346>
- Sadek, M.A., Chen, Y., Liu, J., 2011. Simulating shear behavior of a sandy soil under different soil conditions. *J. Terramechanics* 48, 451–458.  
<https://doi.org/10.1016/j.jterra.2011.09.006>
- Saffer, D.M., Marone, C., 2003. Comparison of smectite- and illite-rich gouge frictional properties: Application to the updip limit of the seismogenic zone along subduction megathrusts. *Earth Planet. Sci. Lett.* 215, 219–235. [https://doi.org/10.1016/S0012-821X\(03\)00424-2](https://doi.org/10.1016/S0012-821X(03)00424-2)
- Salgado, R., Bandini, P., Karim, A., 2000. Shear strength and stiffness of silty sand. *J. Geotech. Geoenvironmental Eng.* 126, 451–462.
- Saltzer, S.D., Pollard, D.D., 1992. Distinct element modeling of structures formed in sedimentary overburden by extensional reactivation of basement normal faults. *Tectonics* 11, 165–174. <https://doi.org/10.1029/91TC02462>
- Savidge, D.K., 2002. Wintertime shoreward near-surface currents south of Cape Hatteras. *J. Geophys. Res.* 107, 3205. <https://doi.org/10.1029/2001JC001193>
- Sawyer, D.E., DeVore, J.R., 2015. Elevated shear strength of sediments on active margins: Evidence for seismic strengthening. *Geophys. Res. Lett.* 42, 10,216-10,221.  
<https://doi.org/10.1002/2015GL066603>
- Sawyer, D.E., Flemings, P.B., Buttles, J., Mohrig, D., 2012. Mudflow transport behavior and deposit morphology: Role of shear stress to yield strength ratio in subaqueous experiments. *Mar. Geol.* 307–310, 28–39. <https://doi.org/10.1016/j.margeo.2012.01.009>
- Sawyer, D.E., Reece, R.S., Gulick, S.P.S., Lenz, B.L., 2017. Submarine landslide and tsunami hazards offshore southern Alaska: Seismic strengthening versus rapid sedimentation. *Geophys. Res. Lett.* 44, 8435–8442. <https://doi.org/10.1002/2017GL074537>
- Schambach, L., Grilli, S.T., Kirby, J.T., Shi, F., 2019. Landslide Tsunami Hazard Along the Upper US East Coast: Effects of Slide Deformation, Bottom Friction, and Frequency Dispersion. *Pure Appl. Geophys.* 176, 3059–3098. <https://doi.org/10.1007/s00024-018-1978-7>
- Schellart, W.P., 2000. Shear test results for cohesion and friction coefficients for different granular materials: scaling implications for their usage in analogue modelling. *Tectonophysics* 324, 1–16.
- Schmiedel, J., 2017. Anfertigung einer Auswerterroutine zur 3D Modellierung anhand eines

- numerischen Modells. der Universität Bremen.
- Schöpfer, M.P.J., Abe, S., Childs, C., Walsh, J.J., 2009. The impact of porosity and crack density on the elasticity, strength and friction of cohesive granular materials: Insights from DEM modelling. *Int. J. Rock Mech. Min. Sci.* 46, 250–261.  
<https://doi.org/10.1016/j.ijrmms.2008.03.009>
- Schöpfer, M.P.J., Childs, C., Manzocchi, T., 2013. Three-dimensional failure envelopes and the brittle-ductile transition. *J. Geophys. Res. Solid Earth* 118, 1378–1392.  
<https://doi.org/10.1002/jgrb.50081>
- Schulten, I., Mosher, D.C., Krastel, S., Piper, D.J.W., Kienast, M., By, N.S., Kiel, C., 2018. Surficial sediment failures due to the 1929 Grand Banks Earthquake , St Pierre Slope Natural Resources Canada , Bedford Institute of Oceanography , 1 Challenger. *Geol. Soc. London*.
- Shanmugam, G., 2018. Slides, Slumps, Debris Flows, Turbidity Currents, and Bottom Currents: Implications, in: *Reference Module in Earth Systems and Environmental Sciences*. Elsevier. <https://doi.org/10.1016/B978-0-12-409548-9.04380-3>
- Sheridan, R., 1987. The Passive Margin of the U.S.A. *Episodes* 10, 254–258.
- Steventon, M., Jackson, C.-L., Johnson, H., Hodgson, D., 2020. Lateral variability of shelf edge and basin floor deposits, Santos Basin, offshore Brazil. *J. Sediment. Res.*
- Stoecklin, A., Friedli, B., Puzrin, A.M., 2017. Sedimentation as a Control for Large Submarine Landslides: Mechanical Modeling and Analysis of the Santa Barbara Basin. *J. Geophys. Res. Solid Earth* 44, 1–15. <https://doi.org/10.1002/2015JB012419>. Received
- Stoecklin, A., Trapper, P., Puzrin, A.M., 2020. Controlling factors for post-failure evolution of subaqueous landslides. *Géotechnique* 1–14. <https://doi.org/10.1680/jgeot.19.p.230>
- Sultan, N., Cochonat, P., Canals, M., Cattaneo, A., Dennielou, B., Haflidason, H., Laberg, J.S., Long, D., Mienert, J., Trincardi, F., Urgeles, R., Vorren, T.O., Wilson, C., 2004. Triggering mechanisms of slope instability processes and sediment failures on continental margins: a geotechnical approach. *Mar. Geol.* 213, 291–321.  
<https://doi.org/10.1016/j.margeo.2004.10.011>
- Talling, P., Clare, M., Urlaub, M., Pope, E., Hunt, J., Watt, S., 2014. Large Submarine Landslides on Continental Slopes: Geohazards, Methane Release, and Climate Change. *Oceanography* 27, 32–45. <https://doi.org/10.5670/oceanog.2014.38>
- Talling, P.J., 2014. On the triggers, resulting flow types and frequencies of subaqueous sediment density flows in different settings. *Mar. Geol.* 352, 155–182.  
<https://doi.org/10.1016/j.margeo.2014.02.006>

- ten Brink, U.S., Andrews, B.D., Miller, N.C., 2016. Seismicity and sedimentation rate effects on submarine slope stability. *Geology* 44, 563–566. <https://doi.org/10.1130/G37866.1>
- ten Brink, U. S., Barkan, R., Andrews, B.D., Chaytor, J.D., 2009. Size distributions and failure initiation of submarine and subaerial landslides. *Earth Planet. Sci. Lett.* 287, 31–42. <https://doi.org/10.1016/j.epsl.2009.07.031>
- ten Brink, U.S., Geist, E.L., 2021. On the Use of Statistical Analysis to Understand Submarine Landslide Processes and Assess Their Hazard, in: *Understanding and Reducing Landslide Disaster Risk*. pp. 329–341. [https://doi.org/10.1007/978-3-030-60196-6\\_23](https://doi.org/10.1007/978-3-030-60196-6_23)
- ten Brink, U.S., Lee, H.J., Geist, E.L., Twichell, D., 2009. Assessment of tsunami hazard to the U.S. East Coast using relationships between submarine landslides and earthquakes. *Mar. Geol.* 264, 65–73. <https://doi.org/10.1016/j.margeo.2008.05.011>
- Thieler, E.R., Foster, D.S., Himmelstoss, E.A., Mallinson, D.J., 2014. Geologic framework of the northern North Carolina, USA inner continental shelf and its influence on coastal evolution. *Mar. Geol.* 348, 113–130. <https://doi.org/10.1016/j.margeo.2013.11.011>
- Thornton, C., 2000. Numerical simulations of deviatoric shear deformation of granular media. *Géotechnique* 50, 43–43.
- Turcotte, D., Schubert, G., 2014. *Geodynamics*. Cambridge university press.
- Twichell, D.C., Chaytor, J.D., ten Brink, U.S., Buczkowski, B., 2009. Morphology of late Quaternary submarine landslides along the U.S. Atlantic continental margin. *Mar. Geol.* 264, 4–15. <https://doi.org/10.1016/j.margeo.2009.01.009>
- Urgeles, R., Camerlenghi, A., 2013. Submarine landslides of the Mediterranean Sea: Trigger mechanisms, dynamics, and frequency-magnitude distribution. *J. Geophys. Res. Earth Surf.* 118, 2600–2618. <https://doi.org/10.1002/2013JF002720>
- Urlaub, M., Talling, P.J., Zervos, A., Masson, D., 2015. What causes large submarine landslides on low gradient (<2) continental slopes with slow (~0.15 m/kyr) sediment accumulation? *J. Geophys. Res. Solid Earth* 120, 6722–6739. <https://doi.org/10.1002/2015JB012347>
- Vachtman, D., Mitchell, N.C., Gawthorpe, R., 2013. Morphologic signatures in submarine canyons and gullies, central USA Atlantic continental margins. *Mar. Pet. Geol.* 41, 250–263. <https://doi.org/10.1016/j.marpetgeo.2012.02.005>
- van Gent, H.W., Holland, M., Urai, J.L., Loosveld, R., 2010. Evolution of fault zones in carbonates with mechanical stratigraphy - Insights from scale models using layered cohesive powder. *J. Struct. Geol.* 32, 1375–1391.

- <https://doi.org/10.1016/j.jsg.2009.05.006>
- Vanneste, M., Sultan, N., Garziglia, S., Forsberg, C.F., L'Heureux, J.S., 2014. Seafloor instabilities and sediment deformation processes: The need for integrated, multi-disciplinary investigations. *Mar. Geol.* 352, 183–214.  
<https://doi.org/10.1016/j.margeo.2014.01.005>
- Verrucci, L., Tommasi, P., Boldini, D., Graziani, A., Rotonda, T., 2019. Modelling the instability phenomena on the NW flank of Stromboli Volcano (Italy) due to lateral dyke intrusion. *J. Volcanol. Geotherm. Res.* 371, 245–262.  
<https://doi.org/10.1016/j.jvolgeores.2019.01.007>
- Vousdoukas, M.I., Mentaschi, L., Voukouvalas, E., Verlaan, M., Jevrejeva, S., Jackson, L.P., Feyen, L., 2018. Global probabilistic projections of extreme sea levels show intensification of coastal flood hazard. *Nat. Commun.* 9, 2360.  
<https://doi.org/10.1038/s41467-018-04692-w>
- Wanatowski, D., Chu, J., 2008. Undrained behaviour of Changi sand in triaxial and plane-strain compression. *Geomech. Geoengin.* 3, 85–96.  
<https://doi.org/10.1080/17486020701742608>
- Wang, Q. J., Zhu, D., 2013. Hertz Theory: Contact of Spherical Surfaces, in: Wang, Q. Jane, Chung, Y.-W. (Eds.), *Encyclopedia of Tribology*. Springer US, Boston, MA.  
<https://doi.org/10.1007/978-0-387-92897-5>
- Weber, M.E., Niessen, F., Kuhn, G., Wiedicke, M., 1997. Calibration and application of marine sedimentary physical properties using a multi-sensor core logger. *Mar. Geol.* 136, 151–172. [https://doi.org/10.1016/S0025-3227\(96\)00071-0](https://doi.org/10.1016/S0025-3227(96)00071-0)
- Wenk, L., Huhn, K., 2013. The influence of an embedded viscoelastic–plastic layer on kinematics and mass transport pattern within accretionary wedges. *Tectonophysics* 608, 653–666. <https://doi.org/10.1016/j.tecto.2013.08.015>
- Wentworth, C.K., 1922. A Scale of Grade and Class Terms for Clastic Sediments. *J. Geol.* 30, 377–392. <https://doi.org/10.1086/622910>
- Wiemer, G., Dziadek, R., Kopf, A., 2017. The enigmatic consolidation of diatomaceous sediment. *Mar. Geol.* 385, 173–184. <https://doi.org/10.1016/j.margeo.2017.01.006>
- Wiemer, G., Moernaut, J., Stark, N., Kempf, P., De Batist, M., Pino, M., Urrutia, R., De Guevara, B.L., Strasser, M., Kopf, A., 2015. The role of sediment composition and behavior under dynamic loading conditions on slope failure initiation: a study of a subaqueous landslide in earthquake-prone South-Central Chile. *Int. J. Earth Sci.* 1439–1457. <https://doi.org/10.1007/s00531-015-1144-8>

- Yamada, Y., Yamashita, Y., Yamamoto, Y., 2010. Submarine landslides at subduction margins: Insights from physical models. *Tectonophysics* 484, 156–167.  
<https://doi.org/10.1016/j.tecto.2009.09.007>
- Yamamoto, T., Nye, T., Kuru, M., 1994. Porosity, permeability, shear strength: Crosswell tomography below an iron foundry, *GEOPHYSICS*.
- Yamamuro, J.A., Abrantes, A.E., Lade, P. V., 2011. Effect of Strain Rate on the Stress-Strain Behavior of Sand. *J. Geotech. Geoenvironmental Eng.* 137, 1169–1178.  
[https://doi.org/10.1061/\(ASCE\)GT.1943-5606.0000542](https://doi.org/10.1061/(ASCE)GT.1943-5606.0000542)
- Yao, M., Anandarajah, A., 2003. Three-dimensional discrete element method of analysis of clays. *J. Eng. Mech.* 129, 585–596. [https://doi.org/10.1061/\(ASCE\)0733-9399\(2003\)129:6\(585\)](https://doi.org/10.1061/(ASCE)0733-9399(2003)129:6(585))
- Yenes, M., Monterrubio, S., Nespereira, J., Casas, D., 2020. Apparent overconsolidation and its implications for submarine landslides. *Eng. Geol.* 264.  
<https://doi.org/10.1016/j.enggeo.2019.105375>
- Yimsiri, S., Soga, K., 2011. Effects of soil fabric on behaviors of granular soils: Microscopic modeling. *Comput. Geotech.* 38, 861–874.  
<https://doi.org/10.1016/j.compgeo.2011.06.006>
- Zhang, S., Luo, Y., Rothstein, L.M., Gao, K., 2016. A numerical investigation of the interannual-to-interpentadal variability of the along-shelf transport in the Middle Atlantic Bight. *Cont. Shelf Res.* 122, 14–28. <https://doi.org/10.1016/j.csr.2016.03.022>



## **השפעת התכונות הפיזיקליות של הסדימנט על התניית יצירתן של**

**גלישות תת ימיות:**

**מחקר סדימנטולוגי ונומרי**

מוגש על ידי:

**הדר אלישיב**

דוקטורט פרסומים

הוגש כחלק ממילוי הדרישות לתואר דוקטור תחת ההסכם הדו-לאומי בין הפקולטה למדעי הגאולוגיה שבאוניברסיטת ברמן (גרמניה) לבין הפקולטה למדעי הטבע שבאוניברסיטת חיפה (ישראל).

ברמן, אוגוסט 2021